



**FACULTY OF PHYSICS, ASTRONOMY AND  
INFORMATICS**

---

# **Towards Autonomous Operation of Optical Atomic Clocks and Tweezers Machine**

---

*Author:*  
**Mehrdad Zarei**

*Supervisors:*  
**Michał Zawada**  
**Piotr Morzyński**

Toruń, October 2024





# Funding

This project 18SIB05 ROCIT has received funding from the EMPIR programme co-financed by the Participating States and from the European Union's Horizon 2020 research and innovation programme. This project has received funding from the European Union's Horizon 2020 Research and Innovation Programme No 820404, (iq-Clock project). This project has received funding from the European Union's Horizon 2020 research and innovation programme under grant agreement No 860579 (MoSaiQC project). The project is partially performed at the National Laboratory FAMO (KL FAMO) in Toruń, Poland and were supported by a subsidy from the Polish Ministry of Science and Higher Education.

# Acknowledgments

First and foremost, I would like to express my deepest gratitude to my supervisors, Michał Zawada and Piotr Morzyński, for their support, guidance, and mentorship throughout my PhD. I am incredibly grateful for the opportunities and knowledge they have provided me.

I am incredibly grateful to Marcin Bober and Sławomir Bilicki for their friendship, collaboration, and the scientific discussions that helped shape this work. I extend my thanks to Omid Vartehparvar and all other my colleagues at the KL FAMO lab for their help and friendship, which made my time in the lab both productive and enjoyable. To Monika Czajkowska and all other staff for their help with endless paperwork we had to make this thesis possible.

I would also like to acknowledge Florian Schreck, Alexander Urech, Ivo Knottnerus and all other my colleagues in the Strontium Quantum Gas Group for their invaluable support during my secondment in Amsterdam. Additionally, I extend my gratitude to Sana at Toptica for her assistance during my visit and for helping me carry out to test my developed program on their laser.

I am deeply appreciative of all my colleagues involved in the MoSaiCQ project, whose collaborative spirit and shared passion for science were truly inspiring. I am also thankful to Ineke Brouwer, the project manager, for ensuring everything ran smoothly.

Lastly, I wish to give my heartfelt thanks to my wonderful wife Spozmai Panezai, who became a part of my life at the beginning of this journey and has been a constant source of love and encouragement ever since. To my son Eissa, who joined us at the end of my PhD, you have been the brightest light in these final stages. I also want to thank my parents for their unconditional love and support, allowing me to pursue my studies far from home.



# Abstract

In this thesis, I present my contribution to optical atomic clocks and tweezers machines to make these complicated experiments more robust and easy to operate in clock and Rydberg spectroscopy, respectively. Therefore, I am presenting two sets of results for the performance of the automatic system and real measurement while the experiments are automatic.

In the first part of this thesis, I describe the development of an automatic system for stabilizing lasers and auto relocking them after the introduction and theory. Alongside building an autonomous and robust optical atomic clock, an automatic control system has been developed for compensation coils to control magnetic fields during the clock cycle and for direct digital synthesis (DDS). These systems have been built and tested successfully in optical atomic clock and tweezer machines at Nicolaus Copernicus University and the University of Amsterdam, respectively.

In the second part, after implementing these automation systems in the experiments, I performed clock spectroscopy to measure the temperature of the strontium (Sr) atoms in the ground state in the lattice, linewidth of the clock line, and Rabi oscillation. Zeeman shift and probe light shift have been measured as well. In the end, the stability of the atom-cavity was measured during campaign 2022 and has been compared with campaign 2015.

Additionally, the temperature of atoms in the lattice has been measured while they are excited on  $^3P_0$  state. This measurement is to study the temperature changes of the trapped Sr atoms in the lattice after interacting with a magic-zero wavelength at 390 nm. Unfortunately, as the 390 nm laser was broken, there was no possibility of studying the effect of magic-zero on the trapped Sr atoms.

The auto relocking system has also been tested successfully in an optical tweezers machine project for the Rydberg laser. Additionally, I have characterized the Rydberg laser locked to the cavity. In the end, a Rydberg spectroscopy was performed while the Rydberg laser was locked by this system.

# Streszczenie

W niniejszej pracy przedstawiam mój wkład w dziedzinie optycznych zegarów atomowych oraz układów z optycznymi szczypcami, aby uczynić te skomplikowane eksperymenty bardziej stabilnymi i łatwiejszymi w obsłudze w zegarze oraz spektroskopii stanów Rydbergowskich. Dlatego przedstawiam dwa zestawy wyników dotyczących wydajności automatycznego systemu oraz rzeczywistych pomiarów, gdy eksperymenty są zautomatyzowane.

W pierwszej części tej pracy opisuję teorię oraz rozwój automatycznego systemu do stabilizacji laserów. Wraz z budową autonomicznego i stabilnego optycznego zegara atomowego, został opracowany automatyczny system sterowania cewkami kompensacyjnymi do kontroli pól magnetycznych podczas cyklu pracy zegara oraz kontroli cyfrowych generatorów częstotliwości (DDS). Systemy te zostały zbudowane i pomyślnie przetestowane w zegarach atomowych oraz eksperymencie z optycznymi szczypcami, na Uniwersytecie Mikołaja Kopernika oraz Uniwersytecie Amsterdamskim.

W drugiej części, po wdrożeniu tych systemów automatyzacji w eksperymentach, przeprowadziłem spektroskopię zegarową, aby zmierzyć temperaturę atomów strontu (Sr) w stanie podstawowym w sieci optycznej, szerokość linii zegarowej oraz oscylacje Rabiego. Zostały również zmierzone przesunięcie Zeemana i przesunięcie Starka. Na końcu zmierzono stabilność wnęki atomowej podczas kampanii z 2022 roku i porównano ją z kampanią z 2015 roku.

Dodatkowo zmierzono temperaturę atomów w sieci optycznej podczas ich wzbudzenia do stanu  $^3P_0$ . Pomiar ten ma na celu zbadanie zmian temperatury uwięzionych atomów Sr w sieci po interakcji z magiczną zerową długością fali wynoszącą 390 nm. Niestety, z powodu awarii lasera o długości 390 nm, nie było możliwości zbadania wpływu światła o częstotliwości "zero magic" na uwięzione atomy Sr.

System automatycznej stabilizacji został również pomyślnie przetestowany w eksperymencie z optycznymi szczypcami dla lasera Rydberga. Dodatkowo scharakteryzowałem laser Rydberga stabilizowany do wnęki. Na końcu przeprowadzono spektroskopię stanów Rydbergowskich, podczas której laser Rydberga był stabilizowany przez ten system.



# Contents

<b>Funding</b>	<b>i</b>
<b>Acknowledgments</b>	<b>ii</b>
<b>Abstract</b>	<b>iv</b>
<b>Streszczenie</b>	<b>v</b>
<b>1 Introduction</b>	<b>1</b>
1.1 Laser in cold atom experiment . . . . .	1
1.1.1 External cavity diode laser . . . . .	1
1.1.2 Laser frequency stabilization . . . . .	3
1.2 Laser spectroscopy . . . . .	5
1.3 Atomic clocks . . . . .	6
1.3.1 Sr clock in KL FAMO . . . . .	8
1.4 Optical Tweezers in quantum simulation . . . . .	8
1.5 Outline . . . . .	10
<b>2 Theory</b>	<b>14</b>
2.1 Magneto-optical trap . . . . .	14
2.2 Strontium . . . . .	15
2.3 Dipole trap . . . . .	16
2.3.1 Magic wavelength . . . . .	18
2.3.2 Lamb-Dicke regime . . . . .	19
2.3.3 Temperature measurement . . . . .	24
2.4 Ultra-precise spectroscopy . . . . .	25
2.5 Rabi oscillation . . . . .	27
2.6 Evaluation of systematic shifts . . . . .	29
2.6.1 Zeeman shift . . . . .	29
2.6.2 Probe light shift . . . . .	30
<b>3 Designing an automated control system for compensation coils</b>	<b>33</b>
3.1 Introduction . . . . .	33
3.2 Hardware and software . . . . .	34
3.3 Flow chart and algorithm . . . . .	36
3.4 Test . . . . .	38

<b>4</b>	<b>Designing a control system for direct digital synthesis</b>	<b>42</b>
4.1	Introduction . . . . .	42
4.2	Hardware and software . . . . .	43
4.3	Flow chart and algorithm . . . . .	44
4.4	Test . . . . .	45
<b>5</b>	<b>Automatic relocking program</b>	<b>49</b>
5.1	Introduction . . . . .	49
5.2	Experimental setup . . . . .	50
5.2.1	Schematic diagram . . . . .	50
5.2.2	Setup . . . . .	52
5.2.3	Experiment performed in Toptica company . . . . .	52
5.3	Flow chart and algorithm . . . . .	53
5.3.1	Scanning procedure . . . . .	55
5.3.2	Optimisation . . . . .	57
5.3.3	Relocking by cavity transmission and/or wavemeter . . . . .	59
5.4	GUI settings . . . . .	61
5.4.1	First version . . . . .	61
5.4.2	Second version . . . . .	62
5.5	Results . . . . .	63
5.5.1	Relocking by cavity transmission and/or wavemeter . . . . .	64
5.5.2	Laser drift . . . . .	67
5.5.3	Tests in Toptica company . . . . .	73
<b>6</b>	<b>Strontium optical atomic clock</b>	<b>76</b>
6.1	Introduction . . . . .	76
6.1.1	Vacuum chamber and Zeeman slower . . . . .	76
6.1.2	Laser cooling . . . . .	78
6.1.3	Optical lattice . . . . .	81
6.1.4	Clock interrogation . . . . .	82
6.2	Optimization . . . . .	86
6.3	Lattice lifetime measurement . . . . .	92
6.4	Clock spectroscopy . . . . .	93
6.4.1	Temperature measurement on ground state . . . . .	95
6.4.2	Temperature measurement on excited state . . . . .	95
6.4.3	Clock line measurement . . . . .	96
6.4.4	Rabi oscillation . . . . .	98
6.5	Evaluation of systematic shifts . . . . .	99
6.5.1	Zeeman shift . . . . .	99
6.5.2	Probe light shift . . . . .	99
6.6	Campaign's comparison . . . . .	100
<b>7</b>	<b>Optical tweezers machine</b>	<b>104</b>
7.1	Introduction . . . . .	104
7.2	Experimental setup . . . . .	105
7.2.1	Schematic diagram . . . . .	105
7.2.2	Setup . . . . .	107
7.3	Web application for auto relocking . . . . .	109



7.4	Red laser lock . . . . .	109
7.4.1	Cavity characterization . . . . .	109
7.4.2	Laser linewidth . . . . .	110
7.5	Rydberg spectroscopy . . . . .	111
<b>Summary and conclusions</b>		<b>115</b>
<b>Appendix A Instruction to work with automated control system for magnetic field</b>		<b>117</b>
<b>Appendix B Registering and instruction to work with DDS</b>		<b>120</b>
<b>Appendix C Step-by-step instructions for auto relocking of the ECDLs by Python</b>		<b>124</b>
<b>Appendix D Auto relocking resources using Red Pitaya</b>		<b>129</b>
<b>Bibliography</b>		<b>139</b>

# List of Figures

1.1	a) Littrow configuration and a movable optical element (grating) for tuning the laser's frequency by a piezoelectric transducer (PZT) which is attached to the grating. b) Selection mode of ECDL. Taken from [5]. . .	2
1.2	Interferometer pattern of ECDL while operating in a) single-mode and b) multi-mode. The graph's horizontal axis represents the pixel number of the CCD line array. The vertical axis represents the light intensity for the given pixel in arbitrary units. . . . .	2
1.3	Schematic of PDH method for laser locking. Abbreviations: EOM- electro-optic modulator, PBS- polarising beam splitter, PD- photodetector, $\frac{\lambda}{4}$ - quarterwave plate, LD- laser diode. . . . .	3
1.4	PDH error signal, when the modulation frequency is high with 10% of the $\Delta\nu_{FSR}$ . . . . .	5
1.5	Ramsey and Rabi spectroscopy revealed spectroscopic lineshapes in an $^{87}\text{Sr}$ lattice clock. Laser excitation techniques are shown above. Rabi spectroscopy (right) produces a single fringe when scanning the laser across resonance, while Ramsey spectroscopy produces a fringe pattern. The width of the fringes is inversely proportional to the free evolution time between excitation pulses. Taken from [10]. . . . .	6
1.6	Passive atomic clock system. An atomic cloud is used to stabilize the local oscillator. Taken from [12]. . . . .	7
1.7	A simplified scheme of two optical lattice clocks in KL FAMO lab. Two ultrastable lasers (689 and 698 nm) are inside the cavity room with two repumpers (679 and 707 nm). The optical frequency comb is inside another room, which is not included in this schematic. . . . .	8
1.8	A schematic of the optical tweezers created by a high numerical aperture objective (NA = 0.5). The objective is also to collect the atomic fluorescence from imaging. Taken from [36]. . . . .	9
1.9	Different patterns of single atoms trapped in tweezers arranged by light modulators. All the images are averaged from many fluorescence imaging. Taken from [36]. . . . .	9
1.10	The simplified schematic for the Rydberg laser design in optical tweezers experiment. The UV output beam is used for the Rydberg spectroscopy. Taken from [37]. . . . .	10
2.1	a) The setup of MOT includes two pairs of coils with anti-Helmholtz configuration and optical molasses beams, red detuned and circularly polarized. b) Energy shift for the sublevels in a uniform magnetic field gradient and linearly increasing from the center. Taken from [8]. . . .	15

2.2	Energy level diagram of bosonic strontium, which is important for clock operation. Taken from [38]. . . . .	17
2.3	The light-shift for $^1S_0 - ^3P_0$ states of Sr atoms based on the lattice laser wavelength. The intersection of two curves at 813.4 nm is the magic wavelength. Taken from [39]. . . . .	19
2.4	Schematic concept of the optical power buildup cavity for 1D optical lattice trap. Taken and modified from [39]. . . . .	19
2.5	Clock laser spectroscopy under Lamb-Dicke regime. . . . .	20
2.6	Clock transition spectroscopy. a) From ground state to excited state, b) from excited state to ground state. . . . .	23
2.7	Transition probability for sidebands and carrier. a) Only sidebands from Equation 2.38, b) Sidebands and carrier both at the same time. . . . .	25
2.8	Linewidth limitation measurement due to the Fourier transform. a) Pulse time to interrogate with trapped Sr atoms, b) corresponding power spectrum. . . . .	27
2.9	Rabi oscillation. a) Without radial motion effect, plotted by Equation 2.50, b) effected by radial motion as it is in Equation 2.52. . . . .	28
3.1	Compact current driver controller for compensation coils. This compact device has 3 outputs (ch 1, ch 2, and ch 3) for three pairs of coils in x, y, and z directions. The compact device is accessible through Ethernet, and the configuration of TTL signals is used to define which current values should be applied for each pair of coils. . . . .	34
3.2	Diagram of compensation coils controller board [84]. . . . .	35
3.3	The compensation coils installed around the science chamber for lattice optical clock in Sr1 room in KL FAMO lab. . . . .	37
3.4	3D drawing of the configuration of the compensation coils around the science chamber in a general case. . . . .	37
3.5	The working principle of the compact current driver controller. . . . .	38
3.6	Flow chart of the algorithm running in two threads. One thread handles the clients to read and save new values on the memory. Other thread handles the events like set bit signal (TTL4) to switch output values on the current driver. . . . .	38
3.7	The implementation of applying a ramp signal while changing the voltage on the current driver proportional to the current on the coils. The orange color is when the voltage is changed without a ramp signal, and the blue color is when the voltage is changed with a ramp signal. . . . .	39
3.8	Voltage change during each cycle of the clock for MOT coils (yellow) and coils on the Y axis connected to channel 2 (blue). . . . .	40
3.9	Voltage change during one clock cycle for main coils and all the compensation coils [84]. Blue shows how the voltage on the main coils for the MOT changes in each state, and orange, yellow, and purple colors show the voltage changes for compensation coils on the X, Y, and Z axes, respectively. . . . .	40
4.1	A compact module for controlling the DDS board, including an evaluation board, an electronic board, and a microcontroller (NUCLEO-H743ZI2). . . . .	43

4.2	Evaluation board, which has been modified for this project. . . . .	44
4.3	Schematic of evaluation board which shows two resistors for selecting SYSCLK PLL bypassed or enabled. To use SYSCLK PLL as enabled, R24 should be removed and R3 connected. . . . .	45
4.4	A schematic diagram of DDS controller in the experiments. . . . .	45
4.5	Flow chart of the algorithm, working in an infinite loop. . . . .	46
4.6	Output of DDS AD9912. This frequency has been applied remotely through the Ethernet on the device. . . . .	47
5.1	Schematic diagram of the auto relocking system in the experiment [94]. Abbreviations: PD- photodetector, ADC- analog-to-digital converters, and DAC- digital-to-analog converter. . . . .	51
5.2	Experimental setup to perform auto relocking of ECDL. a) DAQ card, b) laser driver, c) ECDL, d) wavemeter. . . . .	52
5.3	Server program running on wavemeter computer which sends the infor- mation of laser beam to the client (Auto Relocking program). . . . .	53
5.4	Auto relocking program running on the computer. . . . .	54
5.5	Schematic of Auto Relocking program. . . . .	55
5.6	Scanning procedure to relock the laser. a) Normal procedure scanning, b) small scanning range, c) reverse direction, d) switch start direction strategies. . . . .	56
5.7	Flow chart of the algorithm for relocking by cavity transmission and/or wavemeter. . . . .	59
5.8	GUI developed using PyQt5 for auto relocking of the laser. . . . .	62
5.9	Switch mode of GUI. . . . .	63
5.10	Overview tab for the extra setting of GUI. . . . .	63
5.11	Auto relocking program when it is running. . . . .	64
5.12	Relocking procedure by wavemeter for 707 nm ECDL in 12 minutes test. The frequency difference is the present laser beam frequency devi- ation from the target frequency at 423.91355 THz. . . . .	65
5.13	Relocking procedure by cavity transmission and wavemeter for 689 nm ECDL in 11 minutes test. The frequency difference is the present laser beam frequency deviation from the target frequency at 434.82920 THz. . . . .	66
5.14	Relocking procedure by wavemeter for TiSa laser in 14 minutes test. The frequency difference is the present laser beam frequency deviation from the target frequency at 376.86015 THz. . . . .	66
5.15	Histogram of the relock time for relocking by wavemeter for 707 nm ECDL for about 30 hours test. In this test, 55 times, the laser was un- locked, and the relock time took about 1 second for most of the time. . . . .	67
5.16	Histogram of the relock time for relocking by wavemeter for 679 nm ECDL for about 24 hours test. In this test, 48 times, the laser was un- locked, and the relock time took about 1 second for most of the time. . . . .	68
5.17	Histogram of the relock time for relocking by cavity and wavemeter for 689 nm ECDL for about 24 hours test. . . . .	68

5.18	Histogram of the relock time for relocking by wavemeter for 707 nm laser when laser drift is off for one-week measurement. In this test, 266 times, the laser was unlocked, and the relock time took about 1 second for most of the time. . . . .	69
5.19	Histogram of the relock time for relocking by wavemeter for 707 nm laser when laser drift is on for one-week measurement. In this test, 412 times, the laser was unlocked, and the relock time took about 1 second for most of the time. . . . .	70
5.20	Histogram of the relock time for relocking by wavemeter for 679 nm laser when laser drift is off for one-week measurement. In this test, 254 times, the laser was unlocked, and the relock time took about 1 second for most of the time. . . . .	70
5.21	Histogram of the relock time for relocking by wavemeter for 679 nm laser when laser drift is on for one-week measurement. In this test, 387 times, the laser was unlocked, and the relock time took about 1 second for most of the time. . . . .	71
5.22	Histogram of the relock time for relocking by cavity transmission and wavemeter for 689 nm laser when laser drift is off for one-week measurement. In this test, 362 times, the laser was unlocked, and the relock time took about 1 second for most of the time. . . . .	71
5.23	Histogram of the relock time for relocking by cavity transmission and wavemeter for 689 nm laser when laser drift is on for one-week measurement. In this test, 255 times, the laser was unlocked, and the relock time took about 1 second for most of the time. . . . .	72
5.24	Relocking procedure of 1064 nm ECDL by the wavemeter in Toptica company in 15 minutes test. The frequency difference is the present laser beam frequency deviation from the target frequency at 281.79220 THz. . . . .	74
5.25	Histogram of the relock time for relocking by wavemeter for 1064 nm laser in Toptica company for 45 hours measurement. In this test, 19 times, the laser was unlocked, and the relock time took about 2 seconds for most of the time. . . . .	74
6.1	Schematic of the ultrahigh vacuum setup of the lattice clock in Sr1 room. The setup consists of an oven, a Zeeman slower, and a vacuum chamber. Blue and red arrows indicate laser beams; green arrows indicate the atomic beam. Taken and modified from [27]. . . . .	77
6.2	A view of the vacuum chamber in Sr1 room for the lattice clock. . . . .	77
6.3	Frequency detuning for different blue laser beams from $^1S_0 - ^1P_1$ resonance. The blue laser is 150 MHz red detuned from resonance; therefore, it needs to be red detuned 350 MHz more for Zeeman slower, 110 MHz blue detuned for 3D MOT cooling, and 150 MHz blue detuned for saturation spectroscopy and probe beam. . . . .	79

6.4	Optical setup schematic for 461 nm blue laser in Sr1 room. There are four AOMs to shift the frequency of the laser beam for each part of the experiment based on Figure 6.3. AOM 1 and 2 shift the frequency of the laser beam to the $^1S_0 - ^1P_1$ resonance for saturation spectroscopy and probe beam, respectively. AOM 3 and 4 are for Zeeman slower and 3D MOT, respectively. Abbreviations: PBS- polarising beam splitter, AOM- acousto-optic modulator, PD- photodetector, IF- interference filter, HCL- hollow cathode lamp, $\frac{\lambda}{2}$ - half-wave plate, $\frac{\lambda}{4}$ - quarterwave plate. Schematic is taken from [38]. . . . .	79
6.5	Optical setup for blue laser in Sr1 room related to Figure 6.4. . . . .	80
6.6	Frequency detuning for different red laser beams from $^1S_0 - ^3P_1$ resonance. The red laser is 212 MHz red detuned from resonance; therefore, it needs to be red detuned 222 MHz more for injection to slave laser, then from slave laser, 433.16 MHz blue detuned for red MOT A and 433.912 MHz blue detuned for red MOT B. . . . .	81
6.7	Optical setup schematic for 689 nm red laser cooling in Sr1 room. The red laser beam from the master, after locking to the frequency comb, is transferred to Sr1 room, and the frequency is red detuned by 212 MHz from resonance. From there, it needs to be red detuned 222 MHz more with AOM 5 for injection to slave laser based on Figure 6.6. AOM 6 shifts the frequency of the laser beam by 433.16 MHz blue detuned for red MOT A and 433.912 MHz blue detuned for red MOT B. Abbreviations: PBS- polarising beam splitter, AOM- acousto-optic modulator, PD- photodetector, IF- interference filter, FI- Faraday isolator, $\frac{\lambda}{2}$ - half-wave plate, $\frac{\lambda}{4}$ - quarterwave plate. . . . .	81
6.8	Optical setup for red laser cooling in Sr1 room related to Figure 6.7. . .	82
6.9	Frequency detuning for clock laser beam from $^1S_0 - ^3P_0$ resonance. The clock laser beam frequency in the Sr1 room for slave laser has a 404 MHz difference from resonance; therefore, it must be red detuned 404 MHz for clock spectroscopy. . . . .	83
6.10	Optical setup schematic for 698 nm clock laser in Sr1 room with phase noise cancellation. The clock laser beam from the slave has been red detuned by 404 MHz with AOM 16 based on Figure 6.9. Abbreviations: PBS- polarising beam splitter, GT pol.- Glam-Taylor polariser, LO- local oscillator, BS- beam splitter, AOM- acousto-optic modulator, PD- photodetector, IF- interference filter, FI- Faraday isolator, $\frac{\lambda}{2}$ - half-wave plate, $\frac{\lambda}{4}$ - quarterwave plate, DDS- direct digital synthesiser, MIX- mixer, PC- phase comparator, PI- proportional–integral controller, SG- signal generator, AMP- operational amplifier. Schematic is taken from [38] with some modification. . . . .	83
6.11	Optical setup for clock laser to go through the chamber in Sr1 room. . .	84
6.12	The clock and lattice laser beams while not overlapping on the beam profiler. . . . .	84
6.13	The whole sequence of the clock operation in each cycle [27]. $N_g$ , $N_e$ , and $N_b$ in detection by probe beam are used to calculate the transition probability by Equation 6.1. . . . .	85

6.14	Clock sequence for sideband spectroscopy from $^3P_0 - ^1S_0$ . The big dashed box is a new procedure added to the main sequence of the clock operation in Figure 6.13. Rep. in the detection part stands for repumpers.	85
6.15	Scanning frequency of blue laser beam for the Zeeman slower using AOM 3. (Top) coarse scanning with 5 MHz steps, (bottom) fine scanning with 1 MHz steps. The maximum number of trapped atoms achieved with 175 MHz red detuned. The measurement has been repeated only once. . . . .	87
6.16	Scanning frequency of blue laser beam for blue MOT by AOM 4 with a 2.5 MHz scanning step. The maximum number of trapped atoms was achieved with 117.5 MHz blue detuned. The measurement has been repeated only once. . . . .	88
6.17	Estimated time to turn off the blue MOT at 375 ms roughly from the starting of the blue MOT. The measurement has been repeated six times.	88
6.18	Scanning frequency of red laser beam for red MOT A laser by AOM 6. The maximum number of trapped atoms achieved with 216.56 MHz ( $\times 2 = 433.12$ MHz) blue detuned. The measurement has been repeated only once. . . . .	89
6.19	The optimal quadrupole magnetic field ramp time from 3 to 10 G/cm during red MOT A. The maximum number of trapped atoms in the lattice is achieved when the magnetic field rises during 7 ms. The measurement has been repeated six times. . . . .	90
6.20	Scanning RF amplitude on DDS for AOM 6 in red MOT B. The maximum number of trapped atoms in the lattice is achieved when the RF amplitude is set at 8 percent. The measurement has been repeated only once. . . . .	90
6.21	Scanning frequency on AOM 6 for red MOT B. The maximum number of trapped atoms achieved with 216.96 MHz ( $\times 2 = 433.92$ MHz) blue detuned. The measurement has been repeated six times. . . . .	91
6.22	The optimal time for turning off red MOT B is after 60 ms of illuminating red laser. The measurement has been repeated seven times. . . . .	91
6.23	Scanning voltage of compensation coils on the Z axis. The maximum number of trapped atoms is achieved with applying 0.6 V voltage on the pair of coils for the Z axis. The voltage on the X and Y axis was set at zero. The measurement has been repeated eleven times. . . . .	92
6.24	Scanning voltage of compensation coils on 3D axis. The maximum number of trapped atoms is achieved with applying -0.5, -0.5, and 0.5 V voltage on the pair of coils for the X, Y, and Z axes, respectively. The measurement has been repeated only once. . . . .	93
6.25	Trapped atoms in the lattice: a) before optimization, b) after optimization.	94
6.26	Lifetime of Sr atoms in the lattice. By fitting equation 6.3 to the dataset, the lifetime is achieved with 1611 ms. The measurement has been repeated twelve times. . . . .	94
6.27	Scanning the clock laser frequency with AOM 16 to determine the clock line. The clock transition is around 101.064 MHz on DDS or 404.256 MHz on the clock laser frequency red detuned. The measurement has been repeated only once. . . . .	95

6.28	Sideband spectroscopy with fitting the Equations 2.38 and 2.39 to the measured data to find out the transverse temperature ( $T_r$ ) for the trapped atoms. $T_r = 6.2$ (1.7) $\mu K$ is approximated and $T_z = 2.5$ (1.1) $\mu K$ calculated from Equation 2.37. The measurement has been repeated only once. . . . .	96
6.29	Sideband spectroscopy with fitting the Equations 2.38 and 2.39 to the measured data to find out the transverse temperature ( $T_r$ ) for the trapped atoms on the excited state. $T_r = 5.7$ (1.0) $\mu K$ is approximated and $T_z = 1.7$ (0.4) $\mu K$ calculated from Equation 2.40. The measurement has been repeated only once. . . . .	97
6.30	Clock spectroscopy and the Lorentzian function (Equation 2.39) fitted to the data for two different magnetic fields and intensity of clock laser beam with 200 ms interrogation time. a) Higher magnetic field and clock laser beam intensity (FWHM = 42 (1) Hz), b) lower magnetic field and clock laser beam intensity (FWHM = 3 (1) Hz). RF power on the DDS applied on the AOM 16 (Figure 6.10) is used to control the intensity of the clock laser beam. The measurement has been repeated only once. . .	97
6.31	Sr atoms in the ground state (Photo 0 on the left) and excited state (Photo 1 on the right) after interrogation. a) The clock laser frequency is off-resonance, and b) the clock laser frequency is on resonance. . . . .	98
6.32	a) Rabi oscillations with the radial temperature of 5.9 $\mu K$ and longitudinal frequency 66.7 kHz. The Rabi oscillation is achieved at 59 (1) ms. b) Rabi oscillations with the radial temperature of 4.2 $\mu K$ and longitudinal frequency 58.2 kHz. The Rabi oscillation is achieved at 58 (2) ms. The measurement has been repeated only once. . . . .	99
6.33	Quadratic Zeeman shift for different voltages on the current driver (corresponding to the current in the coils). A parabola $\Delta_B^{(2)} = a + cB^2$ function has been fitted to the measured data. The measurement has been repeated only once. . . . .	100
6.34	Probe light shift for different probe light powers using the AOM 16 (Figure 6.10). A linear function has been fitted to the measured data. The measurement has been repeated only once. . . . .	101
6.35	Comparing atom-cavity's stability during campaigns 2015 and 2022. The graph shows the Allan deviation of the frequency difference between the Sr1 clock and the ultra-stable cavity. . . . .	101
7.1	Fluorescence image taken from an array of single Sr atoms trapped in tweezers. . . . .	105
7.2	Histogram of the number of collected photons in the tweezer ROI. . . .	105
7.3	Energy level diagram of bosonic strontium, which is important for optical tweezers machine. Taken from [36]. . . . .	106
7.4	Schematic diagram of the auto relocking system for the Rydberg laser [103]. . . . .	107
7.5	Experimental setup for the laser driver on the right and the Red Pitaya on the left. . . . .	108
7.6	Optical setup for the transfer cavity to lock the cavity and 633 nm laser by PDH method. . . . .	108



7.7	Schematic diagram for the transfer cavity to lock the cavity and 633 nm laser by PDH method. Abbreviations: PBS- polarising beam splitter, EOM- electro-optic modulator, PD- photodetector, $\frac{\lambda}{4}$ - quarterwave plate, DM- dichroic mirror, CAM- camera. Taken and modified from [37].	108
7.8	Developed web application on Red Pitaya for auto relocking of the Rydberg laser. . . . .	109
7.9	Web application and monitoring system for Relocking Rydberg laser and transfer lock cavity [103]. . . . .	110
7.10	The error signal described by equation 1.6 is fitted to the measured data.	111
7.11	Averaged cavity linewidth after many times measuring the error signal. .	111
7.12	The linear fit around the locking point of the error signal. . . . .	112
7.13	Frequency deviation of the error signal time series. . . . .	112
7.14	Laser linewidth, after measuring many times the error signal. . . . .	113
7.15	Rydberg spectroscopy with 100 percent power of the UV laser and 500 $\mu s$ duration of UV light. The measurement has been repeated only once.	113
A.1	Applying state 1 (001) to the coils through the real-time program. . . .	119
C.1	Server program running on the computer, which the wavemeter is installed on. . . . .	127
C.2	Auto relocking program when it is running. . . . .	128
D.1	GitHub QR Code . . . . .	129
D.2	YouTube QR Code . . . . .	129

# List of Tables

3.1	The pattern directs the controller output to the pre-programmed value. .	35
5.1	Laser drift results at a glance. The results are presented for the first week, in which the laser drift is off, and the second week, in which the laser drift is on. . . . .	73
6.1	The power of the red laser beam for red MOT B measured before the chamber. . . . .	89
6.2	Uptime comparison between campaigns 2015 and 2022. . . . .	102
A.1	The most common parameters and addresses. . . . .	118
A.2	The pattern directs the controller output to the pre-programmed value. .	118
B.1	The most common NAMES . . . . .	123

# Chapter 1

## Introduction

### 1.1 Laser in cold atom experiment

Lasers emitting incredibly coherent, narrow-linewidth light has led to advancements in science and technology. There are a wide variety of laser types (such as gas, dye, diode, and quasi-molecular lasers) and techniques (such as laser modulation, Q-modulation, amplifying, frequency stabilizing, and nonlinear technologies) that can be used to match an application's requirements as closely as possible [1].

The development of laser technology is closely related to the subject of quantum physics. With specific developments in laser technology, numerous advances in the various fields of quantum physics were conceivable. The development of laser cooling and trapping techniques in the 1980s, for which William D. Phillips, Claude Cohen-Tannoudji, and Steven Chu were given the Nobel Prize in 1997, is one well-known example of this reality.

Lasers in these research fields frequently face the most challenging requirements regarding frequency stability, intensity stability, absolute wavelength controllability, directionality, and mode properties because the world of quantum physics and precision measurements deals with delicate systems. While many advances in laser technology have been made in recent years, the development of ultrastable lasers with exceptional frequency stability and accuracy has undoubtedly been one of the most important.

These lasers have fractional frequency stabilities on the order of  $10^{-16}$  at 1 s [2, 3], making them suitable for a wide range of intensively precise research. The most accurate time and frequency measurement tools today are optical clocks built on these ultrastable lasers, reaching fractional inaccuracies of  $8.6 \times 10^{-18}$  [4].

#### 1.1.1 External cavity diode laser

External cavity diode lasers (ECDLs) utilize low-cost diode lasers with frequency selective feedback to produce small linewidth and tunability. Frequency selective feedback is commonly obtained using diffraction gratings in the Littrow (Figure 1.1 a taken from [5]) or Littman-Metcalf designs [6]. The terms of the external cavity are due to the additional diffraction gratings placed external to the diode lasers, which extend the cavity. Littman configuration employs an extra mirror in the external cavity to reflect first-order light into the laser diode, whereas Littrow configuration uses the grating for optical stability. Toptica chose the Littrow setup over the more sophisticated Littman setup, which

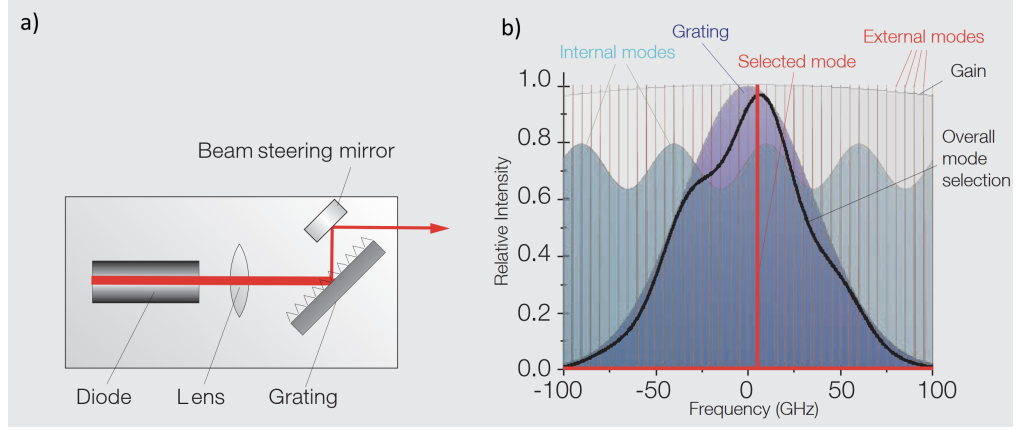


Figure 1.1: a) Littrow configuration and a movable optical element (grating) for tuning the laser's frequency by a piezoelectric transducer (PZT) which is attached to the grating. b) Selection mode of ECDL. Taken from [5].

is sensitive to acoustic vibrations and temperature fluctuations. All the ECDLs used in this thesis are DL 100 from Toptica.

Each ECDL design has a moveable optical element in the external cavity that may be modified to tune the laser's wavelength. Coarse wavelength alignment is often achieved with a micrometer screw. In contrast, fine-tuning involves applying voltages to a piezo actuator that holds the grating or directly changing the laser diode current.

Figure 1.1 b presents the selected mode of ECDL [5]. The lasing mode is determined by the semiconductor gain profile, internal laser diode modes, external cavity modes, and grating filter. Stable single-mode operation (Figure 1.2 a) also requires precise temperature and current control. However, the multi-mode operation (Figure 1.2 b) of ECDL may include transitions between multiple modes of external cavity.

The transition of mode is called mode hop, which is usually caused by external influences like temperature drift of gain medium or length drift of laser resonator. To achieve mode-hop-free tuning of the laser, the grating angle, cavity lengths, and laser current must be adjusted simultaneously to guarantee the same mode always has the highest gain.

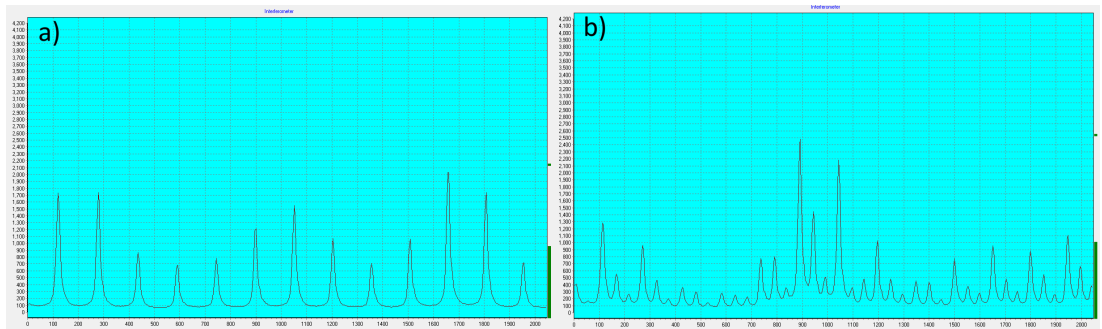


Figure 1.2: Interferometer pattern of ECDL while operating in a) single-mode and b) multi-mode. The graph's horizontal axis represents the pixel number of the CCD line array. The vertical axis represents the light intensity for the given pixel in arbitrary units.

### 1.1.2 Laser frequency stabilization

Lasers appear to be steady light sources but are subject to external influences such as source current fluctuations, temperature variations, mechanical vibrations, and component aging. This causes the laser to drift in frequency or phase over time. This will affect our experiment, which needs an ultrastable laser frequency over the entire measurement time.

There are several techniques to stabilize a laser. One of the most popular is the Pound-Drever-Hall (PDH) method. Figure 1.3 shows that the configuration requires a laser source, electro-optic modulator (EOM), RF synthesizer, photodiode (PD), and frequency demodulator (usually a lock-in amplifier). The final component, the frequency reference, is an optical cavity containing extremely reflective mirrors. The cavity's mirrors strong reflectiveness results in an extremely narrow linewidth.

The PDH method provides an asymmetric error signal around the resonance with a steep slope (Figure 1.4). However, there is also a non-vanishing signal for significant deviations from the set point. The PID (Proportional – Integral – Derivative) controller must have an asymmetric error signal to know whether the system is above or below the set point. Therefore, it allows the system to lock at resonance, and if the system drifts far from the set point, it will capture it.

Assume an incident beam as  $E_{inc} = E_0 e^{i\omega t}$  entering a Fabry-Perot resonator cavity, where  $E_0$  is the amplitude of the electric field and  $\omega$  is the angular frequency of the wave. If the mirrors are symmetric with reflectivity of  $r$  and transmissivity of  $t = \sqrt{1 - r^2}$ , the reflected beam, assumed to have approximately the same frequency as the incident beam, will be

$$E_{ref} = E_0 (r e^{i(\omega t + \pi)} + t r t e^{i(\omega t - 2L/c)} + t r^3 t e^{i(\omega t - 4L/c)} + \dots). \quad (1.1)$$

The reflection coefficient of the cavity is defined as the ratio of the reflected electric field to the incident electric field, which is written as

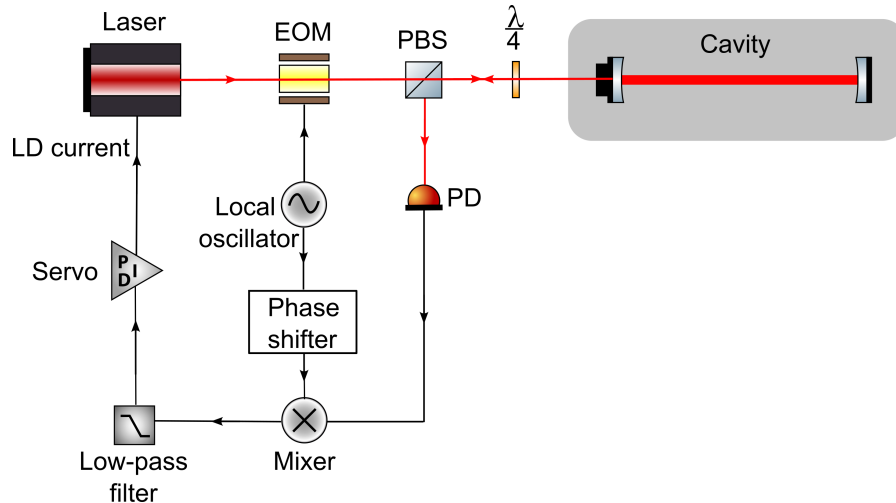


Figure 1.3: Schematic of PDH method for laser locking. Abbreviations: EOM- electro-optic modulator, PBS- polarising beam splitter, PD- photodetector,  $\frac{\lambda}{4}$ - quarterwave plate, LD- laser diode.

$$F(\omega) \equiv \frac{E_{ref}}{E_{inc}} = \frac{r(e^{i\omega/\Delta\nu_{FSR}} - 1)}{1 - r^2 e^{i\omega/\Delta\nu_{FSR}}}, \quad (1.2)$$

where  $\Delta\nu_{FSR} = c/2L$  is the free spectral range of the cavity.  $c$  is the light speed and  $L$  is the length of the cavity. The reflected beam's phase must be measured to know whether the laser's frequency is above or below the set point. An EOM should modulate the phase of the incident beam to measure the reflected beam's phase in the PDH method. This way, two sidebands are generated with a definite phase relationship between incident and reflected beams. However, the frequency of the incident and reflected sidebands will not be the same. By interfering with the sidebands with the reflected beam, a beat pattern will be shown at the modulation frequency, and its phase can be measured.

After passing the laser beam through an EOM with an angular radio frequency of  $\Omega$  and modulation depth of  $\beta$ , the electric field will be [7]

$$E_{inc} = E_0 e^{i(\omega t + \beta \sin \Omega t)} \approx E_0 (J_0(\beta) e^{i\omega t} + J_1(\beta) e^{i(\omega + \Omega)t} - J_1(\beta) e^{i(\omega - \Omega)t}). \quad (1.3)$$

Which is expanded by Bessel functions. Three different frequencies incident on the cavity, including a carrier with an angular frequency of  $\omega$  and two sidebands with  $\omega \pm \Omega$ .

The reflected beam can be treated as three beams and multiply each one by the reflection coefficient with different frequencies. The total reflected beam is

$$E_{ref} = E_0 [F(\omega) J_0(\beta) e^{i\omega t} + F(\omega + \Omega) J_1(\beta) e^{i(\omega + \Omega)t} - F(\omega - \Omega) J_1(\beta) e^{i(\omega - \Omega)t}]. \quad (1.4)$$

As the electric field is not measurable directly, the power of the reflected beam is

$$\begin{aligned} P_{ref} = & P_c |F(\omega)|^2 + P_s \{|F(\omega + \Omega)|^2 + |F(\omega - \Omega)|^2\} + \\ & 2\sqrt{P_c P_s} \{ \text{Re}[F(\omega) F^*(\omega + \Omega) - F^*(\omega) F(\omega - \Omega)] \cos \Omega t + \\ & \text{Im}[F(\omega) F^*(\omega + \Omega) - F^*(\omega) F(\omega - \Omega)] \sin \Omega t \} + O[2\Omega]. \end{aligned} \quad (1.5)$$

Where  $P_c$  and  $P_s$  are the power of the carrier and sideband, respectively. The reflected power contains several components, including a DC power from the carrier, two components oscillating at the modulation frequency from the sidebands, and higher-order components from the interactions between the sidebands. However, only two oscillating terms, modulated at frequency  $\Omega$ , are attractive here as they sample the phase of the reflected carrier. Usually, one of the terms of the sin or cos remains, which depends on the modulation frequency.

The imaginary component with sin term will dominate for a fast modulation frequency. Therefore, the error signal in PDH after removing DC components with a low pass filter will be

$$\varepsilon = 2\sqrt{P_c P_s} \text{Im}[F(\omega) F^*(\omega + \Omega) - F^*(\omega) F(\omega - \Omega)]. \quad (1.6)$$

Figure 1.4 shows the error signal versus laser frequency offset from cavity mode resonance when the modulation frequency is 10% of the  $\Delta\nu_{FSR}$  of the cavity.

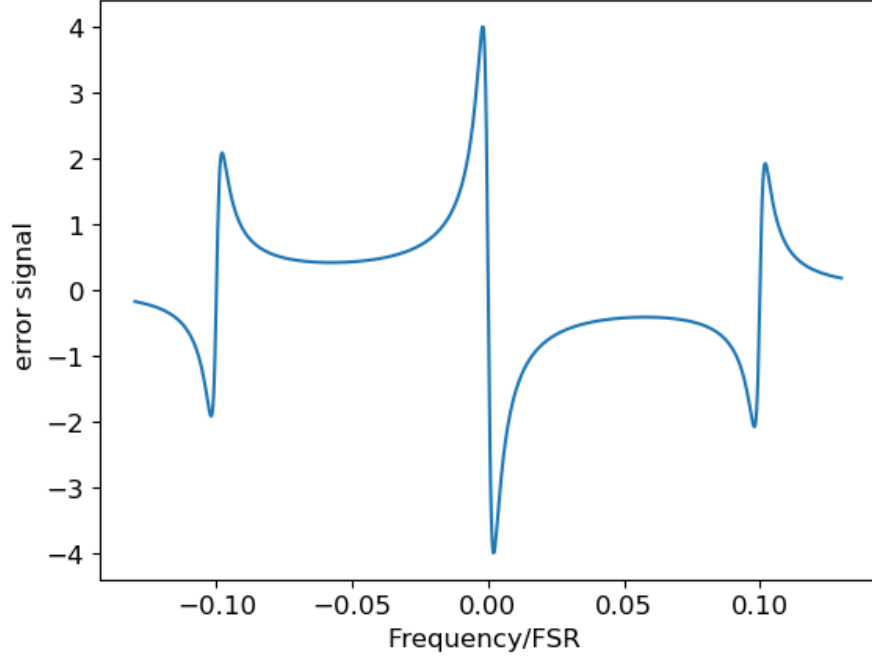


Figure 1.4: PDH error signal, when the modulation frequency is high with 10% of the  $\Delta\nu_{FSR}$ .

## 1.2 Laser spectroscopy

A narrow linewidth spectroscopy signal at an atomic resonance can be used to stabilize laser frequency. To maintain a narrow (less than kHz) and stable atomic resonance, atoms must be cooled, confined, and protected from external fields that could cause frequency shifts during the reference transition.

Applying a laser beam at a frequency close to the transition's resonance frequency ( $\omega_0 = \Delta E/\hbar$ ) generates coupling between the ground and excited states. At resonance with Rabi frequency  $\Omega$ , the population bounces between two levels over time ( $\sin^2(\frac{\Omega t}{2})$ ) [8]. An on-resonance laser beam can excite atoms using Rabi or Ramsey spectroscopic methods.

In Rabi spectroscopy, a single excitation pulse is used with a duration of  $t = \frac{\pi}{\Omega}$ , which is called a  $\pi$  pulse. In Ramsey spectroscopy, two separate pulses with a duration of  $t = \frac{\pi}{2\Omega}$  are used and are known as  $\frac{\pi}{2}$  pulses. These two pulses are separated with a dark evolution time [9]. The initial pulse transitions the atom into a coherent superposition of ground and excited states. This superposition, which is highly sensitive to atom laser detuning, is allowed to evolve freely. A following pulse projects any accumulated phase difference onto the atomic state population, which can be read via fluorescence measurements. Figure 1.5 presents these two spectroscopy methods.

Ramsey spectroscopy optimizes the atom's sensitivity to detuning over similar interrogation times, resulting in narrower fringes when measuring the excited state population compared to Rabi spectroscopy, which is simpler and uses less light intensity. Both methods should be tested to find the best clock performance for a given system. For the optical lattice clock and optical tweezers machine in this thesis, Rabi spectroscopy is used.

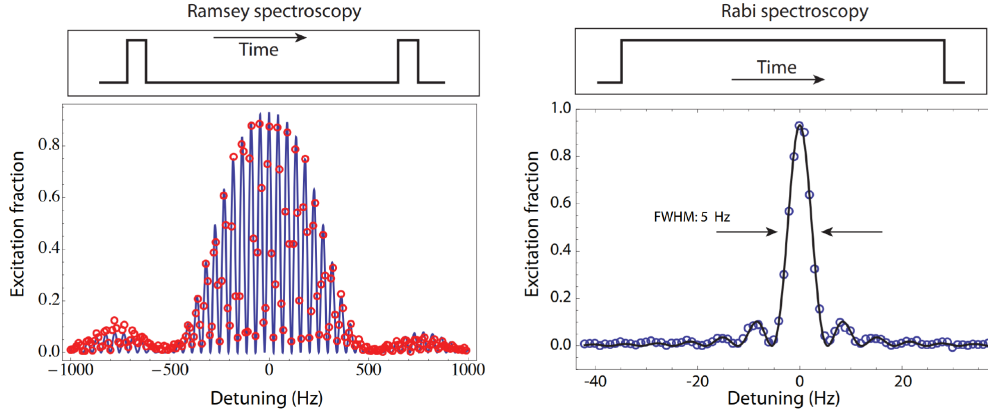


Figure 1.5: Ramsey and Rabi spectroscopy revealed spectroscopic lineshapes in an  $^{87}\text{Sr}$  lattice clock. Laser excitation techniques are shown above. Rabi spectroscopy (right) produces a single fringe when scanning the laser across resonance, while Ramsey spectroscopy produces a fringe pattern. The width of the fringes is inversely proportional to the free evolution time between excitation pulses. Taken from [10].

### 1.3 Atomic clocks

Atomic clocks reach more accuracy and precision than mechanical or celestial frequency reference, which became possible after the discovery of quantum mechanics in the last century. Absorption and emission of electromagnetic radiation are possible due to the structure of atoms. Therefore, the precise frequency of radiation ( $\nu$ ) equals the difference energy levels ( $\Delta E$ ) involved in the radiation as  $\nu = \Delta E/h$ , where  $h$  is Planck's constant. In an optical atomic clock, the natural frequency of a transition serves as a reference frequency, and the radiation source is compared with it [11].

Figure 1.6 illustrates an atomic clock's operation. A local oscillator, including a laser and ultrastable cavity, creates coherent radiation. Radiation is shined on an atomic sample to detect the transition probability. The fraction of excited atoms is determined by oscillator frequency, interrogation field intensity, pulse duration, and atomic characteristics. The transition probability indicates the oscillator's deviation from the reference frequency, which is then corrected to bring it back to the right frequency.

The optical clocks are good candidates for future primary standards, which right now is the Caesium clock. However the optical clocks can be used as a sensor for detection in areas like variations of fundamental constants [13–16], relativistic geodesy [17, 18], test of relativity [19, 20] and searches for dark matter [21].

Two parameters, accuracy and precision, characterize the clock's performance. The accuracy is determined by how the measured frequency matches the correct frequency. Precision refers to stability. It presents repeatability of measuring clock frequency after averaging over  $\tau$ . The theoretical stability is given by

$$\delta_y(\tau) = \frac{\delta\nu(\tau)_{rms}}{\nu} = \frac{\chi}{2\pi QS/N} \sqrt{\frac{\tau_c}{\tau}}, \quad (1.7)$$

where  $Q$  equals  $\nu/\Delta\nu$ , which is the ratio of the oscillation frequency to its linewidth, and it is called the line quality factor of the clock transition with linewidth of  $\Delta\nu$  [11].  $S/N$  is the signal-to-noise ratio measured over the  $\tau_c$  cycle.  $\chi$  is a constant and depends on



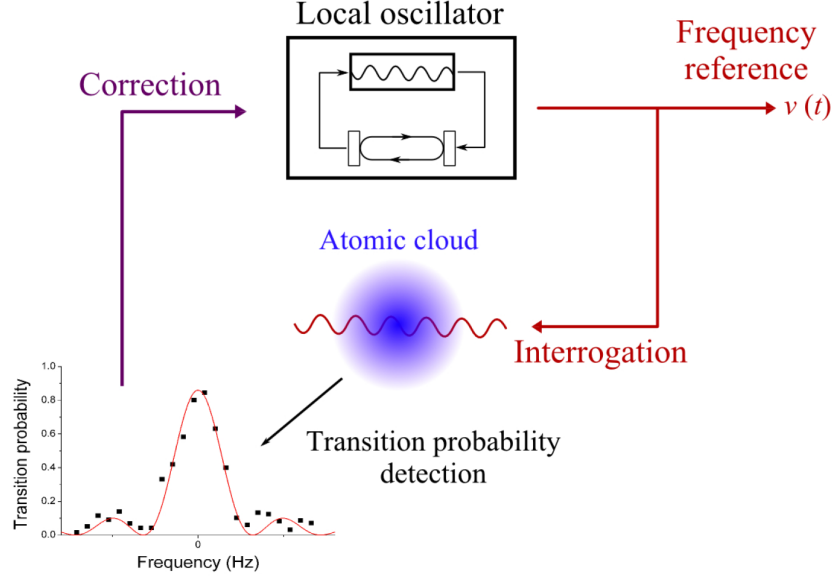


Figure 1.6: Passive atomic clock system. An atomic cloud is used to stabilize the local oscillator. Taken from [12].

the transition lineshape. The main constraint for clock stability is the quantum projection noise (QPN) limit [22] due to the quantum fluctuations of the transition probability measurements. For this noise,  $S/N = \sqrt{n}$ , where  $n$  is the number of atoms. For optical lattice clocks with more than  $10^4$  atoms, the instability is less than  $10^{-17}$  per second. This limit is so low that the stability of optical clocks is limited by another effect which is pointed out by Dick [23]. Non-continuous probing of atoms degrades the stability of the clock. The clock transition is interrogated once per clock cycle; the rest of the cycle is a dead time for atomic ensemble preparation.

Frequency instability is assessed in the lab using the Allan deviation [24]. For continuous measurements, the two-sample Allan deviation is defined as

$$\delta_y(\tau) = \sqrt{\frac{(\bar{y}_{i+1} - \bar{y}_i)^2}{2}}, \quad (1.8)$$

where  $\bar{y}_i$  is the averages over time interval  $\tau$  of fractional frequency  $\nu/\nu_0$ , at the  $i$ th interval.

The optical lattice clocks are based on trapping neutral atoms in a dipole periodic potential. The alkaline earth (like) atoms are the best candidate for the optical clocks as they have an atomic structure that allows efficient cooling, narrow intercombination, and forbidden transition on  $^1S_0 - ^3P_0$ . This transition linewidth is very narrow at the mHz level when allowed due to perturbation from the magnetic field. The typical species that many groups worldwide use are Sr [25–27], Yb [28–31], and Hg [32, 33]. In this thesis, the optical lattice clock and tweezers machine in chapter 7 are based on Sr atoms. Total systematic uncertainty for optical lattice clock based on  $^{87}\text{Sr}$  is in the level of  $10^{-18}$  [25].

### 1.3.1 Sr clock in KL FAMO

There are two optical lattice clocks based on  $^{88}\text{Sr}$  in the National Laboratory of Atomic, Molecular, and Optical Physics (KL FAMO) in Toruń, Poland. These two clocks are Strontium1 (Sr1) and Strontium2 (Sr2). All clock measurements in this thesis are from Sr1. Furthermore, the automation system has been tested using the Sr1 clock.

Figure 1.7 presents a simplified scheme of these two optical lattice clocks in the KL FAMO lab. Two ultrastable lasers (689 and 698 nm) and repumpers (679 and 707 nm) are inside the cavity room. The wavemeter (used in place of the wavelength meter in this thesis) from HighFinnese is also inside the cavity room. Blue laser (461 nm) is placed in the Sr1 room, and TiSa laser (813 nm) is placed in the Sr2 room. The optical frequency comb is inside another room and is not included in the schematic. This system has been described in more detail in Chapter 6.

## 1.4 Optical Tweezers in quantum simulation

Neutral atoms are an extremely effective and diverse species for quantum simulations [34]. High numerical aperture (NA) optics enabled single-atom imaging and addressing, which is widely employed in optical tweezer studies nowadays. An optical tweezer traps atoms in a tightly focused laser beam, as shown in Figure 1.8. Light modulators can shape tweezer beams, allowing for the transport and arrangement of atoms (Figure 1.9) in up to three dimensions [35].

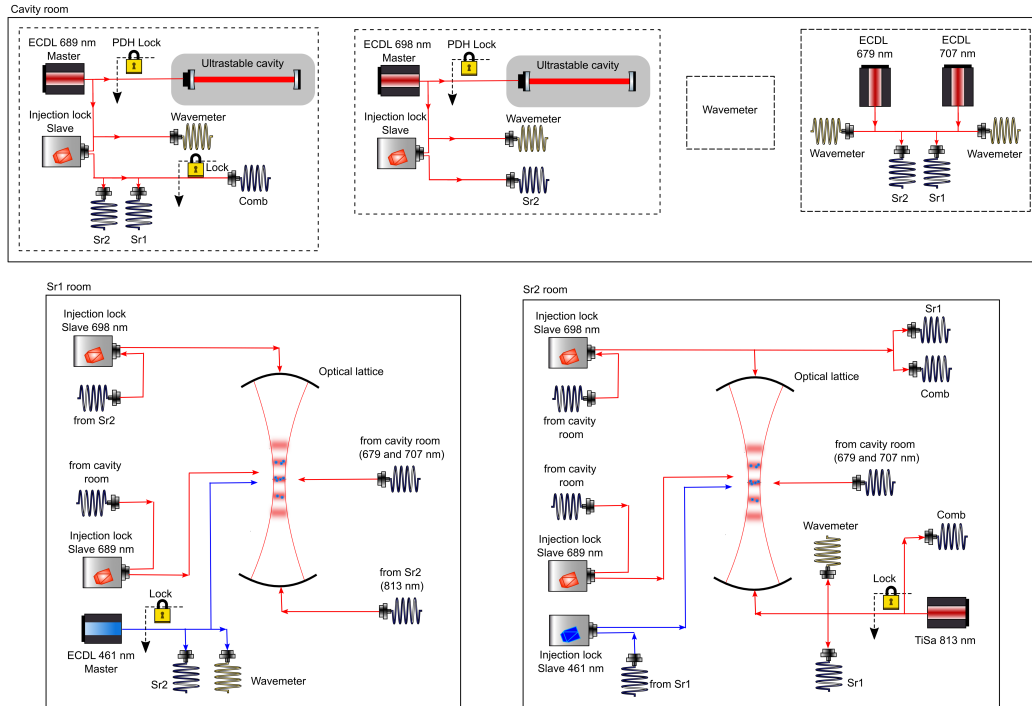


Figure 1.7: A simplified scheme of two optical lattice clocks in KL FAMO lab. Two ultrastable lasers (689 and 698 nm) are inside the cavity room with two repumpers (679 and 707 nm). The optical frequency comb is inside another room, which is not included in this schematic.

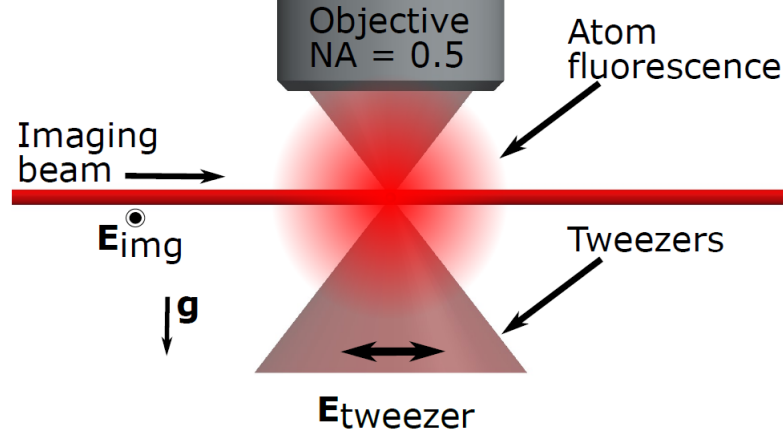


Figure 1.8: A schematic of the optical tweezers created by a high numerical aperture objective ( $NA = 0.5$ ). The objective is also to collect the atomic fluorescence from imaging. Taken from [36].

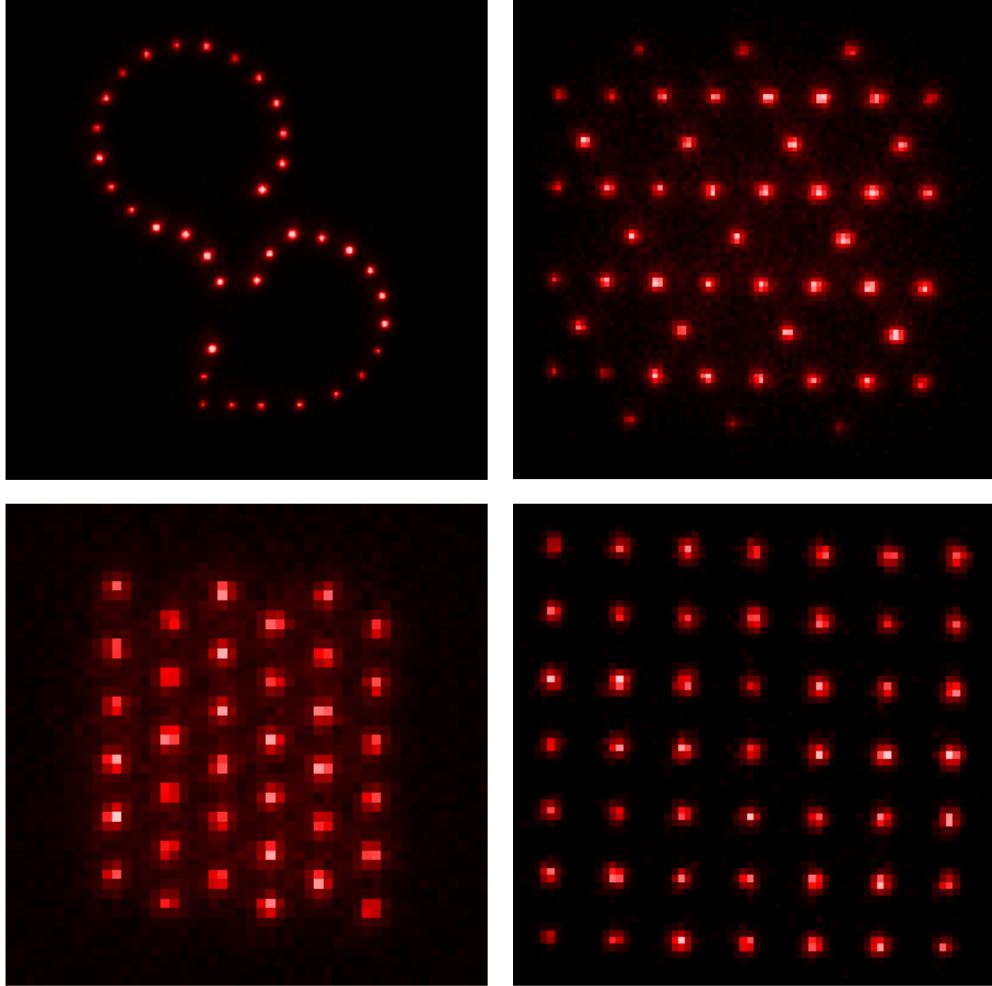


Figure 1.9: Different patterns of single atoms trapped in tweezers arranged by light modulators. All the images are averaged from many fluorescence imaging. Taken from [36].

Quantum simulations aim to understand emergent phenomena in associated many-body systems that classical algorithms cannot model due to their large Hilbert space. Tweezer arrays offer a defect-free many-body system. However, the space between sites reduces interactions for ground state atoms. Single atoms interact via being stimulated to Rydberg states, which are highly excited states with strong interactions because of their large dipole moment. A Rydberg laser is used to tailor the interactions between neutral atoms in tweezers by exciting them to Rydberg states.

Figure 1.10 presents a simplified scheme of the Rydberg laser design that uses two highly tunable ECDLs boosted by fiber amplifiers to produce 5W output power. The output beams are beam-shaped and overlapped using a dichroic mirror before passing through a periodically poled lithium niobate (PPLN) crystal. The crystal generates red light at 632.8 - 647.8 nm and separates it from the infrared input light using a dichroic mirror. Most light is directed to a second-harmonic generation (SHG) cavity, where a Beta barium borate (BBO) crystal produces the necessary 316.4 - 323.9 nm ultraviolet (UV) radiation for the experiment. A portion of the red light is locked in a transfer cavity. The 1.5  $\mu\text{m}$  ECDL controls the output frequency. The 1  $\mu\text{m}$  ECDL is pre-stabilized by locking it to another cavity, minimizing its contribution to the overall linewidth.

## 1.5 Outline

This thesis is not the first one about optical atomic clocks and optical tweezers machine. There are many more dissertations [10–12, 36–40] in these fields with excellent explanations, which I have used during my PhD and while writing my thesis. This thesis will contribute to these fields by making these complicated experiments more robust and easy to operate.

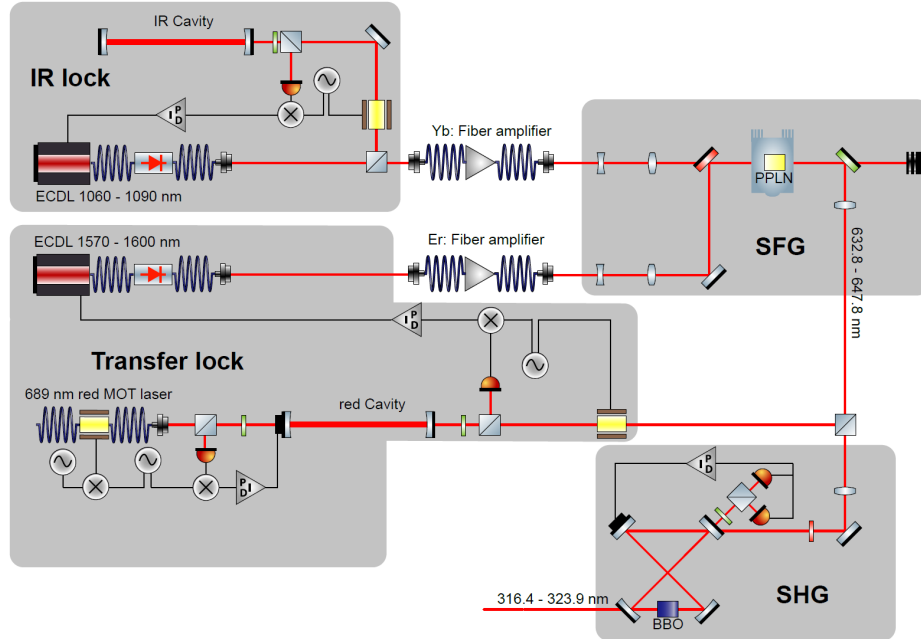


Figure 1.10: The simplified schematic for the Rydberg laser design in optical tweezers experiment. The UV output beam is used for the Rydberg spectroscopy. Taken from [37].

When I started my PhD in the KL FAMO group, the optical atomic clocks were already constructed and working. However, as I depicted very simplified the schematic of the clocks in the KL FAMO lab in Figure 1.7, the system is complicated to operate, especially when the clock needs to operate non-stop for at least one month. One of the biggest challenges not only in the optical atomic clocks but in many cold atom experiments, including optical tweezers machines, is to have a stable laser precisely locked on a specific frequency as long as possible. Additionally, as described briefly in the last two sections, many lasers are involved in the experiments, which are distributed in different rooms and need to be stabilized.

Therefore, I started my PhD on autonomous frequency stabilisations in a superradiant clock as part of the Modular Systems for Advanced Integrated Quantum Clocks (MoSaiQC) project to build an automatic system for stabilizing the lasers and auto reload them. Alongside building an autonomous and robust optical atomic clock, an automatic control system has been developed for compensation coils to control magnetic fields during the clock cycle and for direct digital synthesis (DDS). The DDS is used for precise (sub Hz level) frequency control and locking systems like PDH method and fiber noise cancellation.

I had successfully built an automatic system for reloading the lasers and an automatic system for compensation coils and DDS. After implementing these automation systems in the Sr1 clock, I started optimizing and operating the clock. I have performed many clock spectroscopy to measure the temperature of the Sr atoms on the ground state in the lattice, linewidth of the clock line, and Rabi oscillation. Zeeman shift and probe light shift have been measured as well. In the end, the stability of the atom-cavity was measured during campaign 2022 and has been compared with campaign 2015.

The optical clock has also been prepared to study the temperature changes of the trapped Sr atoms in the lattice while in the excited state of  $^3P_0$  and interact with a magic-zero wavelength at 390 nm. Unfortunately, as the 390 nm laser was broken, there was no possibility of studying the effect of magic-zero on the trapped Sr atoms. However, as will be discussed in Chapter 6, the experiment is ready to study this effect and the temperature of atoms that have been measured while they are excited on  $^3P_0$  state.

As part of the MoSaiQC project, the developed system for auto reloading lasers should be tested at the University of Amsterdam in the Strontium Quantum Gas Group. The system has been tested successfully in an optical tweezers machine project for the Rydberg laser. Additionally, I have characterized the Rydberg laser lock by the cavity, and at the end, a Rydberg spectroscopy has been performed to make sure the system is working easily by this system.

The thesis is structured as follows:

- Chapter 2 explains the theory of the optical atomic clock procedure, which is almost the same as the optical tweezers machine. The procedure starts with a magneto-optical trap (MOT) apparatus. Then, the properties of the strontium (Sr) atom are described as a selected species for the optical atomic clock and tweezers machine. The next step after cooling the Sr atoms, the optical lattice, is described as the last step for trapping. In the end, clock spectroscopy, Rabi oscillation, and evaluation of the systematic shifts are explained.
- Chapter 3 focuses on developing an automated system for controlling the magnetic fields of the compensation coils. This compact and robust device connects to

a real-time computer and allows it to be controlled through TTL signals from the real-time computer. This compact device has been installed and tested in the lattice optical atomic clock working in the Sr1 room of the KL FAMO lab.

- Chapter 4 is about controlling remotely and possibly automatically the DDS. This controller is dedicated to 100, 250, and 1000 MHz reference frequency signals. This controller has been tested for the DDS AD9912 model.
- Chapter 5 explains an automatic relocking program to stabilize the frequency of the laser beam. This system has been tested with many different lasers at KL FAMO lab with an optical atomic clock experiment, at the UvA with the Rydberg laser in an optical tweezers experiment refer to chapter 7, and also at Toptica company.
- Chapter 6 will discuss the optimization of the clock after implementing new features in the system, including the automatic control of compensation coils and auto relocking of the ECDLs, the system of the passive optical atomic clock in the Sr1 room of the KL FAMO group has been optimized. The main parameters have been discussed to improve the trapped atoms in the lattice to have enough atoms for clock interrogation. In the end, clock spectroscopy was performed to measure the temperature of the trapped atoms on the ground state, linewidth, and Rabi oscillation. The evaluation shift due to the Zeeman effect and probe light shift has been measured. Additionally, a new experiment and method are explained to measure the effect of magic-zero wavelength on the temperature of the trapped Sr atoms while they are excited to  $^3P_0$  state.
- Chapter 7 is about an optical tweezers machine in which the auto relocking program described in Chapter 5 is implemented to make the system automatic and robust for easily performing the Rydberg spectroscopy. Auto relocking is performed for the Rydberg laser in the optical tweezers machine project at the University of Amsterdam in the Strontium Quantum Gas Group.

I feel obliged to point out that, all the electronic boards which are described in my thesis were designed and fabricated by my colleagues in the KL FAMO lab.



# Chapter 2

## Theory

This chapter explains the theory of the optical atomic clock and the optical tweezers machine. At the beginning, the magneto-optical trap (MOT) apparatus is described. Then, the properties of the strontium (Sr) atom are described as a selected species for the optical atomic clock and tweezers machine. The next step after cooling the Sr atoms, the optical lattice, is described as the last step for trapping. In the end, clock spectroscopy, Rabi oscillation, and evaluation of the systematic shifts are explained.

### 2.1 Magneto-optical trap

A MOT is an apparatus for trapping neutral atoms using laser cooling and a spatially varying magnetic field, Figure 2.1 a. A pair of coils in an anti-Helmholtz configuration generates a spatially varying magnetic field. The magnetic field gradient is uniform and varies linearly with the position near the field zero, which is halfway between the two coils. Due to the Zeeman effect, each state of the atom will split to  $2J + 1$ , which  $J$  is the total angular momentum. For an atom with total angular momentum  $J_g = 0$  for ground state and  $J_e = 1$  for excited state, there is  $|J_g = 0, m_g = 0\rangle$  without splitting and  $|J_e = 0, m_e = 0, \pm 1\rangle$  with three split energy levels respectively. Therefore, the energy shift for the sublevels in the excited state is spatially dependent as the Zeeman shift is proportional to the magnetic field strength, Figure 2.1 b.

In addition to the magnetic field, pairs of counter-propagating circularly polarized laser beams are sent along three orthogonal axes. Optical molasses beams are red-detuned from the transition. The energy shift in the center of the coils is zero, and the atoms are not absorbing any laser photons as they are red detuned. So, the coldest atoms are accumulating in the center of the MOT, where they scatter very few photons. If an atom moves towards +z direction, the energy of the  $|J_e = 0, m_e = -1\rangle$  state decreases to be in the resonance with the red detuned propagating laser beam in -z direction with  $\sigma^-$  polarization. When an atom absorbs a  $\sigma^-$  photon, it is excited to  $|J_e = 0, m_e = -1\rangle$  state and gets one photon recoil momentum,  $\hbar k$ , opposite to its direction. Now, spontaneous emission will happen, and a photon will be emitted in a random direction. After many absorption and emission events, on average, spontaneous emission will not change the atom's velocity. Therefore, the only force is from the photon, which pushes the atom back to the center. The same procedure occurs for the atoms moving in the -z direction. However, the energy level of  $|J_e = 0, m_e = 1\rangle$  state will decrease in this part, and the photon propagating in +z direction with  $\sigma^+$  polarization will be absorbed.



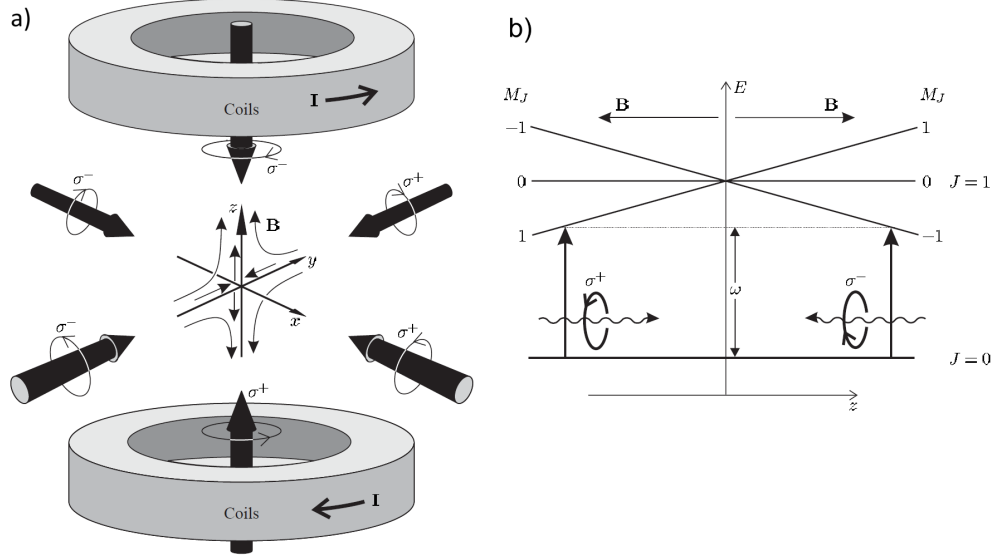


Figure 2.1: a) The setup of MOT includes two pairs of coils with anti-Helmholtz configuration and optical molasses beams, red detuned and circularly polarized. b) Energy shift for the sub-levels in a uniform magnetic field gradient and linearly increasing from the center. Taken from [8].

This process of absorption and emission reduces the atom's velocity, referred to as Doppler cooling [41]. The Doppler cooling method is the first step in the cold atom experiments, including optical atomic clocks and optical tweezers machine. By reducing the atom's velocity, the kinetic energy will be reduced. Because the temperature of an ensemble of atoms is a measure of their random internal kinetic energy, this is comparable to cooling the atoms. The Doppler cooling limit is the minimum temperature achievable with Doppler cooling. This temperature is called the Doppler temperature and is given as [42]

$$T_D = \frac{\hbar\Gamma}{2k_B}, \quad (2.1)$$

where  $\Gamma = 2\pi\gamma$ , and  $\gamma$  is the natural linewidth of the transition. The experimental temperature is higher than this limit due to the extra heating mechanism induced by transverse spatial intensity fluctuations of the optical molasses [43].

In addition to the coils for the MOT, three pairs of compensation coils are installed along the x, y, and z directions with Helmholtz configuration. As their name conveys, these coils are added to the system to compensate for the Earth's magnetic field and any stray magnetic fields in the laboratory. This part has been described in more detail in Chapter 3.

## 2.2 Strontium

The number and variety of species subjected to cold atom experiments are continuously expanding, enhancing the experimental resources with novel prospects such as Sr [25–27, 44–47], Yb [28–31, 48], and Hg [32, 33] which are used by many groups in world-

wide. Several significant characteristics set strontium apart from other elements. These features benefit applications like optical clocks and tweezers machines, which this thesis discusses.

Strontium is an alkaline-earth element with two valance electrons and four stable isotopes, including bosonic  $^{84}\text{Sr}$ ,  $^{86}\text{Sr}$ ,  $^{88}\text{Sr}$ , and fermionic  $^{87}\text{Sr}$ . Since the fermionic isotope has the most significant nuclear spin of any alkaline-earth element ( $I = 9/2$ ), hyperfine splitting of each level results in a richer structure than the bosonic isotopes, which have a more straightforward energy level structure. Energy levels separate into singlets and triplets when two electrons are present in the outer electronic shell. Since the two valance electrons' spins can remain anti-parallel or change to parallel, resulting in singlet and triplet excited states, respectively, the two valance electrons enable two different forms of electron excitation [49]. Because of their different characteristics, transitions from the ground  $^1S_0$  state to the first excited singlet  $^1P_1$  or triplet  $^3P_{0,1,2}$  states allow for various methods of atom manipulation, particularly in the areas of cooling and trapping.

The energy level diagram of the Sr is shown in Figure 2.2, the linewidth of the  $^1S_0 - ^1P_1$  transition is 32 MHz, which is used for the first stage of cooling down the atoms to the temperature of 1 mK roughly [50], this stage is called blue MOT. During blue MOT cooling, two repumper lasers 679 nm for  $^3P_0 - ^3S_1$  transition and 707 nm  $^3P_2 - ^3S_1$  transition are used to avoid atoms relaxing from  $^1P_1$  to other metastable states rather than ground state  $^1S_0$ . On the other hand, the linewidth of the  $^1S_0 - ^3P_1$  intercombination transition between a singlet and a triplet state is 7.4 kHz, which is sufficient to cool a milli-Kelvin cloud of atoms to the micro-Kelvin regime. This is the second cooling stage, referred to as red MOT.

Moreover, the linewidths of the  $^1S_0 - ^3P_{0,2}$  intercombination transitions for fermionic Sr are approximately one mHz, and significantly less for bosonic Sr. The strontium created the interest of researchers from the metrology community due to its ultranarrow linewidth and tiny Zeeman shift of  $^1S_0 - ^3P_0$  transition, which is the valuable quality for establishing exact frequency standards. Using ultranarrow transitions is one of the more promising aspects of implementing ideas from the quickly expanding field of quantum simulation [51].

## 2.3 Dipole trap

To perform the ultra-precise spectroscopy of the ultra-narrow optical transition  $^1S_0 - ^3P_0$ , the motion of atoms must be extremely well controlled. Therefore, the dipole potential is used in a 1D optical lattice to trap the Sr atoms.

The dipole trap at 813 nm of wavelength is far detuned frequency for clock transition of  $^1S_0 - ^3P_0$ . Therefore, the photons with the Sr atoms have a low scattering rate. By considering the atoms as a simple oscillator interacting with a laser beam  $E$  with amplitude  $E_0$ , polarization of  $\epsilon$ , and angular frequency of  $\omega$ . A dipole moment  $d$  with amplitude of  $d_0$  in the atom is induced. So the average interaction potential due to the effect of atom laser coupling can be written as [52]

$$U_{dip} = -\frac{1}{2}\langle dE \rangle. \quad (2.2)$$

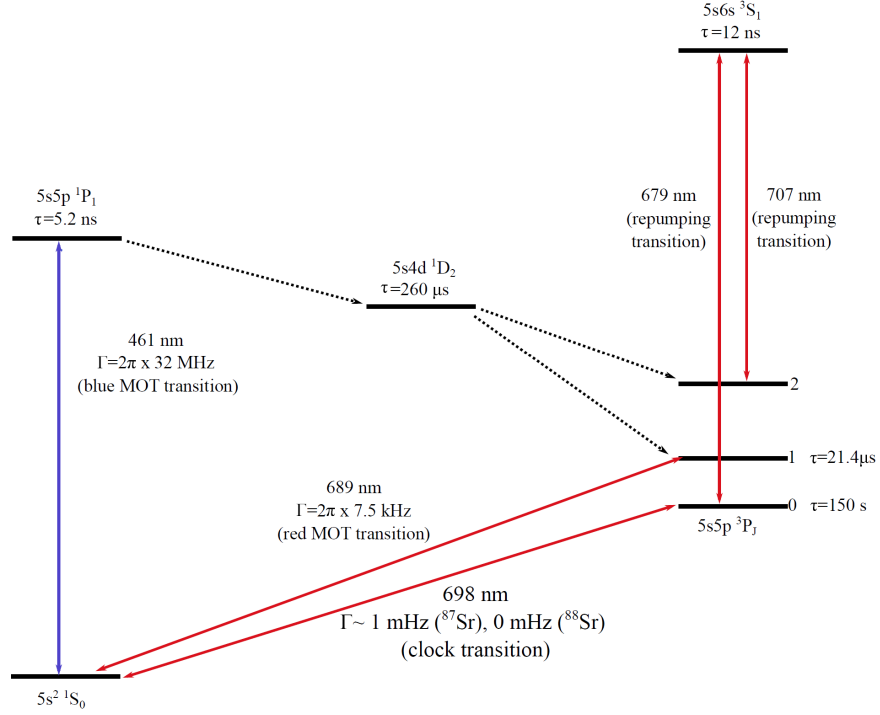


Figure 2.2: Energy level diagram of bosonic strontium, which is important for clock operation. Taken from [38].

The interaction potential determines the dipole force  $f_{dip} = -\nabla U_{dip}$ . The other important parameter is the scattering rate, which is defined as the absorption rate by the atom, and it should be as low as possible,

$$\Gamma_s = \frac{\langle dE \rangle}{\hbar \omega}. \quad (2.3)$$

The interaction potential and scattering rate could be rewritten as [52]

$$U_{dip}(r) = \frac{3\pi c^2 \Gamma}{2\omega_0^3 \Delta} I(r) = -\frac{Re[\alpha(\omega)]}{2\epsilon_0 c} I(r), \quad (2.4)$$

$$\Gamma_s(r) = \frac{3\pi c^2}{2\hbar \omega_0^3} \left( \frac{\Gamma}{\Delta} \right)^2 I(r) = \frac{Im[\alpha(\omega)]}{\hbar \epsilon_0 c} I(r), \quad (2.5)$$

where  $\alpha(\omega)$  is the atomic polarizability,  $I(r)$  is the lattice intensity,  $\omega_0$  is the angular frequency of the resonance,  $\Gamma$  is the linewidth of the resonance,  $\Delta = \omega - \omega_0$  is the detuning from the resonance, and  $r$  denotes the radial coordinate of the lattice beam. Therefore, the scattering rate and the interaction potential are related by

$$\hbar \Gamma_s = \frac{\Gamma}{\Delta} U_{dip}. \quad (2.6)$$

As it is evident in this equation, to have a large dipole force, the intensity has to be high enough for the lattice. Furthermore, the detuning has to be far enough to have

a low scattering rate. When the  $\Delta < 0$ , the atoms are attracted to the maximum light intensity, called red detuned. It is blue detuned when  $\Delta > 0$ , so the atoms are trapped in the minimum of the lattice intensity.

### 2.3.1 Magic wavelength

The dipole interaction is a way to confine the trapped atoms. However, a light shift called AC Stark shift is applied to energy levels due to perturbation from high-intensity lattice beam interaction with atoms. The energy shift  $\delta E$  depends on the polarizability  $\alpha(\omega)$  of the atom for a given level and lattice beam intensity and is written as

$$\delta E = -\frac{\alpha(\omega)}{2\epsilon_0 c} I(r), \quad (2.7)$$

due to this energy shift, there is a shift in the transition frequency as well  $\Delta\omega$ , which is written as [53]

$$\Delta\omega \approx -\frac{1}{4}\Delta\alpha(\omega)E^2 - \frac{1}{64}\Delta\gamma(\omega)E^4, \quad (2.8)$$

where  $\Delta\alpha = \alpha_e - \alpha_g$  and  $\Delta\gamma = \gamma_e - \gamma_g$  are the relative polarizability and hyperpolarizabilities between the excited state and ground state, respectively. Therefore, there is a frequency shift as the polarizability on  $^1S_0 - ^3P_0$  states differ during clock interrogation. Katori has solved this problem [54] by introducing magic wavelength. The magic wavelength is the wavelength in which the polarizability for  $^1S_0 - ^3P_0$  states are the same  $\Delta\alpha = 0$ . Therefore, the energy shift, as shown in Figure 2.3 for both states at 813.4 nm, is the same, and the AC Stark shift is due to the lattice beam being equal to zero.

However, the energy shift at 813.4 nm magic wavelength is not equal to zero. When this shift is equal to zero, the wavelength is called magic-zero wavelength, which has been measured by Katori's group to be 389.9 nm for  $^1S_0 - ^3P_0$  states [55]. The potential feasibility of the magic-zero wavelength for optical lattice trap has been discussed in [38, 56]. In Chapter 6, a new experiment and method are explained to measure the effect of magic-zero wavelength on the temperature of the trapped Sr atoms while they are excited to  $^3P_0$  state.

The magic frequency for the  $^{88}\text{Sr}$  was calculated based on the isotope shift of  $^{87}\text{Sr}$  for different lattice intensities. The cancellation of higher order lattice shift between the isotopes allows the differential lattice shift to change linearly with the lattice intensity  $I$  [57],

$$\Delta\nu = \Delta\nu_0 + \delta\nu_L^{88}(\omega_L^{88}) - \delta\nu_L^{87}(\omega_L^{87}) = \Delta\nu_0 + a[\Delta\omega_L - (\omega_{E1}^{88} - \omega_{E1}^{87})]I. \quad (2.9)$$

Therefore, the frequency shift depends only on the frequency difference  $\Delta\omega_L = \omega_L^{88} - \omega_L^{87}$  of the lattice frequency applied for each isotope. The magic frequency for  $^{87}\text{Sr}$  is reported as  $\omega_L^{87} = 368554490$  (3) MHz [58]. The isotope shift is measured to be  $\omega_{E1}^{88} - \omega_{E1}^{87} = 288$  (7) MHz of the electric-dipole ( $E1$ ) polarizability in the clock transition [57]. To cancel the higher order lattice shift  $\Delta\omega_L = \omega_{E1}^{88} - \omega_{E1}^{87}$ , so  $\omega_L^{88} = 368554778$  (10) MHz which is close to the wavelength of 813.4 nm.

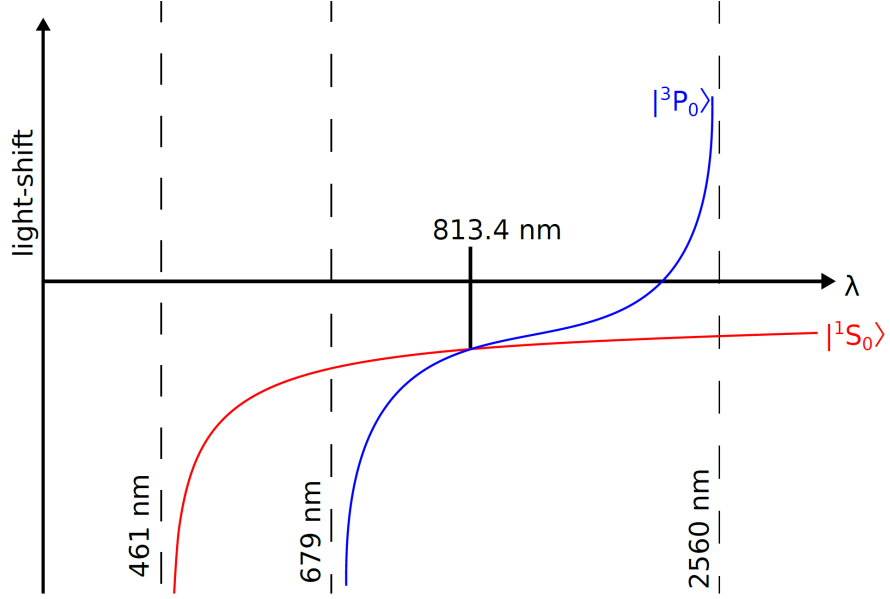


Figure 2.3: The light-shift for  $^1S_0 - ^3P_0$  states of Sr atoms based on the lattice laser wavelength. The intersection of two curves at 813.4 nm is the magic wavelength. Taken from [39].

### 2.3.2 Lamb-Dicke regime

The intensity of the lattice beam  $I(r)$  with Gaussian distribution is given as [52]

$$I(r) = \frac{2P}{\pi w_0^2} e^{-\frac{2r^2}{w_0^2}}, \quad (2.10)$$

where  $P$  is the power of the lattice light,  $w_0$  is the minimum beam waist, and  $r$  denotes the radial coordinate of the lattice beam. Usually, the trapped atoms from MOT take place in an optical lattice with an area around 1 millimeter or even less, which is much smaller than the Rayleigh length ( $\pi w_0^2/\lambda \approx 9$  cm for lattice wavelength at 813 nm and  $w_0 = 152 \mu\text{m}$ ). Therefore, the axial dependence is removed in these equations. The 1D lattice potential (Figure 2.4), which forms a standing wave, is equal to [52]

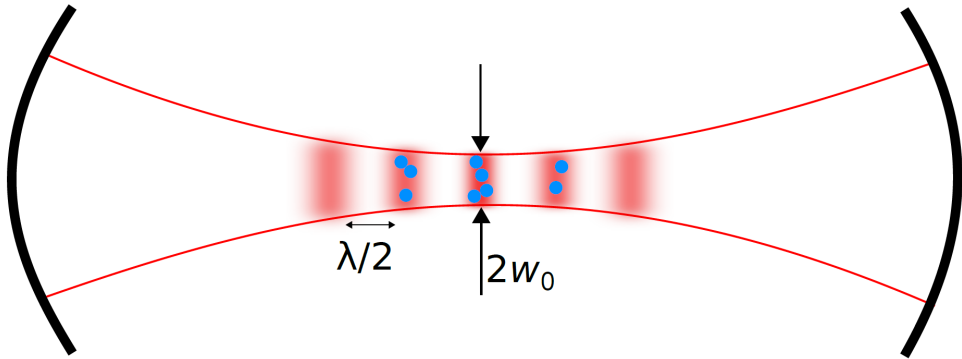


Figure 2.4: Schematic concept of the optical power buildup cavity for 1D optical lattice trap. Taken and modified from [39].

$$U(r, z) = U_0 e^{\frac{-2r^2}{w_0^2}} \sin^2(kz), \quad (2.11)$$

where  $U_0$  is the depth of the optical lattice, and it is usually measured in recoil energy  $E_r$  (Equation 2.14) and  $z$  denotes the axial coordinate of the lattice potential. The potential of a single node is harmonic with motional energy levels equal to  $\hbar\omega_z(n + 1/2)$ , shown in Figure 2.5. The oscillation frequency and the radial frequency are given by, respectively

$$\hbar\omega_z = 2\sqrt{U_0 E_r}, \quad (2.12)$$

$$v_r = \frac{v_z \lambda}{\sqrt{2\pi} w_0}, \quad (2.13)$$

$$E_r = \frac{h^2}{2m\lambda^2}, \quad (2.14)$$

where  $m$  is the mass of the confined atom. The potential trap depth of the lattice proportional to  $E_r$  is calculated from Equation 2.12 and is equal to

$$U_0 = \frac{mv_z^2 \lambda^2}{2} = \frac{m^2 v_z^2 \lambda^4}{h^2} E_r, \quad (2.15)$$

To avoid perturbing the atoms due to recoil energy during spectroscopy, a recoil-free regime could be achieved by transferring the photon's momentum to the lattice instead of the atoms [59]. For the atom confined in a well with a width of  $a$ , there is a probability that the momentum of the photon transfers to the walls of the well instead of the atom, which is equal to

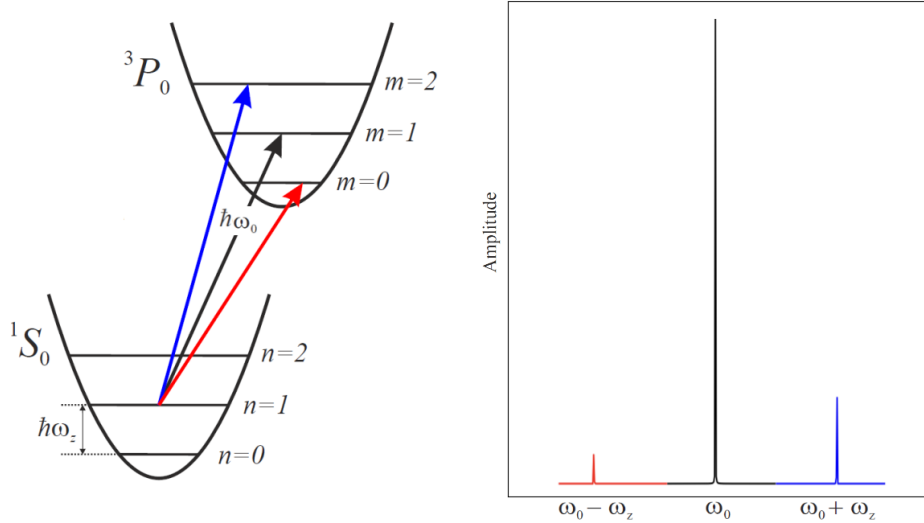


Figure 2.5: Clock laser spectroscopy under Lamb-Dicke regime.

$$P = \frac{\sin^2(\pi a/\lambda)}{(\pi a/\lambda)^2}. \quad (2.16)$$

If the atom is confined to a region smaller than  $a < \lambda/2$ , the photon's momentum is transferred to the walls of the well instead of exciting the vibrational states of the atom. This regime is called the Lamb-Dicke regime.

A Lamb-Dicke parameter is defined to see if the atom in the lattice is in the Lamb-Dicke regime or not by

$$\eta \equiv kz_0 = \sqrt{\frac{E_r}{\hbar\omega_z}} \ll 1, \quad (2.17)$$

where  $k$  is the wave vector of the lattice beam, and  $z_0$ , is the characteristic oscillator length and is defined as

$$z_0 = \sqrt{\frac{\hbar}{2m\omega_z}}. \quad (2.18)$$

The Lamb-Dicke regime condition is  $\eta \ll 1$  when the potential depth is much higher than recoil energy  $U_0 \gg E_r$ . Therefore, the atom is well trapped in the harmonic potential of the lattice. The laser spectroscopy of the atom reveals a carrier at  $\omega_0$  and two sidebands separated by  $\pm\omega_z$ , as presented in Figure 2.5. As shown in Figure 2.5 right, the amplitude of the carrier has maximum amplitude. However, the blue and red sidebands amplitude is reduced due to low probability  $\eta^2(n+1)$  and  $\eta^2n$ , respectively.

Let us get in more detail to find out these amplitudes. The total Hamiltonian of a confined atom in a harmonic oscillator interacting with a laser beam has three terms which are written:

$$H = H_m + H_{int} + H_i. \quad (2.19)$$

The first term is for the motional confinement in the 1D harmonic oscillator, the second is for the internal two-level system, and the third is for the interaction Hamiltonian. The motional Hamiltonian is

$$H_m = \frac{p^2}{2m} + \frac{1}{2}m\omega^2x^2 = \hbar\omega(n + \frac{1}{2}), \quad (2.20)$$

where  $m$  is the mass,  $\omega$  is the trap frequency,  $p$  and  $x$  are momentum and position operators respectively.  $n$  is the number operator, equal to  $aa^\dagger$ .  $a$  and  $a^\dagger$  are the annihilation and creation operators, respectively. The annihilation and creation operators operate on the motional quantum state  $|n\rangle$  as [60]

$$a|n\rangle = \sqrt{n}|n-1\rangle, \quad (2.21)$$

$$a^\dagger|n\rangle = \sqrt{n+1}|n+1\rangle. \quad (2.22)$$

The internal Hamiltonian for the two-level system is given by [61]

$$H_{int} = \frac{\hbar\omega_0}{2}(|e\rangle\langle e| - |g\rangle\langle g|), \quad (2.23)$$

where  $\omega_0 = \omega_e - \omega_g$ ,  $|g\rangle$ , and  $|e\rangle$  are the ground and excited states respectively. The interaction Hamiltonian is given by [62]

$$H_i = \frac{\hbar\Omega}{2}(|e\rangle\langle g|e^{ikz} + H.c.), \quad (2.24)$$

where  $\Omega$  is the Rabi frequency, operator  $e^{ikz}$  is describing the absorption or emission of a photon by inducing a displacement of the atomic momentum by  $\hbar k$  for absorption and  $-\hbar k$  for emission. In the basis of motional state  $|n\rangle$ , this is equivalent to  $|n\rangle$  to  $|m\rangle$  transition, with probability amplitude defined by the Franck-Condon factors as

$$F_{n,m} = |\langle m|e^{ikz}|n\rangle|. \quad (2.25)$$

Which it means, atom in the ground state  $|g, n\rangle$  will be coupled to several excited states  $|e, m\rangle$  with Rabi frequencies  $\Omega F_{n,m}$  and transition frequencies equal to  $\omega_{m,n} = \omega_0 + (m - n)\omega_z$ .

By position operator  $z$ , Rabi frequencies are written as [63]

$$\Omega_{n,m} = \Omega F_{n,m} = \Omega |\langle m|e^{ikz}|n\rangle| = \Omega |\langle m|e^{ikz_0(a+a^\dagger)}|n\rangle|, \quad (2.26)$$

where  $kz_0$  is the Lamb-Dicke parameter as it is defined in Equation 2.17 and  $\eta \ll 1$ . Therefore, the exponential function in Equation 2.26 could be Taylor expanded as

$$\Omega_{n,m} \approx \Omega |m\langle 1 + i\eta(a + a^\dagger)|n\rangle| = \Omega [|\langle m|1|n\rangle| + \eta(|\langle m|a|n\rangle| + |\langle m|a^\dagger|n\rangle|)], \quad (2.27)$$

using Equations 2.21 and 2.22, this equation can be rewritten as

$$\Omega_{n,m} \approx \Omega(\delta_{m,n} + \eta\sqrt{n}\delta_{m,n-1} + \eta\sqrt{n+1}\delta_{m,n+1}). \quad (2.28)$$

As this equation shows, only one term will remain in each transition from  $|g, n\rangle$  to  $|e, m\rangle$ . Therefore, the first term ( $m = n$ ) is due only to internal transition, which is called carrier transition. The second term ( $m = n - 1$ ) is the first red sideband, and the last term ( $m = n + 1$ ) is the first blue sideband, as shown schematically in Figure 2.6 a. The Rabi frequencies are given individually as

$$\Omega_{n,n} = \Omega, \quad (2.29)$$

$$\Omega_{n,n-1} = \Omega\eta\sqrt{n}, \quad (2.30)$$

$$\Omega_{n,n+1} = \Omega\eta\sqrt{n+1}. \quad (2.31)$$



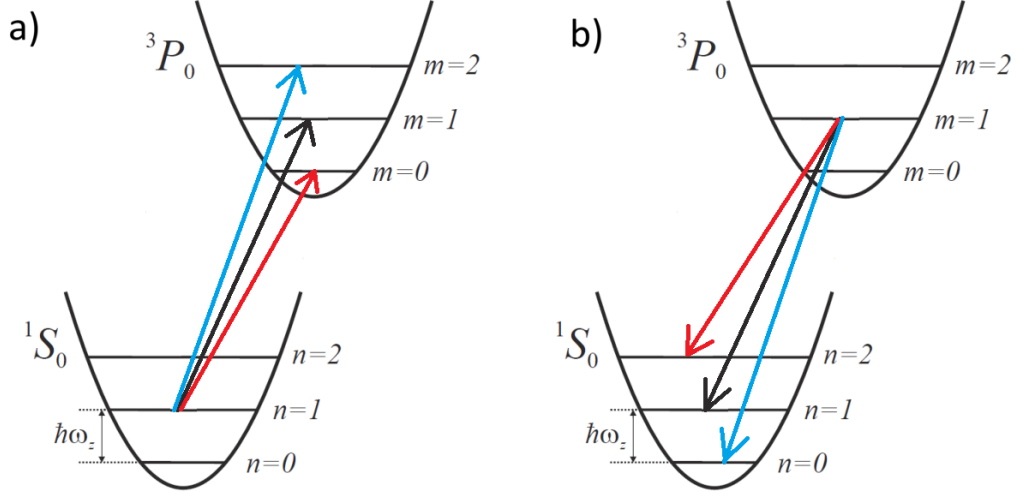


Figure 2.6: Clock transition spectroscopy. a) From ground state to excited state, b) from excited state to ground state.

These are the situations in which the Sr atoms are tightly confined in the harmonic oscillator with the Lamb-Dicke regime. Additionally, Sr atoms are in the ground state  $^1S_0$  while interacting with the clock laser. Therefore, the red and blue sideband amplitude are  $\Omega\eta\sqrt{n}$  and  $\Omega\eta\sqrt{n+1}$ , respectively. So, the amplitude of the blue sideband is slightly bigger. The other reason is that when the Sr atoms are cold enough, most occupy the first level ( $n=0$ ); therefore, a red sideband ( $n-1$ ) for these atoms is impossible.

When the Sr atoms are excited to the  $^3P_0$  during interrogation time, they will stay there for a long time due to the long lifetime of this state. They will be de-excited by interrogating these atoms again and return to the ground state  $^1S_0$ . In this situation, Hamiltonian interaction in Equation 2.24 is like

$$H_i = \frac{\hbar\Omega}{2}(|g\rangle\langle e|e^{ikz} + H.c.). \quad (2.32)$$

Therefore, the Equation 2.28 is written as

$$\Omega_{m,n} \approx \Omega(\delta_{n,m} + \eta\sqrt{m}\delta_{n,m-1} + \eta\sqrt{m+1}\delta_{n,m+1}). \quad (2.33)$$

Only  $n$  and  $m$  are swapped. So, the Rabi frequencies are these three terms:

$$\Omega_{m,m} = \Omega, \quad (2.34)$$

$$\Omega_{m,m-1} = \Omega\eta\sqrt{m}, \quad (2.35)$$

$$\Omega_{m,m+1} = \Omega\eta\sqrt{m+1}. \quad (2.36)$$

In this case, the carrier has the same amplitude as seen in Equation 2.34. The second

term with  $n = m - 1$  is the opposite of the other case ( $m = n - 1$ ) for the red sideband in Equation 2.30. In this case, the  $m - 1$  is for the blue sideband. For example, when the  $m = 1$ ,  $n$  must be equal to 0; in other words, transition from  $|e, m = 1\rangle$  to  $|g, n = 0\rangle$  as it is also depicted in Figure 2.6 b has a larger frequency, or it is blue detuned. The last term with  $n = m + 1$  also has the same situation, and it is for the red sideband.

The amplitude for the red sideband is equal to  $\Omega\eta\sqrt{m+1}$  and  $\Omega\eta\sqrt{m}$  for the blue sideband. Therefore, when the spectroscopy is performed on the Sr atoms while they are excited, the red sideband is expected to have a slightly higher amplitude than the blue sideband. Usually, in this situation, when the atoms are tightly confined with the Lamb-Dicke regime and cold enough, most occupy the lowest level with  $m = 0$  as they are excited from  $n = 0$ . So when they are de-excited, there is no blue sideband as the lowest level is  $n = 0$ .

### 2.3.3 Temperature measurement

The temperature of the trapped atoms is much lower than the potential depth of the trap. Therefore, most of the atoms occupy lower motional states of the potential [64]. To measure the temperature of trapped atoms, the sideband shape should be studied [12]. The relative height of the two sidebands indicates the longitudinal (axial or along the lattice beam) temperature, and the sidebands' shape indicates the atoms' transverse (radial or perpendicular to the lattice beam) temperature.

By assuming that the atoms are distributed among the states according to the classical Maxwell-Boltzmann distribution, the longitudinal temperature of the trap can be approximated by [12]

$$T_z = \frac{h\nu_z}{k_B \ln(b_{br})}, \quad (2.37)$$

which  $k_B$  is Boltzmann's constant and  $b_{br}$  is the height ratio between the blue and red sideband. With the same approach, the transition probability for the sideband transition as a function of frequency detuning  $\delta = \nu_{sb\pm}$  from resonance can be approximated by [12]

$$P(\delta) = \begin{cases} A \frac{4U_0}{h\nu_r} \left(1 - \frac{|\delta|}{\nu_z}\right) e^{\frac{h\nu_r}{k_B T_r}} e^{-\frac{4U_0}{k_B T_r} \left(1 - \frac{|\delta|}{\nu_z}\right)}, & \text{if } -\nu_z < \delta < \nu_z, \\ 0, & \text{elsewhere,} \end{cases} \quad (2.38)$$

the probability function is truncated in two parts to keep the function validated between  $-\nu_z < \delta < \nu_z$  of detuning frequency. Transverse temperature ( $T_r$ ) is extracted by fitting this function to measured sideband data.

By plotting Equation 2.38 with the parameters which are set in our experiment,  $\lambda = 813$  nm of lattice laser wavelength,  $w_0 = 152$   $\mu\text{m}$  for lattice beam radius,  $\nu_z = 65$  kHz which is measured from spectroscopy of  $^1S_0 - ^3P_0$ , and  $T_r = 6$   $\mu\text{K}$ . The sidebands will look like Figure 2.7 a, which the carrier extracts from. To fit the carrier as well and estimate the full width at half maximum (FWHM), the Lorentzian function should fit the data as written in Equation 2.39, as a function of frequency detuning ( $\delta$ ).

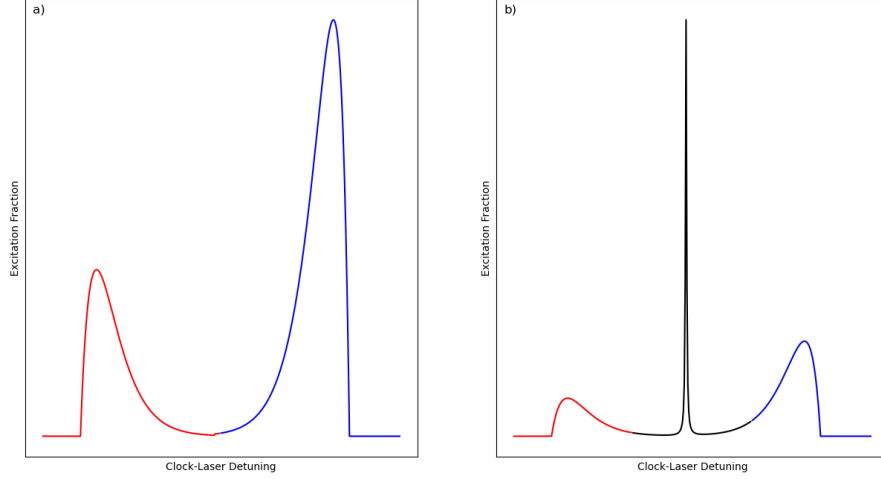


Figure 2.7: Transition probability for sidebands and carrier. a) Only sidebands from Equation 2.38, b) Sidebands and carrier both at the same time.

$$L(\delta) = \frac{A}{\pi} \frac{\gamma}{(\delta - \delta_0)^2 + \gamma^2}, \quad (2.39)$$

in this equation,  $\gamma$  is the carrier's FWHM, and  $\delta_0$  is the peak of carrier frequency, which is set on zero for simplicity by shifting the peak of measurement data to zero. By combining these two Equations 2.38 and 2.39, the total function looks like Figure 2.7 b. This is similar to sideband spectroscopy and can be directly fitted to measurement data.

The same method can be used to measure the temperature of the Sr atoms while they are excited. The Equation 2.38 should be fitted to the sidebands measurement to determine the radial temperature  $T_r$ . However, the axial temperature can be calculated by modified Equation 2.37 as

$$T_z = \frac{h\nu_z}{k_B \ln(b_{rb})}, \quad (2.40)$$

where the  $b_{rb}$  is the only difference in this equation and is equal to

$$b_{rb} = \frac{A_{red}}{A_{blue}}, \quad (2.41)$$

where  $A_{red}$  and  $A_{blue}$  are the amplitude of the red and blue sidebands respectively.

## 2.4 Ultra-precise spectroscopy

The clock transition of  $^1S_0 - ^3P_0$  is forbidden for boson  $^{88}\text{Sr}$ . For inducing a coupling between these two states, a coupling between  $^3P_0$  and  $^3P_1$  should be induced by a strong bias magnetic field [65]. Due to this perturbation in the system,  $^3P_0$  get a small mixture of  $^3P_1$ :

$$|{}^3P'_0\rangle = |{}^3P_0\rangle + \frac{\Omega_B}{\Delta_{10}}|{}^3P_1\rangle, \quad (2.42)$$

where  $\Omega_B$  is coupling matrix element and is equal to:

$$\Omega_B = \frac{\langle {}^3P_0 | \hat{\mu} \cdot \vec{B} | {}^3P_1 \rangle}{\hbar}, \quad (2.43)$$

$\hat{\mu}$  is the magnetic dipole operator, and  $\Delta_{10}$  is splitting frequency between  ${}^3P_0$  and  ${}^3P_1$ .

Due to this perturbation, transition between  ${}^1S_0$  and  ${}^3P'_0$  is weakly allowed. An electric dipole transition between  ${}^1S_0$  and  ${}^3P_1$  is partially allowed with  $\gamma$  decay rate due to the high intensity of an optical field with frequency of  $\omega$  and amplitude  $\vec{E}$ . The coupling matrix element corresponds to the Rabi frequency:

$$\Omega_L = \frac{\langle {}^3P_1 | \vec{d} \cdot \vec{E} | {}^1S_0 \rangle}{\hbar}, \quad (2.44)$$

where  $\vec{d}$  is the electric dipole operator [66]. Due to mixture of  ${}^3P_1$  in  ${}^3P'_0$ , a resonance will be allowed on the forbidden transition of  ${}^1S_0 - {}^3P_0$  when  $\omega \approx \omega_{00}$ , which  $\omega_{00}$  is transition frequency between  ${}^1S_0 - {}^3P_0$ . The effective Rabi frequency for excitation  ${}^1S_0 - {}^3P_0$  of the clock transition can be write as Equation 2.45 using Equation 2.42,

$$\Omega_{00} = \frac{\langle {}^3P'_0 | \vec{d} \cdot \vec{E} | {}^1S_0 \rangle}{\hbar} = \frac{\Omega_L \Omega_B}{\Delta_{10}}. \quad (2.45)$$

The state  ${}^3P'_0$  has a finite lifetime due to a small mixture of  ${}^3P_1$ , so this makes the forbidden transition broad. The total broadening due to this broadening and also power broadening can be estimated from perturbation theory as [65]:

$$\gamma_{00} \sim \gamma \frac{\Omega_L^2/4 + \Omega_B^2}{\Delta_{10}^2}. \quad (2.46)$$

This broadening is inversely proportional to the square of the splitting frequency  $\Delta_{10}^2$  between two states. This broadening is very small, and only by applying a high magnetic field and high-intensity clock laser beam can it be broad enough to be detectable in the experiment. These perturbations introduce a significant shift in the clock transition.

Linewidth of  ${}^1S_0 - {}^3P_0$  resonance is practically limited by the Fourier transform of the interrogation beam. The finite interaction time  $\tau_p$  of the clock laser beam with trapped Sr atoms leads to a finite homogeneous width of the corresponding spectrum in the frequency domain [67]. If the interrogation beam ( $f(t) = A_0 \cos(\omega_0 t)$ ) is switched on for a finite duration  $\tau_p$ , the inverse Fourier transformation of the beam is  $F(\omega) \equiv F_+(\omega - \omega_0) + F_-(\omega + \omega_0)$  the second one is the negative mirror frequencies. Calculating the first term is given by

$$F_+(\omega - \omega_0) = \frac{A_0 \tau_p}{2} \frac{\sin[(\omega - \omega_0) \tau_p / 2]}{[(\omega - \omega_0) \tau_p / 2]}, \quad (2.47)$$

which  $\omega$  is clock laser frequency and  $\omega_0$  is transition frequency of  $^1S_0 - ^3P_0$ . The power spectrum  $|F_+(\omega - \omega_0)|^2$  is

$$P(\omega - \omega_0) = A \frac{\sin^2[(\omega - \omega_0)\tau_p/2]}{[(\omega - \omega_0)\tau_p/2]^2}. \quad (2.48)$$

To determine the FWHM of this spectrum, Equation 2.48 should be set to half of the amplitude ( $A/2$ ). By solving the equation, the FWHM is equal to:

$$\Gamma = 0.8859 \frac{1}{\tau_p}. \quad (2.49)$$

For example, if the interrogation time is 200 ms, FWHM is limited by Fourier transform of  $\approx 4$  Hz. Figure 2.8 presents the pulse shape of the interrogation beam in a, and its power spectrum from Equation 2.48 in b. There are side lobes around the main peak at  $\omega_0$ . The side lobes are caused by steep slopes when the interaction is turned on and off [67].

## 2.5 Rabi oscillation

The transition probability on resonance for a two-level system as a function of interrogation time is written in Equation 2.50, for excited state [68]:

$$P(t) = \frac{1}{2}(1 - \cos(\Omega_0 t)e^{-t/\tau_c}), \quad (2.50)$$

where  $\Omega_0$  is the Rabi frequency and is given by Equation 2.51, and  $\tau_c$  is the coherence time of the clock laser beam.

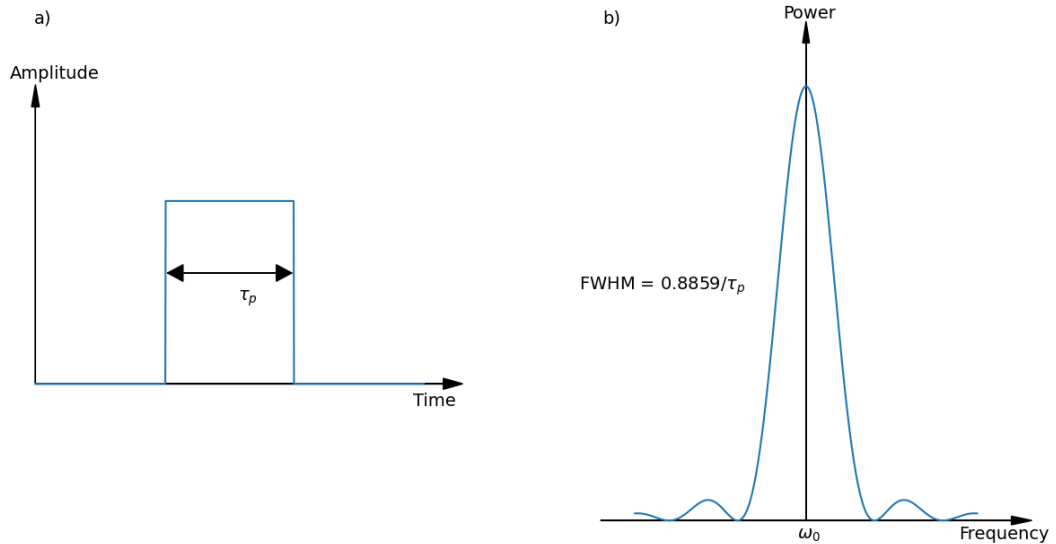


Figure 2.8: Linewidth limitation measurement due to the Fourier transform. a) Pulse time to interrogate with trapped Sr atoms, b) corresponding power spectrum.

$$\Omega_0 = \frac{\vec{d} \cdot \vec{E}}{\hbar}, \quad (2.51)$$

where  $\vec{d}$  is the dipole moment of the clock transition  $^1S_0 - ^3P_0$ , and  $\vec{E}$  is the electric field of the clock laser beam which is interrogate trapped atoms. For clock spectroscopy, Rabi frequency is proportional to the square root of the intensity of the interrogation light field. Figure 2.9 a is the Rabi oscillation plotted by Equation 2.50 for different Rabi pulse time and coherence time.

Considering the radial motion effect, the transition probability on resonance for the excited state is written in Equation 2.52; to see how this equation is driven, refer to [64].

$$P_e(t) = \frac{1}{2} + \frac{1 - \zeta_r}{2} \frac{\zeta_r \cos[\phi t(1 - \eta_r^2)] - \cos(\phi t)}{1 + \zeta_r^2 - 2\zeta_r \cos(\phi t \eta_r^2)}, \quad (2.52)$$

where  $\zeta_r$  is defined as:

$$\zeta_r = e^{-h\nu_r/k_B T_r}, \quad (2.53)$$

$\phi$  is defined in the Equation 2.54.

$$\phi = \Omega_0 e^{-(\eta_r^2 + \eta_z^2)/2}, \quad (2.54)$$

where  $\eta_r$  and  $\eta_z$  are defined as:

$$\eta_r = \frac{\Delta\theta \sqrt{h/2m\nu_r}}{\lambda_p}, \quad (2.55)$$

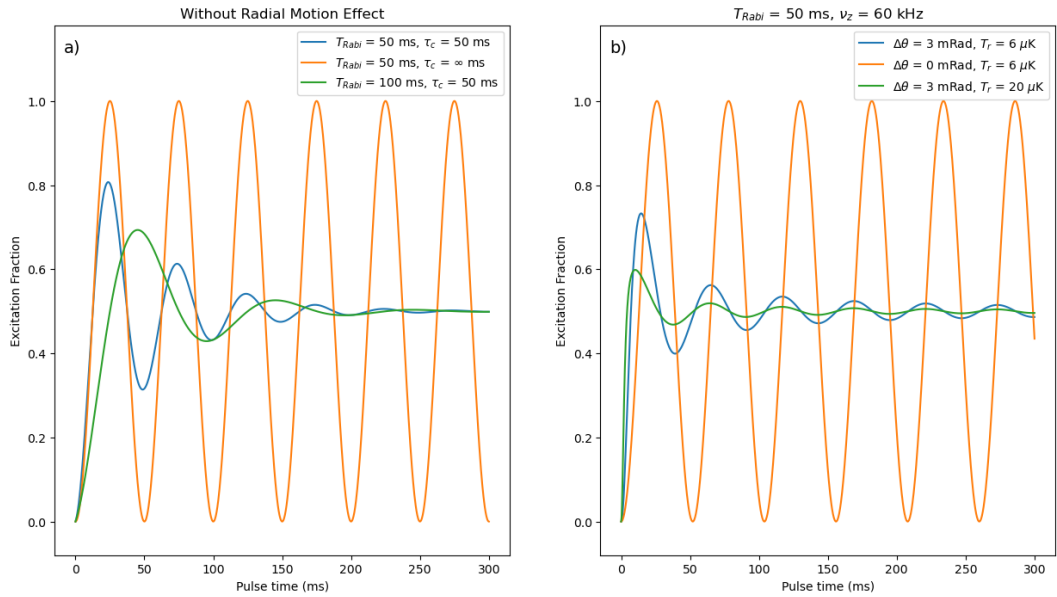


Figure 2.9: Rabi oscillation. a) Without radial motion effect, plotted by Equation 2.50, b) affected by radial motion as it is in Equation 2.52.

$$\eta_z = \frac{\sqrt{h/2m\nu_z}}{\lambda_p}, \quad (2.56)$$

in these equations,  $\lambda_p$  is clock laser wavelength, and  $\Delta\theta$  is misalignment of clock beam and lattice beam. Figure 2.9 b is plotted with a fixed Rabi period of 50 ms and longitudinal frequency  $\nu_z$  of 60 kHz. However,  $\Delta\theta$  and radial temperatures are different. When the clock and lattice beams are perfectly aligned  $\Delta\theta = 0$ , the transition probability is the same as Equation 2.50 if the coherence time of the laser beam is infinitely long. By increasing radial temperature, oscillation is damped faster.

The Equation 2.52 is used to extract the  $\Omega_0$  and  $\Delta\theta$  by reducing the number of parameters for the fit, the radial temperature  $T_r$  and longitudinal frequency  $\nu_z$  is extracted first by studying the shape of sidebands from scanning clock laser frequency over the carrier and covering the sidebands as it is discussed in the previous sections.

## 2.6 Evaluation of systematic shifts

There are two parameters to characterize the quality of an optical atomic clock: stability and accuracy. The stability characterizes the changes in optical clock frequency in time. The optical clock frequency is measured as the transition frequency of  $^{88}\text{Sr}$  atoms. The typical way to characterize these changes is the Allan variance [69], as was discussed at the beginning of this chapter. On the other hand, the accuracy characterizes how much the optical clock frequency may be different from the theoretical transition frequency without any perturbation on the atoms.

The measured optical clock frequency is perturbed and shifted from the clock transition  $^1S_0 - ^3P_0$  frequency due to several effects. These effects include Zeeman shift, probe light shift, blackbody radiation, AC Stark shift, and collision shift. The collision shift is estimated by many body calculations [70]. The AC Stark shift, which could be the most significant shift, has been suppressed very well due to using magic wavelength for the lattice laser [71]. The blackbody radiation shift due to thermal radiation surrounding the trapped atoms is also well controlled [72]. However, shifts due to the high magnetic fields, which are used to allow the forbidden transition of  $^1S_0 - ^3P_0$  and clock laser beam for interrogation with trapped  $^{88}\text{Sr}$  atoms, are still the most dominant perturbation in the accuracy budget of the optical clocks. Therefore, only the Zeeman shift and probe light shift are discussed in this section.

### 2.6.1 Zeeman shift

The Zeeman shift is due to the coupling of total magnetic momentum  $\mu$  with an external magnetic field  $B$ . The Hamiltonian of the system for the Zeeman effect is written by:

$$H_Z = \vec{\mu} \cdot \vec{B}, \quad (2.57)$$

where  $\vec{\mu}$  is the total magnetic momentum operator of the Sr atom. It consists of three components including:

$$\vec{\mu}_L = -g_L \mu_B \vec{L} / \hbar, \quad (2.58)$$

$$\vec{\mu}_S = -g_S \mu_B \vec{S} / \hbar, \quad (2.59)$$

$$\vec{\mu}_I = g_I \mu_B \vec{I} / \hbar, \quad (2.60)$$

$\vec{\mu}_L$ ,  $\vec{\mu}_S$ , and  $\vec{\mu}_I$  are orbital, spin, and nuclear magnetic momentum respectively. Where  $g_L = 1$ ,  $g_S \approx 2$ , and  $g_I = \frac{\mu_I(1-\sigma_d)}{I\mu_B/\hbar}$  are the orbital, spin, and nuclear Landé factors respectively.  $\mu_I$  is the nuclear magnetic momentum,  $\sigma_d$  is the diamagnetic correction, and  $\mu_B = \frac{e\hbar}{2m_e}$  is the Bohr magneton. Therefore the Hamiltonian in the Equation 2.57 for  $\vec{B} = B\hat{z}$  and nuclear quantum number  $\vec{I} = 0$  for boson  $^{88}\text{Sr}$  is:

$$H_Z = (L_z + 2S_z) \frac{\mu_B B}{\hbar}. \quad (2.61)$$

The linear Zeeman shift is given by:

$$\Delta_B^{(1)} = -\frac{\delta g \mu_B}{h} m_F B, \quad (2.62)$$

where  $\delta g$  is the differential  $g$  factor due to hyperfine mixing between different states [73]. As  $^{88}\text{Sr}$  is a boson, it is free of hyperfine states, so the linear Zeeman shift equals zero.

However, the second-order Zeeman shift should be considered for high-accuracy clock operation. The clock states  $^1S_0$  and  $^3P_0$  are both  $J = 0$ , so the shift comes from the separation in the energy of levels by the fine structure splitting. The main contribution is from the interaction of excited state  $^3P_0$  and  $^3P_1$  as the ground state  $^1S_0$  is separated from all other energy levels by optical frequencies. Therefore, the total shift is approximated by the repulsion of two triplet states as given by [69]:

$$\Delta_B^{(2)} = -\frac{2\mu_B^2}{3\Delta v_{10} h^2} B^2, \quad (2.63)$$

where  $h\Delta v_{10}$  is the energy separation of  $^3P_0$  and  $^3P_1$  states.

### 2.6.2 Probe light shift

The interaction of the external electric fields with Sr atoms shifts the energy levels of the atoms, similar to a magnetic field, as discussed in the previous section. This effect is called the Stark effect and could be calculated by perturbation theory. The polarisability is the ratio of the dipole moment  $d$  to the electric field  $E$  [67]

$$\alpha = \frac{d}{E}, \quad (2.64)$$



the induced dipole moment  $\vec{d}$  is proportional to the electric field  $\vec{E}$ . The Stark shift is calculated as a second-order perturbation for an atom without a permanent dipole moment

$$\Delta E_m = \sum_n \frac{|\langle m | \vec{d} | n \rangle|^2}{E_m - E_n} E^2, \quad (2.65)$$

when the summation is on all the  $n$  states, coupled with the  $m$  state when the electric field oscillates with a frequency  $\nu$  and is comparable with the transition frequency of  $m$  and  $n$  states, the Stark effect is dynamic. In this case, the polarisability becomes a function of frequency  $\nu$  as

$$\alpha = 6\pi\epsilon_0 c^3 \frac{\Gamma/\omega_0^2}{\omega_0^2 - \omega^2 + i(\omega^3/\omega_0^2)\Gamma}, \quad (2.66)$$

where  $\Gamma \equiv \Gamma_{\omega_0} = (\frac{\omega_0}{\omega})^2 \Gamma_{\omega}$ , and  $\Gamma_{\omega}$  is damping rate due to the radiative loss [74] which is

$$\Gamma_{\omega} = \frac{e^2 \omega^2}{6\pi\epsilon_0 m c^3}, \quad (2.67)$$

and the Stark shift energy for far detuning from resonance is [67]

$$\Delta E_m = \frac{1}{2} \sum_n |\langle m | \vec{d} | n \rangle|^2 E_0^2 \frac{E_m - E_n}{(E_m - E_n)^2 - (\hbar\omega)^2}. \quad (2.68)$$

When the frequency of the electric field is resonant with an allowed transition ( $\hbar\omega \approx E_m - E_n$ ), transitions between states can be induced. Therefore, the coupling between states splits the states. The Rabi frequency  $\Omega_R$  gives the splitting exactly at the resonance.

AC stark shift due to very high power lattice intensity, which is far detuned for  $^1S_0$  and  $^3P_0$  transition is zero as the polarisability is identical for these states in Sr atom at 813 nm magic wavelength. However, for probe light at 698 nm of clock laser during interrogation, polarisability is very different for transition states. Therefore, there is a frequency shift despite the light intensity being very low, around  $400 \text{ mW/cm}^2$  [75] for bosonic Sr. This intensity can be reduced, but it should be compensated by increasing the magnetic field during interrogation to allow the transition. So, there should be a balance between magnetic fields and probe light intensity.



# Chapter 3

## Designing an automated control system for compensation coils

This chapter focuses on developing an automated system for controlling the magnetic fields of the compensation coils. The compact current driver is developed to improve the trapped Sr atoms automatically. This compact and robust device is connected to a real-time computer and allows it to be controlled through TTL signals from the real-time computer. This compact device has been installed and tested in the lattice optical atomic clock working in the Sr1 room of the KL FAMO lab.

### 3.1 Introduction

In any cold atom experiment, precise control over the magnetic field is necessary. It is essential to have a 3D control to compensate for the Earth's magnetic field and any stray magnetic fields in the laboratory. On the other hand, transferring atoms between different stages of cooling, such as MOT and optical lattice, is usually enhanced by adding static offset fields, for instance, to compensate for imbalances of laser light intensity in retroreflected beams [76]. Three pairs of different Helmholtz coils usually ensure all these conditions. Due to experimental space constraints, the pairs are usually not identical and require different currents.

In the case of a passive optical lattice strontium clock, the presence of the magnetic field induces systematic shifts to the atomic clock line, such as first- and second-order Zeeman shifts. Electromagnetic fields are the most dominant source of perturbations [69]. The achievable stability of the magnetic field determines the uncertainty of these systematic shifts and, thus, the clock's accuracy. Moreover, the magnetic field fluctuations will directly deteriorate the clock's stability.

The current controller for the compensation coils should be able to tune the currents' values and change their directions independently for each pair of coils. Here, the design of a compact device is presented for real-time control of the current of coils automatically via TTL signals and Ethernet during the clock operation. This device can be used for any cold atom experiments. It may be beneficial outside of the laboratory for portable and transportable clocks where the background magnetic field needs to be compensated all the time [77–82].

## 3.2 Hardware and software

The picture of the compact current driver controller is shown in Figure 3.1. The device comprises a high-power current driver, a low-power board, and a microcontroller (NUCLEO-H743ZI2). The current driver should be supplied by 18 V with a power supply. The current driver provides the microcontroller's power supply. As shown in Figure 3.1 by the yellow circle in the middle of the current driver, the device has three output channels (Ch 1, Ch 2, and Ch 3). Each channel is dedicated to one pair of coils. The compact device is accessible through Ethernet with the microcontroller, and individual current values for each pair of coils are registered on the microcontroller's memory via the configuration of TTL signals.

The microcontroller is programmed by STM32 CubeIDE software. As we face a real problem with high-accuracy timing, the code should be written in parallel to handle all the events, interruptions, and multiple client connections. The FreeRTOS library is used for parallel programming. FreeRTOS is available for STM32 microcontrollers and is commonly used for real-time operating systems in embedded systems development. The FreeRTOS library provides a real-time kernel for microcontrollers, offering various functionalities for task scheduling, inter-task communication, synchronization, and more.

For Ethernet communication, the Lightweight IP (lwIP) library is used. The lwIP stack is a popular open-source TCP/IP stack designed for embedded systems and is commonly used with STM32 microcontrollers to enable networking capabilities.

The maximum number of addresses that it is possible to define for this device is defined by the number of TTL input ports. Each address is registered in the microcontroller's memory and has a unique value for each channel, which the operator wants to

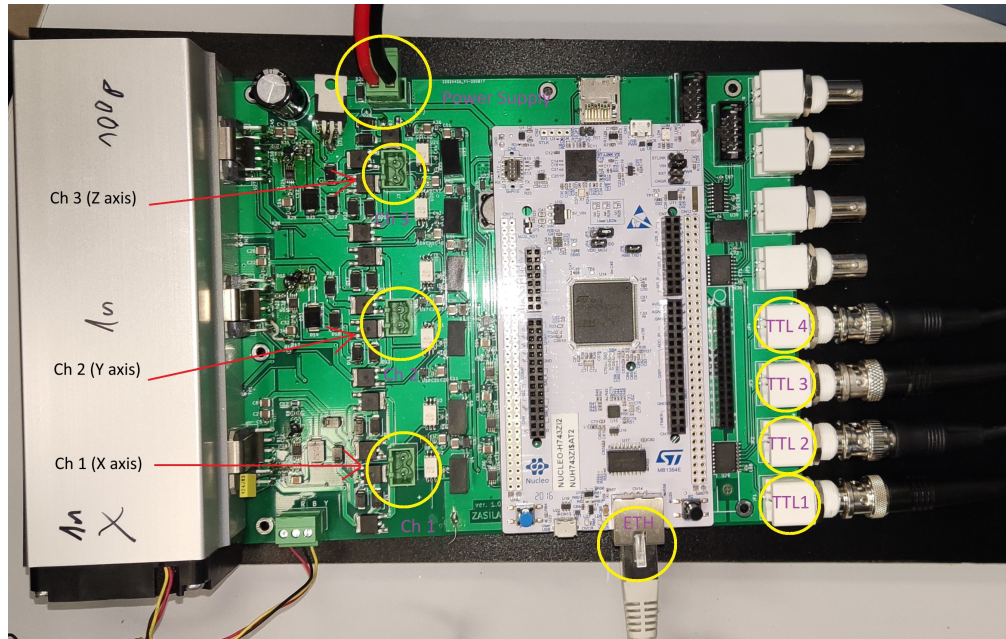


Figure 3.1: Compact current driver controller for compensation coils. This compact device has 3 outputs (ch 1, ch 2, and ch 3) for three pairs of coils in x, y, and z directions. The compact device is accessible through Ethernet, and the configuration of TTL signals is used to define which current values should be applied for each pair of coils.

apply on the coils at a specific stage of cooling the atoms. There are eight input/output ports, as shown in Figure 3.1; two of them are dedicated to output and the rest for input; also, one of the inputs is dedicated to a set bit. Therefore, we are left with five inputs, which we can calculate the number of addresses by equation (3.1):

$$\text{number of addresses} = 2^{(\text{number of inputs})}. \quad (3.1)$$

This compact device can have 32 addresses. However, in our case, three of the TTLs are used as input, which is indicated by the yellow circle on the right side of the picture, and there are eight addresses that the operator can use. As mentioned, one input is dedicated to a set bit signal on this board named TTL4. At any stage of the experiment where the operator wants to apply a registered address, a signal is applied from this set bit signal.

The first three TTL signals configure the required memory address, and TTL4 triggers switching outputs to the new address. TTL1 is the least significant, and TTL3 is the most significant. The patterns in Table 3.1 show three different registered addresses in the memory of the microcontroller. By applying TTL4, new values are applied to the output of the current driver.

Figure 3.2 presents a conceptual diagram of the current driver. The complete PCB schematics and fabrication files for PCB design and manufacturing are available at [83].

The output in the range of -3 A to 3 A for each channel of this board is directly connected to the coils. Each output is provided by the DAC8560, a digital-to-analog converter (DAC) manufactured by Texas Instruments. This DAC offers high-resolution

Table 3.1: The pattern directs the controller output to the pre-programmed value.

Address	TTL1	TTL2	TTL3	TTL4
000	0	0	0	
001	1	0	0	
010	0	1	0	

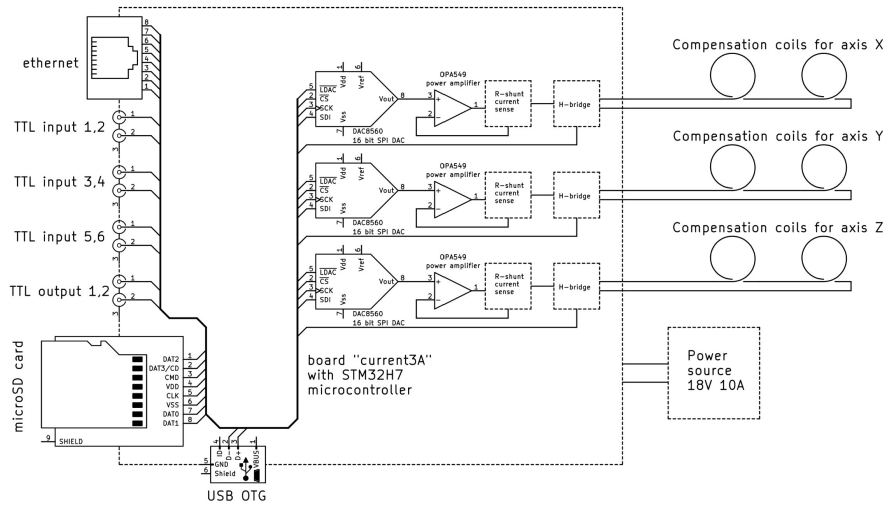


Figure 3.2: Diagram of compensation coils controller board [84].

conversion capabilities of 16 bits. This device usually uses a standard serial interface such as SPI (Serial Peripheral Interface) or similar serial communication protocols, allowing easy integration with microcontrollers, FPGAs, or other digital systems. This DAC is stabilized to the ultrastable ADR443BRZ voltage reference manufactured by Analog Devices. After amplifying the output of DAC by the OPA549 power amplifier, the current is sensed using high-quality shunt resistors from the output of this power amplifier. At the end, coils are connected through a TTL-controlled H-bridge. An H-bridge is an electronic circuit configuration used to control the direction of currents. It consists of four switching elements (transistors or MOSFETs) arranged in a configuration that allows current to flow through the coils in either direction. TTL signal is applied from the microcontroller based on the value registered on its memory. If the current value is positive, the TTL signal is high; otherwise, it is ground for negative currents.

The current driver (specifically DAC8560) and the microcontroller communicate via SPI. This communication is set with master mode, 2-line direction, 8-bit data size, and baud rate prescaler set on 4. SPI speed is calculated by the equation 3.2,

$$\text{SPI speed} = \frac{\text{Clock Frequency}}{\text{Prescaler}}. \quad (3.2)$$

The clock frequency for this SPI is set to 100 MHz by prescaler 4. This means the SPI peripheral would operate with a maximum communication speed of 25 MHz.

A server-client model is created to build a TCP/IP protocol to allow microcontrollers and operators to communicate and exchange data efficiently over networks via Ethernet communication. The microcontroller is set as a server because it provides services like receiving information from operators (clients), processing it, and registering it in the memory.

### 3.3 Flow chart and algorithm

Figure 3.3 shows a view of the compensation coils around the science chamber in the Sr1 room in the KL FAMO lab, and Figure 3.4 is a 3D drawing view of that. Figure 3.5 shows how the compact current driver controller works in principle. The real-time computer is used to apply different TTL signals to the current driver. The operator can connect to the device through Ethernet and register new values on the microcontroller's memory.

The algorithm's flow chart working in an infinity loop on this microcontroller is shown in Figure 3.6. After initialization, only one thread is responsible for replying to new clients and saving their messages in memory. On the other hand, if any event (TTL4) interrupts, another thread will take care of it and send the addressed values from memory to the DAC on the current driver via an SPI connection.

Another possibility implemented in the algorithm is applying a new value by a ramp signal, not instantly jumping to the new value. A ramp signal is applied to avoid this jump, which may create a voltage spike in the coils due to sudden changes in current. The operator defines the time of the ramp signal, and it is registered in the microcontroller's memory. As shown in Figure 3.7, by applying a ramp signal, the current on the coils changes from 0.5 to -0.5 V step by step in 100 ms, not instantly. The whole ramp's time can not be shorter than 1 ms; this limitation is set in the code to avoid sudden



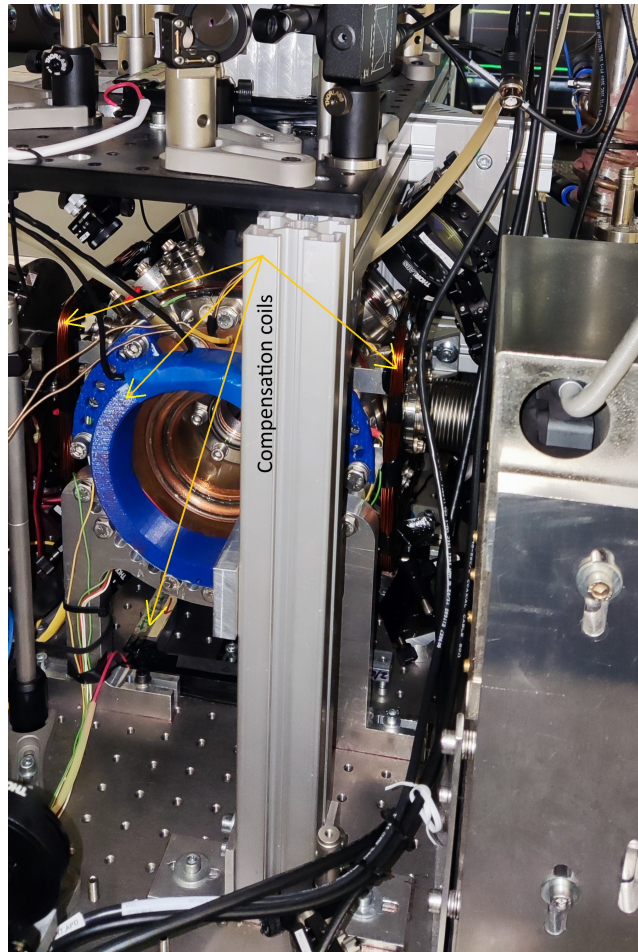


Figure 3.3: The compensation coils installed around the science chamber for lattice optical clock in Sr1 room in KL FAMO lab.

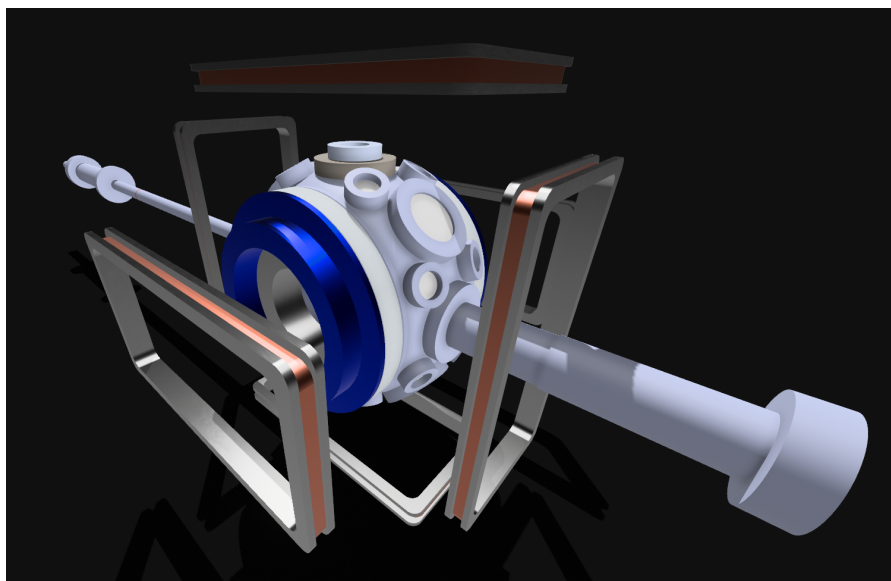


Figure 3.4: 3D drawing of the configuration of the compensation coils around the science chamber in a general case.

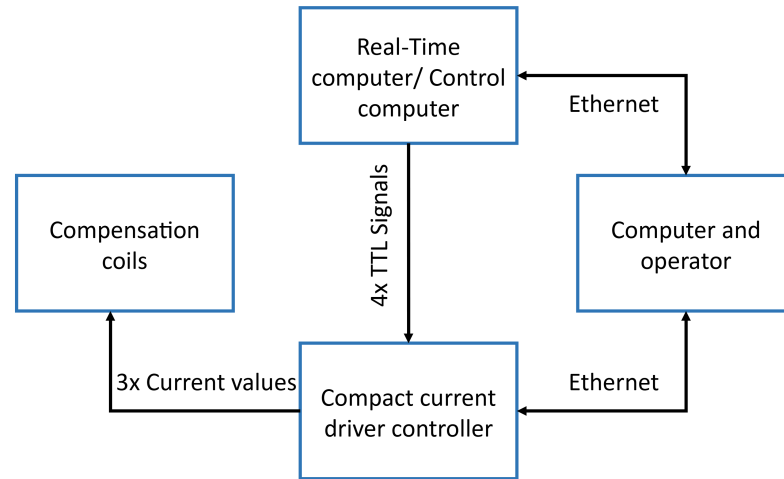


Figure 3.5: The working principle of the compact current driver controller.

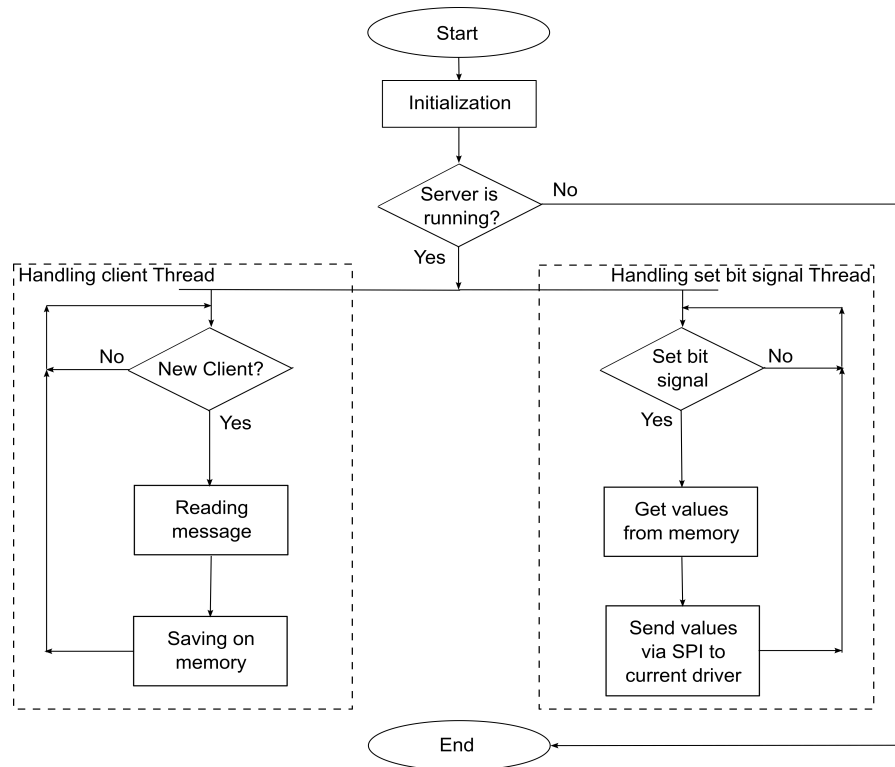


Figure 3.6: Flow chart of the algorithm running in two threads. One thread handles the clients to read and save new values on the memory. Other thread handles the events like set bit signal (TTL4) to switch output values on the current driver.

changes due to a mistaken command from the operator side.

## 3.4 Test

In this project, channel 1 on the current driver is dedicated to the pair of coils in the X direction, channel 2 to the Y direction, and channel 3 to the Z direction. Four TTLs



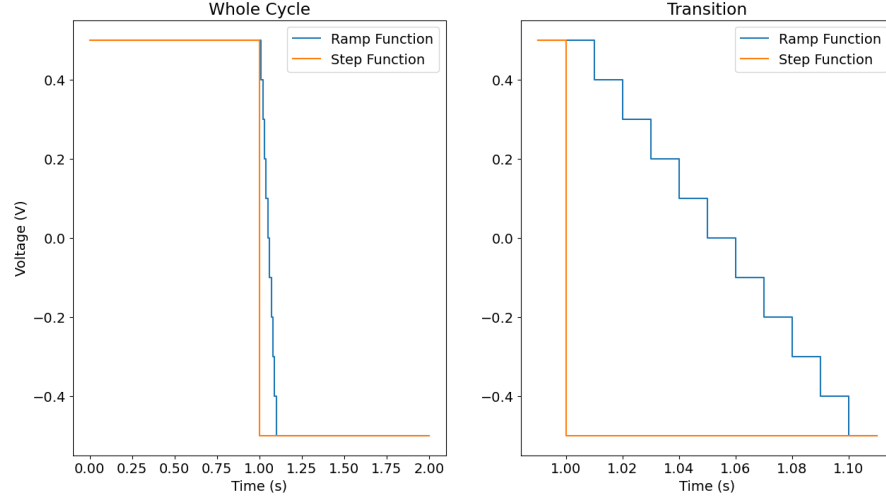


Figure 3.7: The implementation of applying a ramp signal while changing the voltage on the current driver proportional to the current on the coils. The orange color is when the voltage is changed without a ramp signal, and the blue color is when the voltage is changed with a ramp signal.

from a real-time computer must be connected to the current driver by order, as shown in Figure 3.1. The microcontroller should be connected to the network so that it can be accessible by the operator's computer. By turning on the current driver, currents are applied to the coils, and the microcontroller is accessible.

The compact device is installed in the passive optical atomic clock in the Sr1 room in the KL FAMO lab. The values of the following command are registered on the memory of the microcontroller to measure the efficiency of the device; refer to Appendix A for more information about this command:

```
#CDC DAC: 000: 1.25; -1.8; 0.37; 10; & 001: -1.25; -0.8; 1.37; 60;
& 010: 0.0; 0.0; 0.6; 20
```

There are three addresses in this command, which they are applying at a specific time in each cycle of clocks; each address has three values with the unit of V for channels 1, 2, and 3, respectively, and time with the unit of ms for the linear ramp signal. The main program of the clock is running on a real-time computer. The microcontroller applies a new state immediately after receiving TTL's set bit signal. Figure 3.8 shows how the voltage changes during each cycle of the clock for MOT coils (yellow) and coils on the Y axis connected to channel 2 (blue). Figure 3.9 shows the voltage changes for all channels in one cycle. As is evident in the figures, changing values of compensation coils during each cycle of the clock is done automatically by a linear ramp; for example, state 2 (001) is applied in 60 ms.

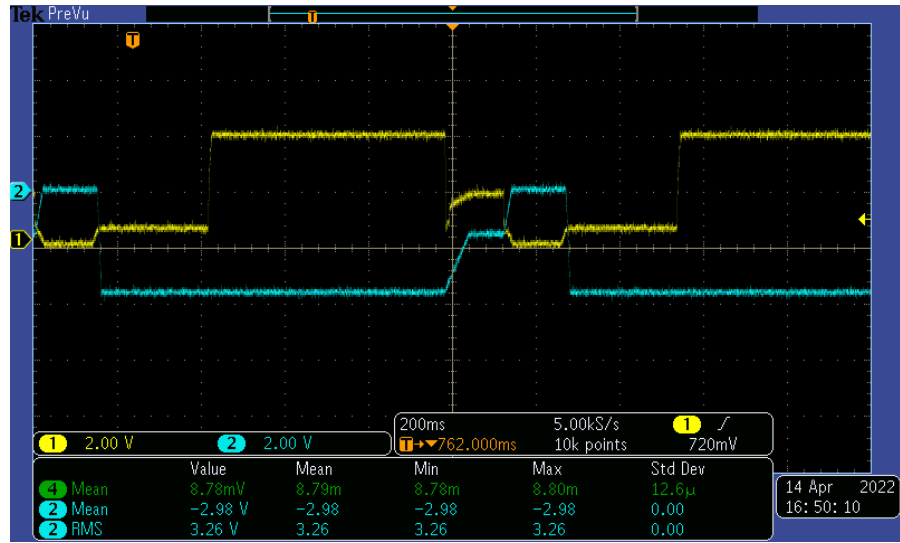


Figure 3.8: Voltage change during each cycle of the clock for MOT coils (yellow) and coils on the Y axis connected to channel 2 (blue).

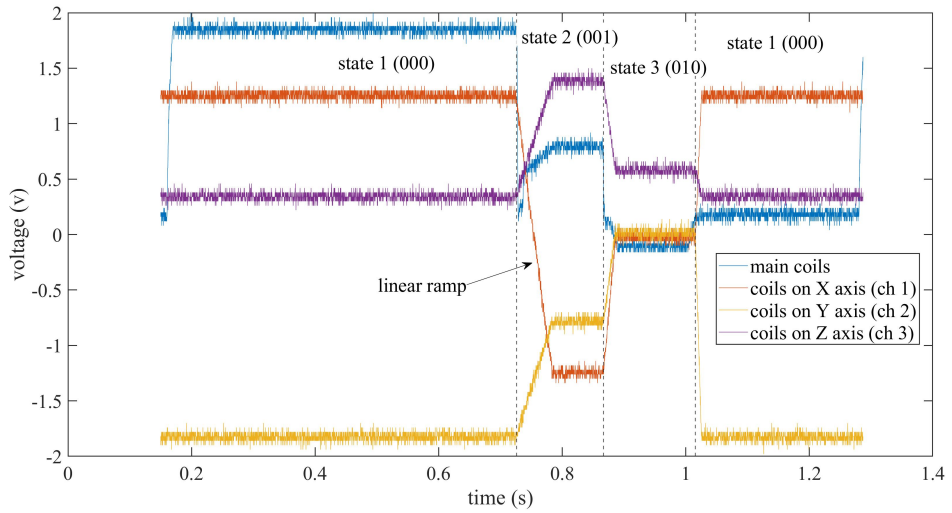


Figure 3.9: Voltage change during one clock cycle for main coils and all the compensation coils [84]. Blue shows how the voltage on the main coils for the MOT changes in each state, and orange, yellow, and purple colors show the voltage changes for compensation coils on the X, Y, and Z axes, respectively.



# Chapter 4

## Designing a control system for direct digital synthesis

This chapter is about controlling the DDS remotely and possibly automatically. The device was developed to provide easy remote access to DDS. The controller is dedicated to 100, 250, and 1000 MHz reference frequency signals. Additionally, it has been tested with the DDS AD9912 model.

### 4.1 Introduction

Many parts of optical clocks require precise control of the laser frequency. This is especially important in clock transition spectroscopy, for capturing cold atoms in optical traps when operating on the magic wavelength, and for frequency transfer. For all these tasks, acousto-optical modulators (AOMs) or electro-optical modulators (EOMs), driven by radio frequency generators, are used. A precise frequency generator could also be used as a reference signal for locking different systems. Therefore, precise frequency generators are essential. For the best performance, the resolution of the frequency control should be on the order of  $\mu\text{Hz}$  level, with the possibility to use an external precise frequency reference.

It is often required to switch between different frequencies in a short time (less than  $1\ \mu\text{s}$ ) and to have the ability to change parameters by other programs via the Ethernet network. Most frequency generators available on the market only meet some of these requirements, and custom solutions are needed. Commercial DDS evaluation boards from Analog Devices (such as AD9912 or AD9959) are a choice for our project. However, they need to be controlled via fast SPI interfaces. The DDS is a frequency synthesizer that generates precise and stable analog waveforms, such as sine waves, with digital control over frequency, phase, and amplitude.

A compact module compatible with the AD9912 evaluation board based on the microcontroller is introduced here. It significantly extends the board's capabilities, makes it easier to use, and has the vast majority of the functionality needed in an optical atomic clock laboratory. All of the DDSs in the KL FAMO lab are referenced to a stable radio frequency signal from UTC (AOS).

## 4.2 Hardware and software

Figure 4.1 shows the picture of the DDS controlling device. This device comprises an evaluation board, a developed electronic board, and a microcontroller (NUCLEO-H743ZI2). The module requires a 5 V power supply connected to a developed electronic board; this board provides a power supply for the evaluation board and the microcontroller. The complete PCB schematic of this board, fabrication files for manufacturing, and software for the microcontroller are available at [85].

In Figure 4.2, the AD9912 evaluation board is shown. The AD9912 is a DDS with an integrated 14-bit DAC. The AD9912 features a 48-bit frequency tuning word (FTW) that can synthesize frequencies in step sizes as small as 4  $\mu\text{Hz}$ . Absolute frequency accuracy can be achieved by adjusting the DAC system clock. The AD9912 also features an integrated system clock phase-locked loop (PLL) that allows system clock inputs as low as 25 MHz.

The frequency of the sinusoid generated by the DDS is determined by the FTW, a digital (numeric) value. Unlike an analog sinusoidal generator, a DDS uses digital building blocks and operates as a sampled system. Thus, it requires a sampling clock ( $f_s$ ) that serves as the fundamental timing source of the DDS.

An external time base connects to the AD9912 at the SYSCLK pins to generate the internal high-frequency system clock ( $f_s$ ). The SYSCLK inputs can be operated in one of the following three modes:

- SYSCLK PLL bypassed,
- SYSCLK PLL enabled with input signal generated externally,
- Crystal resonator with SYSCLK PLL enabled.

It is important to note that when bypassing the system clock PLL, the LOOP\_FILTER pin (Pin 31) should be pulled down to the analog ground with a 1 k $\Omega$  resistor, as it

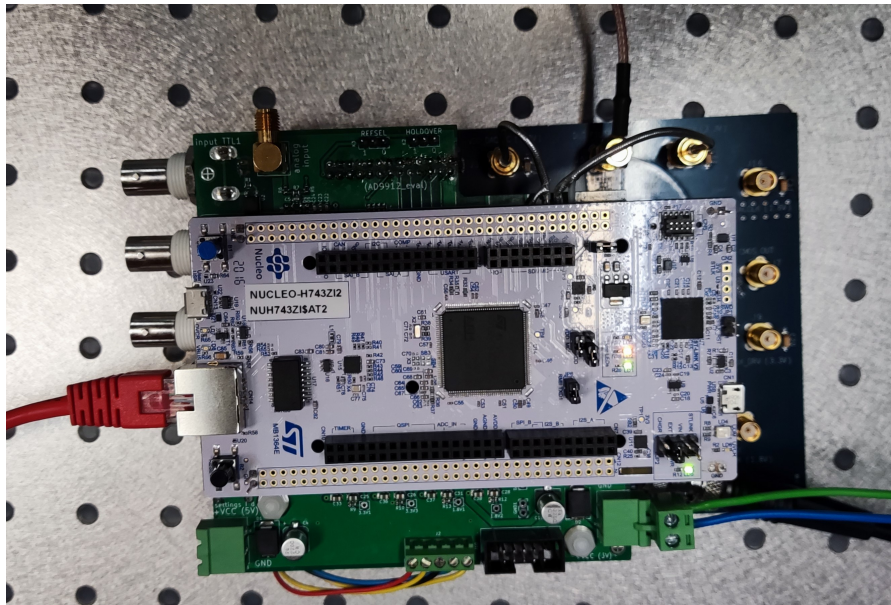


Figure 4.1: A compact module for controlling the DDS board, including an evaluation board, an electronic board, and a microcontroller (NUCLEO-H743ZI2).

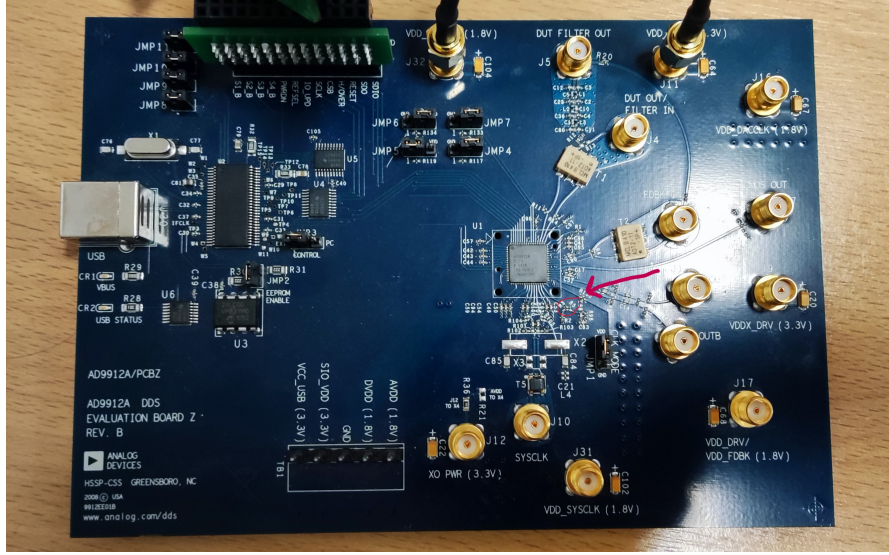


Figure 4.2: Evaluation board, which has been modified for this project.

is shown in Figure 4.3 from datasheet [86]. Also, its place is mentioned in Figure 4.2 on the evaluation board. By default, the evaluation board is pulled down to the ground by R24, underlined by blue in Figure 4.3, and R3 is not connected. Therefore, the SYSCLK PLL multiplier path is deactivated by default. When the SYSCLK PLL multiplier path is disabled, the AD9912 must be driven by a high-frequency signal source (250 MHz to 1 GHz). The signal thus applied to the SYSCLK input pins becomes the internal DAC sampling clock ( $f_s$ ) after passing through an internal buffer.

In this project, SYSCLK PLL is used as enabled. Thus, R24 is removed, and R3 is connected (short circuit) to the evaluation board. The SYSCLK input pins are fed by a 100 MHz reference frequency signal with the multiplier set to 10. Therefore, the internal high-frequency system clock ( $f_s$ ) is 1 GHz. In the program, there is a possibility to use a high-frequency signal source as well (only 250 MHz and 1 GHz) by bypassing the system clock PLL, which is the default of the evaluation board, and there is no need to modify R24 or R3.

The AD9912 DDS chip does not have direct digital control over the amplitude of the output signal, unlike some other DDS chips like AD9959. However, it controls the amplitude scale factor through the on-chip DAC.

Registering values on the evaluation board is very complicated; it needs a good understanding of this evaluation board. Appendix B has a manual on registering new values for frequency through SPI communication in the code. The whole code is available [87].

### 4.3 Flow chart and algorithm

Figure 4.4 shows a schematic diagram of the DDS controller. The DDS controller is accessible remotely by a computer through Ethernet communication. This controller needs to be fed by a reference frequency signal, and the output can be applied to AOMs or EOMs. The output (frequency and amplitude) is fixed until the operator sets a new value. The reference signal is selectable remotely between 100, 250, and 1000 MHz frequencies, but the operator should provide it for the evaluation board first.

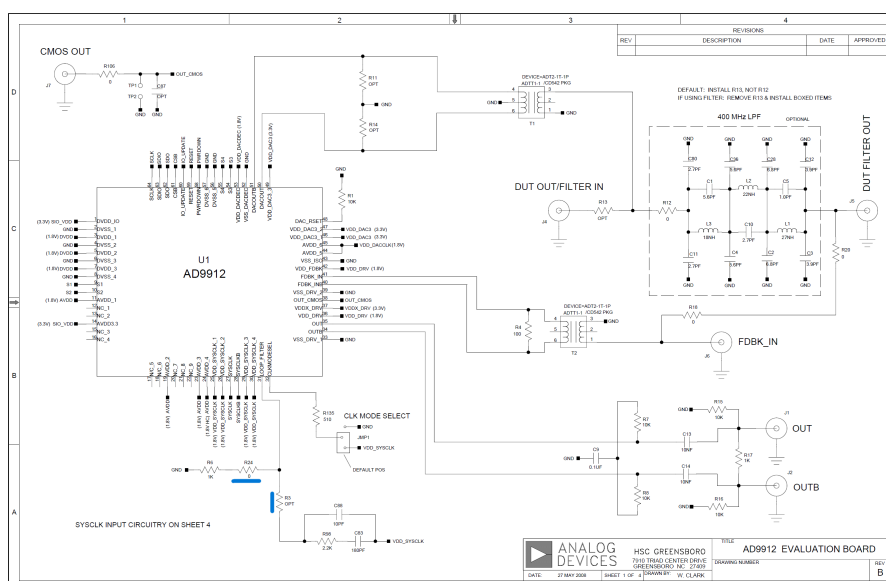


Figure 4.3: Schematic of evaluation board which shows two resistors for selecting SYSCLK PLL bypassed or enabled. To use SYSCLK PLL as enabled, R24 should be removed and R3 connected.

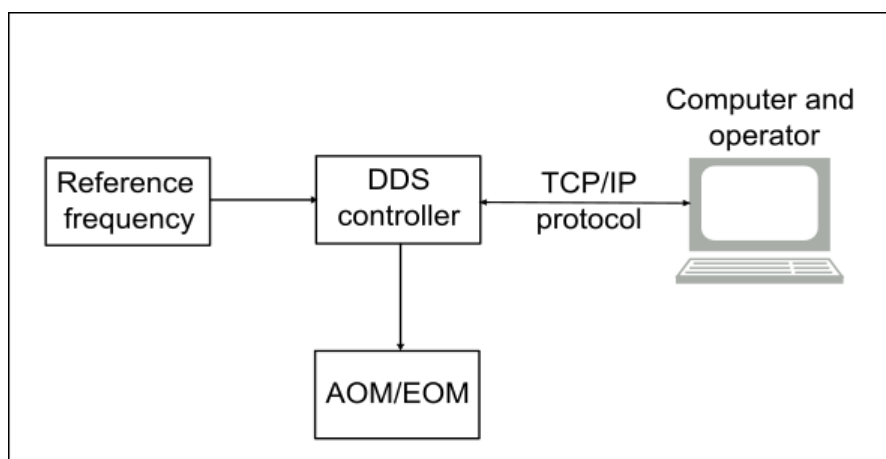


Figure 4.4: A schematic diagram of DDS controller in the experiments.

The flow chart of operation in an infinity loop on this microcontroller is shown in Figure 4.5. After reading the client's (operator) message, there are two possibilities. The first is to get information like the evaluation board's frequency, amplitude, reference frequency, or the minimum or maximum value each parameter can accept. The second is to set a frequency, amplitude, or reference frequency value. After setting a new value, it will be applied to the evaluation board instantly.

## 4.4 Test

To test the DDS controlling device, a 100 MHz reference signal, a 5 V power supply, an Ethernet connection, and an oscilloscope were used to see the output of the DDS. The following commands are sent to the microcontroller using Putty:

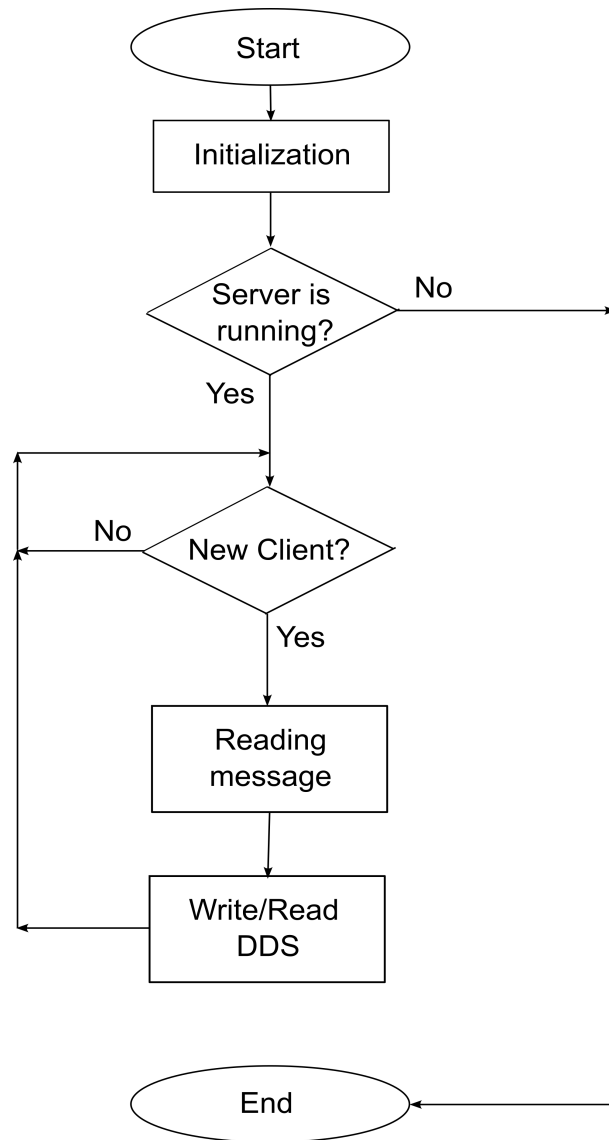


Figure 4.5: Flow chart of the algorithm, working in an infinite loop.

```

DDS:REF 100
DDS:FREQ 100.0; AMP 20.0

```

The first command sets the reference frequency and the second for the desired frequency and amplitude. The result on the spectrum analyzer is shown in Figure 4.6. The marker on the spectrum analyzer shows 100.000010 MHz, which is different from the desired frequency at 100 MHz due to the flatness of the peak; therefore, the marker is not exactly in the right position. Also, the resolution bandwidth (RBW) on the spectrum analyzer was set at 100 Hz, which limits to see precisely the peak.



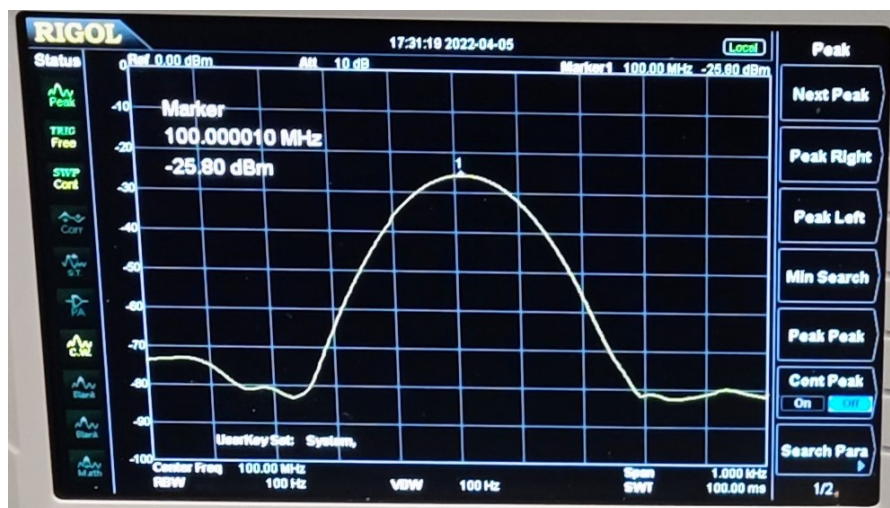


Figure 4.6: Output of DDS AD9912. This frequency has been applied remotely through the Ethernet on the device.



# Chapter 5

## Automatic relocking program

In this chapter, an automatic relocking program is presented to stabilize the frequency of the laser beam. This auto relocking program is tested with ECDLs and Titanium-Sapphire (TiSa) laser. The system is capable of automatic and real-time control of the laser frequency, enabling fast relocking of the ECDLs compared to manual relocking by an operator. The algorithm uses cavity transmission and wavemeter signals as input parameters. This system has been tested with many different lasers at KL FAMO group with an optical atomic clock experiment, at the UvA with the Rydberg laser in an optical tweezers experiment refer to chapter 7, and also at Toptica company. ECDL lasers' stabilization and relocking work as intended in the long-term for several weeks non-stop.

### 5.1 Introduction

When using optical clocks to maintain time scales or perform basic research, it is sometimes necessary to be resilient and function constantly without interruption for several weeks. As a result, substantial effort is expended on identifying vulnerable components of the experimental system and enhancing their operational dependability. The unstable behavior of lasers for cooling, trapping, and probing the atomic reference in an optical clock is a typical cause of optical clock failure. This instability in the KL FAMO lab is caused by instability mainly with 707 nm and 679 nm repumping ECDLs and 689 nm and 698 nm ECDLs locked to ultra-stable cavities.

ECDLs are commonly used in cold atom studies such as optical atomic clocks, quantum computers and simulators, optical communication, and timekeeping. The TiSa laser is also used for optical lattices. As a result of the increasing intricacy of cold atom investigations, an automated method for relocking and stabilizing is critical. Furthermore, such a program can significantly accelerate the procedure for initiating the clock experiment and enhance calibration operations. Automatic relocking of ECDLs, on the other hand, is critical in high Technological Readiness Levels (TRLs) cold atom applications such as transportable optical clocks [88–90], quantum computers [91], future satellite missions [92], and space missions [77, 93].

Stabilizing a laser's frequency to a specific reference is known as laser locking. The laser locking process, including the one used here, creates an error signal proportional to the difference between the laser frequency and a target reference (such as an atomic transition or an optical cavity resonance). This error signal is then used in a feedback

loop to alter the laser frequency, ensuring it remains locked or stabilized to the desired reference.

However, sophisticated laser stabilizing techniques may be costly and complex, whereas in many experiments, like the repumpers in our experiments, just modest accuracy and bandwidth are needed. Stabilization systems that are straightforward, reliable, and scalable to several lasers are greatly desired for such studies.

Therefore, this chapter presents a simple, universal locking and relocking system for many lasers like ECDL, TiSa, etc. The developed procedure and software could improve the uptime of cold-atom experiments. It is mainly achieved by autonomous systems keeping the lasers in optimal condition. The program is based on Python software that runs on the PC. The Python software has been integrated with the High-Finesse wavemeter to detect deviations from the target frequency (for creating an error signal) and multi-mode operation of the ECDL laser. A National Instruments card to control the laser systems by applying feedback and monitoring the state of the laser to the optical cavity lock has been used. An algorithm has been developed for locking and relocking the lasers, which need moderate precision and recovery of the single-mode operation of the ECDLs. Additionally, this algorithm can relock (after unlocking) the already locked lasers by a fast locking technique like Pound-Drever-Hall (PDH).

This system has been tested with many different lasers at KL FAMO group for an optical atomic clock experiment, Rubidium Mercury lab for TiSa laser, at the UvA with the Rydberg laser in an optical tweezers experiment 7, and also at Toptica company.

## 5.2 Experimental setup

In this section, the schematic diagram and experimental setup have been described. At the end of this section, the experimental configuration performed in Toptica company to test the system is presented.

### 5.2.1 Schematic diagram

Figure 5.1 presents a schematic diagram illustrating the process of the automatic relocking system employed in the passive optical atomic clock in KL FAMO. The laser beam originates from an ECDL, whose frequency can be modulated via a piezo and current controller with voltage inputs inside the laser driver. Alternatively, a TiSa laser with frequency control voltage input is used as a light source. Initial frequency stabilization is achieved with a wavemeter, and a subsequent, more precise stabilization is obtained with a high-finesse optical cavity. Therefore, part of the laser beam is directed to the wavemeter while another portion is routed to the ultra-stable high-finesse cavity.

Locking to the optical cavity is crucial in subsystems requiring a narrow spectrum of laser, such as using a red laser for cooling atoms at intercombination (689 nm) transition of 7 kHz linewidth and using a clock laser to interrogate atoms at sub-Hz linewidth 698 nm transition. The wavemeter is pivotal in initial frequency tuning to ensure tuning with the correct cavity mode and absolute target frequency. For some lasers, like repumper lasers, stabilization to within tens of MHz suffices. In these scenarios, relocking is performed using only a wavemeter.

Part of the laser beam goes to the switcher of the wavemeter through an optical fiber. The switcher enables access to eight optical fibers, which can be measured by just one

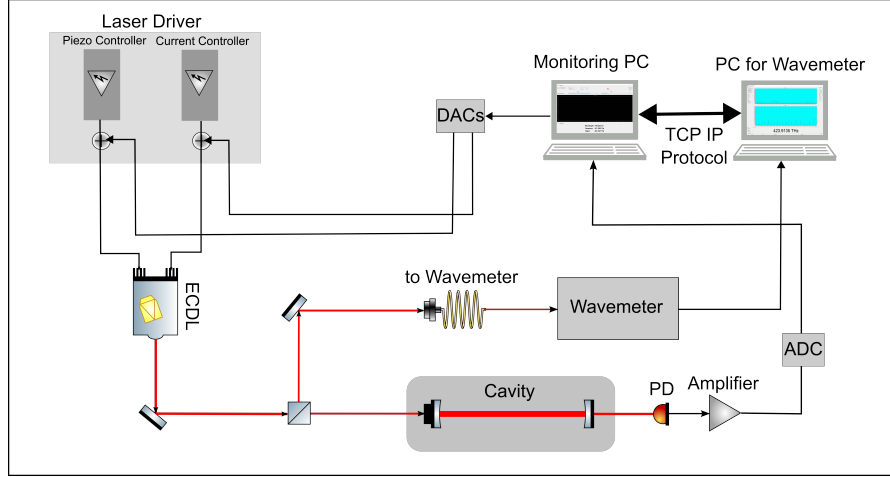


Figure 5.1: Schematic diagram of the auto relocking system in the experiment [94]. Abbreviations: PD- photodetector, ADC- analog-to-digital converters, and DAC- digital-to-analog converter.

wavemeter. This is a commercial wavemeter from High-Finesse. The wavemeter software is based on the dynamic-link library (DLL) C/C++ module and is integrated into the CType Python package. Therefore, a Python package is developed to fully access the wavemeter, including running the software, starting measurement, controlling exposure time, swapping between different channels, and stopping the software. This package can be run on any operating system that supports commercial wavemeter software and has Python installed with all the libraries needed for this package.

The developed Python package is directly imported to the main auto relocking program in the first version of the program, which is presented in the graphical user interface section. However, this package was later developed into separate software with more functionality as a server program. The benefit of this system is that it has more flexibility in running the main auto relocking program. In this case, the server is running on the computer hosting the wavemeter software, and the auto relocking program as a client can be run on the same computer or any other one but connected to the same network. In chapter 7, the auto relocking program is running on the RedPitay. Communicating with the wavemeter through this server-client system is easy and fast (Ethernet speed). Developing this auto relocking program on the STM32 and relocking the laser on this microcontroller is also possible.

A National Instruments (NI) card USB-6229 is used in this experiment to collect the signal (ADC) from the photodiode (PD), which detects the transmission signal out of the cavity and also sends the feedback (DAC) to the laser driver for piezo and current controllers. This card is a multifunction data acquisition (DAQ) device for high-performance measurement and control applications. It has 32 Analog Input (AI) to collect the signal from a photodiode with 16-bit resolution, 250 kS/s sample rate, and up till  $\pm 10$  V input range. Also, it has 4 Analog Output (AO) to send the feedback to the laser driver with 16-bit resolution, 833 kS/s sample rate, and  $\pm 10$  V output range.

NI-DAQmx driver software offers a programming interface for configuring and controlling the device in various programming languages, such as Python. A Python library is developed to facilitate communication with the card via a Universal Serial Bus (USB) port. This library is imported to the main auto relocking program and gives access to the

program to read the signal from the photodiode and write the signal to send the feedback to the laser driver.

### 5.2.2 Setup

The auto relocking program has been tested with two different models of High-Finesse wavemeters, WS6 (with an accuracy of 200 MHz and resolution of 100 MHz) and WS7-UV (with an accuracy of 60 MHz and resolution of 10 MHz), available in the KL FAMO laboratory. If the laser is locked by a cavity, transmission of the laser beam is detected by a photodiode, and the output needs to be connected to an input of the DAQ card. The DAQ card should be connected to the computer on which the auto relocking program will be run. One of the output signals from DAQ should be connected to the laser driver to apply voltage to the piezo. Another output can be connected to the modulation input port of the current controller module to apply voltage to the current.

The experimental setup is shown in Figure 5.2 to auto relock the ECDL only by wavemeter. The NI DAQ output in part a is connected to the laser driver in part b from the analog interface module. The laser beam from the laser diode in part c is coupled to an optical fiber and sent to the wavemeter directly without the switcher in part d of the figure.

Three lasers are involved in testing the software. Two of them are repumpers, including 707 nm and 679 nm. These two are relocked only by the wavemeter with a similar setup shown in Figure 5.2. The other laser is 689 nm; this laser needs to be locked first by an ultra-stable cavity; therefore, this laser is relocked by cavity transmission and wavemeter.

### 5.2.3 Experiment performed in Toptica company

The auto relocking program has been tested with one of the ECDLs in Toptica company to validate the software and improve it to be more versatile. The laser used to perform the test was 1064 nm (281 THz) DL 100. The wavemeter was the WS U version with

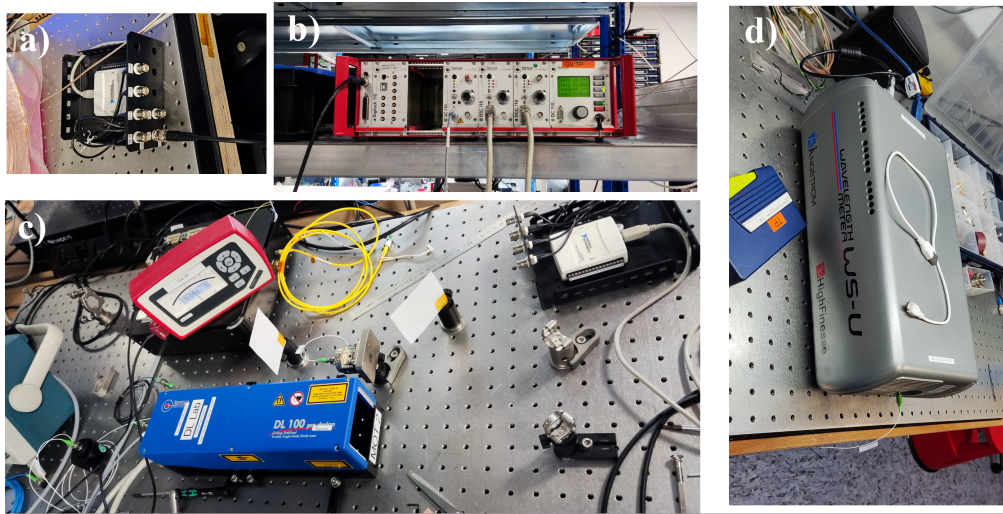


Figure 5.2: Experimental setup to perform auto relocking of ECDL. a) DAQ card, b) laser driver, c) ECDL, d) wavemeter.

an accuracy of 30 MHz and a resolution of 10 MHz; relocking was done only by the wavemeter, and there was no cavity. A NI DAQ has been used to apply feedback on the laser driver.

Wavemeter software is installed separately from the computer on which the auto relocking program runs. Figure 5.3 shows the server program running on the wavemeter computer. This server replies to the client or auto relocking program and provides information about the wavemeter for it. In Figure 5.4, a view of auto relocking program running in a different computer than the one for the wavemeter is shown, but they are connected in the same network; therefore, TCP/IP socket connection is possible between server and client. NI DAQ is also connected to the computer on which the auto relocking program runs.

### 5.3 Flow chart and algorithm

Figure 5.5 shows the procedure to run the auto relocking program. The whole system has three parts, including:

1. Laser,
2. Detection,
3. Auto relocking program.

The laser can be an ECDL, TiSa laser, or any other laser whose frequency can be tuned by applying a voltage. Here, the focus is on ECDLs, but the program has also been tested on TiSa laser, and the results are presented in the results section.

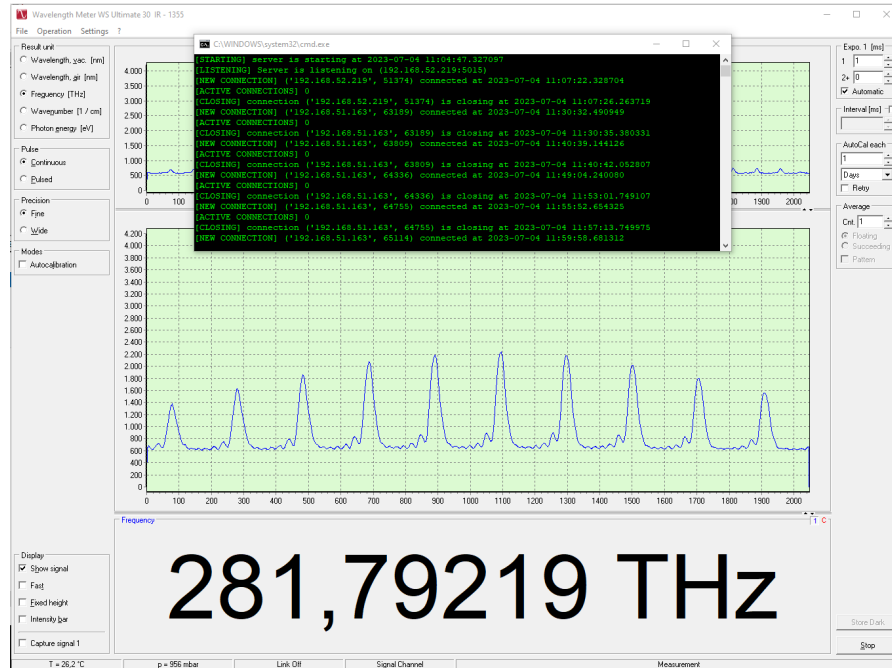


Figure 5.3: Server program running on wavemeter computer which sends the information of laser beam to the client (Auto Relocking program).



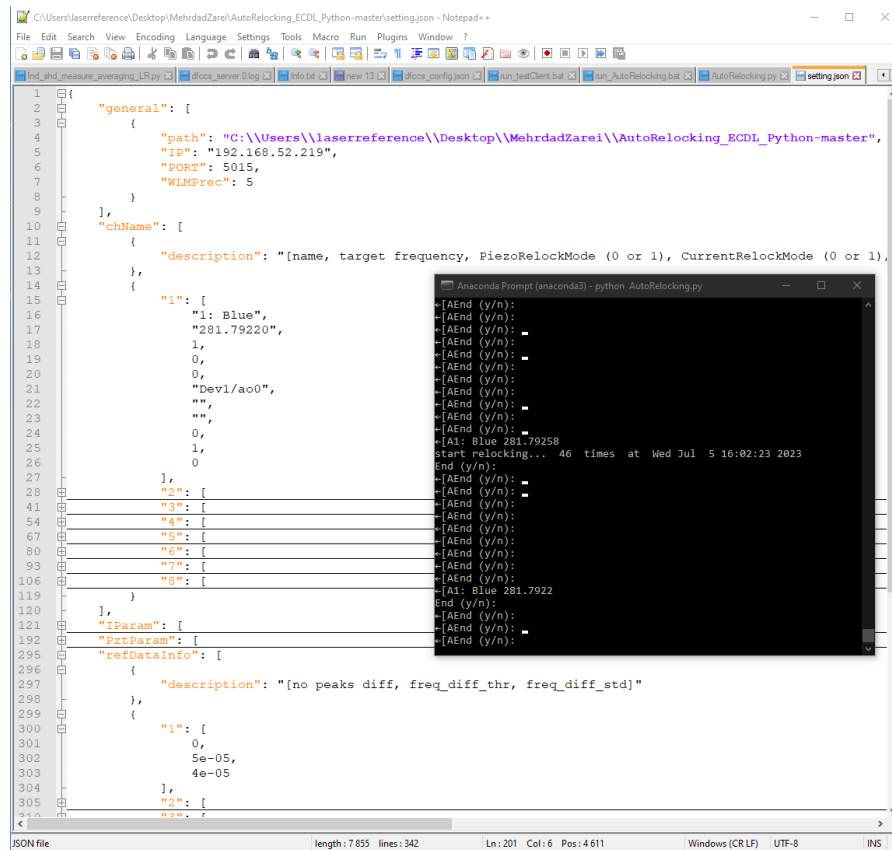


Figure 5.4: Auto relocking program running on the computer.

A wavemeter can monitor the frequency and interferometer pattern of the laser beam. At the same time, this laser can be locked to a cavity by the PDH method, which is a fast locking technique. Additionally, the transmission of the laser through the cavity can be monitored. In general, the laser can be monitored by a cavity transmission and/or wavemeter at the same time or only by one of them, which depends on the application for which the laser is used and the availability of the wavemeter.

The auto relocking program part is the core of this system, which monitors, processes, and sends feedback to the lasers. The auto relocking program continuously monitors the cavity transmission and/or wavemeter signal. This signal is processed, and based on the cavity transmission threshold for the cavity and the target frequency dedicated to the wavemeter, the program will decide whether to start relocking the program or not. If the relocking is based on the cavity transmission or wavemeter, the process is called relocking by cavity or wavemeter, respectively, or it can be relocked by both simultaneously. If the program decides to start relocking the laser, a desired signal is sent to the laser to relock it again as if it had been unlocked.

The feedback signal from the auto relocking program can be applied to the piezo scan controller or current controller of the laser driver of the ECDL for tuning the frequency. However, two feedbacks can be applied, one for the scan controller and the other for the current controller. A scan controller swaps the laser frequency by scanning the voltage of the piezo. On the other hand, the current controller changes the current of the laser driver and is used to maintain a single-mode. In the case of the TiSa laser, only one feedback is applied to a voltage controller for tuning the frequency.



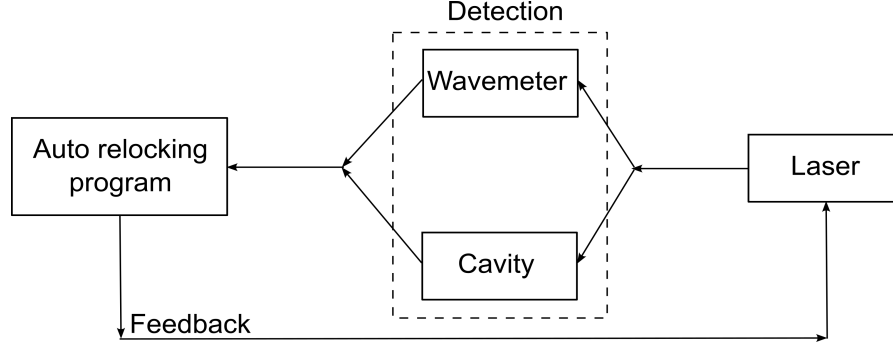


Figure 5.5: Schematic of Auto Relocking program.

If the laser is locked to the cavity, the only used information is the signal from cavity transmission. If the transmission level is lower than the threshold, the only possible way to find the transmission at a higher level is to scan the voltage of the piezo. Nevertheless, if the wavemeter monitors the laser, there are two pieces of information: the frequency of the laser beam and the interferometer pattern, which lets us know if the laser is single-mode or multi-mode (Figure 1.2). Therefore, the wavemeter makes it possible to keep the laser on target frequency and single-mode.

### 5.3.1 Scanning procedure

The algorithm for relocking is based on scanning, and the procedure to relock the laser (find target frequency or single-mode) appears in Figure 5.6 a. A minimum and maximum value is set in the program to avoid applying extra voltage to the scan controller. These values are changeable by the operator through the software. Thus, the program can scan the maximum in this range to find the target frequency and single-mode. This range should be extensive enough for the program to relock the laser.

Based on the present value (the last value applied on the scan controller), the program scans the whole range from minimum to maximum. Scanning starts with step 1 from the present value to the right, then step 2 goes back to the end of the scan range, and at the end of the scan range, step 3 will go back to the starting point. Scanning will be stopped at any point where the laser is on target frequency or single-mode, and that point will be saved as a present value for the next relocking time. However, if the program cannot relock the laser, it will repeat the process until it is locked. It will be stopped if it can not relock the laser after repeating the whole range from minimum to maximum five times. This is the normal procedure of the relocking algorithm. However, this algorithm has been optimized to make the relocking procedure as fast as possible, as discussed in the following section.

Total scanning is divided by the scanning step size, set to 0.001 V for this project. The scanning step size depends on the resolution of the DAC. If the resolution of the DAC does not support this value, it can be changed to different values. Therefore, each step would apply one scanning step size (0.001 V) to the scan controller driver. After applying one scanning step, there should be some delay in seeing the effect of the change on the laser frequency. This delay in this algorithm is set at 10 ms. However, depending on the experiment, the wavemeter's exposure time, and the detector that detects transmission through the cavity, it can be variable.

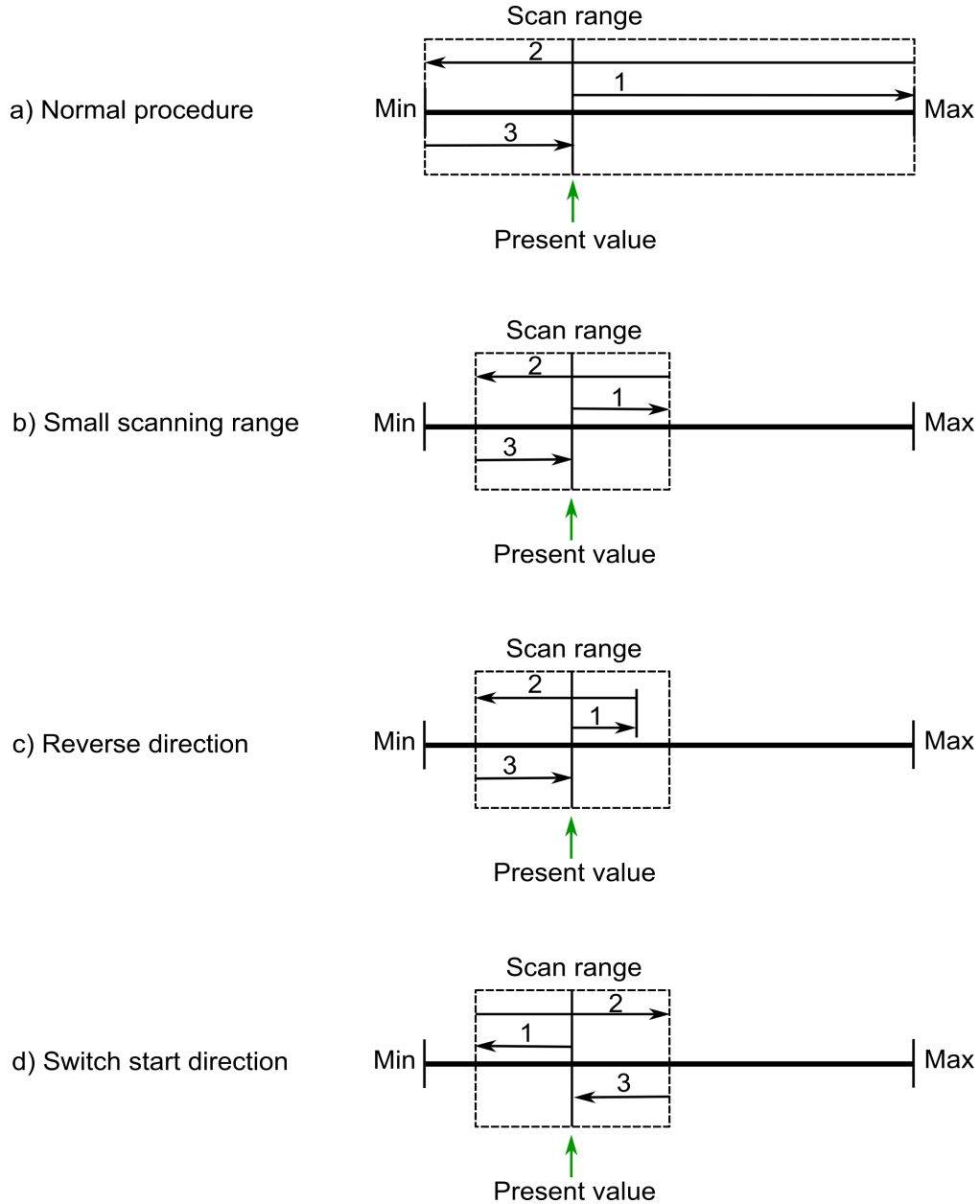


Figure 5.6: Scanning procedure to relock the laser. a) Normal procedure scanning, b) small scanning range, c) reverse direction, d) switch start direction strategies.

For example, to see roughly the speed of relocking by these procedures, the minimum and maximum allowed values for scanning are from 0.5 V to 3 V. The present value is 1 V, the total scanning range considering two times scanning is equal to 5 V  $((3 - 0.5) \times 2)$ , and the total number of steps is 5000 with 0.0001 V for each step. So, to scan the whole range once with a 10 ms delay after each step, the total time will take at least 50 seconds for only one complete scan. This is one of the reasons why this relocking program is called slow relocking compared to PDH lock, which is high-speed. Now, let us delve into the next section and see how optimizing the algorithm makes the relocking as fast as possible.

### 5.3.2 Optimisation

To optimize the procedure of the relocking of the laser to make it as fast as possible, five strategies are implemented in the algorithm:

1. Small scanning range,
2. Reverse direction,
3. Variable scanning step size,
4. Laser drift compensation,
5. Switch start direction.

A small scanning range (Figure 5.6 b) is an excellent strategy, significantly improving the relocking speed, which is vital in cold atom experiments. Instead of scanning the whole range from minimum to maximum, it is divided into five parts from 5, 10, 20, 40, and 200 percent of the whole range and starts from a small range till the whole range or 200 percent. Based on this strategy, when the laser becomes unlocked, which is usually due to laser drift, the frequency is very close to the target frequency. Therefore, it should start scanning from a small range around the present value on the scan controller, so this helps to relock the laser as fast as possible.

Almost 80 percent of the time, the laser will be relocked again by a small scan range of 5 percent of the whole range. So let us compare it with scanning the whole range, which is calculated of 5000 steps in the previous section, to see how fast it become by this strategy. The first range of scans, which is 5 percent, reduces 5000 to 250 steps, so the total time it takes to scan this small range is 2.5 seconds, 20 times faster than before, which is a significant improvement.

Another optimization strategy that can improve relocking is to reverse the scanning direction (Figure 5.6 c) in the middle of the scan if the frequency goes farther than the target. This option is available only if a wavemeter monitors the laser. Cavity transmission will not give this information whether the frequency is going closer or farther. Based on this idea, after applying a new value on the scan controller, frequency is checked and compared with the previous frequency to see if the direction is going closer. If not, it will change the direction. Nevertheless, this strategy might not let the program catch the target frequency due to mode hopping or anything else that depends on the laser. Therefore, after one time scanning the whole range, this option is ignored to let the program scan more carefully.

The third strategy, which is variable scanning step size, also has a good improvement on the relocking of the laser time. These two strategies of reverse direction and variable scanning step size are only available when the wavemeter is used for the detection. Otherwise, these two strategies are ignored when relocking is based only on cavity transmission. Let us imagine the operator wants to find the target frequency manually (by the way, this is a regular way to relock the laser before introducing this automatic relocking program). When the operator sees the frequency of the laser is far from the target. The operator tries to turn the knob of the scan controller faster (in other words, coarser), and as the frequency gets closer to the target, the operator will turn the knob slowly to reach the target. This is exactly how the algorithm is intelligent, and by playing

with step size based on how far it is from the target, it tries to reach the target frequency as fast as possible.

The operator can define a frequency threshold for the laser, which means if the frequency of the laser does not exceed this limit, the laser is on the desired target frequency, but this will work if the wavemeter relocks the laser. So, variable scanning step size depends on this threshold. If the frequency is closer than two times this threshold, the laser is very close to the target. Therefore, step size should be minimal to catch the target. Otherwise, it will be missed by the big step size, and the program has a meager chance of relocking the laser. If the frequency is four times farther than this threshold, the step size will increase to 5 times bigger than the minimum step size. When the frequency is six times far, the step size will increase to 10 times the minimum step size.

The next strategy is laser drift compensation. Laser drift is when a laser's output characteristic, such as frequency, changes over time or under changing environmental conditions; this drift may happen slowly or quickly and is affected by a variety of circumstances, including:

1. Temperature changes: Temperature variations affect the physical properties of the laser's components, producing changes in the properties of the lasing medium, cavity parameters, or thermal expansion, producing drift in the output characteristics.
2. Aging and degradation: Chemical interactions, or other causes, the components of a laser can change with time, resulting in changes in the laser's output qualities.
3. Environmental factors: Factors such as humidity, dust, vibrations, and electromagnetic interference can all affect the laser's stability and cause performance drift.
4. Control electronics: Drift can also be caused by drifts in the control electronics or feedback systems that steady the laser's output.

Laser drift is calculated based on information of every lock after relocking. This way, the current value and time are recorded when the program relocks the laser. After some time, the laser gets unlocked. Let us suppose it is due to laser drift. As it gets relocked by the program, this new value and time will also be recorded. So now the program calculates how much the laser is drifting, which direction it is drifting in, and how long it took for this amount of drift. In other words, what is the speed of drift? Based on this speed, the program applies a minor correction in the laser drift direction to keep the laser lock longer or to avoid unlocking the laser due to laser drift. Applying laser drift is optional, and the operator can select whether to apply this correction. Also, in some cases and for some lasers, this correction might make the laser much more unstable; therefore, it is better not to apply it. So, it is better to be checked before doing the experiment. When the program starts, no laser drift is applied for the first two relocking because the program needs to calculate the drift's speed and find its direction. After getting this information, the correction of laser drift will also start. Initially, this correction might make the laser unlock forcefully because the correction speed may be higher than the laser drift. Still, after many times relocking and calculating the speed of laser drift more precisely, this can be improved.

The last strategy is to switch the start direction (Figure 5.6 d) based on the direction of the laser drift. It can improve the speed of relocking if the laser is not drifting randomly. Keeping track of the laser drift and scanning first toward the laser drift direction can relock the laser faster. Suppose that frequency drift is in the left direction. If the program starts scanning from the left direction, the laser will be relocked after a few steps. These last two strategies are implemented only for the scan voltage controller to find the target frequency.

### 5.3.3 Relocking by cavity transmission and/or wavemeter

In the previous section, the algorithm for relocking is described. Now, let's take a step back and look at the algorithm from a broader perspective. A flow chart of the program is drawn in Figure 5.7. After initialization, one thread monitors the cavity transmission if the laser is locked by the cavity and if the operator wants to relock the laser by the cavity. Another thread is dedicated to monitoring the frequency of the desired laser. If any of the signals from the cavity or wavemeter shows that the laser is unlocked, the program goes for auto relocking by another thread and does the procedure of relocking. If the operator stops the program, the code will be ended.

The software can monitor and relock up to eight lasers simultaneously. This limitation of eight comes from the wavemeter's switcher, which supports only eight channels, but the software can be adapted for more than eight lasers. The relocking procedure can be done only for one laser at a time. If two or many lasers get unlocked, the program

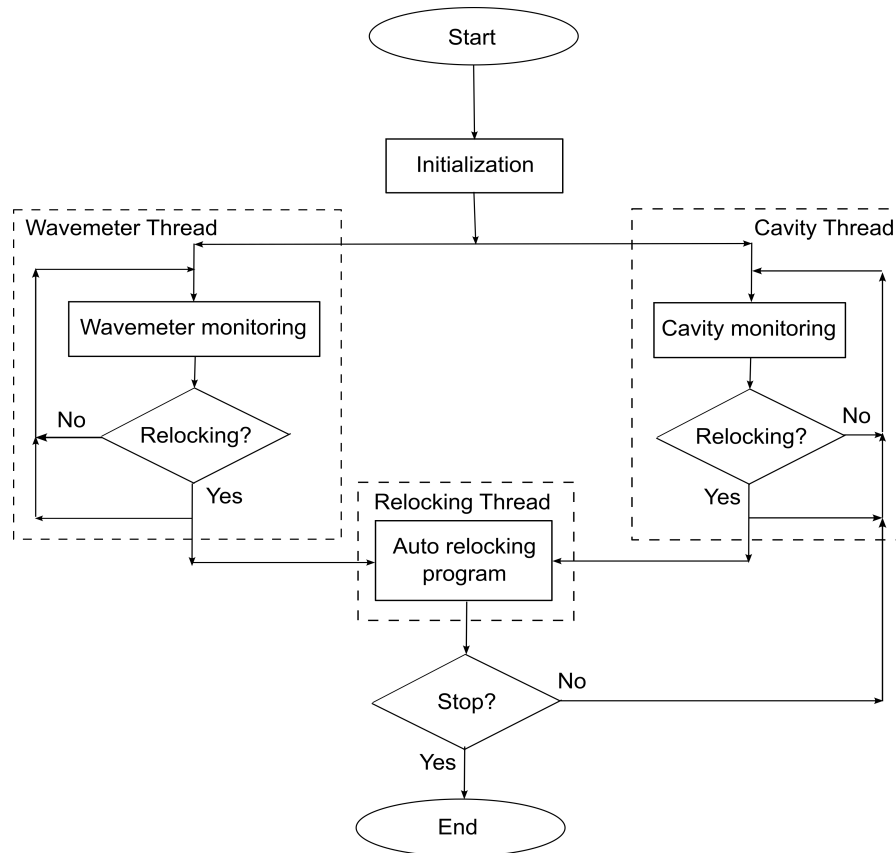


Figure 5.7: Flow chart of the algorithm for relocking by cavity transmission and/or wavemeter.

will relock them individually.

When one or more lasers are going to be relocked by the cavity, the program monitors the cavity transmission for each of them one by one every second. As the transmission level drops from the threshold for any lasers, the program will start instantly relocking the laser. The operator can define the transmission level threshold.

If the laser is going to be relocked by a wavemeter, the program monitors the wavemeter every 60 seconds. The operator can modify this value. The reason for this long delay is to keep the wavemeter free most of the time for any operators if they need to use any other channels of the wavemeter. But when the program is relocking for any of the lasers by wavemeter, the wavemeter is bounded specifically on that channel dedicated to the laser, and no one can use the wavemeter during the relocking time. There is no limitation when the wavemeter is in switch mode (Figure 5.9).

Relocking the laser by the cavity has a significant advantage, and that is fast detection of the unlocked laser. If the laser is unlocked, the software will detect it and start relocking in a few seconds. Also, if the laser is relocked, the transmission level increases over the threshold and the software becomes aware of it and stops relocking. But when relocking the laser by the wavemeter, and one of the lasers gets unlocked, the software might take up to 60 seconds to realize that the laser is unlocked. On the other hand, when relocking is in progress, it sometimes takes a few seconds for the software to detect that the laser is unlocked because of the wavemeter's exposure time. If the wavemeter is on switch mode, it can be even longer. Suppose relocking the laser is done by the cavity transmission and wavemeter. In this case, there are both benefits of fast detection due to the cavity transmission and fast relocking of the laser due to the wavemeter, which the program can use the strategies implemented in the algorithm and discussed in the previous section. In this situation, cavity transmission has priority for detection, and the wavemeter is used to improve the relocking procedure as the program has the frequency information.

For both relocking the laser by cavity transmission and wavemeter, it is possible to send the feedback to the scan controller and relock the laser. In the case of wavemeter relocking, the program needs a target frequency. A threshold for transmission level is needed for cavity relocking, both defined by the operator. Then, the program will decide if the laser is unlocked by getting information from the wavemeter and comparing it with the target frequency. An extra parameter, a frequency threshold, is mentioned in the previous section to avoid frequently relocking the laser while the frequency is slightly far from the target. The operator defines this threshold based on the laser's stability, the wavemeter's resolution, and the accuracy needed for the experiment. For example, if the short-term instability of the laser is 5 MHz, the threshold should be more than 5 MHz. If the resolution of the wavemeter is 10 MHz, the threshold should be bigger than 10 MHz. This threshold indicates that the laser is still locked if the frequency does not exceed this threshold. On the other hand, when relocking the laser by the cavity transmission, there is no need for this threshold because the transmission level indicates that the laser is locked.

In most cases, the laser is stable, and only by sending feedback to the scan controller would it be relocked again. But sometimes mode hop happens, and the laser goes on multi-mode, which needs to be single-mode almost always, except in a few cases in which we need to have a multi-mode to perform the experiment. In this situation, the program relocks the laser by sending feedback to the current controller to make the laser

single-mode. After that, if the frequency is still far from the target, the relocking for the scan controller will start. This cycle will be repeated many times to have a single-mode laser and frequency on target. Finding single-mode by the auto relocking program is only available for ECDL, not TiSa laser.

The algorithm to detect whether the laser is in single-mode or multi-mode is to analyze the interferometer pattern of the laser beam, which can be accessed from the wavemeter. The way to do that is to lock the laser first while it is in single-mode, then count the number of peaks with a height higher than some threshold, which can also be defined. So, this is set as a reference pattern for single-mode. When the laser is multi-mode (Figure 1.2), there are more peaks with lower heights. Therefore, the program detects whether the laser is multi-mode. The pattern and number of peaks might change due to power fluctuation of the laser beam, and the program realizes the laser is on multi-mode. Due to this, after every relocking, the pattern is updated to avoid this kind of error.

## 5.4 GUI settings

For communication with the auto relocking program, a GUI has been developed for the operator to monitor, control, and change settings for auto relocking system. PyQt5 was used to create the first version of the auto relocking application. The second version of the program is without GUI, but a JSON file is provided to apply the setting by the operator.

### 5.4.1 First version

The GUI developed by PyQt5 is shown in Figure 5.8. The software gives full access to the wavemeter software and retrieves all the information, such as wavelength and frequency. GUI even provides information about the desired target frequency. In this GUI, there are possibilities to change the channel, exposure time, hide or show the main wavemeter software, and switch mode, as shown in Figure 5.9.

If feedback is applied to the scan controller, the piezo relock has to be checked. Otherwise, the program will not be able to relock the laser. The same goes for the current relock. This option should be checked if that laser needs to be kept in single-mode. For this case, the operator must set a reference pattern by pressing the set ref button after locking the laser and keeping it in single-mode.

The program has two possibilities: manual mode and auto mode. When it is set on manual mode, it is possible to manually change the voltage of the piezo and current by sliders (Figure 5.8). However, as the operator presses the start relocking button, the auto relocking mode is active, and it is impossible to change the piezo and current values manually. The program's status would let the operator know if anyone wants to use other channels. The status includes switch mode (Figure 5.9) or relocking when one of the lasers is unlocked and the program is doing relock.

The GUI also has an overview tab to access information about all channels, as shown in Figure 5.10. The overview tab shows the channels' information, including frequency, target frequency, and single-mode or multi-mode. It is possible to activate or deactivate any of them simply by checking/unchecking the box next to their names. If they are active, their information can be updated by user-defined fixed time. It is possible to assign

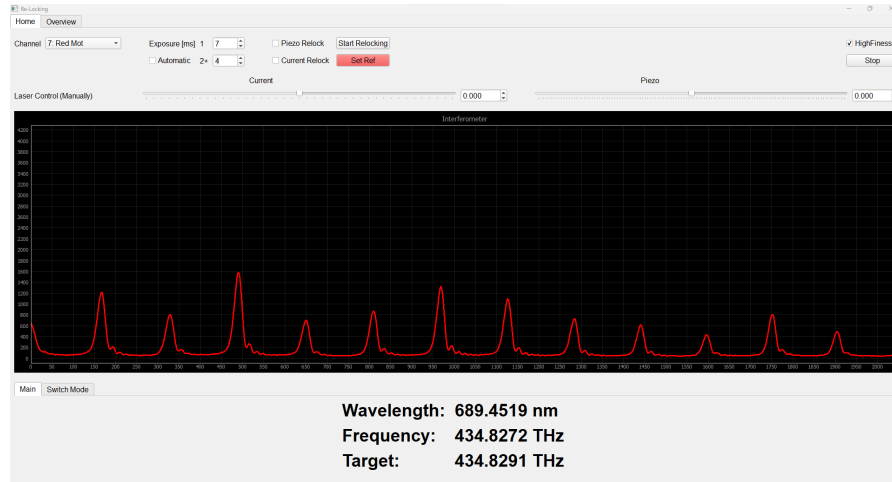


Figure 5.8: GUI developed using PyQt5 for auto relocking of the laser.

feedback signals for piezo or current. Ultimately, the operator must carefully assign port names for piezo, current (output ports), and input ports; otherwise, connection with NI DAQ is impossible.

Also, there are four general parameters which can be modified. First is update time (min); this parameter sets an update time for all the active channels. For example, every 10 minutes, all the channels get updated, and their information is sent to the database to save them. The second parameter is the relock time (s) for the delay of the relocking program. For example, every 15 seconds, all the channels that will be automatically relocked will be checked, and if they are unlocked, the program will start relocking them. Third is stop relock time (s), a limit for auto relocking. If the program cannot relock the laser in 120 seconds, it will stop relocking that laser to be rechecked by the operator. The last parameter is switch mode time (ms) when the GUI is in switch mode. The switch mode designed for this GUI differs from the wavemeter software. After updating each active channel, the next channel is updated on the wavemeter software, which might take 1 to 2000 ms. Nevertheless, in this software, after one cycle (updating all the active channels), there is a delay in the switch mode time, for example, 300 ms, and then updating the next cycle will start.

This version of the relocking program has to be run on the computer which the wavemeter is running. Wavemeter software and NI DAQ software must be installed before running this software. Refer to [95] to access and download this software.

### 5.4.2 Second version

After almost one month of working non-stop, the first version of the program with a few operators during clock measurements, it was found that GUI caused the main bugs of the first version of the program. Therefore, the program is developed without GUI in the new version. However, to interact with the program and apply new changes, a JSON file is prepared with all the parameters that need to be modified by the operator. This file is in the main directory of the source code as 'setting.json'. Refer to Appendix C for more information about this file.

After running the auto relocking program, the program will start working by checking all the laser frequencies, as shown in Figure 5.11. To stop the program, the operator



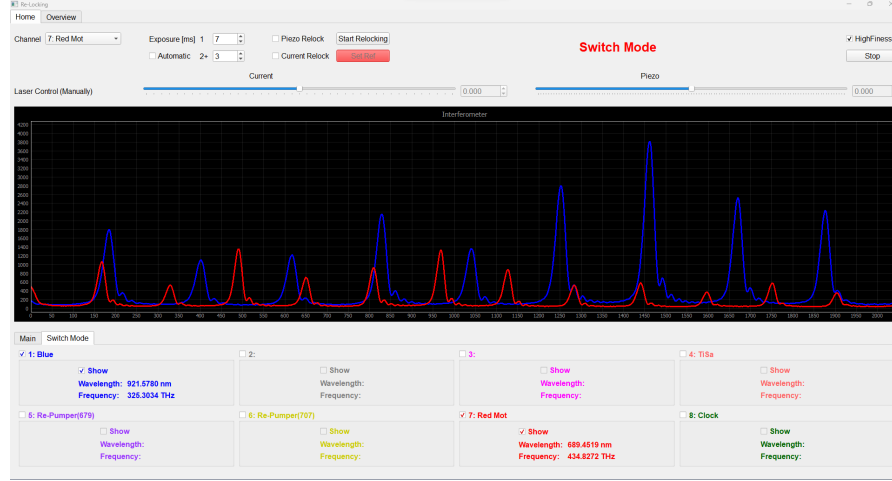


Figure 5.9: Switch mode of GUI.

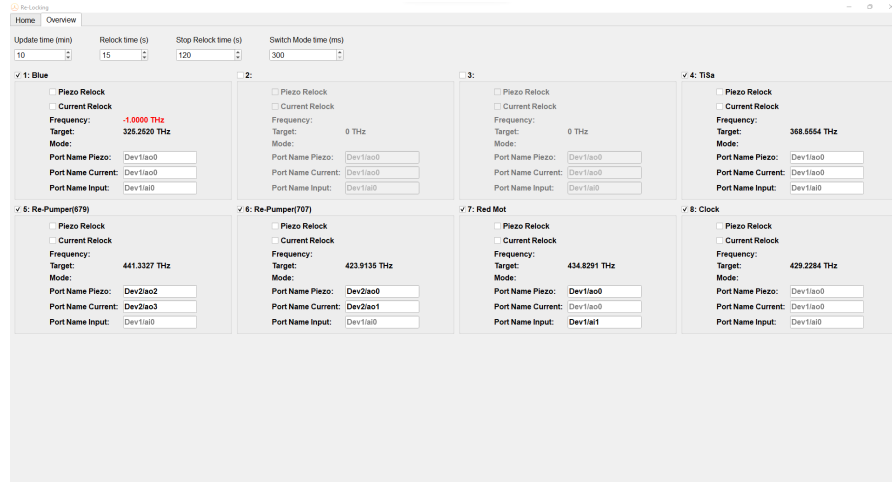


Figure 5.10: Overview tab for the extra setting of GUI.

must write y and click the enter key. Also, a status is printed to let the operators know. For example, if one of the lasers is in the mode of relocking, a message shows that this laser is relocking; therefore, the wavemeter is bound to that channel. Alternatively, it will be written if relocking is unsuccessful, and that laser will not be checked for relocking after that. The auto relocking program's complete documentation and open-source code are available here [96].

## 5.5 Results

The auto relocking system makes the optical atomic clocks and tweezers machine experiments more robust. As the lasers are locked for a long time, and if one of them gets unlocked, it will be relocked quickly by this system. Therefore, it is unnecessary to stop the measurement, find out which laser is unlocked, and try to relock it manually. If the operator finds it out quickly, at least 10 minutes of measurement is lost, which is much time in cold atom experiments. Sometimes, the whole night measurement is missed if the laser was unlocked during the night and no one was controlling the exper-

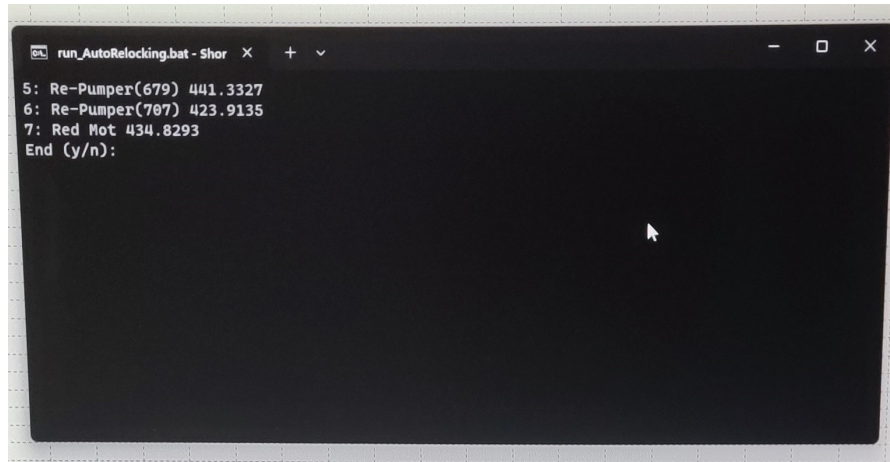


Figure 5.11: Auto relocking program when it is running.

iment. However, this auto relocking system will take care of this part of the experiment and keep track of the relocking events. Moreover, the operator knows precisely when the laser got unlocked and how long it was unlocked, so it can easily remove the false results from the measurement session.

In this section, the results of the auto relocking system are presented, and its performance is explained. The next chapter shows the optical atomic clock measurement results when this system automatically locks the lasers.

### 5.5.1 Relocking by cavity transmission and/or wavemeter

In this section, I present tests of relock operation for a long time. The experiment is performed simultaneously for 707 nm, 679 nm, and 689 nm ECDLs in the cavity room of the KL FAMO laboratory. Also, a separate experiment shows the system's performance for the TiSa laser performed in the Rubidium and Mercury room of the KL FAMO laboratory. Optimization is included in the algorithm for all the results, including small scanning range, reverse direction, variable scanning step size, and switch start direction. In this section, the laser drift compensation is off, and no correction is applied to the laser to correct the laser drift. In the next section, the results of laser drift are presented.

Figure 5.12 presents the 707 nm ECDL laser procedure algorithm. Relocking is done only by the wavemeter (WS7-UV) with a target frequency set at 423.91355 THz. The frequency difference is the present laser beam frequency deviation from the target frequency. The frequency threshold is set at  $\pm 50$  MHz. The threshold can be reduced to  $\pm 10$  MHz, which is the resolution of the wavemeter. For the 707 nm and 679 nm repumper lasers, a  $\pm 500$  MHz threshold in our lattice optical clock is also enough. Therefore, setting the frequency threshold far from the wavemeter's resolution is better to avoid the frequent relocking process. In this 12 minutes test, the laser got unlocked two times intentionally by changing the voltage of the piezo knob on the laser driver and was quickly ( $\sim 1$  s) relocked by the program. Relocking is started when the frequency is farther than 50 MHz or going outside of the green range (shown in Figure 5.12).

Figure 5.13 presents how the procedure algorithm works for the 689 nm ECDL laser. In this case, relocking is done by the cavity transmission and wavemeter (WS7-UV) together with a target frequency set at 434.82920 THz. For this case, the frequency

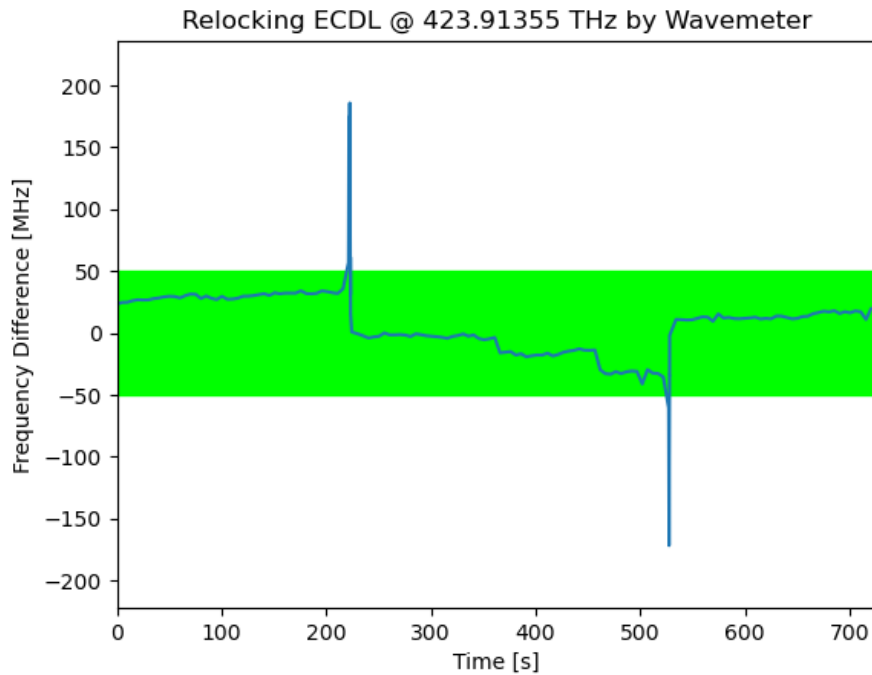


Figure 5.12: Relocking procedure by wavemeter for 707 nm ECDL in 12 minutes test. The frequency difference is the present laser beam frequency deviation from the target frequency at 423.91355 THz.

threshold is not affected; the transmission level is only important to detect whether the laser is locked. Here, two pieces of information will be processed: frequency, similar to the previous result, and cavity transmission. The frequency from the wavemeter is used to improve the relocking process. For this result also, the laser got unlocked two times intentionally by changing the voltage of the piezo knob on the laser driver and, in the same way, was quickly relocked by the program. As transmission is dropped, relocking is started.

Figure 5.14 presents how the procedure algorithm works for the TiSa laser, a different type of laser than ECDL. Relocking is done only by the wavemeter for this one with a target frequency set on 376.86015 THz and  $\pm 50$  MHz of the frequency threshold. In this 14-minute test, the laser was unlocked intentionally and quickly relocked by the program four times. This result shows that the algorithm can relock a different type of laser than ECDL, which makes it universal, but different types of laser will need modification of the parameters.

Let us focus on results for a longer time to see two critical factors that show this system's specification. These two factors are the number of events, which shows how many times the laser got unlocked during the experiment. The other factor is relocking time to see how fast this system can relock the laser.

Figure 5.15 presents a histogram of relock time for the number of events. Relocking is done by the wavemeter (WS6) for 707 nm ECDL. This measurement is performed for about 30 hours in a typical working day. Sometimes, the frequency was 5 GHz, far from the target frequency, simply because of the mode hop. Therefore, relocking took more than 100 seconds in these cases. This laser's minimum and maximum allowed scan range is set at -2.5 to 2.5 V; therefore, the average relock time based on a simple scanning

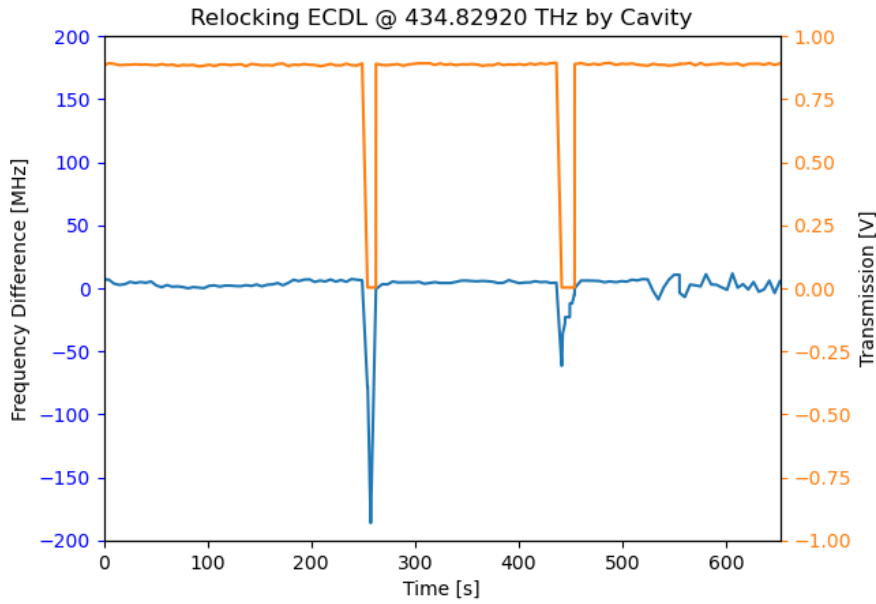


Figure 5.13: Relocking procedure by cavity transmission and wavemeter for 689 nm ECDL in 11 minutes test. The frequency difference is the present laser beam frequency deviation from the target frequency at 434.82920 THz.

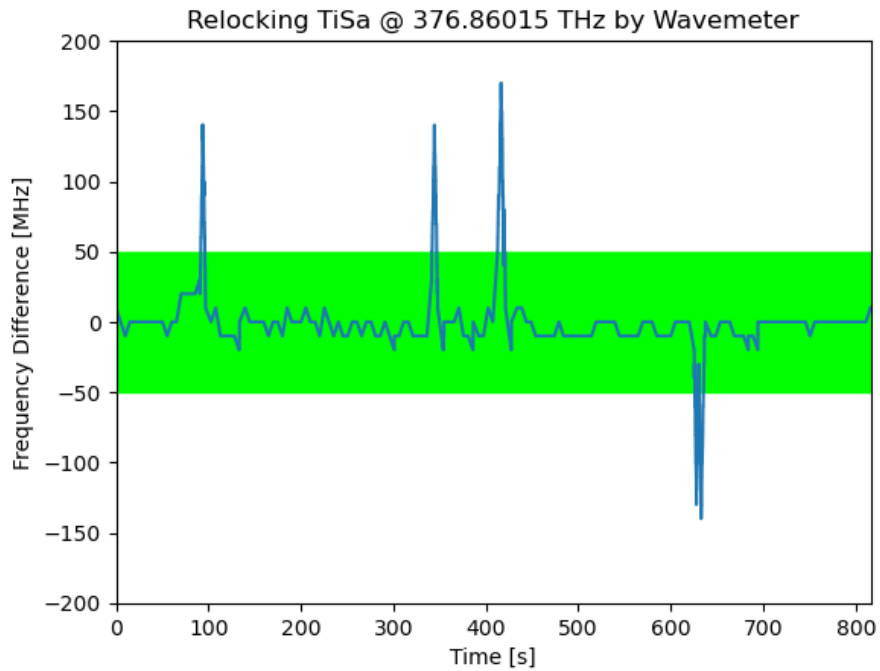


Figure 5.14: Relocking procedure by wavemeter for TiSa laser in 14 minutes test. The frequency difference is the present laser beam frequency deviation from the target frequency at 376.86015 THz.

procedure without optimization should take 100 seconds. After analyzing the data, the number of events, average relock time, and most frequent relock time (Mode relock time) are calculated. In this analyzes, 55 times, the laser was unlocked and successfully relocked. The average relock time is 6.43 seconds, more than ten times faster than a

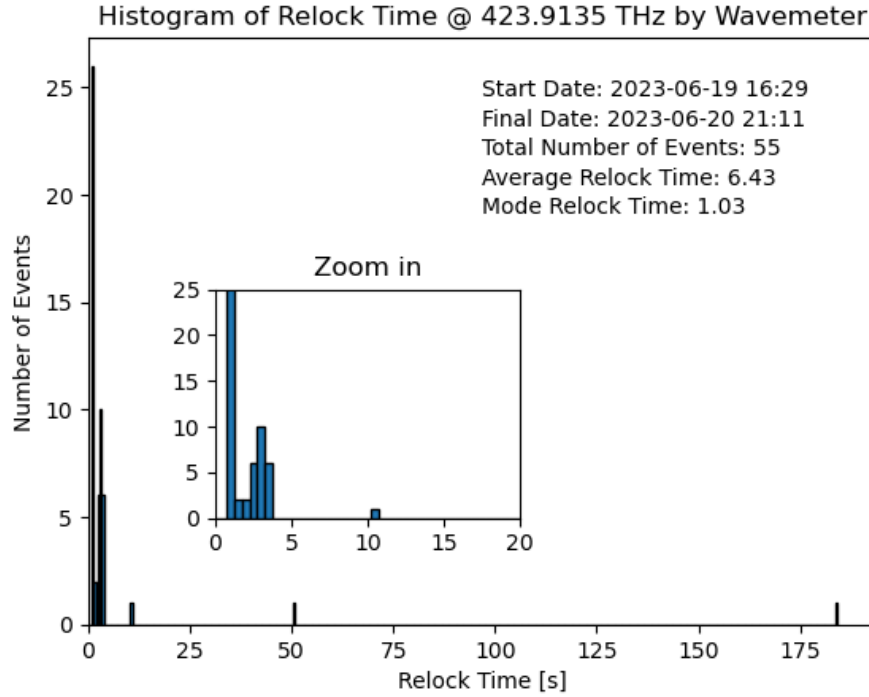


Figure 5.15: Histogram of the relock time for relocking by wavemeter for 707 nm ECDL for about 30 hours test. In this test, 55 times, the laser was unlocked, and the relock time took about 1 second for most of the time.

simple procedure. However, most of the time, relock time took about 1 second (100 times faster), which is excellent for keeping the laser lock for a long time.

Figure 5.16 presents a histogram for relocking by wavemeter (WS6) for another repumper 679 nm ECDL. This measurement is performed for about 24 hours at the same time. This laser's minimum and maximum allowed scan range is set from -1 to 1 V; therefore, the average relock time based on a simple scanning procedure without optimization should take 40 seconds. In this analyzes, 48 times, the laser unlocked and successfully relocked. The average relock time is 2.23 seconds, almost 17 times faster than a simple procedure. In most cases, the relock time took about 1 second as well.

Now let us look at the auto relocking by cavity transmission and wavemeter (WS6) together for 689 nm ECDL. This measurement is performed for about 24 hours at the same time. This laser's minimum and maximum allowed scan range is set at -1.5 to 1.5 V; therefore, the average relock time based on a simple scanning procedure without optimization should take 60 seconds. The histogram of relock time for the number of events is presented in Figure 5.17. This analysis shows that the laser only gets unlocked and successfully relocked eight times. The average relock time is 43.45 seconds, which is not that good because the number of events is not that much to rely on this result. In most cases, the relock time took about 1 second as well.

## 5.5.2 Laser drift

In the following experiments, the efficiency of laser drift optimization is checked. The experiment is performed in two weeks of non-stop measurement; wavemeter WS6 is used for all the measurements. In the first week, the laser drift is off, and at the end of

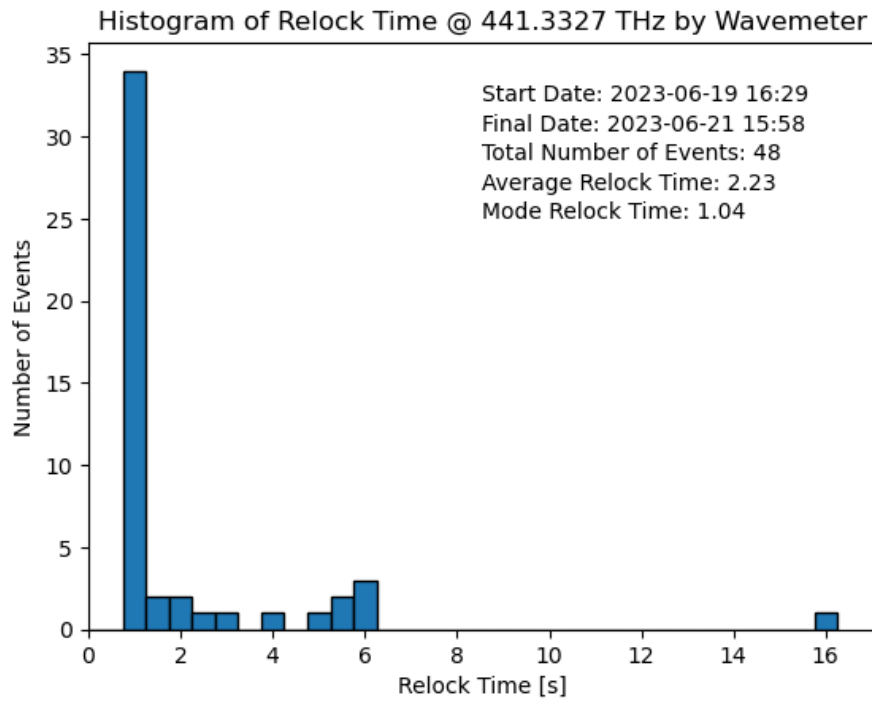


Figure 5.16: Histogram of the relock time for relocking by wavemeter for 679 nm ECDL for about 24 hours test. In this test, 48 times, the laser was unlocked, and the relock time took about 1 second for most of the time.

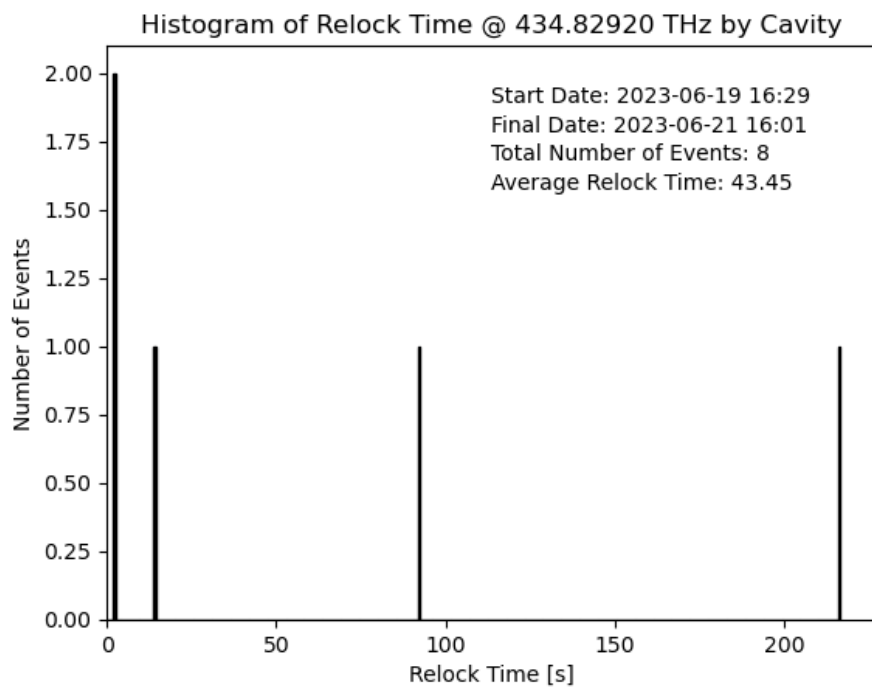


Figure 5.17: Histogram of the relock time for relocking by cavity and wavemeter for 689 nm ECDL for about 24 hours test.

the first week, the program is stopped for two minutes, and the laser drift optimization is turned on for the next week.

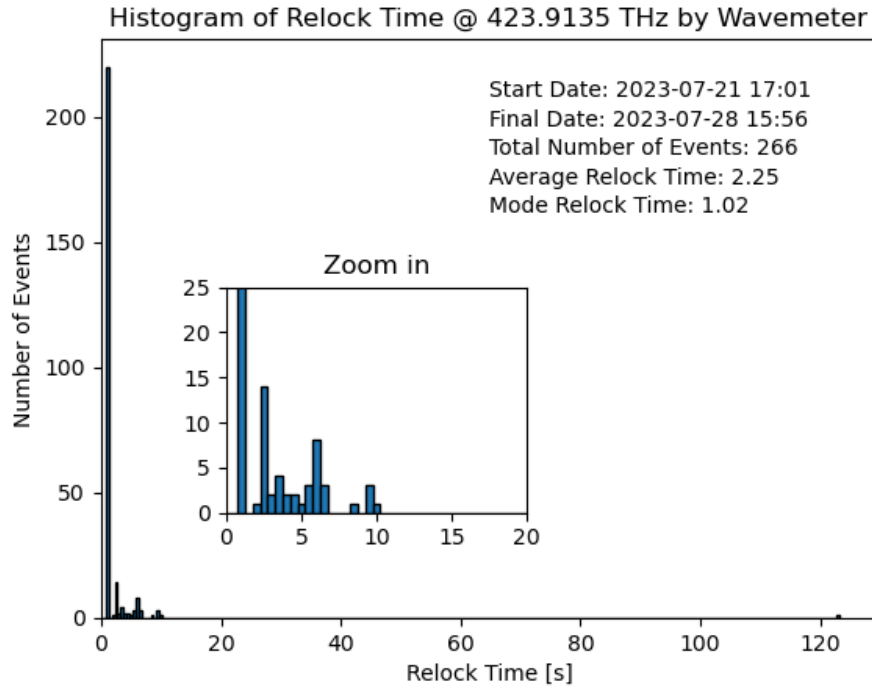


Figure 5.18: Histogram of the relock time for relocking by wavemeter for 707 nm laser when laser drift is off for one-week measurement. In this test, 266 times, the laser was unlocked, and the relock time took about 1 second for most of the time.

Histogram of relock time for relocking by wavemeter for 707 nm laser when laser drift is off during the first week is shown in Figure 5.18. During this one week, 266 times, the laser got unlocked, and it took about 2.25 seconds to relock it again by auto relocking program. The histogram of relock time for relocking by wavemeter for 707 nm laser when laser drift is on during the second week is shown in Figure 5.19. During this one week, 412 times, the laser got unlocked, and it took about 4.51 seconds to relock it again by auto relocking program.

The histogram of relock time for relocking by wavemeter for 679 nm laser when laser drift is off during the first week is shown in Figure 5.20. During this one week, 254 times, the laser got unlocked, and it took about 1.45 seconds to relock it again by auto relocking program. Histogram of relock time for relocking by wavemeter for 679 nm laser when laser drift is on during the second week is shown in Figure 5.21. During this week, 387 times, the laser got unlocked, and it took about 3.38 seconds to relock it again by auto relocking program.

The histogram of relock time for relocking by cavity transmission and wavemeter for 689 nm laser when laser drift is off during the first week is shown in Figure 5.22. During this week, 362 times, the laser got unlocked, and it took 10.94 seconds to relock it again by auto relocking program. This result is much more reliable than Figure 5.17. The histogram of relock time for relocking by cavity transmission and wavemeter for 689 nm laser when laser drift is on during the second week is shown in Figure 5.23. During this one week, 255 times, the laser got unlocked, and it took 26.65 seconds to relock it again by auto relocking program.

In Table 5.1, all the results are presented for the first week in which the laser drift is off and the second week with laser drift on. As it is straightforward for 707 nm and

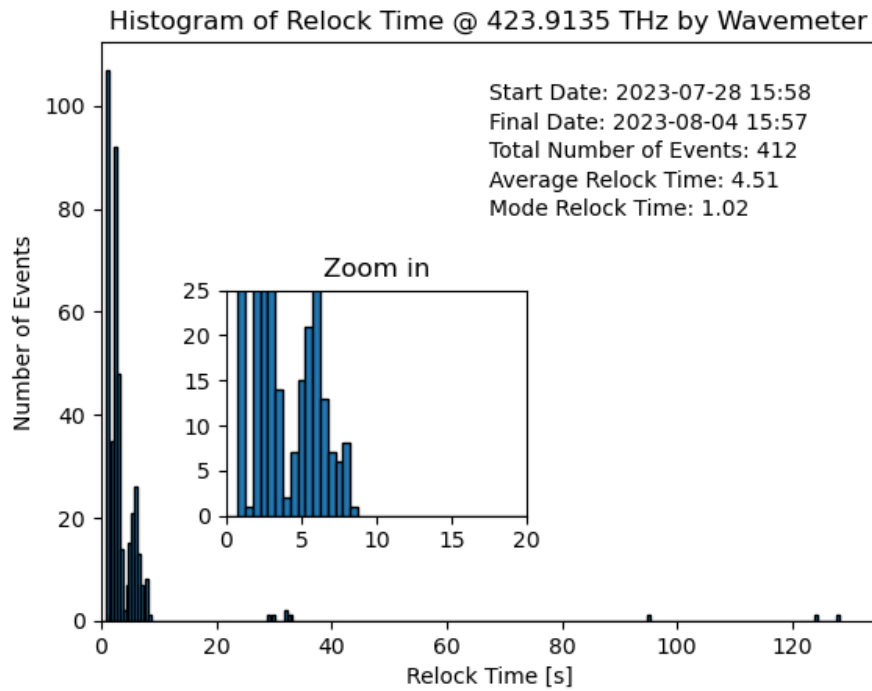


Figure 5.19: Histogram of the relock time for relocking by wavemeter for 707 nm laser when laser drift is on for one-week measurement. In this test, 412 times, the laser was unlocked, and the relock time took about 1 second for most of the time.

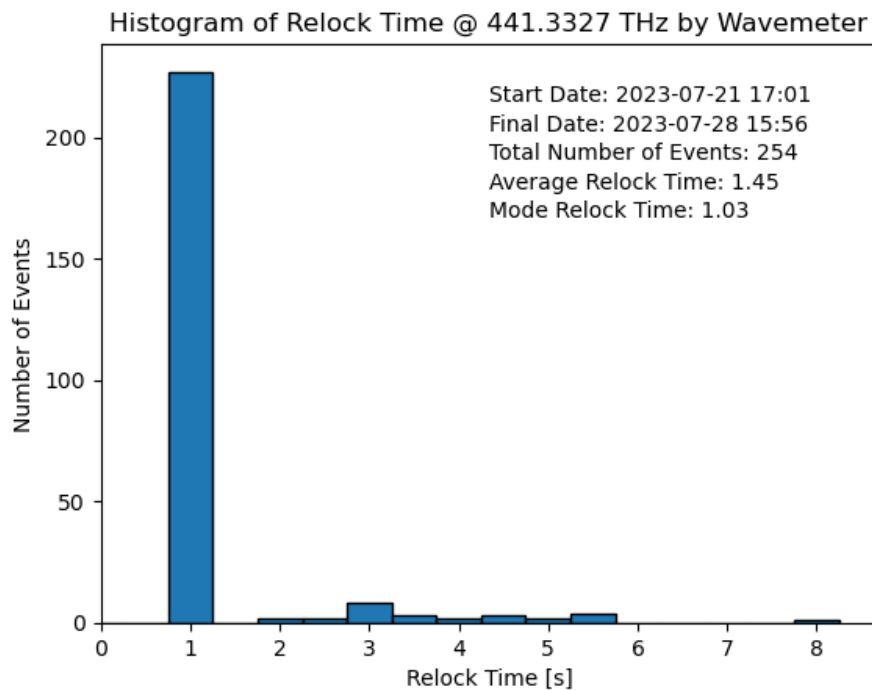


Figure 5.20: Histogram of the relock time for relocking by wavemeter for 679 nm laser when laser drift is off for one-week measurement. In this test, 254 times, the laser was unlocked, and the relock time took about 1 second for most of the time.

679 nm ECDLs when laser drift is on, the total number of events increased almost 1.5



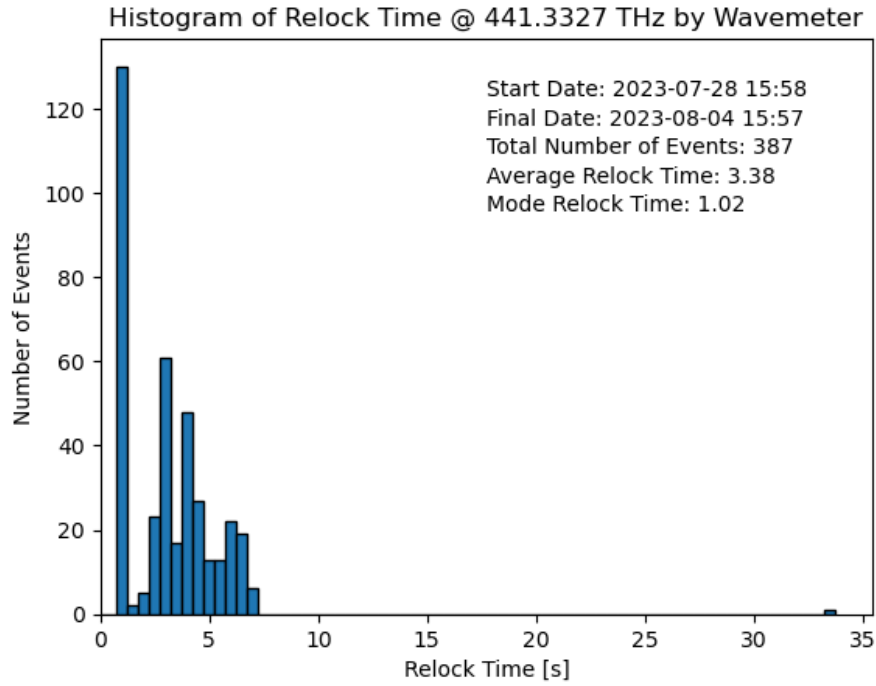


Figure 5.21: Histogram of the relock time for relocking by wavemeter for 679 nm laser when laser drift is on for one-week measurement. In this test, 387 times, the laser was unlocked, and the relock time took about 1 second for most of the time.

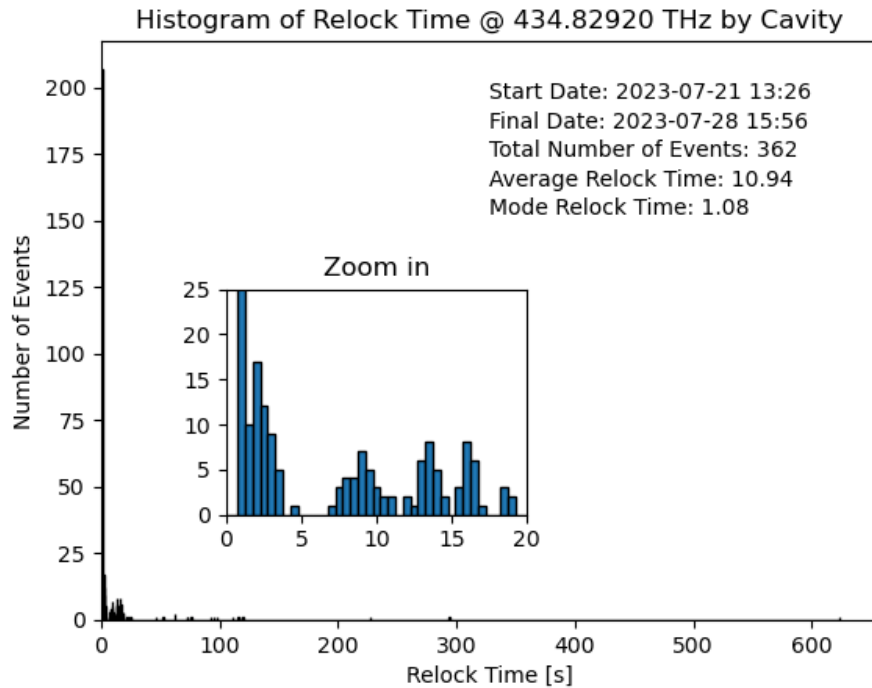


Figure 5.22: Histogram of the relock time for relocking by cavity transmission and wavemeter for 689 nm laser when laser drift is off for one-week measurement. In this test, 362 times, the laser was unlocked, and the relock time took about 1 second for most of the time.

times. However, for the 689 nm ECDL, which is relocked by cavity transmission and

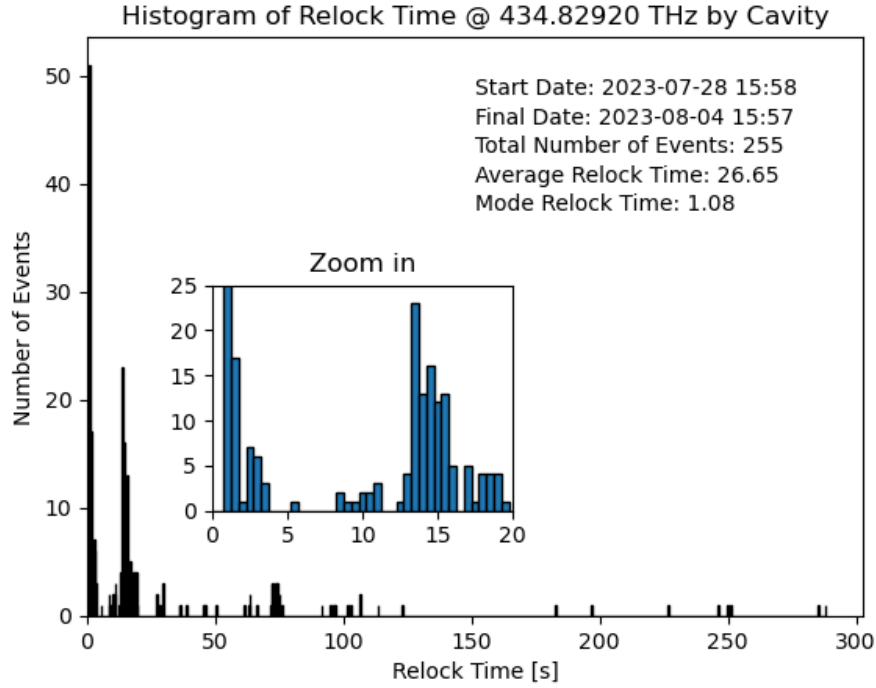


Figure 5.23: Histogram of the relock time for relocking by cavity transmission and wavemeter for 689 nm laser when laser drift is on for one-week measurement. In this test, 255 times, the laser was unlocked, and the relock time took about 1 second for most of the time.

wavemeter simultaneously, the total number of events dropped by almost 30 percent. Nevertheless, the average relock time increased more than two times for all the lasers, which is not a good result. Mode relock time is almost the same for all the situations, but if you consider the number of events for mode despite the total number of events increased for 707 nm and 679 nm ECDLs, at least this one is dropped for all the lasers. Therefore, the histogram distribution is distorted when the laser drift is on. This shows the increase in average relock time.

The reason for increasing the total number of events can be interfered with in the following way: in the laser drift algorithm, correction is applied based on the calculated drift speed. Corrections can be over if this speed is incorrectly calculated and caused by repeatedly unlocking the laser, or the drift speed may change over time. Also, this extra correction can change the calculated direction for scanning from the right or left algorithm. Suppose the calculated direction is left, and laser drift applies correction in the left direction when the laser gets unlocked due to extra correction. Instead of going back, the algorithm starts scanning from the left, which increases the average relock time. Therefore, if laser drift speed is not calculated correctly, it does not improve the algorithm by decreasing the total number of events, also influences scanning from the switch start direction algorithm, and increases the average relock time.

Let us talk about the total number of events. As shown, without laser drift correction, each laser got unlocked more than 254 times during only one week. This experiment was done almost at the end of July, a summer holiday, and almost no one was working in the lab, meaning everything was almost stable. On average, almost 1.5 times unlocking per hour. Imagine if the operator wants to perform an experiment for at least one month, and during this one month, all the lasers should be locked all the time. To relock

Table 5.1: Laser drift results at a glance. The results are presented for the first week, in which the laser drift is off, and the second week, in which the laser drift is on.

<b>ECDL</b>	<b>707 nm</b>		<b>679 nm</b>		<b>689 nm</b>	
<b>Laser drift</b>	<b>Off</b>	<b>On</b>	<b>Off</b>	<b>On</b>	<b>Off</b>	<b>On</b>
<b>Total number of events</b>	266	412	254	387	362	255
<b>Average relock time (s)</b>	2.25	4.51	1.45	3.38	10.94	26.65
<b>Mode relock time (s)</b>	1.02	1.02	1.03	1.02	1.08	1.08
<b>Number of events for mode</b>	235	120	240	130	210	52

the lasers manually by stopping the measurement and starting again, almost half of the time is wasted due to this issue, and this is if an operator is available 24/7. It is excruciating to perform an experiment for a long time. However, this auto relocking system, which has been developed, almost entirely solves this factual issue in really challenging fundamental physics experiments.

### 5.5.3 Tests in Toptica company

Now let us see how this system works in a completely different environment for the experiment performed in Toptica company. Figure 5.24 presents the 1064 nm ECDL laser procedure algorithm. Relocking is done only by the wavemeter (WS U) with a target frequency set on 281.79220 THz and  $\pm 50$  MHz of the frequency threshold. In this 15-minute test, as it is shown, three times, the laser got unlocked intentionally by changing the voltage of the piezo knob on the laser driver and quickly was relocked by the program.

The histogram of relock time for relocking by wavemeter for 1064 nm ECDL is presented in Figure 5.25. The measurement is performed for about 45 hours. In this analysis, 19 times, the laser was unlocked and successfully relocked. The average relock time is 12.57 seconds. Most of the time, relock time took about 2.31 seconds, but as the number of events is less, it is unreliable.

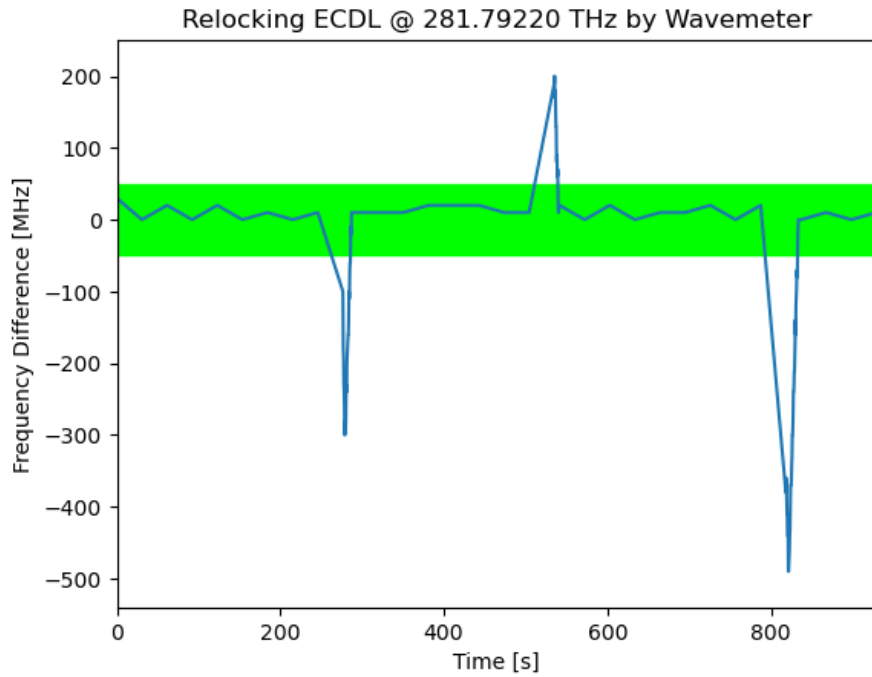


Figure 5.24: Relocking procedure of 1064 nm ECDL by the wavemeter in Toptica company in 15 minutes test. The frequency difference is the present laser beam frequency deviation from the target frequency at 281.79220 THz.

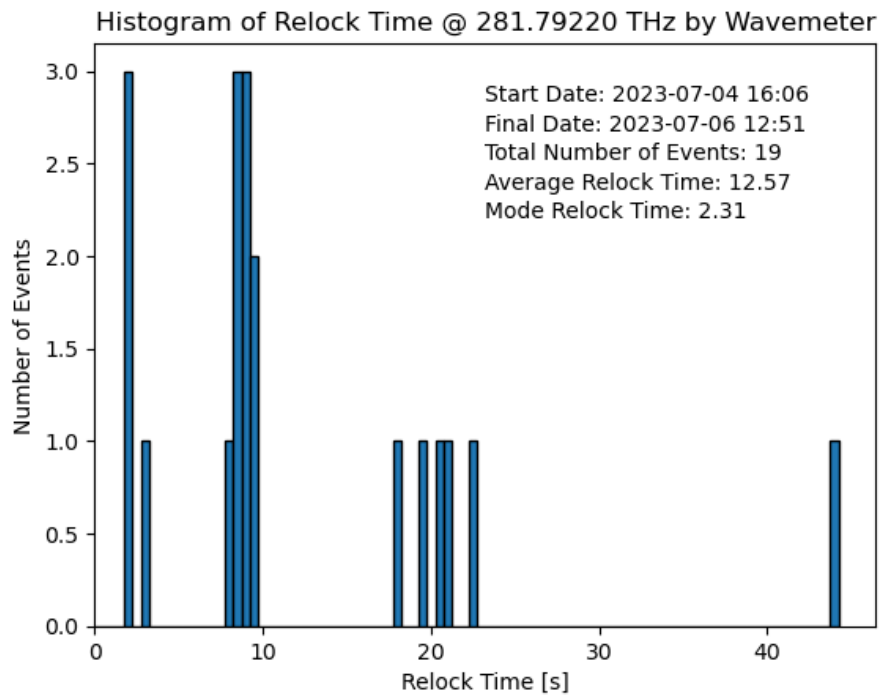


Figure 5.25: Histogram of the relock time for relocking by wavemeter for 1064 nm laser in Toptica company for 45 hours measurement. In this test, 19 times, the laser was unlocked, and the relock time took about 2 seconds for most of the time.



# Chapter 6

## Strontium optical atomic clock

After implementing new features in the system, including the automatic control of compensation coils and auto relocking of the ECDLs, the system of the passive optical atomic clock in the KL FAMO group has been optimized. The main parameters have been discussed to improve the trapped atoms in the lattice to have enough atoms for clock interrogation. In the end, clock spectroscopy was performed to measure the temperature of the trapped atoms on the ground state, linewidth, and Rabi oscillation. Also, the evaluation shift due to the Zeeman effect and probe light shift has been measured.

Additionally, a new experiment and method are explained to measure the effect of magic-zero wavelength on the temperature of the trapped Sr atoms while they are excited to  $^3P_0$  state.

### 6.1 Introduction

This section briefly describes the optical lattice clock in Sr1 room of KL FAMO that was constructed before I joined the group.

#### 6.1.1 Vacuum chamber and Zeeman slower

The schematic for the vacuum setup used for the lattice clock in Sr1 room is presented in Figure 6.1 [27]. Figure 6.2 shows the vacuum chamber in the experiment. Ultra-high vacuum conditions are necessary for the long trapping lifetime of optical lattices [27]. The vacuum system is divided into two portions joined by a long, thin tube for efficient differential pumping. The first section includes an atomic oven for evaporating the strontium atoms. The second section, with a vacuum of  $10^{-9}$  mbar, includes a Zeeman slower and a scientific chamber. There is a gate valve before Zeeman slower to block the unnecessary accumulation of strontium atoms on the last window of the science chamber when the clock is not working.

The high temperature in the oven causes atoms in the atomic beam to exit the oven with a mean velocity of around 500 m/s, resulting in a significant Doppler shift. To trap atoms, they must first be slowed down. For this aim, the Zeeman slower is used. Part of the Zeeman slower is a series of magnetic coils that produce a spatially varying magnetic field  $B(z)$ , in which  $z$  is the direction of the atomic beam and laser beam. The field strength changes along the direction of the atomic beam. Another part of the Zeeman slower is the laser beam, which is aligned counter-propagating to the atomic

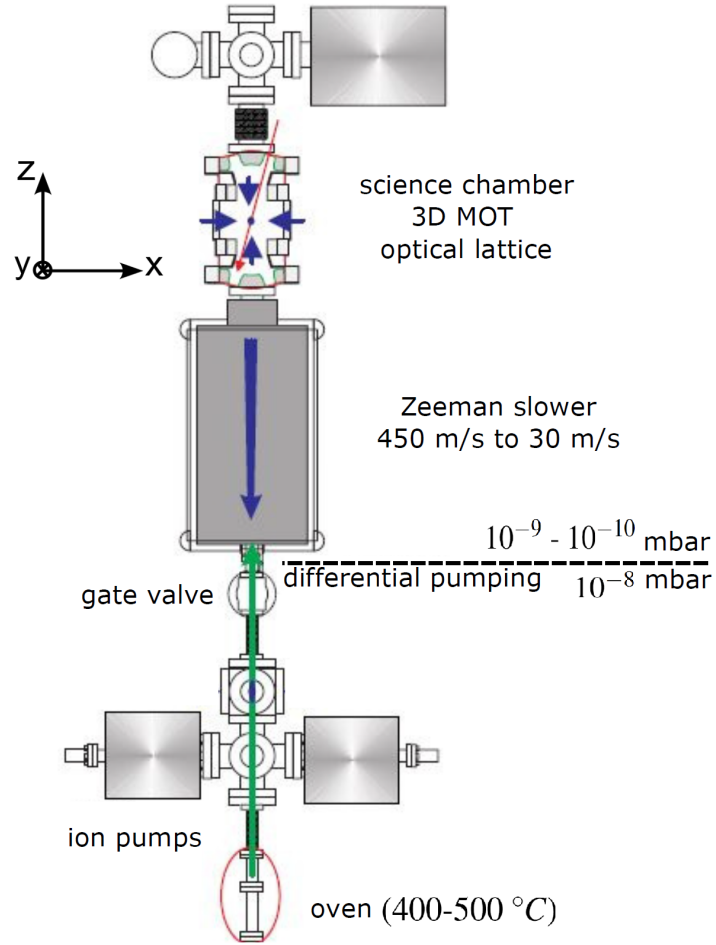


Figure 6.1: Schematic of the ultrahigh vacuum setup of the lattice clock in Sr1 room. The setup consists of an oven, a Zeeman slower, and a vacuum chamber. Blue and red arrows indicate laser beams; green arrows indicate the atomic beam. Taken and modified from [27].

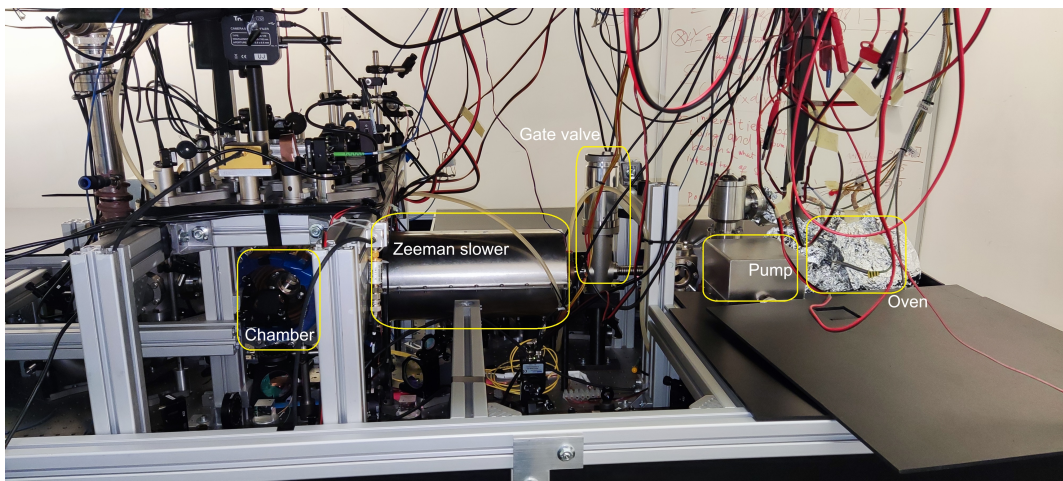


Figure 6.2: A view of the vacuum chamber in Sr1 room for the lattice clock.

beam and must be significantly red-detuned to slow down atoms based on the magnetic fields produced by the Zeeman slower. This experiment's detuning is around  $\frac{\Delta}{2\pi} = -500$  MHz from the blue MOT transition.

**Design and Implementation Tapered Magnetic Field:** A typical Zeeman slower has a magnetic field that decreases in strength along the direction of the atom beam. This tapering ensures that the energy levels of the atoms shift appropriately to keep them resonant with the slowing laser.

**Laser Configuration:** The slowing laser is usually aligned counter-propagating to the atomic beam. The frequency and intensity of the laser are chosen to maximize the slowing efficiency while minimizing heating effects from spontaneous emissions.

**Atomic Beam Source:** Atoms are initially ejected from an oven or a supersonic expansion source at high speeds. The Zeeman slower is positioned to intercept and slow these atoms before they enter a trapping region, such as a magneto-optical trap (MOT).

The Zeeman shift cancels the Doppler shift by selecting a proper gradient. As the atom slows down, the Doppler shift causes the laser to go out of resonance with the atomic transition. The Zeeman slower linearly slows down the atoms from 450 m/s to 30 m/s. The flux of the atoms is  $3.5 \times 10^9 \text{ s}^{-1}$  at the oven temperature of 460°C. The design of Zeeman slower is described in [97].

Two anti-Helmholtz solenoids are installed in special holders along the science chamber's main axis (x-axis, which is horizontal and perpendicular to the atoms beam from the oven) to provide the MOT gradient field. The solenoids can produce a gradient field of approximately up to 60 G/cm. Three sets of compensation coils in Helmholtz configuration are positioned in orthogonal directions (x, y, and z) as was discussed in Chapter 3 with more details.

### 6.1.2 Laser cooling

Frequency detuning for different blue laser (461 nm) beams from  $^1S_0 - ^1P_1$  resonance is shown in Figure 6.3. The optical setup schematic and a view of that in the experiment for blue laser in Sr1 room are presented in Figure 6.4 and 6.5. The blue laser is 150 MHz red detuned from resonance; therefore, it needs to be red detuned 350 MHz more for Zeeman slower, 110 MHz blue detuned for 3D MOT cooling, and 150 MHz blue detuned for saturation spectroscopy and probe beam.

The blue laser used at the first stage of cooling is locked to the  $^1S_0 - ^1P_1$  transition of  $^{88}\text{Sr}$  atom by the saturation spectroscopy in a hollow cathode lamp (Hamamatsu L233-38NB). A digital laser locking module (DigiLock 110) from Toptica has been used. Therefore, AOM 1 is used to blue detune the frequency of the laser beam to the resonance by double pass configuration and frequency of 75 MHz with +1 order. AOM 2 has the same configuration as AOM 1 to blue detune the laser frequency on resonance for the probe beam. After that, the blue laser beam is divided into two parts, and the frequencies are detuned by the AOM 3 and 4 for cooling. The first part of the beam is used for Zeeman slower with 350 MHz red detuning by AOM 3 with single pass configuration and order -1. The other part is for blue MOT with 110 MHz blue detuning by AOM 4 with single pass configuration and order +1.

During blue MOT cooling, two repumper lasers 679 nm for  $^3P_0 - ^3S_1$  transition and 707 nm  $^3P_2 - ^3S_1$  transition are used to avoid atoms relaxing from  $^1P_1$  to other metastable states rather than ground state  $^1S_0$ . These repumpers are locked by wavemeter as it is



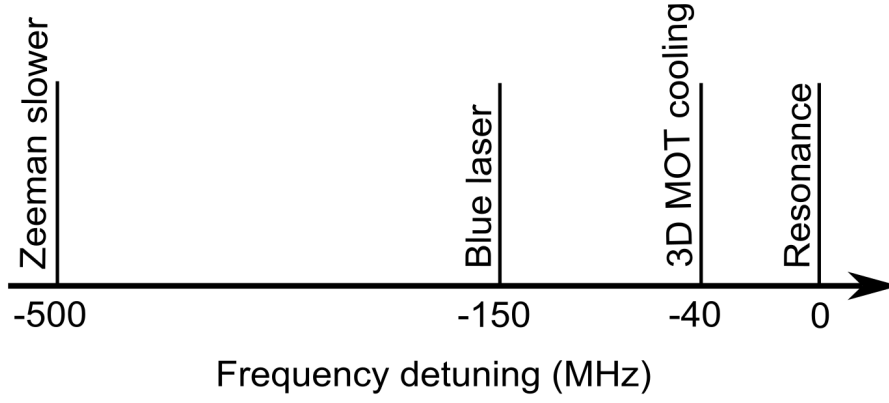


Figure 6.3: Frequency detuning for different blue laser beams from  $^1S_0 - ^1P_1$  resonance. The blue laser is 150 MHz red detuned from resonance; therefore, it needs to be red detuned 350 MHz more for Zeeman slower, 110 MHz blue detuned for 3D MOT cooling, and 150 MHz blue detuned for saturation spectroscopy and probe beam.

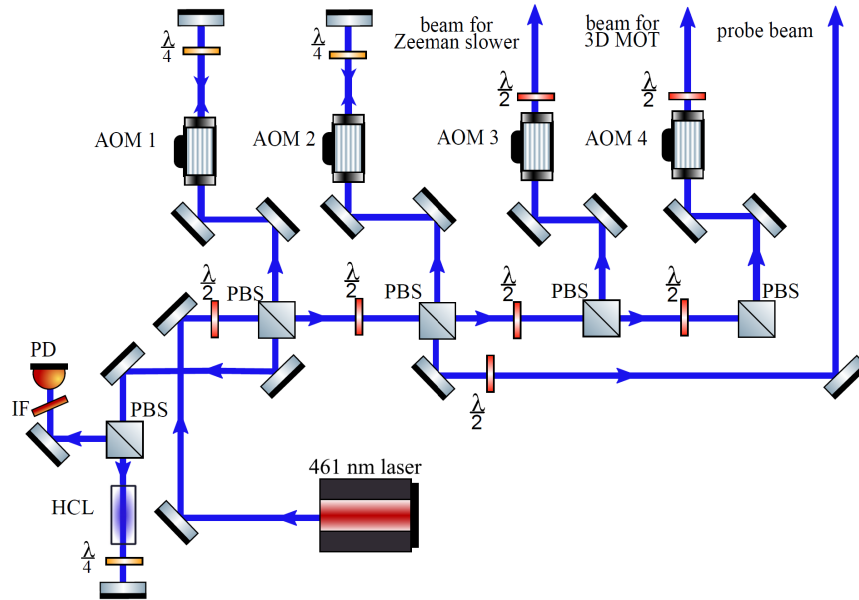


Figure 6.4: Optical setup schematic for 461 nm blue laser in Sr1 room. There are four AOMs to shift the frequency of the laser beam for each part of the experiment based on Figure 6.3. AOM 1 and 2 shift the frequency of the laser beam to the  $^1S_0 - ^1P_1$  resonance for saturation spectroscopy and probe beam, respectively. AOM 3 and 4 are for Zeeman slower and 3D MOT, respectively. Abbreviations: PBS- polarising beam splitter, AOM- acousto-optic modulator, PD- photodetector, IF- interference filter, HCL- hollow cathode lamp,  $\frac{\lambda}{2}$ - half-wave plate,  $\frac{\lambda}{4}$ - quarterwave plate. Schematic is taken from [38].

described in Chapter 5. Additionally, a 10 kHz frequency modulation is applied to the lasers with an amplitude of around 500 MHz to cover all the states to be repumped and neglect frequency fluctuation in the free-running ECDLs. This modulation is applied to the piezo laser driver. During the first cooling stage, around  $6-8 \times 10^8$  Sr atoms are loaded into the blue MOT and cooled down to 2-3 mK [27].

The second cooling stage is red MOT by 689 nm ECDL on  $^1S_0 - ^3P_1$  transition. The natural linewidth of this transition is 7.6 kHz; therefore, a 689 nm laser has to be

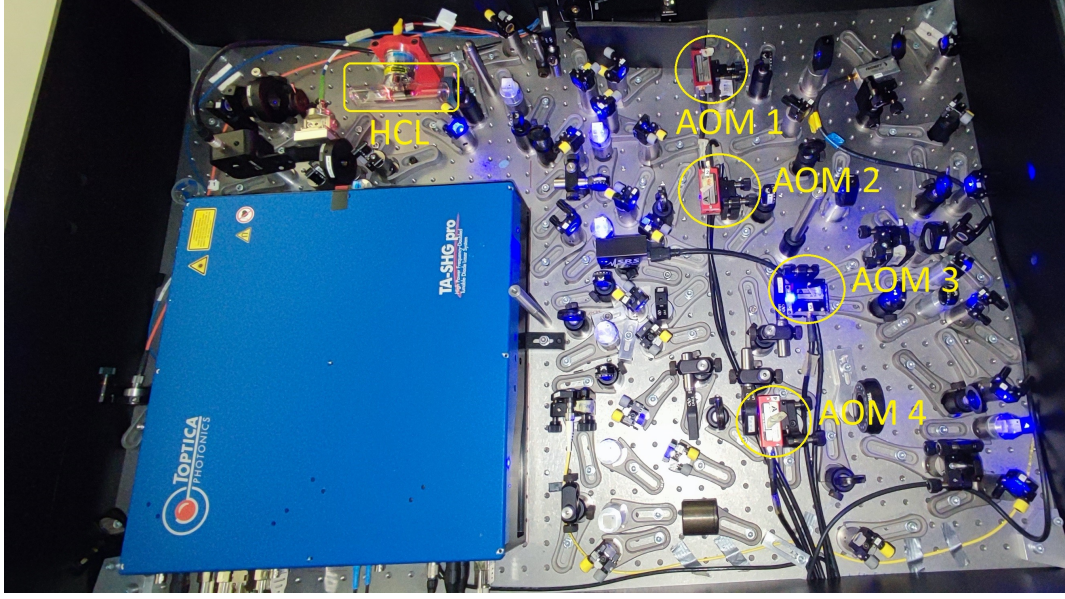


Figure 6.5: Optical setup for blue laser in Sr1 room related to Figure 6.4.

locked to a high-finesse optical cavity and frequency comb for short-term and long-term stability, respectively. As is discussed in Chapter 5, for long-term operation, an auto relocking program is used. A PDH locking scheme is used to narrow the laser linewidth below the natural linewidth of transition. This cavity's free spectral range (FSR) is 1.5 GHz with the finesse of 62800 [27]. The laser frequency stabilized to the cavity is locked to the frequency comb by an AOM frequency shifter. This laser beam has been sent to Sr1 room for red MOT cooling.

Frequency detuning for different red laser beams from  $^1S_0 - ^3P_1$  resonance is shown in Figure 6.6. The optical setup schematic and a view of that in the experiment for red laser in Sr1 room are presented in Figure 6.7 and 6.8. The red laser locked to the frequency comb, which is referenced to UTC (AOS) and transferred to Sr1 room, is 212 MHz red detuned from resonance; therefore, it must be red detuned 222 MHz more for the injection lock to the slave laser by AOM 5. From the slave laser, 433.16 MHz blue detuned for red MOT A and 433.912 MHz blue detuned for red MOT B by AOM 6.

The red beam laser is overlapped with the blue laser for MOT. The magnetic field gradient is dropped down from 0.55 T/m during blue MOT to 0.03 T/m for red MOT. Then, the cloud of Sr atoms is compressed by a linear magnetic field ramp from 0.03 T/m to 0.1 T/m. As the natural linewidth of  $^1S_0 - ^3P_1$  transition is significantly smaller than the Doppler width of this transition at the temperature of blue MOT, significantly fewer atoms could be caught in the red MOT. Therefore, to catch as many Sr atoms as possible from blue MOT to red MOT, the red laser beam has to be broadened by a 20 kHz frequency modulation with an amplitude of 1.6 MHz applied on the AOM. This stage is called red MOT A and the RF signal for AOM is provided by a function generator. After red MOT A, there is red MOT B, whose frequency is provided by a DDS. At the end of the red MOT, the Sr atoms' temperature is cooled below  $10 \mu K$ , which is low enough to capture them by the optical lattice trap.

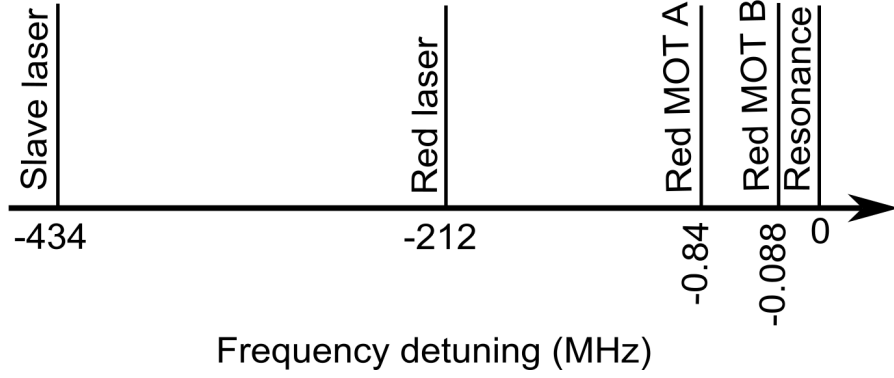


Figure 6.6: Frequency detuning for different red laser beams from  $^1S_0 - ^3P_1$  resonance. The red laser is 212 MHz red detuned from resonance; therefore, it needs to be red detuned 222 MHz more for injection to slave laser, then from slave laser, 433.16 MHz blue detuned for red MOT A and 433.912 MHz blue detuned for red MOT B.

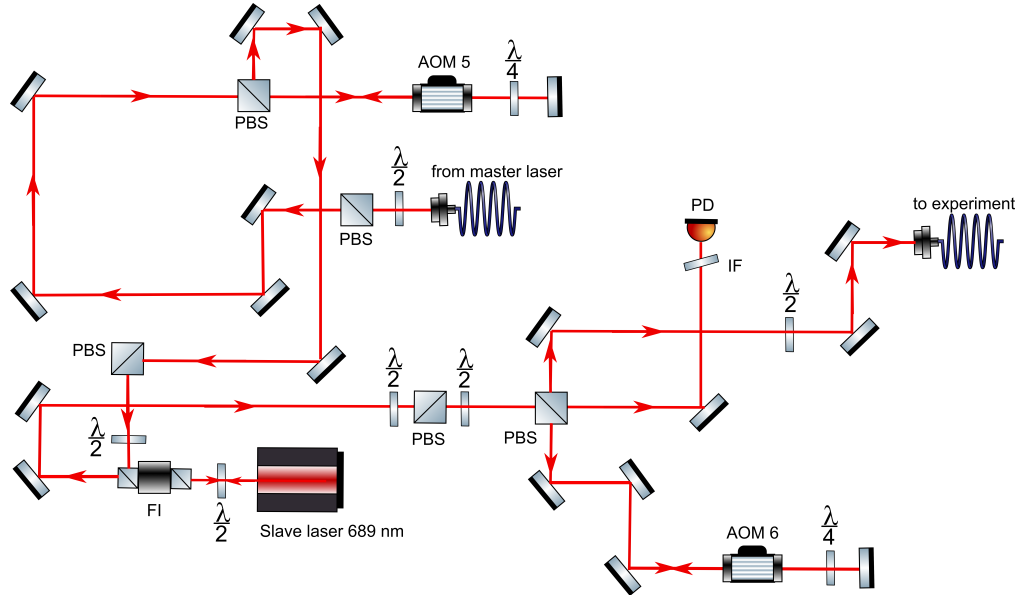


Figure 6.7: Optical setup schematic for 689 nm red laser cooling in Sr1 room. The red laser beam from the master, after locking to the frequency comb, is transferred to Sr1 room, and the frequency is red detuned by 212 MHz from resonance. From there, it needs to be red detuned 222 MHz more with AOM 5 for injection to slave laser based on Figure 6.6. AOM 6 shifts the frequency of the laser beam by 433.16 MHz blue detuned for red MOT A and 433.912 MHz blue detuned for red MOT B. Abbreviations: PBS- polarising beam splitter, AOM- acousto-optic modulator, PD- photodetector, IF- interference filter, FI- Faraday isolator,  $\lambda/2$ - half-wave plate,  $\lambda/4$ - quarterwave plate.

### 6.1.3 Optical lattice

The optical power buildup cavity, used in the Sr1 room for optical lattice, has a finesse of around 120. The mirrors of this cavity are mounted outside the vacuum chamber, and the TEM<sub>00</sub> mode has a beam waist of 152  $\mu\text{m}$  at the wavelength of 813 nm. This large waist reduces the density of trapped atoms; therefore, the collisional shift of the clock

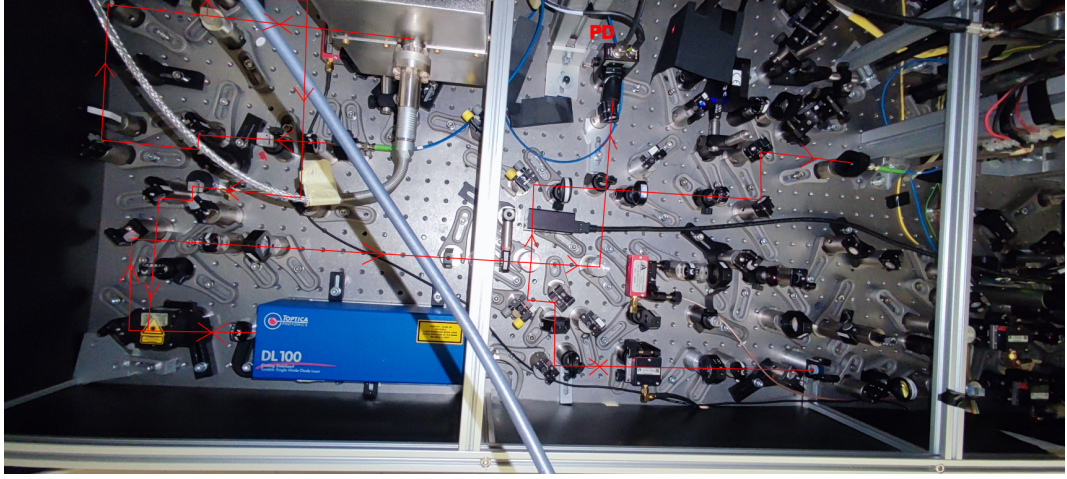


Figure 6.8: Optical setup for red laser cooling in Sr1 room related to Figure 6.7.

line is reduced.

The TiSa laser is used with 2.5 W output power at 813 nm for the lattice laser to produce a sufficient deep dipole trap. This laser is locked to an internal reference cavity, and it is locked additionally to the frequency comb. A polarization-maintained single-mode fiber sends a significant part of the laser beam to the Sr1 room from the Sr2 room, where the laser is placed. At the output of the fiber, there is around a 330 mW lattice beam power, which is coupled into the power buildup cavity. The optical power buildup cavity length is locked to the lattice frequency beam using piezo on one mirror and utilizing the PDH method.

#### 6.1.4 Clock interrogation

The next step of the optical atomic clock cycle procedure is to interrogate the clock laser with trapped Sr atoms in the optical lattice. The clock laser, 698 nm ECDL as a master, is locked to a high-Q optical cavity with 1.5 GHz FSR and finesse of 300000. The light from the master laser in the Cavity room is transferred to the Sr2 room and injected into a slave laser. From Sr2 room is transferred to the Sr1 room and has been injected into another slave laser as well. The laser beam is transferred via a single-mode polarization-maintaining fiber in all parts. Each fiber has a separate active fiber-noise cancellation to ensure stable optical frequency transfer [75].

Frequency detuning for clock laser beam from  $^1S_0 - ^3P_0$  resonance is shown in Figure 6.9. The optical setup schematic and a view of that in the experiment for the clock laser in Sr1 room are presented in Figure 6.10 and 6.11. The clock laser from Sr2 room is transferred to Sr1 room with phase noise cancellation. The clock laser beam is 404 MHz blue detuned from resonance in Sr1 room; therefore, it must be red detuned 404 MHz by AOM 16 with a double pass configuration for clock spectroscopy.

The clock laser beam direction must be perfectly aligned with the lattice axes to eliminate contribution from the radial motion of atoms in the lattice. A beam profiler in Figure 6.12 shows the clock and lattice laser beams while not overlapping. In the Sr1 room lattice clock setup, the lattice beam waist is  $152 \mu\text{m}$ , and the clock beam waist is set roughly four times bigger.

Clock laser is interrogating with trapped Sr atoms to excite them from  $^1S_0$  to  $^3P_0$ .



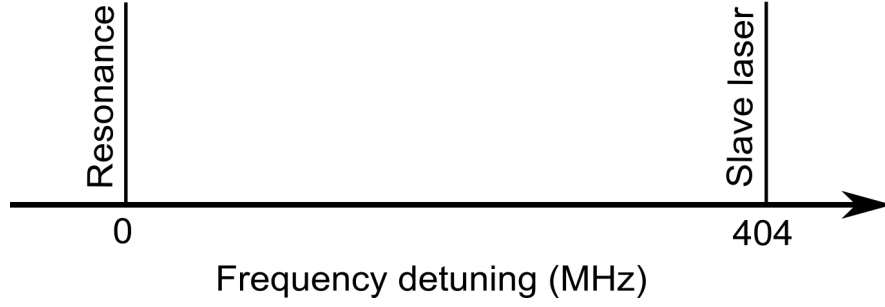


Figure 6.9: Frequency detuning for clock laser beam from  $^1S_0 - ^3P_0$  resonance. The clock laser beam frequency in the Sr1 room for slave laser has a 404 MHz difference from resonance; therefore, it must be red detuned 404 MHz for clock spectroscopy.

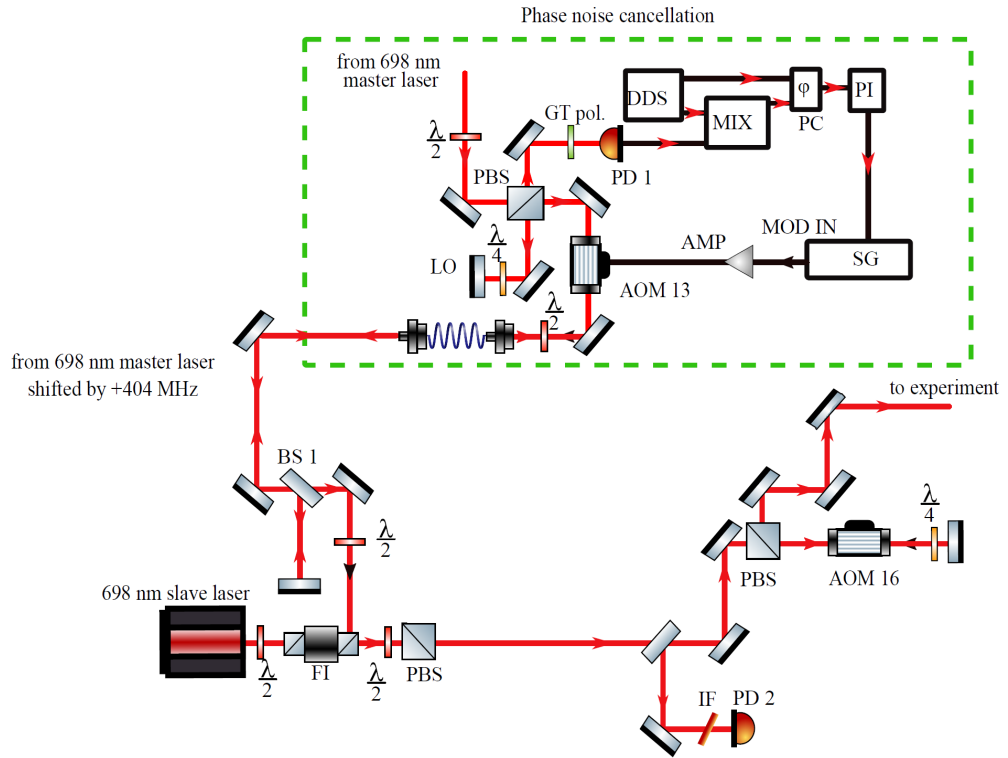


Figure 6.10: Optical setup schematic for 698 nm clock laser in Sr1 room with phase noise cancellation. The clock laser beam from the slave has been red detuned by 404 MHz with AOM 16 based on Figure 6.9. Abbreviations: PBS- polarising beam splitter, GT pol.- Glam-Taylor polariser, LO- local oscillator, BS- beam splitter, AOM- acousto-optic modulator, PD- photodetector, IF- interference filter, FI- Faraday isolator,  $\frac{\lambda}{2}$ - half-wave plate,  $\frac{\lambda}{4}$ - quarterwave plate, DDS- direct digital synthesiser, MIX- mixer, PC- phase comparator, PI- proportional–integral controller, SG- signal generator, AMP- operational amplifier. Schematic is taken from [38] with some modification.

The populations in the ground, excited states, and background noise are measured as the procedure is shown in Figure 6.13. Then, the information on the transition probability will be provided. The excitation probability that the atoms changed their state from  $^1S_0$  to  $^3P_0$  is calculated from Equation 6.1,

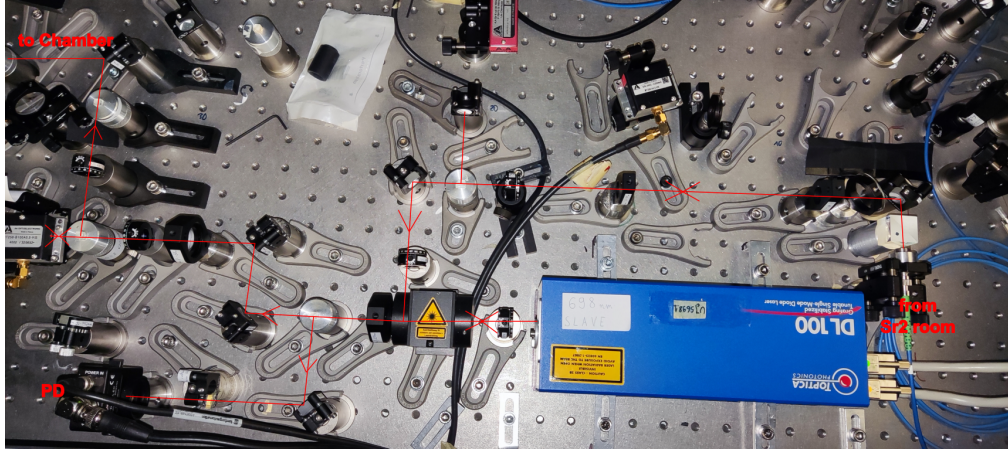


Figure 6.11: Optical setup for clock laser to go through the chamber in Sr1 room.

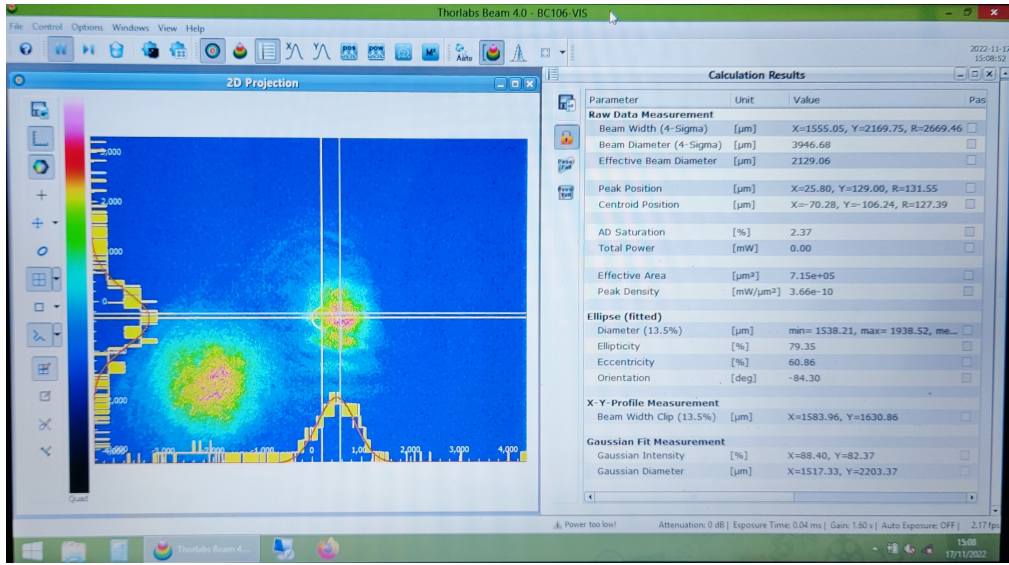


Figure 6.12: The clock and lattice laser beams while not overlapping on the beam profiler.

$$P = \frac{N_e - N_b}{(N_g - N_b) + (N_e - N_b)}, \quad (6.1)$$

in this equation,  $N_g$  and  $N_e$  are the population of the ground state and excited state, respectively. Also,  $N_b$  is background noise, which should be removed from the population of the ground state and excited state. First, the population of  $N_g$  is calculated after clock interrogation. Measurement is done by fluorescence imaging with a blue laser (probe beam). The fluorescence images are recorded by the electron-multiplying CCD camera (Hamamatsu C9100-02), and then the  $N_g$ ,  $N_e$ , and  $N_b$  are calculated from the images. The blue laser pulse will remove the ground state atoms from the lattice trap. However, the imaging pulse does not affect the excited atoms in the  $^3P_0$ . The excited atoms are now de-excited to the ground state by the repumping lasers due to the long lifetime of Sr atoms in the  $^3P_0$  state. Then, another measurement is done to calculate the population of  $N_e$ . In the end, the  $N_b$  population is calculated by the third measurement, which gives the background noise without any atoms in the trap.

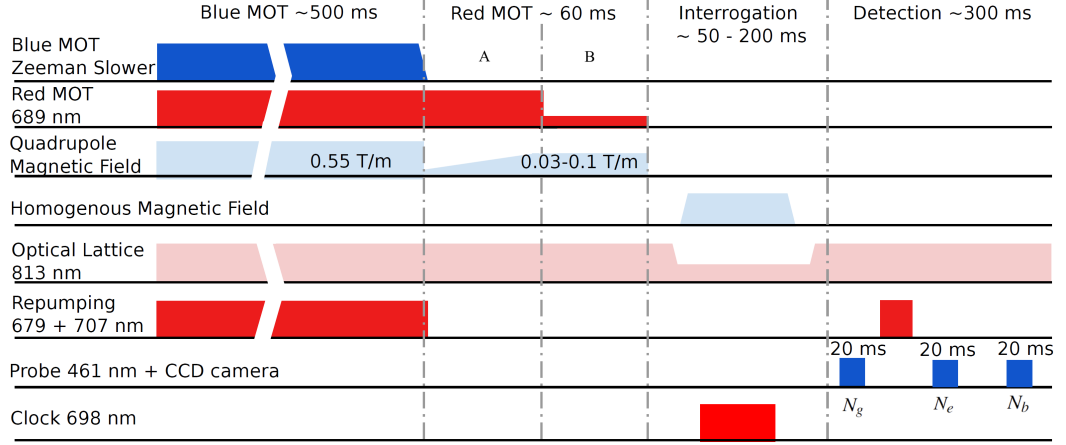


Figure 6.13: The whole sequence of the clock operation in each cycle [27].  $N_g$ ,  $N_e$ , and  $N_b$  in detection by probe beam are used to calculate the transition probability by Equation 6.1.

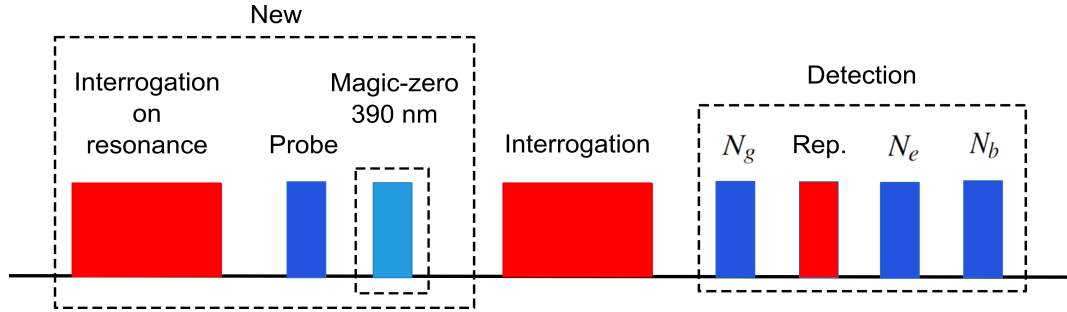


Figure 6.14: Clock sequence for sideband spectroscopy from  $^3P_0 - ^1S_0$ . The big dashed box is a new procedure added to the main sequence of the clock operation in Figure 6.13. Rep. in the detection part stands for repumpers.

In the end, the clock laser is digitally locked to the clock line  $^1S_0 - ^3P_0$  transition. To achieve this, the excitation probability is measured at two frequencies. Each one is offset by half the full width at half maximum (FWHM) of the transition, both red-detuned and blue-detuned from the clock line's central frequency. The difference in the measured excitation probability generates a correction signal. Any drift of the clock laser frequency from the transition is compensated digitally through a feedback loop by DDS designed in Chapter 4.

To perform the spectroscopy from  $^3P_0$  to  $^1S_0$  for measuring the temperature of trapped atoms in the excited state ( $^3P_0$ ), the clock operation sequence should be modified as shown in Figure 6.14 with a big dashed box and label of new. The only difference is that an extra interrogation and probe are added before the last interrogation and detection. After trapping the Sr atoms in the lattice, an interrogation is done on the resonance frequency to excite almost half of the atoms (with a long interrogation time) from the ground state to the excited state. Then, the probe beam of 461 nm is used to remove all the remaining atoms from the ground state in the lattice. After the probe, only excited atoms remain in the lattice. In the end, the interrogation and detection will be done by scanning the whole range of the sidebands. There is also a magic-zero illumination at 390 nm, as shown in Figure 6.14 after the probe beam. This part of the experiment was not done as the 390 nm laser was broken.

The absolute probability that the atoms changed their state from  $^3P_0$  to  $^1S_0$  is equal to

$$P_e = \frac{N_g - N_b}{(N_g - N_b) + (N_e - N_b)}, \quad (6.2)$$

where the  $N_e$  is replaced by  $N_g$  in the numerator of the Equation 6.1.

## 6.2 Optimization

After implementing newly developed features in the optical atomic clock, we are able to optimize the clock operation better. The main features are automatic control on compensation coils described in chapter 3. This feature is implemented in the Sr1 room. The next feature is the automatic relocking of ECDLs presented in chapter 5. The auto relocking of the laser is done for two repumpers, 707 nm and 679 nm, and a red laser for cooling 689 nm. This automatic relocking system works in the cavity room of KL FAMO.

As described in the previous section, the laser beam frequency for each part of the experiment needs to be optimized. For example, the blue laser must be blue detuned 110 MHz to be ready for 3D MOT cooling. However, this 110 MHz is rough and needs to be precisely optimized to catch enough Sr atoms. This section determines most of these parameters, which have more effect on trapping atoms. First, the parameters are optimized to have more atoms in the red MOT A, then red MOT B, and at the end, in the lattice. Here is a list of parameters that need to be optimized:

### 1. Blue laser:

- Frequency lock for saturation spectroscopy by AOM 1,
- Frequency of probe beam by AOM 2,
- Frequency of Zeeman slower by AOM 3,
- Frequency of blue MOT by AOM 4,
- Light intensity for Zeeman slower,
- Light intensity for blue MOT,
- The timing of blue MOT in the program,

### 2. Red laser:

- Frequency of red MOT A on the function generator by AOM 6,
- Frequency of red MOT B in the program on DDS by AOM 6,
- The amplitude of red MOT B in the program on DDS,
- Magnetic fields on MOT coils during red MOT A and B,
- The timing of red MOT A and B,

### 3. And, optimizing current in compensation coils for every stage.



The optimization process focuses on trapping the maximum number of atoms in the lattice; however, in some cases, we are only interested in having colder atoms. Therefore, the target in this thesis is to catch as many atoms in the lattice as possible to have a high signal-to-noise ratio from atoms, which improves the stability (1.7) of the clock. A fluorescence image was taken by a camera to measure the number of trapped atoms in the lattice while the atoms were trapped for 70 ms. Figure 6.15 presents the scanning frequency of the blue laser beam for Zeeman slower by AOM 3. The top figure is for the large step from 165 to 185 MHz, while the bottom figure shows the small step around the peak resulting from the first measurement. The scanning frequency is applied by DDS and it is before the frequency doubler. The figure shows that the maximum number of trapped atoms is achieved with 175 MHz on the DDS or 350 MHz on the AOM. This AOM is set on a single pass and on order -1. So, the laser frequency for Zeeman slower is red detuned with 350 MHz as expected in Figure 6.3.

Figure 6.16 presents the scanning frequency of the blue laser beam for blue MOT by AOM 4 with a scanning range from 100 to 130 MHz; this AOM is run by VCO and is set on order +1. The figure shows that the maximum number of trapped atoms was achieved at 117.5 MHz blue detuned.

Figure 6.17 presents when blue MOT should be turned off to catch more atoms. However, this time should not be too long, as it is increasing the clock cycle's dead time. So, we decided to turn the blue MOT off at 375 ms roughly after starting the blue MOT.

Figure 6.18 presents the scanning frequency of the red laser beam for red MOT A by AOM 6. The AOM for this part is set on double pass with order +1. Therefore,

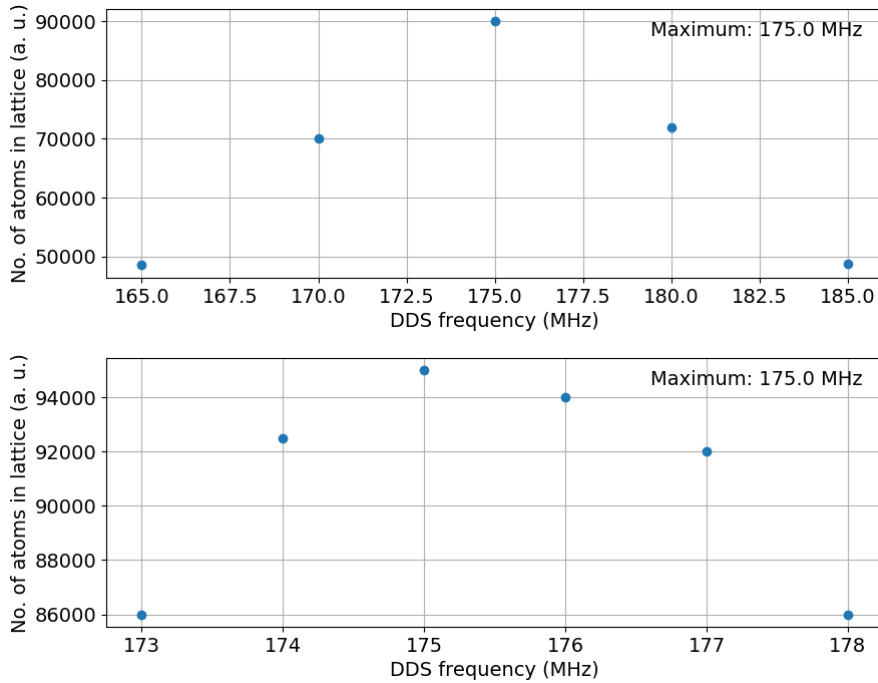


Figure 6.15: Scanning frequency of blue laser beam for the Zeeman slower using AOM 3. (Top) coarse scanning with 5 MHz steps, (bottom) fine scanning with 1 MHz steps. The maximum number of trapped atoms achieved with 175 MHz red detuned. The measurement has been repeated only once.

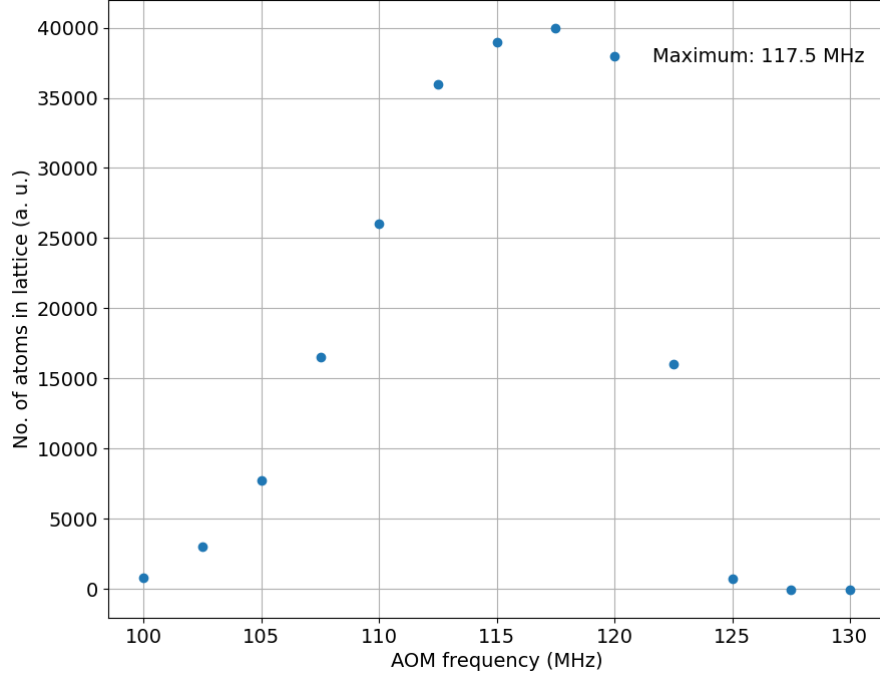


Figure 6.16: Scanning frequency of blue laser beam for blue MOT by AOM 4 with a 2.5 MHz scanning step. The maximum number of trapped atoms was achieved with 117.5 MHz blue detuned. The measurement has been repeated only once.

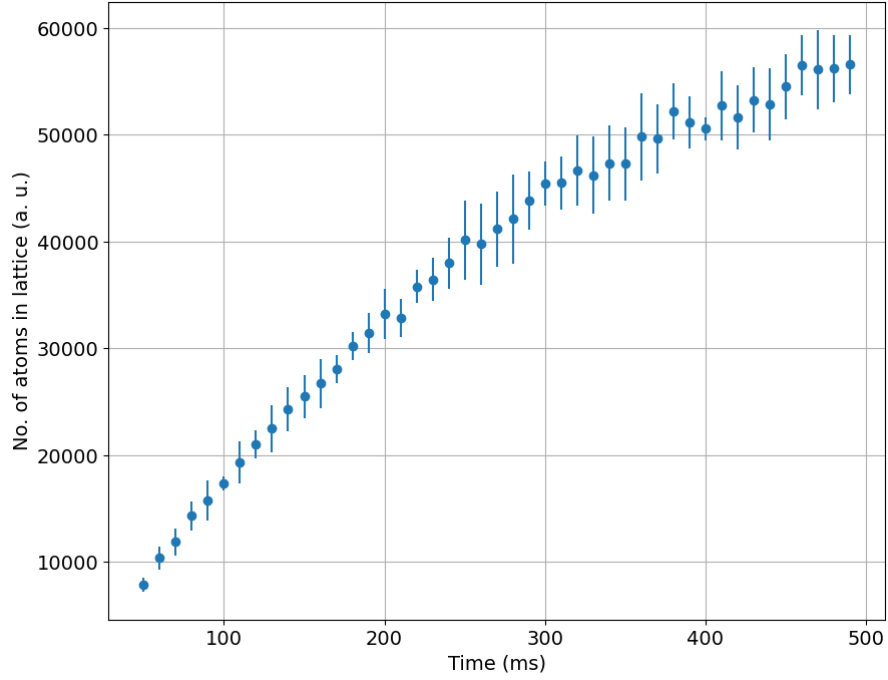


Figure 6.17: Estimated time to turn off the blue MOT at 375 ms roughly from the starting of the blue MOT. The measurement has been repeated six times.

the maximum number of trapped atoms is achieved with 216.56 MHz on the function generator or 433.12 MHz shift on the laser frequency for the experiment. This frequency is modulated with 20 kHz from the function generator, and red MOT A is turned on at

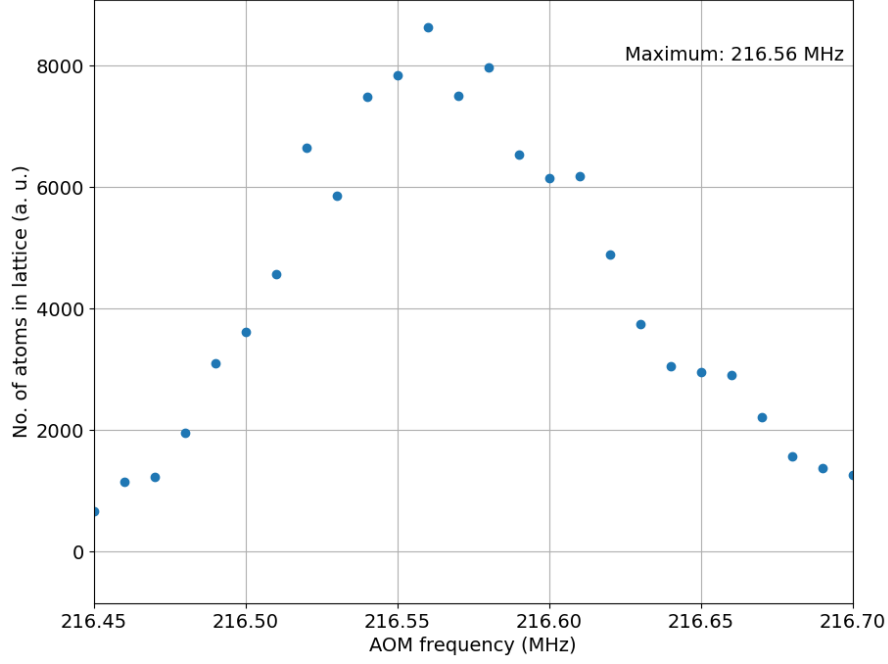


Figure 6.18: Scanning frequency of red laser beam for red MOT A laser by AOM 6. The maximum number of trapped atoms achieved with 216.56 MHz ( $\times 2 = 433.12$  MHz) blue detuned. The measurement has been repeated only once.

the beginning of the cycle, as shown in Figure 6.13.

The optimal time of the quadrupole magnetic field ramp to raise from 3 to 10 G/cm (Figure 6.13) during red MOT A is presented in Figure 6.19. The maximum number of trapped atoms in the lattice is achieved when the magnetic field rises during 7 ms.

Red MOT A is turned off by switching the RF signal from the function generator to DDS for red MOT B. Therefore, frequency is not modulated and is on a single frequency. For red MOT B, the RF power for AOM must be dominated to trap enough atoms in the lattice as presented in Figure 6.20 the RF amplitude should be set at 8 percent on DDS. The red laser power beam for red MOT B before the chamber is presented in Table 6.1. So the laser power should be a little lower than  $56 \mu\text{W}$  to trap enough atoms by setting RF amplitude on 8 percent.

Now, to find out the precise frequency detuning with AOM 6 for red MOT B, a scan is done on the frequency from 216.9 to 217 MHz, as shown in Figure 6.21. The maximum number of trapped atoms is achieved at 216.96 MHz on DDS, which is 433.92 MHz blue detuned of the red laser frequency after a double pass.

Table 6.1: The power of the red laser beam for red MOT B measured before the chamber.

RF Amplitude (%)	Laser Power (mW)
50	2
35	1.6
20	0.6
10	0.056

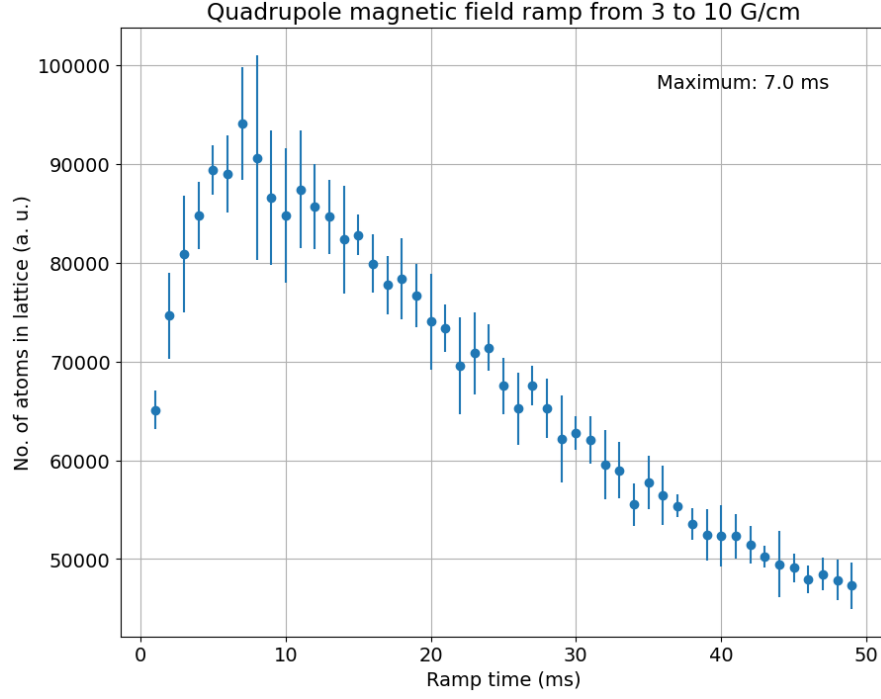


Figure 6.19: The optimal quadrupole magnetic field ramp time from 3 to 10 G/cm during red MOT A. The maximum number of trapped atoms in the lattice is achieved when the magnetic field rises during 7 ms. The measurement has been repeated six times.

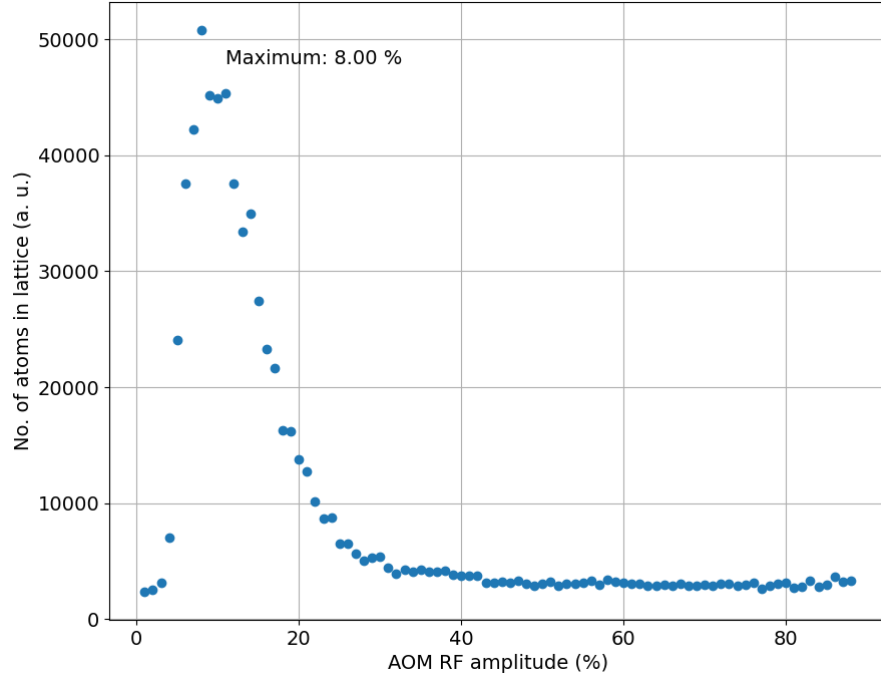


Figure 6.20: Scanning RF amplitude on DDS for AOM 6 in red MOT B. The maximum number of trapped atoms in the lattice is achieved when the RF amplitude is set at 8 percent. The measurement has been repeated only once.

Figure 6.22 presents when red MOT B should be off to achieve the maximum number of trapped atoms in the lattice (this stage is loading atoms in the lattice). The trapped

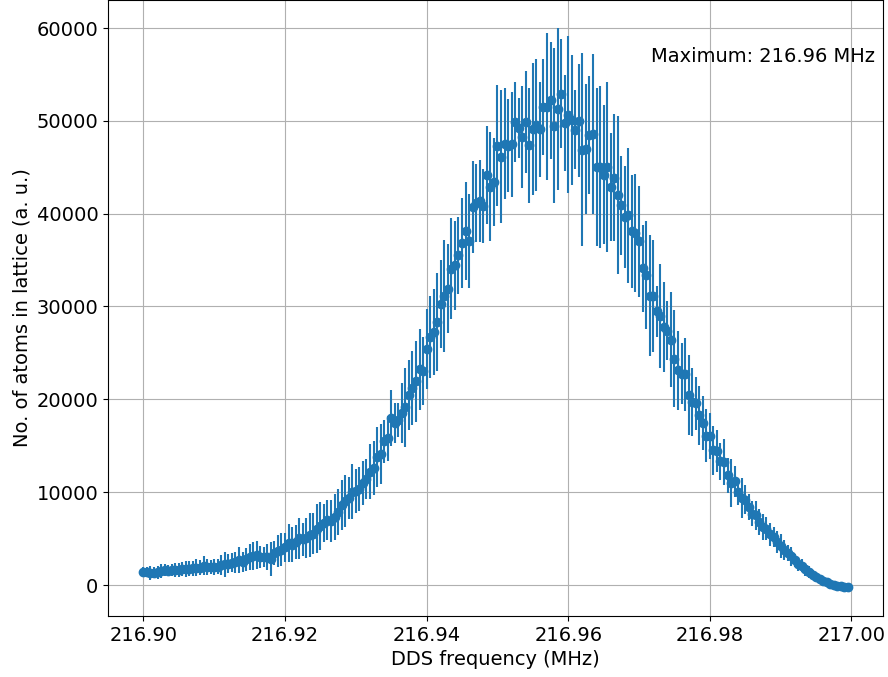


Figure 6.21: Scanning frequency on AOM 6 for red MOT B. The maximum number of trapped atoms achieved with 216.96 MHz ( $\times 2 = 433.92$  MHz) blue detuned. The measurement has been repeated six times.

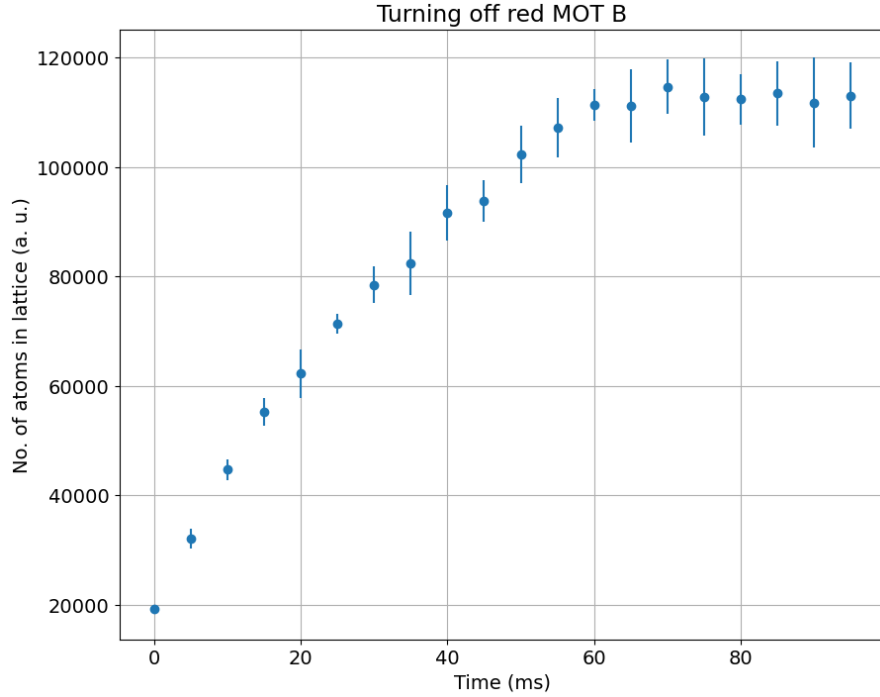


Figure 6.22: The optimal time for turning off red MOT B is after 60 ms of illuminating red laser. The measurement has been repeated seven times.

atoms are increasing exponentially to be saturated after 60 ms of red MOT B. Red MOT B should be turned off after 60 ms of illuminating red laser to have the maximum number of trapped atoms in the lattice.

A scan is applied to the voltage on the driver (corresponding to the current in the coils) for each pair of compensation coils to optimize the trapped atoms in the lattice by compensation coils. In Figure 6.23, the voltage of the compensation coils on the Z axis is scanned from -2 V to 2 V while the voltage on the X and Y axis was set at zero. It is shown how this device can control the trapped atoms in the lattice or any other stage of cooling to improve the experiments.

Three parameters (for X, Y, and Z) must be scanned to find the maximum number of trapped atoms. There should be a 3D scan of all these parameters. In Figure 6.24, the result for the 3D scan is presented; in this situation, to have a maximum trap in the lattice, the voltage of compensation coils for X, Y, and Z axis should be set on -0.5, -0.5, and 0.5 V respectively.

### 6.3 Lattice lifetime measurement

After optimizing all the parameters and realigning the optical system, loading atoms into the optical lattice improved more than three times, as shown in Figure 6.25. When the clock laser interrogates the trapped atoms in the lattice, it is essential to know if there are enough atoms for interrogation. To know this, the lifetime of the atoms in the lattice should be measured. To measure the lifetime of atoms, an image should be taken from the atoms after turning off the red MOT B from 50 to 2950 ms. After measurement, an exponential function Equation 6.3 has been fitted to the data to find the trapped atoms' lifetime.

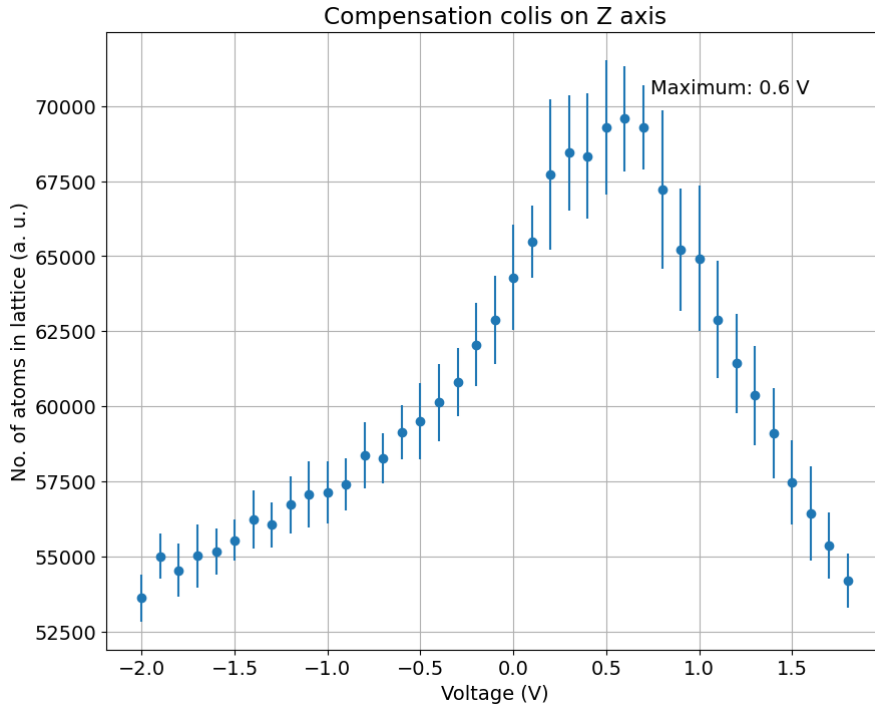


Figure 6.23: Scanning voltage of compensation coils on the Z axis. The maximum number of trapped atoms is achieved with applying 0.6 V voltage on the pair of coils for the Z axis. The voltage on the X and Y axis was set at zero. The measurement has been repeated eleven times.

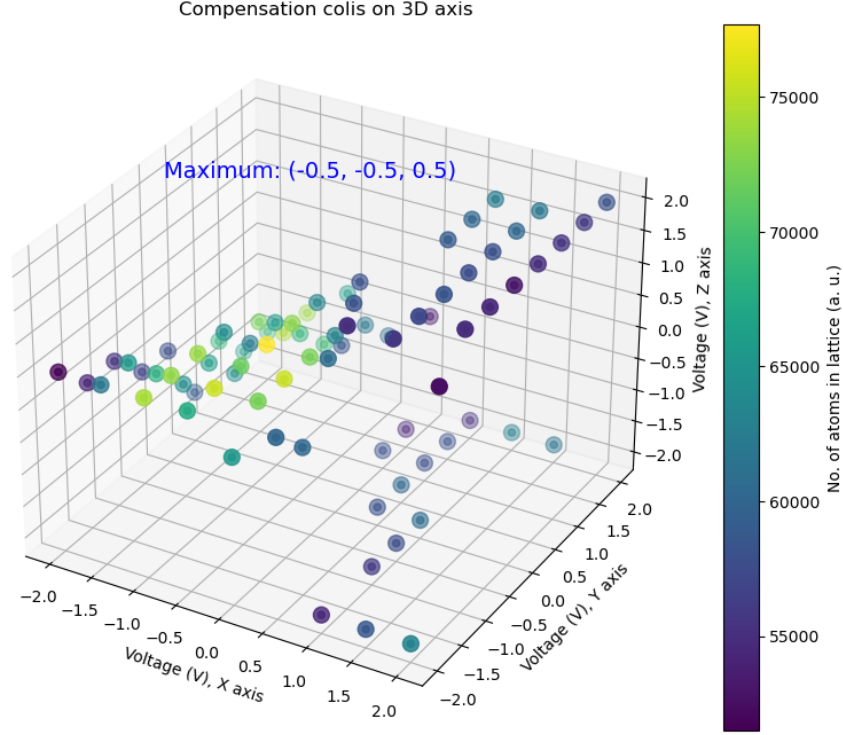


Figure 6.24: Scanning voltage of compensation coils on 3D axis. The maximum number of trapped atoms is achieved with applying -0.5, -0.5, and 0.5 V voltage on the pair of coils for the X, Y, and Z axes, respectively. The measurement has been repeated only once.

$$I = I_0 \times \exp\left(-\frac{t}{\tau}\right), \quad (6.3)$$

in this equation,  $\tau$  is the lifetime of trapped atoms. The result is presented in Figure 6.26. The lifetime of trapped atoms in the lattice is achieved at  $1611 (\pm 14)$  ms by fitting the equation to the data.

## 6.4 Clock spectroscopy

After loading Sr atoms into the lattice, we can do the clock spectroscopy to determine the clock's characterization. This characterization includes sideband spectroscopy to measure the temperature of Sr atoms in the lattice, spectroscopy of  $^1S_0 - ^3P_0$  transition to measure linewidth of the clock line, Rabi oscillation to measure  $\pi$  pulse, and the evaluation of the systematic shift which is discussed in the next section.

The clock line from  $^1S_0$  to  $^3P_0$  should be found from a comprehensive scan around the expected clock line, which is 404 MHz red detuned 6.9. As the linewidth of the clock line is very narrow in the hertz level, the scanning frequency step should be small enough to find the clock line. To find the line quickly, the linewidth of the clock line should be as broad as possible. For that, the magnetic field of the coils should be at its highest value, and the intensity of the clock laser should be at the highest amplitude. Additionally, interrogation time is set to 200 ms to ensure enough atoms (almost half of them) are excited to  $^3P_0$ . A scan frequency with a 100 Hz step size on DDS, which is 400

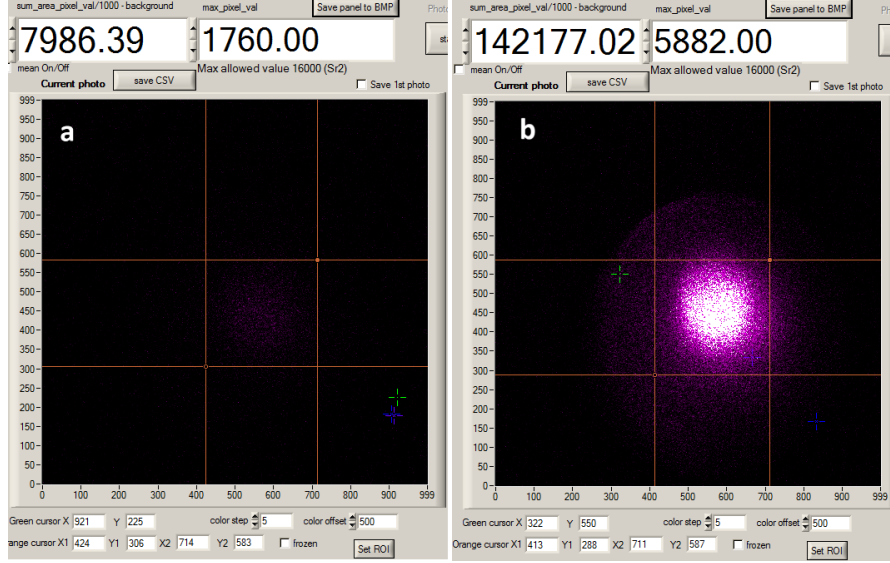


Figure 6.25: Trapped atoms in the lattice: a) before optimization, b) after optimization.

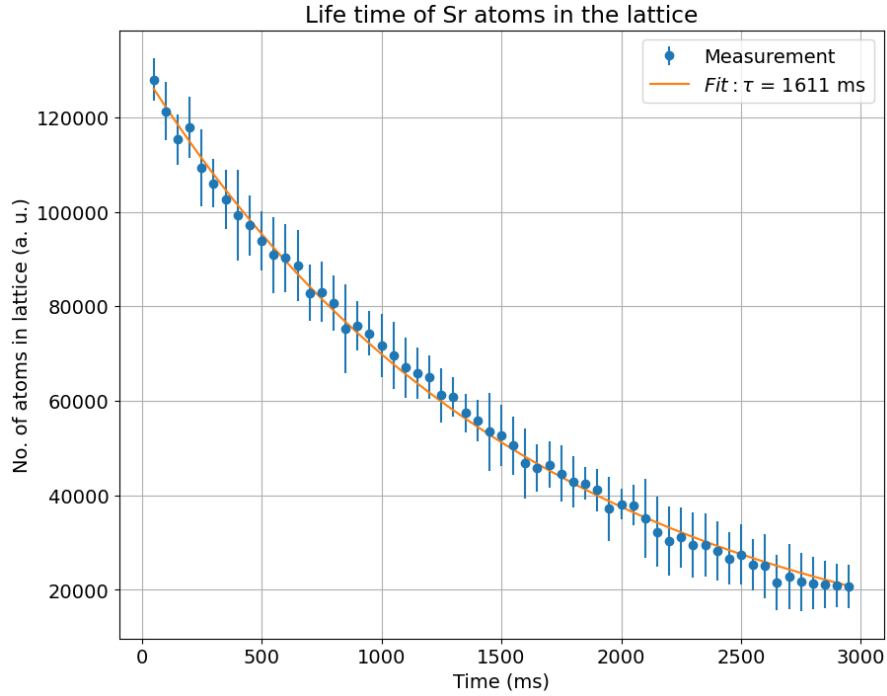


Figure 6.26: Lifetime of Sr atoms in the lattice. By fitting equation 6.3 to the dataset, the lifetime is achieved with 1611 ms. The measurement has been repeated twelve times.

Hz on a clock laser, is done to find the clock line frequency. Figure 6.27 shows a wide frequency scan around 40 kHz with AOM 16. Maximum probability transition is around 101.064 MHz on DDS or 404.256 MHz red detuned on the clock laser frequency. This frequency step size of 400 Hz is huge compared to the linewidth of the transition. That is why only a few points are covered by the scan in the clock line. A scan with small steps should be done around the clock line to find the clock line more precisely.



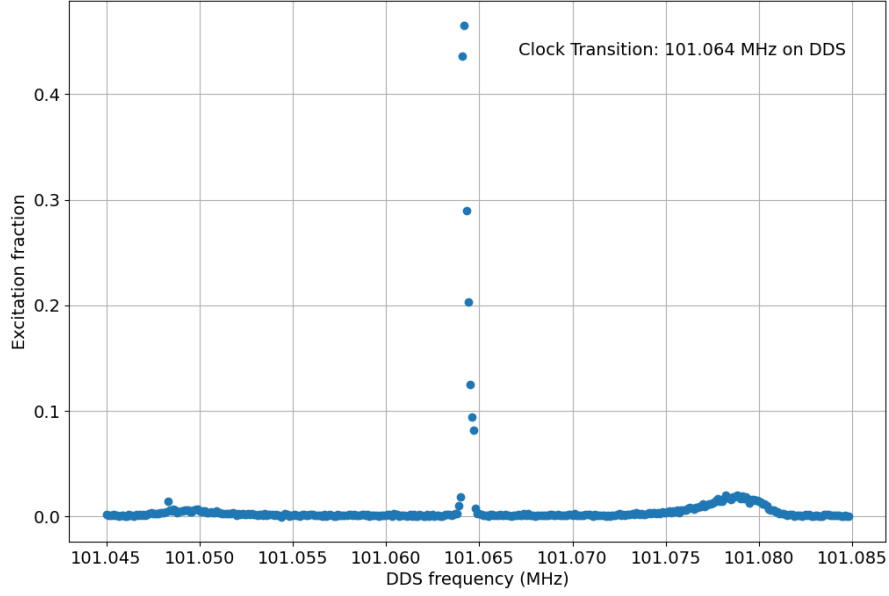


Figure 6.27: Scanning the clock laser frequency with AOM 16 to determine the clock line. The clock transition is around 101.064 MHz on DDS or 404.256 MHz on the clock laser frequency red detuned. The measurement has been repeated only once.

#### 6.4.1 Temperature measurement on ground state

To measure the temperature of the trapped atoms in the lattice, a scan should be done on the clock laser frequency as wide as possible around the clock line (carrier frequency) to cover the first red and blue sidebands completely. A scan frequency with a 100 Hz step size on DDS, which is 400 Hz on the clock laser, is done around the clock line. As the step size for scanning is large, the coils' magnetic field and the clock laser's intensity are set to high values. Interrogation time is also very high at 200 ms to excite enough Sr atoms.

The result of sideband spectroscopy is presented in Figure 6.28, and the Equations 2.38 and 2.39 are fitted to the measured data. Initial estimations for  $v_z$  based on measured data in Figure 6.27 were set on 60 kHz, for temperature  $6 \mu K$ , and FWHM of clock line on 300 Hz. The results of the fitting show  $6.2 (1.7) \mu K$  for the transverse temperature,  $3.57 (2.02)$  height ratio of blue sideband to red sideband, the  $v_z$  is achieved  $65.96 (1.56)$  kHz. Longitudinal temperature ( $T_z$ ) is equal to  $2.5 (1.1) \mu K$ , calculated by Equation 2.37. For comparison, the temperature of lattice depth ( $U_0/k_B$ ), by considering  $U_0 = 92 (4) E_r$  (calculated from Equation 2.15), is measured approximately, which is  $15.2 (0.7) \mu K$ . The FWHM for the carrier is approximated to  $407 (18)$  Hz.

#### 6.4.2 Temperature measurement on excited state

A sideband spectroscopy has been done on the trapped Sr atoms similar to the previous part; however, in this part, almost half of the atoms are excited to  $^3P_0$  first. This spectroscopy proves the theory of having a bigger red sideband than a blue sideband and also measures the temperature of the trapped Sr atoms in the excited state.

To measure the temperature of the trapped atoms in the excited state, almost half of the atoms are excited to  $^3P_0$  state by a long interrogation time on clock resonance

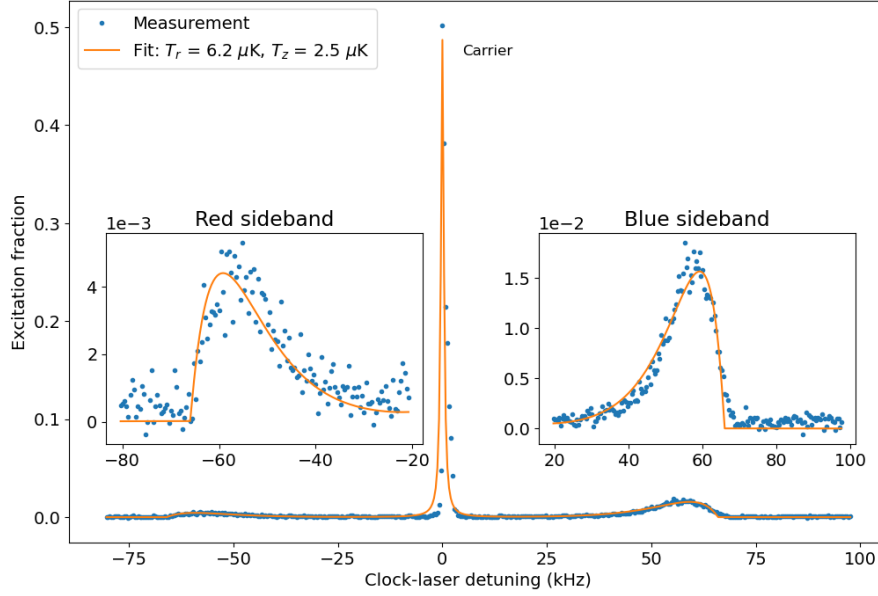


Figure 6.28: Sideband spectroscopy with fitting the Equations 2.38 and 2.39 to the measured data to find out the transverse temperature ( $T_r$ ) for the trapped atoms.  $T_r = 6.2$  (1.7)  $\mu K$  is approximated and  $T_z = 2.5$  (1.1)  $\mu K$  calculated from Equation 2.37. The measurement has been repeated only once.

first. The remaining atoms in the ground state are removed (Figure 6.14). Then, a scan frequency with a 100 Hz step size on DDS, which is 400 Hz on the clock laser, is done to cover the first red and blue sidebands. As the step size for scanning is small, the coils' magnetic field and the clock laser's intensity are set to the highest value. Interrogation pulse time is very long at 200 ms to de-excite enough Sr atoms.

The result of sideband spectroscopy is presented in Figure 6.29, and the Equations 2.38 and 2.39 are fitted to the measured data. The red sideband is bigger than the blue sideband, proving the theory. The results of the fitting show 5.7 (1.0)  $\mu K$  for the transverse temperature, 5.87 (2.56) height ratio of red sideband to blue sideband, and the  $v_z$  achieved 61.16 (0.98) kHz. Longitudinal temperature ( $T_z$ ) equals 1.7 (0.4)  $\mu K$  calculated by Equation 2.40.

### 6.4.3 Clock line measurement

As it is discussed in Chapter 2, clock transition ( $^1S_0 - ^3P_0$ ) is forbidden. Due to applying a magnetic field on coils and the intensity of the clock laser beam, the clock transition is weakly allowed. However, the systematic shift is increasing. The lowest magnetic field and clock laser beam should be set to reduce the shifts due to the magnetic field and probe light. In Figure 6.30, clock spectroscopy is presented for two different magnetic fields and the intensity of the clock laser beam. In both cases, interrogation time is 200 ms, and the Lorentzian function (Equation 2.39) is fitted to the measured data to estimate the FWHM of the clock line. Figure a shows a higher magnetic field magnitude corresponding to 1.0 V voltage from the power supply on the coils and 65 percent (set on DDS) of intensity for the clock laser beam. FWHM is achieved with 42 (1) Hz by fitting the Lorentzian function to the data. Figure b shows a lower magnetic field magnitude corresponding to 0.4 V voltage on the coils and 30 percent intensity for the clock laser

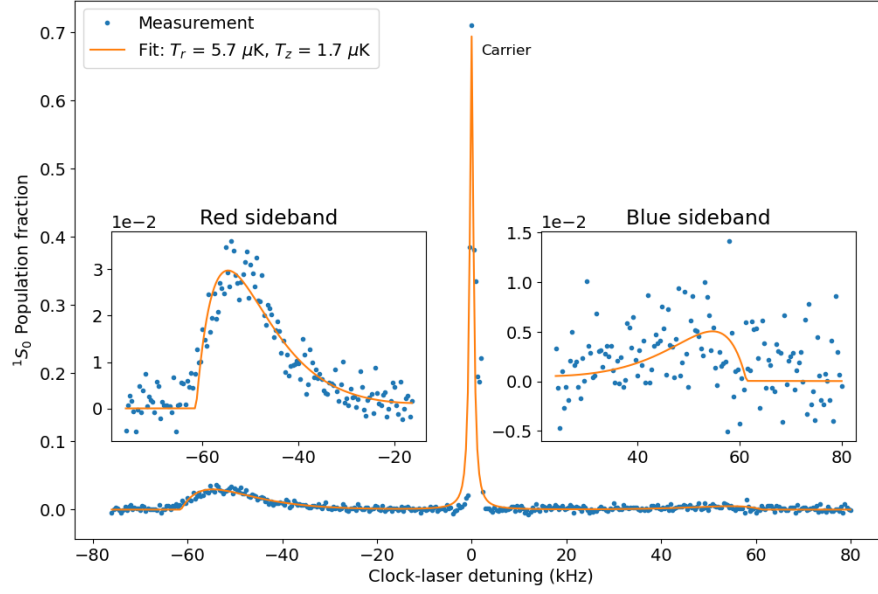


Figure 6.29: Sideband spectroscopy with fitting the Equations 2.38 and 2.39 to the measured data to find out the transverse temperature ( $T_r$ ) for the trapped atoms on the excited state.  $T_r = 5.7$  (1.0)  $\mu K$  is approximated and  $T_z = 1.7$  (0.4)  $\mu K$  calculated from Equation 2.40. The measurement has been repeated only once.

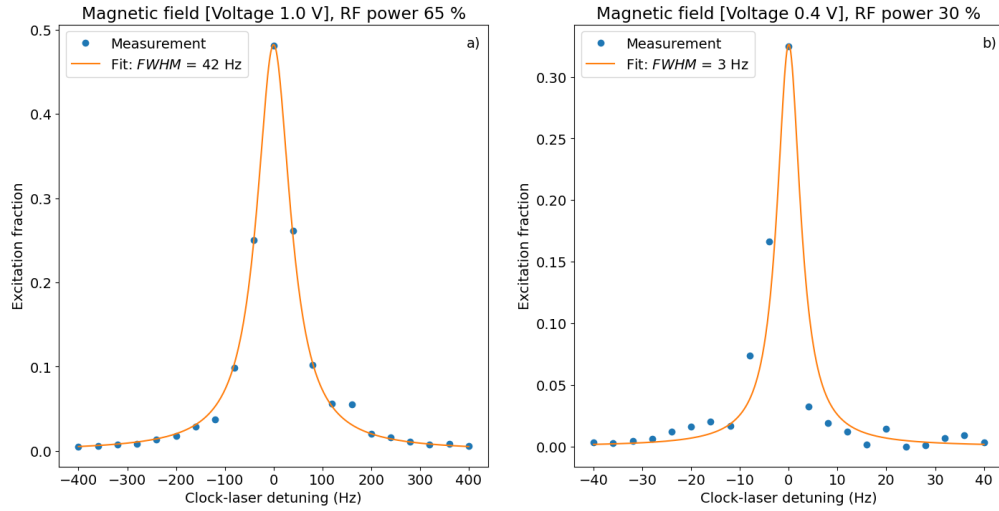


Figure 6.30: Clock spectroscopy and the Lorentzian function (Equation 2.39) fitted to the data for two different magnetic fields and intensity of clock laser beam with 200 ms interrogation time. a) Higher magnetic field and clock laser beam intensity (FWHM = 42 (1) Hz), b) lower magnetic field and clock laser beam intensity (FWHM = 3 (1) Hz). RF power on the DDS applied on the AOM 16 (Figure 6.10) is used to control the intensity of the clock laser beam. The measurement has been repeated only once.

beam. FWHM is achieved with 3 (1) Hz.

Figure 6.31 shows Sr atoms in the ground state (Photo 0 on the left) and excited state (Photo 1 on the right) after interrogation. Figure a is when most of the Sr atoms are in the ground state while the clock frequency is off-resonance, but Figure b is when the frequency is in resonance with more Sr atoms in the excited state. Almost 50 percent of

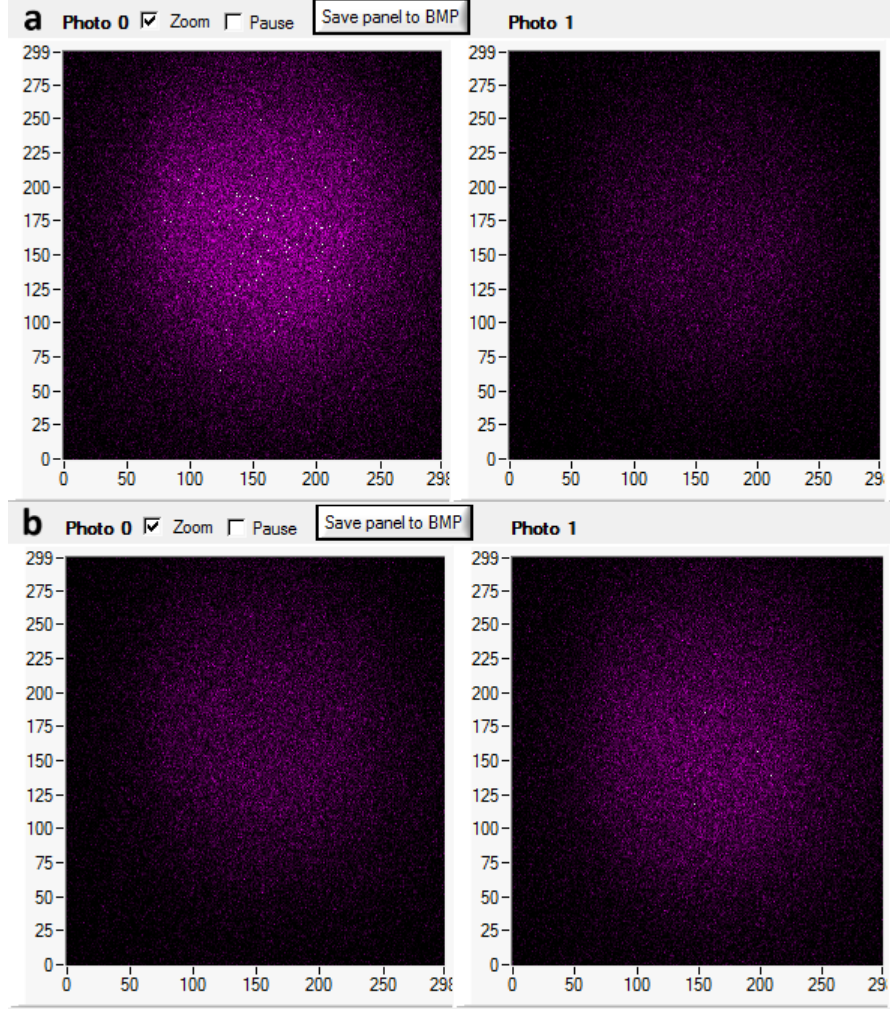


Figure 6.31: Sr atoms in the ground state (Photo 0 on the left) and excited state (Photo 1 on the right) after interrogation. a) The clock laser frequency is off-resonance, and b) the clock laser frequency is on resonance.

the atoms are excited, and 50 percent are in the ground state due to the long interrogation time. This is explained and plotted in the following section.

#### 6.4.4 Rabi oscillation

Figure 6.32 presents Rabi oscillations for two different radial temperatures and longitudinal frequencies. Before measuring each Rabi oscillation, sideband spectroscopy is done, and Equation 2.38 is fitted to the measured data. Therefore, for Figure 6.32 a,  $T_r$  is achieved with  $5.9 (1.0) \mu\text{K}$  and  $\nu_z = 66.7 (1.0) \text{ kHz}$ . In the other side, for Figure 6.32 b,  $T_r$  is  $4.2 (2.4) \mu\text{K}$  and  $\nu_z$  is achieved with  $58.2 (2.4) \text{ kHz}$ . After measuring radial temperature and longitudinal frequency by studying the shape of sidebands, the Rabi oscillation is measured by calculating the excitation fraction on resonance frequency for different interrogation times from zero to 300 and 250 ms. The Equation 2.52 is fitted to measured data. Rabi frequency is achieved at 106 Hz (59 (1) ms) for Figure a and 109 Hz (58 (2) ms) for Figure b.

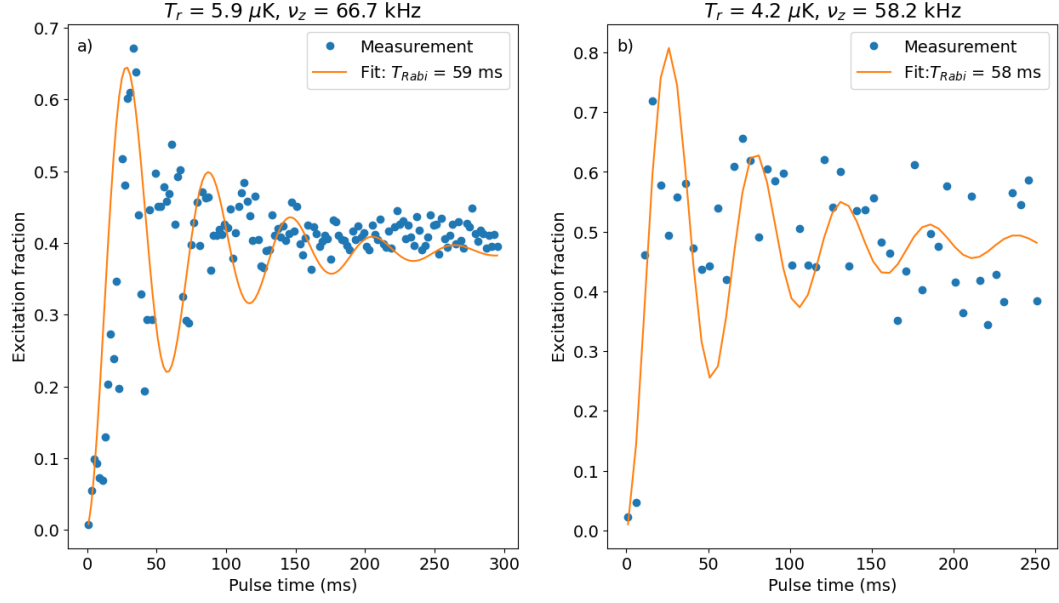


Figure 6.32: a) Rabi oscillations with the radial temperature of  $5.9 \mu\text{K}$  and longitudinal frequency  $66.7 \text{ kHz}$ . The Rabi oscillation is achieved at  $59 (1) \text{ ms}$ . b) Rabi oscillations with the radial temperature of  $4.2 \mu\text{K}$  and longitudinal frequency  $58.2 \text{ kHz}$ . The Rabi oscillation is achieved at  $58 (2) \text{ ms}$ . The measurement has been repeated only once.

## 6.5 Evaluation of systematic shifts

In this section, the shifts of clock transition due to the magnetic fields and clock laser beam for interrogation with trapped Sr atoms are characterized. These two shifts are the most dominant perturbation in the accuracy budget of the optical clocks.

### 6.5.1 Zeeman shift

The Zeeman shift is characterized by applying different voltages on the current driver (corresponding to the current in the coils) from  $0.1 \text{ V}$  to  $1.5 \text{ V}$ . Then, the clock line is found by scanning the frequency of the clock laser beam for each voltage. Figure 6.33 presents the frequency shift of the measured  $^1S_0 - ^3P_0$  clock transition relative to the frequency at zero magnetic fields, as a function of the magnetic field strength, which is proportional to the voltage applied to the coils. A parabola  $\Delta_B^{(2)} = a + cB^2$  function has been fitted to the measured data, and the crossing point  $a$  is achieved at  $19.0 (1.0) \times 10^{-6} \text{ Hz}$  and  $c$  is  $1097.1 (1.5) \text{ Hz/V}^2$ . The clock normally works with a magnetic field magnitude corresponding to  $0.3 \text{ V}$  on the driver, which causes a  $98.7 \text{ Hz}$  shift or uncertainty in the measurement.

### 6.5.2 Probe light shift

The probe light shift is characterized similarly by applying different clock laser powers using AOM 16 (Figure 6.10). Then, the clock line is found by scanning the frequency of the clock laser beam for each probe light power. Figure 6.34 presents the frequency shift of the clock line frequency of  $^1S_0 - ^3P_0$  relative to the frequency at zero probe beam power. A linear function is fitted to measured data, and the frequency shift in normal

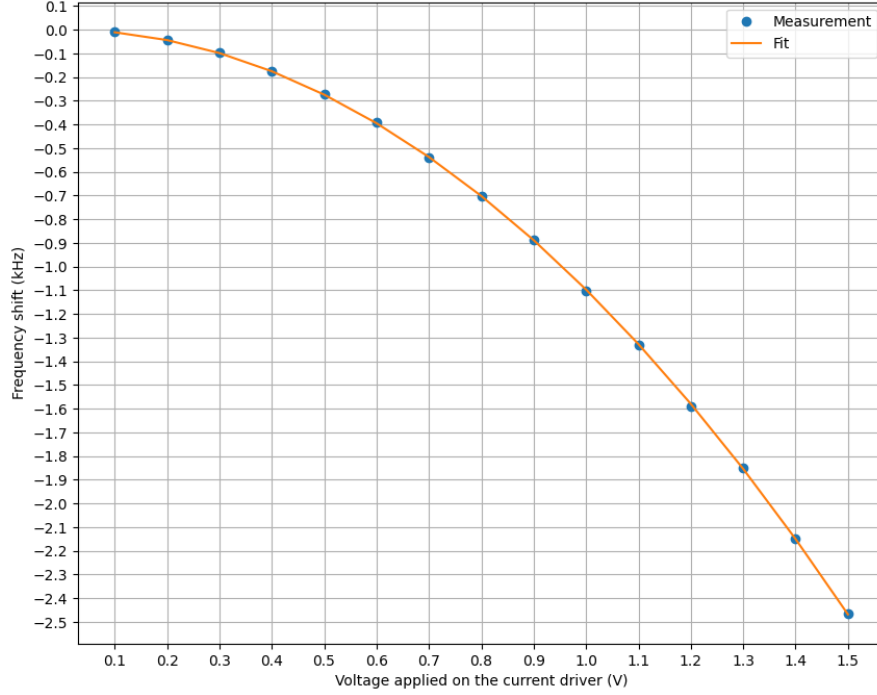


Figure 6.33: Quadratic Zeeman shift for different voltages on the current driver (corresponding to the current in the coils). A parabola  $\Delta_B^{(2)} = a + cB^2$  function has been fitted to the measured data. The measurement has been repeated only once.

working conditions of the clock, which is probe beam power of 0.0658 mW, is equal to 0.3 (0.5) Hz. However, this shift is influenced by cavity drifts, measured at 0.1 Hz per minute, as not all the measurements are conducted simultaneously.

## 6.6 Campaign's comparison

In the end, the stability of the atom-cavity is presented to compare between campaigns 2015 and 2022. My colleagues performed the clock measurement during both campaigns. However, the automatic system for rellocking the lasers and the automatic system for compensation coils and DDS, which I have developed, were used during the 2022 campaign.

The measurement was conducted such that the frequency difference between the clock and the ultra-stable cavity was measured after each cycle of the clock. This difference was corrected using AOM 16 (Figure 6.10). The Allan deviation is calculated based on the frequency applied to AOM 16.

Figure 6.35 shows the Allan deviation of the frequency difference between the Sr1 clock and the ultra-stable cavity. In short-term stability, the result for campaign 2015 is lower, which might be due to a slower filter applied to the correction. We cannot compare the two campaigns in the short-term as different gains were probably applied.

Table 6.2 presents an uptime comparison between two campaigns, 2015 and 2022. In summary, the clock could work 8 days, 14 hours, and 29 minutes during the 2015 campaign. During this time, only 27.85% of the time clock could actively work, equal to 2 days, 9 hours, and 30 minutes. Almost during all the active time, the clock was up



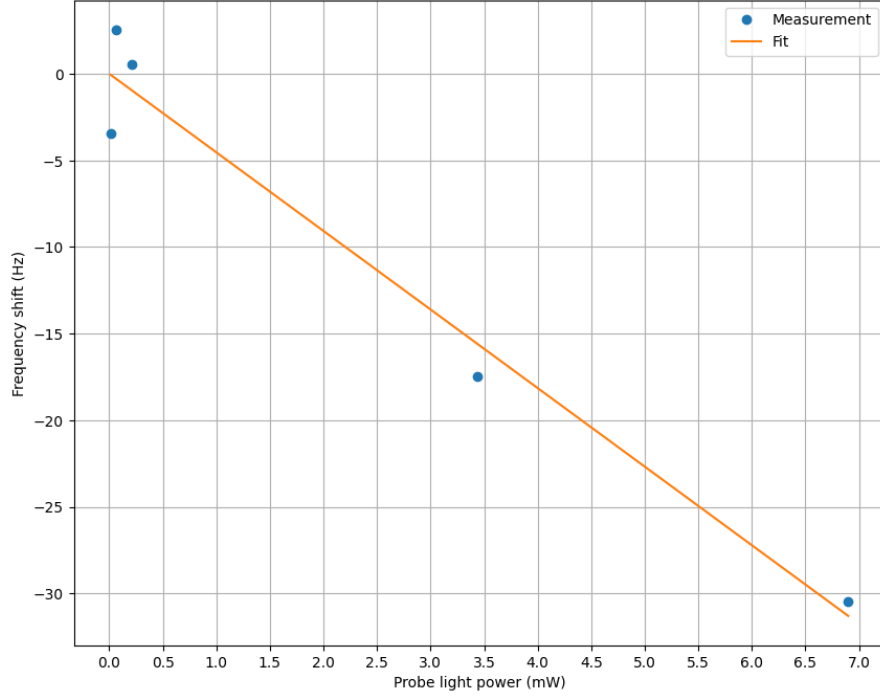


Figure 6.34: Probe light shift for different probe light powers using the AOM 16 (Figure 6.10). A linear function has been fitted to the measured data. The measurement has been repeated only once.

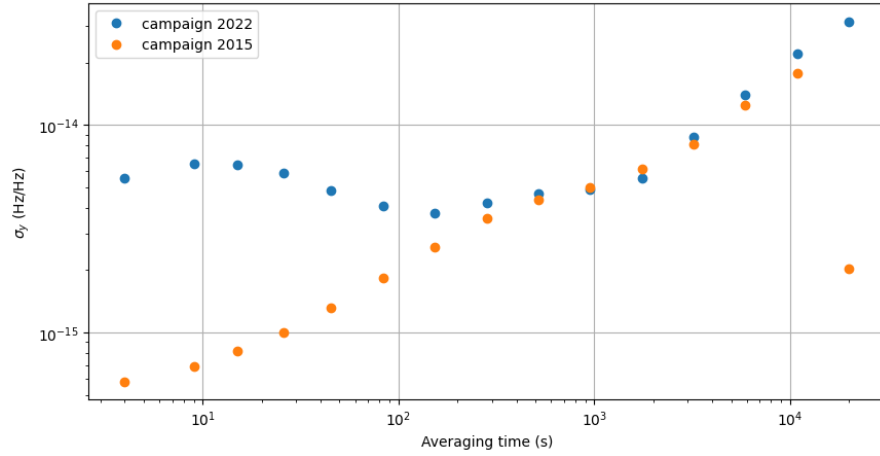


Figure 6.35: Comparing atom-cavity's stability during campaigns 2015 and 2022. The graph shows the Allan deviation of the frequency difference between the Sr1 clock and the ultra-stable cavity.

(measuring data without failure) by 99.74%. The longest uptime during the active time was equal to 1 day, 1 hour, and 53 minutes. Only 12 times the clock was down during active time.

On the other hand, during campaign 2022, the clock could work 29 days, 10 hours, and 59 minutes. The clock was actively working 59.98% of the time, equal to 17 days, 16 hours, and 4 minutes. During this time, the clock was up by 83.35%, and the longest uptime for this campaign reached 1 day, 11 hours, and 52 minutes. The clock was down

Table 6.2: Uptime comparison between campaigns 2015 and 2022.

Metric	Campaign 2015	Campaign 2022
<b>Campaign's time span</b>	8 days, 14 hours, 29 minutes	29 days, 10 hours, 59 minutes
<b>Active working time</b>	2 days, 9 hours, 30 minutes	17 days, 16 hours, 4 minutes
<b>Active working time ratio (%)</b>	27.85	59.98
<b>Uptime</b>	2 days, 9 hours, 21 minutes	14 days, 17 hours, 28 minutes
<b>Uptime ratio (%)</b>	99.74	83.35
<b>Longest Uptime</b>	1 day, 1 hour, 53 minutes	1 day, 11 hours, 52 minutes
<b>Number of Downtime</b>	12	12,766

12,766 times during active time.

During the 2015 campaign, many operators tried to keep the clock working, which is why the clock had high uptime and was only 12 times down, but on the other side, it had a short active working time. During campaign 2022, the clock was working mostly automatically. The uptime is low compared to 2015, but it has higher working active time. During campaign 2022, the first version of the automatic system for relocking the lasers was used.





# Chapter 7

## Optical tweezers machine

This chapter is about an optical tweezers machine in which the auto relocking program described in Chapter 5 is implemented to make the system automatic and robust for easily performing the Rydberg spectroscopy. Auto relocking is used for the Rydberg laser in the optical tweezers machine project at the University of Amsterdam in the Strontium Quantum Gas Group. Optical tweezers machine is used for quantum computing and simulation based on Sr atoms with Rydberg laser. This project has been described very briefly here; for more details, refer to [36, 40].

### 7.1 Introduction

Optical tweezers are a powerful tool for quantum applications such as quantum simulations and computation [98, 99] with alkaline-earth(-like) atoms like Sr, used in this project. In this project, a narrow transition of  $^1S_0 - ^3P_1$  is used for imaging and cooling with the Sisyphus cooling process to detect the scattered photons [100]. A laser tweezer with an 813 nm wavelength has been used, which is the magic wavelength for clock  $^1S_0 - ^3P_0$  transition but non-magic for imaging transition. Decreasing the power required for each tweezer increases the number of tweezers, which will help to have more single atoms [101]. Each single atom is trapped in one tweezer.

The tweezer laser has been modulated by a spatial light modulator (SLM) to create an array of tweezers for trapping a single Sr atom in each tweezer. The distance between each tweezer is around  $8 \mu m$ . After cooling the Sr atoms and trapping them in an array of 36 tweezers, a fluorescence image will be taken, processed, and analyzed to identify which tweezers contain Sr atoms as shown in Figure 7.1. A photon count detection threshold distinguishes between empty tweezers and tweezers with atoms. Figure 7.2 presents a histogram of the number of collected photons in a tweezer region of interest (ROI). Two peaks are visible, one at the beginning, which corresponds to empty tweezers, and the other in the middle, which corresponds to a single atom in tweezers. A vertical line around 6000 is a detection threshold, and as a standard procedure [100, 102], if the photon count is above the detection threshold, there is an atom in that tweezer. Sometimes, there is a wrong detection result due to scattering very few photons, despite an atom being present in the tweezer or vice versa, and it is defined by detection fidelity, which is the probability of the detection being correct.

Generally, a Rydberg state is defined by a high principal quantum number  $n$  in the electronic structure, as shown in Figure 7.3. These states usually have significant en-

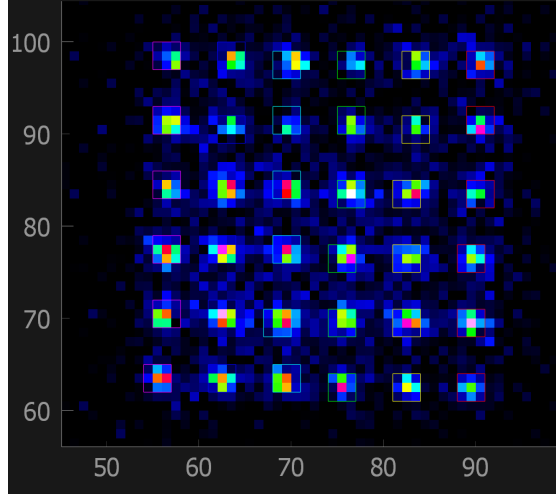


Figure 7.1: Fluorescence image taken from an array of single Sr atoms trapped in tweezers.

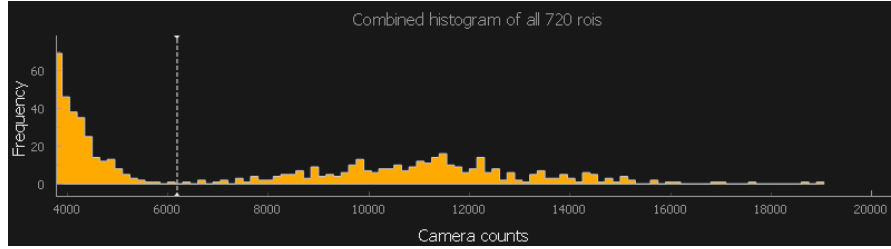


Figure 7.2: Histogram of the number of collected photons in the tweezer ROI.

ergy, so the direct transition from the ground state requires a very short wavelength of ultraviolet lasers. For the Sr in this project, atoms are excited to  $^3P_0$  state as it has a long lifetime and will be considered a ground state for the Rydberg transition for the  $n$  in the range of 40 to 80. Therefore, the atoms are first excited to  $^3P_1$  state from  $^1S_0$  state; then it will be excited to  $5sns\ ^3S_1$  state, and from there, the atoms de-excite to  $^3P_0$  state (Figure 7.3).

## 7.2 Experimental setup

The Auto relocking algorithm developed and explained in Chapter 5 has been tested for the Rydberg laser in the optical tweezers machine. However, in this experiment, the algorithm was developed on a web application for the Red Pitaya board. The Red Pitaya is an open-source platform and control device that replaces bulky and expensive instruments such as oscilloscopes, function generators, etc. In this section, the software and electronics schematic diagram for this experiment has been described.

### 7.2.1 Schematic diagram

Figure 7.4 presents a schematic diagram for auto relocking the Rydberg laser in an optical tweezers machine project. There are two ECDLs used in this project; one is 1070 nm, and the second one is 1550 nm, which are driven by a laser driver from Toptica company. Both laser beams are amplified with fiber amplifiers to raise the intensity to

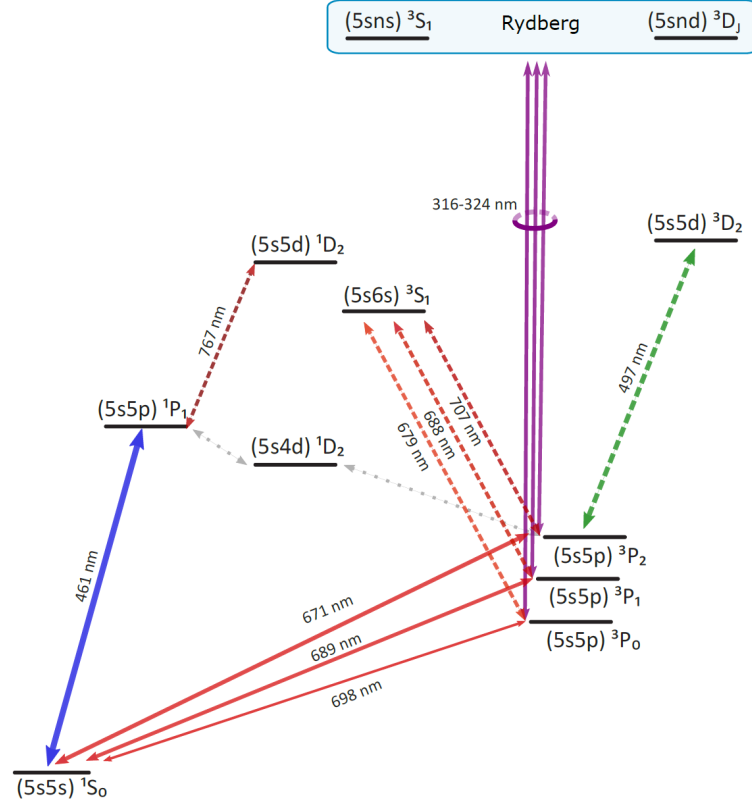


Figure 7.3: Energy level diagram of bosonic strontium, which is important for optical tweezers machine. Taken from [36].

more than watts and sent to the sum frequency generation (SFG) to produce a red light at 633 nm. Part of the red light goes to the second harmonic generation (SHG) to produce an ultraviolet (UV) beam at 316.5 nm, which will be used in the experiment to interact with trapped Sr atoms for Rydberg spectroscopy. Some parts of the red laser are going to the transfer cavity for locking the laser by the PDH method. The transfer cavity is locked to a stable 689 nm laser by the PDH method with a DigiLock controller from Toptica. Therefore, the frequency stability of 689 nm laser is transferred to 633 nm laser by this transfer cavity. To monitor the frequency of 633 nm, part of the beam is sent to the HighFinnese wavemeter.

When the 633 nm laser is locked to the cavity, part of the light is transmitted and is detected by a photodiode (PD) and camera for monitoring. The PD signal is amplified and goes to the input 1 of the Red Pitaya to be processed and monitored. Red Pitaya gets information on the wavemeter and DigiLock from the server running on the PC on which the wavemeter is installed. After processing information on the Red Pitaya, appropriate feedback is sent to the piezo and current controller of the 1550 nm from output #1 and #2, respectively.

In this project, instead of using a NI-DAQ card to measure a transmission signal from the cavity, send feedback to the laser drivers and use a computer to run the auto relocking program, a Red Pitaya board has been used to do all these tasks in one place. Red Pitaya is a multi-functional equipment-based and low-cost electronic board with several components such as a RAM CPU with two cores, fast ADCs, fast DACs, USB,

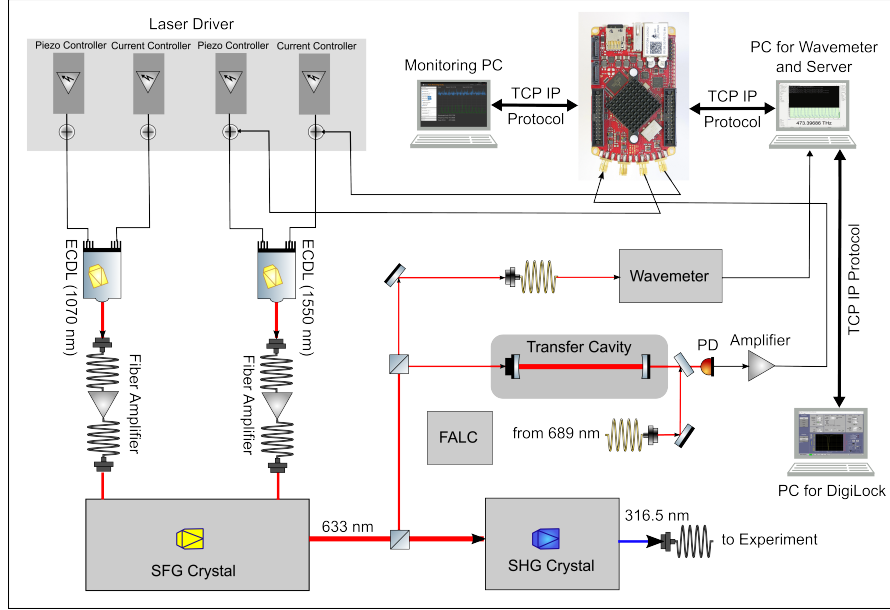


Figure 7.4: Schematic diagram of the auto relocking system for the Rydberg laser [103].

LAN, and the most crucial thing is programmable logic or field programmable gate array (FPGA). The on-chip FPGA allows Red Pitaya for high-performance computing, cutting-edge measurement systems, signal processing, and other applications, including the auto relocking of the ECDLs developed in this project.

Auto relocking of the ECDL by Red Pitaya is limited to only one laser for each Red Pitaya board as the number of input and output ports is limited.

### 7.2.2 Setup

The laser driver and the Red Pitaya board are shown in Figure 7.5. The Red Pitaya board is installed on an amplifier board, providing a power supply for the Red Pitaya. PD signal is connected to the amplifier, which amplifies the signal 25 times, then goes to the input #1 of the Red Pitaya. Output #1 is dedicated to sending the feedback to the piezo controller, and output #2 is dedicated to the current controller. However, in this project, the feedback is sent only to the piezo as the laser is a single mode for the long range of the frequency. Input #2 is dedicated to monitoring any other signal if needed. All the laser drivers for driving the 1070 nm and 1550 nm ECDLs and the feedback controller for DigiLock and FALC are installed in one rack system. The DigiLock (digital laser-locking) and FALC (fast analog linewidth control) are two different modules for laser locking and frequency stabilization.

Optical setup and schematic diagram for the transfer cavity to lock the cavity and 633 nm laser by PDH method are presented in Figure 7.6 and 7.7. In this setup, a 689 nm laser beam is injected from one side, and 633 nm from SFG is injected from another side of the optical cavity. The transmitted signal due to 633 nm is monitored by a PD and sent to the Red Pitaya, and a camera is placed to find the laser beam's  $TEM_{00}$  mode.

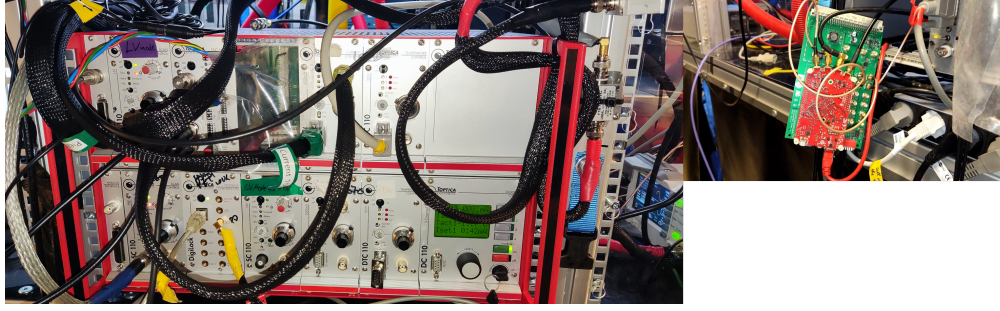


Figure 7.5: Experimental setup for the laser driver on the right and the Red Pitaya on the left.

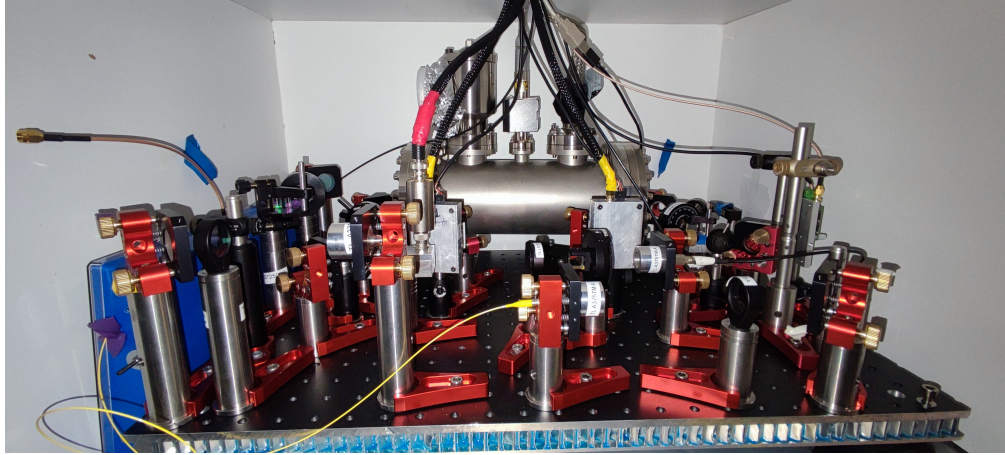


Figure 7.6: Optical setup for the transfer cavity to lock the cavity and 633 nm laser by PDH method.

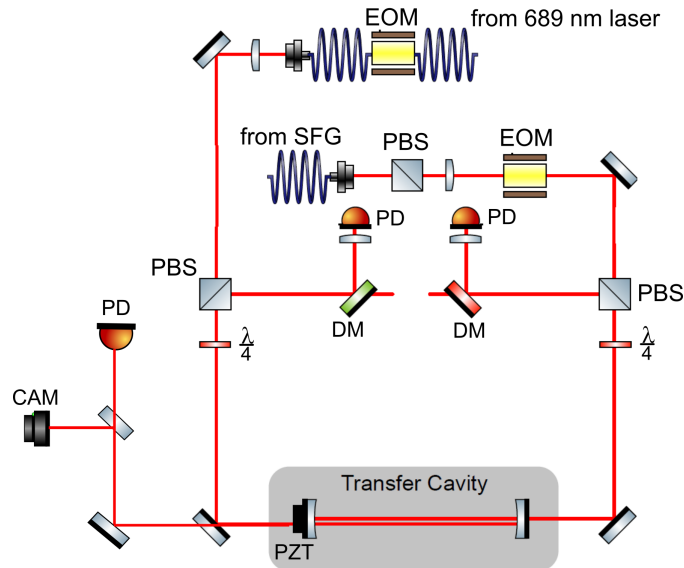


Figure 7.7: Schematic diagram for the transfer cavity to lock the cavity and 633 nm laser by PDH method. Abbreviations: PBS- polarising beam splitter, EOM- electro-optic modulator, PD- photodetector,  $\frac{\lambda}{4}$ - quarterwave plate, DM- dichroic mirror, CAM- camera. Taken and modified from [37].

## 7.3 Web application for auto relocking

Before running the web application, the transfer cavity should be locked to the 689 nm laser using the DigiLock controller. A separate auto relocking program for DigiLock has been developed for this purpose and is implemented in the server program of the wavemeter software [104]. Therefore, the server program monitors and controls the wavemeter software and DigiLock program simultaneously. The auto relocking program for DigiLock is controlled through the web application.

Figure 7.8 shows the developed web application running on the Red Pitaya. Both detection signals, including the interferometer pattern from the wavemeter and cavity transmission, are shown. Figure 7.9 presents a whole view of the system while the auto relocking program is working. The camera on the top right shows the cavity transmission mode. A complete instruction for this web application is described in Appendix D. For more information, instructions, and the source code of the web application, refer to [105].

## 7.4 Red laser lock

In this section, the transfer cavity has been characterized, and the linewidth of the 633 nm laser is measured while the laser is locked.

### 7.4.1 Cavity characterization

The error signal produced by FALC should be recorded to measure the cavity mode linewidth. The 633 nm laser beam has been modulated by a 6.1 MHz RF signal, which is in the bandwidth of FALC, and the cavity has an FSR of 1.5 GHz. Figure 7.10 presents the measured error signal and fitted Equation 1.6 to the measured error signal. The time

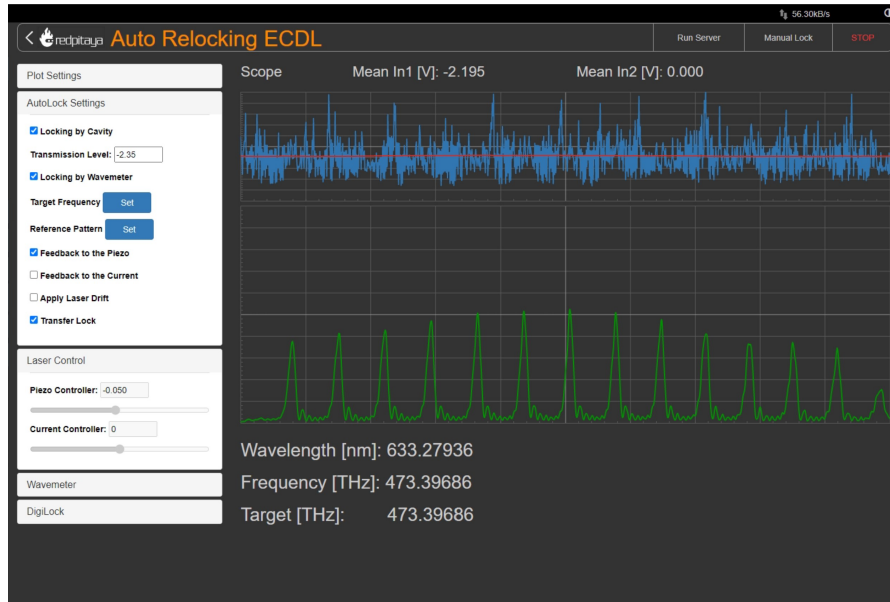


Figure 7.8: Developed web application on Red Pitaya for auto relocking of the Rydberg laser.



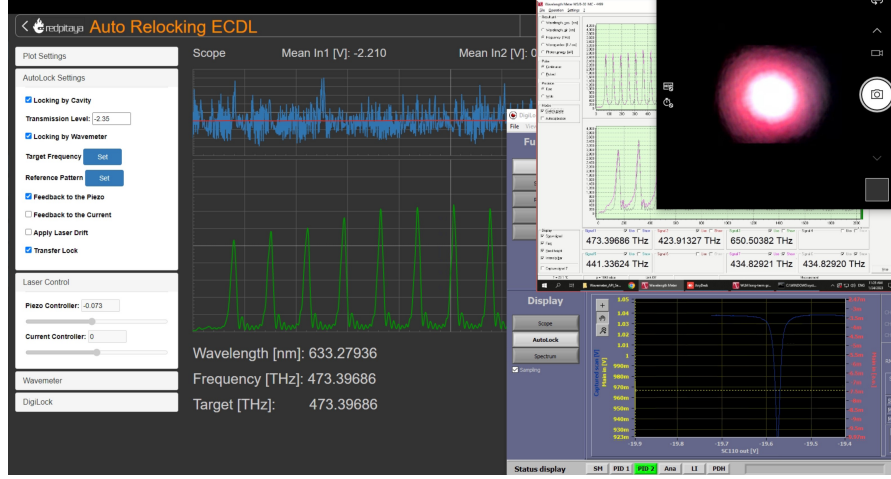


Figure 7.9: Web application and monitoring system for Relocking Rydberg laser and transfer lock cavity [103].

series of the measured data has been converted to the frequency regarding the modulation frequency. The finesse of the cavity will be estimated by Equation 7.1 [7] after estimating the reflectivity  $r$  by fitting the Equation 1.6 to the measured error signal, and then the cavity linewidth will be calculated by Equation 7.2.

$$finesse \approx \frac{\pi}{1 - r^2}, \quad (7.1)$$

$$\Gamma_{cav} = \frac{FSR}{finesse}. \quad (7.2)$$

Figure 7.11 shows the average cavity linewidth equal to 17.3 (3.1) kHz after measuring many times of the error signal.

## 7.4.2 Laser linewidth

After measuring the error signal, the laser frequency will be locked to the cavity mode. There is a simple method to measure the linewidth of the laser by analyzing a time trace of the error signal. The error signal is a deviation of the instantaneous frequency concerning the reference frequency. By the following method, the standard deviation of the frequency deviation from the locking point is calculated. This method assumes that there is a Gaussian distribution of the instantaneous frequency deviations around the locking point, and the FWHM of this distribution is determined as laser linewidth. The error signal amplitude should be related to the frequency to calculate the distribution.

This relation can be extracted from the linear slope fit of the PDH signal around the locking point as presented in Figure 7.12. The slope achieved for this error signal is  $-5.8(2.4)e^{-5}V/Hz$ . Therefore, the amplitude of the error signal can be calibrated into frequency with this slope. Figure 7.13 presents the frequency deviation of the error signal in time series. FWHM, which is achieved for this error signal, is 0.37 (0.26) kHz. After measuring the error signal while the laser is locked, the averaged laser linewidth is presented in Figure 7.14 and equals 1.1 (0.4) kHz.



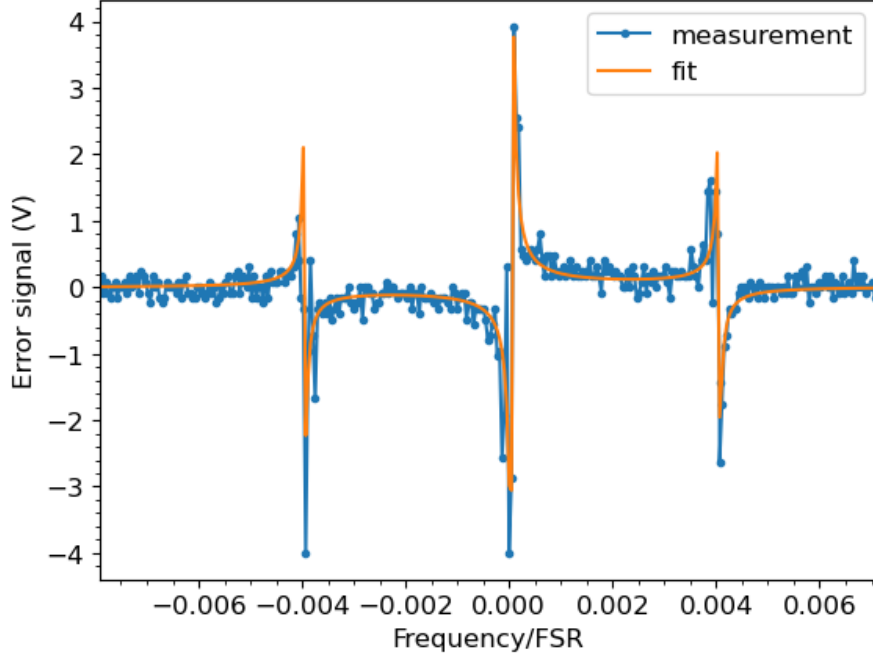


Figure 7.10: The error signal described by equation 1.6 is fitted to the measured data.

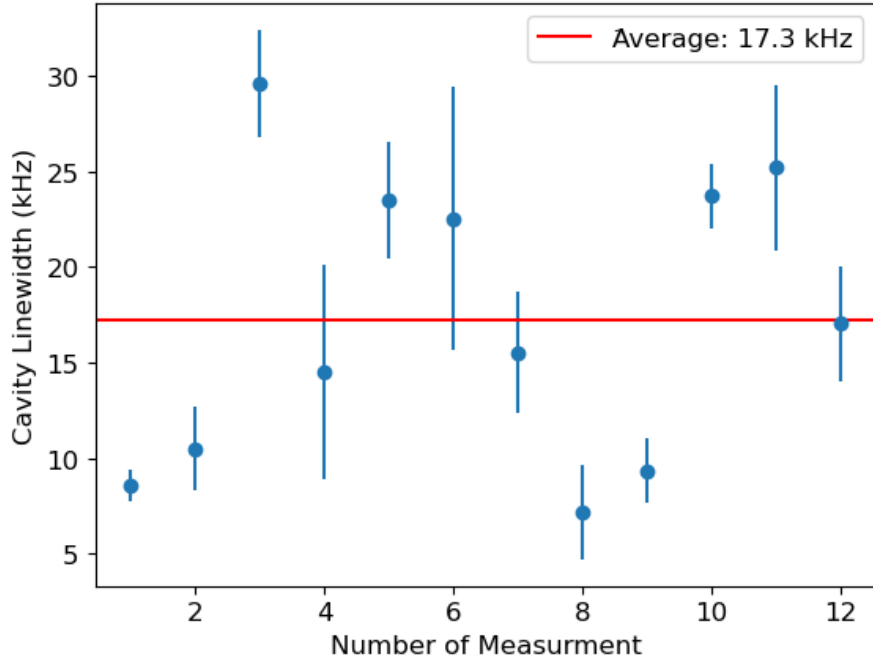


Figure 7.11: Averaged cavity linewidth after many times measuring the error signal.

## 7.5 Rydberg spectroscopy

After locking the 633 nm laser, Sr atoms were loaded into a tweezers array for Rydberg spectroscopy on  $5s5p\ ^3P_0$  to  $5sns\ ^3S_1$  transition. In this spectroscopy,  $n = 61$  for the Rydberg state; however, it can be in the range of 40 to 80. For  $n = 61$ , the UV frequency must be set to 946.794120 THz or 316.6395435578 nm of wavelength. Figure

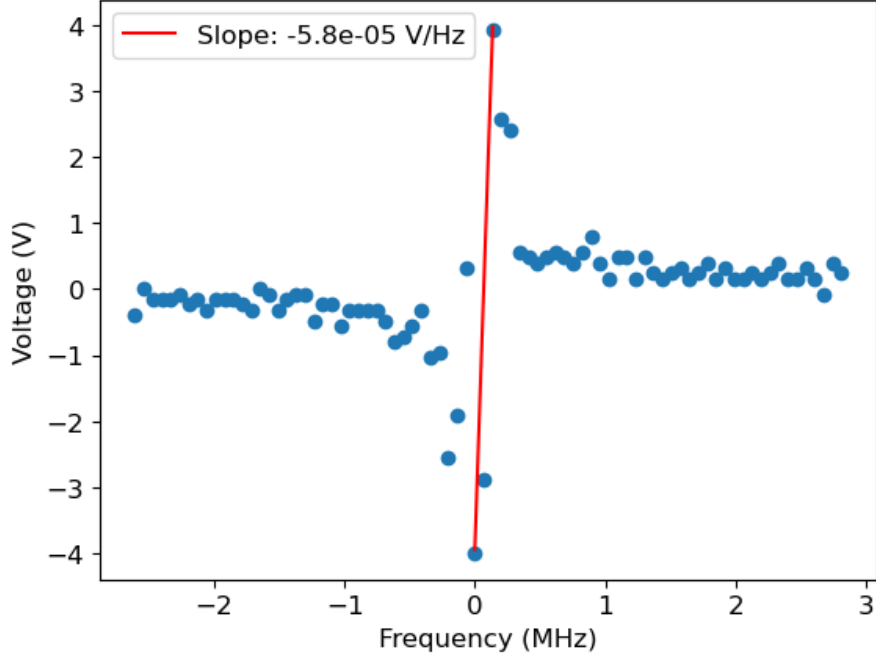


Figure 7.12: The linear fit around the locking point of the error signal.

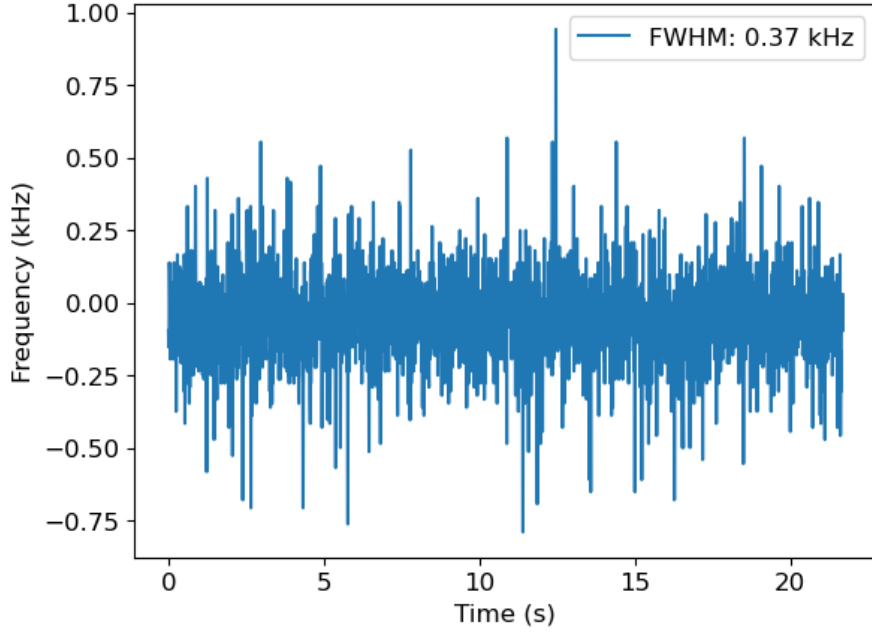


Figure 7.13: Frequency deviation of the error signal time series.

7.15 presents the measured spectroscopy with maximum intensity (on 100 percent RF power of AOM) of the UV light equal to 11.5 mW and 500  $\mu$ s duration of UV light. The population or survival of the remaining atoms on the  $^3P_0$  state is calculated using fluorescence images. The valley in the graph shows how many percent of the atoms survived during interrogation, and the rest are excited to 5s61s  $^3S_1$  state.

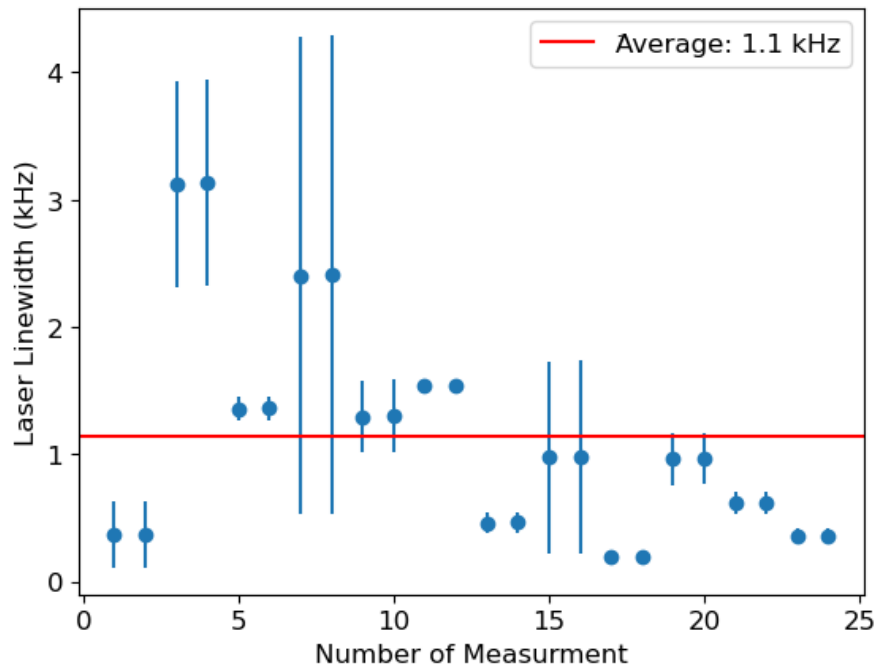


Figure 7.14: Laser linewidth, after measuring many times the error signal.

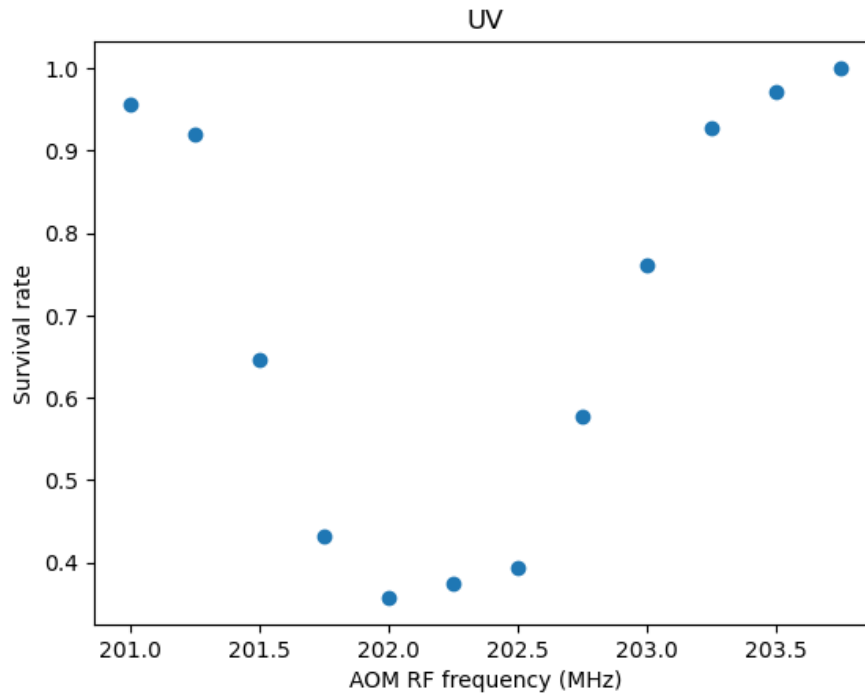


Figure 7.15: Rydberg spectroscopy with 100 percent power of the UV laser and  $500 \mu s$  duration of UV light. The measurement has been repeated only once.



# Summary and conclusions

In this thesis, I presented my works in optical atomic clocks and tweezers machine in the KL FAMO group at Nicolaus Copernicus University in Torun and in the Strontium quantum gas group at the University of Amsterdam in Amsterdam, respectively. The automation system has been developed and tested successfully to make these complicated experiments more robust and easy to operate.

Three main projects along the automation have been developed and implemented in optical atomic clocks in the KL FAMO group, which have been described in Chapters 3, 4, and 5. As explained and presented by the results, the optical atomic clock became much more robust and easy to operate, at least for most parts, even remotely. By auto relocking programs, lasers are kept locked for a long time, like a few weeks, as reported here.

Chapter 6 describes a general road map for optimizing the optical atomic clock. Clock spectroscopy was performed to measure the temperature of the Sr atoms, and the systematic shift was evaluated. Also, the cavity's stability was measured during campaign 2022 and has been compared with campaign 2015. Additionally, the program and experiment have been designed to study the effect of magic-zero wavelength on the trapped Sr atoms in the lattice. Sideband spectroscopy is performed on the excited atoms  $^3P_0$ , and their temperature has been measured. As expected, the red sideband became more significant than the blue sideband in this situation.

Chapter 7 was the project of auto relocking the ECDL in the strontium optical tweezer machine for quantum computing and simulation in Amsterdam. As presented, this algorithm can work with different lasers for different cold atom experiments. In the end, cavity and laser characterization were measured. Rydberg spectroscopy was performed with  $n = 61$  levels of strontium atoms to ensure the experiment worked more robustly after implementing the auto relocking system.



---

# Appendix A

## Instruction to work with automated control system for magnetic field

The software which is developed on the microcontroller is easy to use. The operator can communicate a few commands with the magnetic field controller device. To get help or close the connection, use the commands below, write the command, and send it to the server by applying the enter key.

```
help
exit
```

For pre-programming memory the format of the command used is:

```
< parameter address >: < value1 >; < value2 >; < value3 >; < time >
```

Where “parameter address” chooses the logical address in the memory, “valueX” is the preset current value ranging from -2.5 to 2.5 v. This value is limited due to the voltage reference of DAC8560, which is set at 2.5 v. Moreover, “time” is the length of a linear ramp in ms, and a value of 1 means the fastest possible switching.

Multiple parameters may be set with a single command by separating them with an “&” sign:

```
< parameter address >: < value1 >; < value2 >; < value3 >; < time >;
& < address >: < value1 >; < value2 >; < value3 >; < time >; & ...
```

The table A.1 shows the most commonly used parameters and their respective addresses. For instance, the command to pre-program the initial two memory values would be:

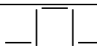

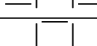
```
DAC: 000: -1.25684; 0.5; 0.0; 1; & 001: 0.52; -2.1; -1.0; 50;
```

Switching to the first memory level (000) takes 1 ms, while switching to the second (001) uses a 50 ms long linear ramp. As mentioned in Chapter 3, in the current version of the software, switching between pre-programmed values is made by 4 TTL signals, which can be easily expanded to use all six available TTL inputs. Three TTL signals address the required memory, and 1 TTL is a set/clock signal that triggers switching outputs to the new memory levels. TTL 1 is the least significant, and TTL 3 is the most significant.

Table A.1: The most common parameters and addresses.

Parameters	Comment
DAC: 000	Set values for memory 1
DAC: 001	Set values for memory 2
DAC: 010	Set values for memory 3
000	Address of memory 1
001	Address of memory 2
010	Address of memory 3

Table A.2: The pattern directs the controller output to the pre-programmed value.

Address	TTL1	TTL2	TTL3	TTL4
000	0	0	0	—   —
001	1	0	0	—   —
010	0	1	0	—   —

The following pattern in Table A.2 switches the controller output to the pre-programmed value stored in the memory address.

For example, Figure A.1 shows how to apply a state (in this case, state one by address 001) by the real-time program on the coils. A real-time program commands the microcontroller to apply values registered on memory for state one on coils every time by TTL4 in each cycle. To change the registered values on the memory by this program (not connecting through Putty or any other program), add this code to this program at the beginning and set your specific values or start scanning one of them to find the optimal value for the experiment to see the result of this check out on chapter 6.

```
#CDC DAC: 000: 1.0; -1.5; 0.0; 20; & 001: -2.0; 1.0; -2.0; 4;
& 010: -1.5; 1.5; -1.0; 10
```



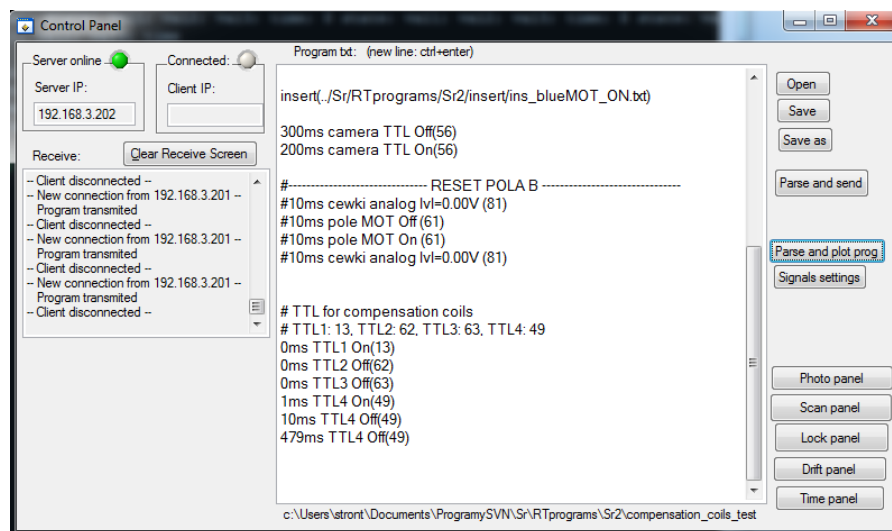


Figure A.1: Applying state 1 (001) to the coils through the real-time program.

---

## Appendix B

# Registering and instruction to work with DDS

Part of the code for registering a new frequency value using SPI communication is written here:

```
// language = C
char spi_addr[20];

const uint16_t FTW_Addr6 = 0x01A6;
const uint16_t FTW_Addr7 = 0x01A7;
const uint16_t FTW_Addr8 = 0x01A8;
const uint16_t FTW_Addr9 = 0x01A9;
const uint16_t FTW_AddrA = 0x01AA;
const uint16_t FTW_AddrB = 0x01AB;
double f_s = 1000.0;    // MHz of sysclk

void send_freq(double fdds)
{
    uint64_t ftw;
    uint8_t value;

    if(fdds > 400.0){
        fdds = 400.0;
    }

    ftw = round((fdds/f_s) * pow(2, 48));

    spi_addr[0] = ((uint8_t*)&FTW_Addr6)[1];
    spi_addr[1] = ((uint8_t*)&FTW_Addr6)[0];
    HAL_GPIO_WritePin(CS_GPIO_Port, CS_Pin, GPIO_PIN_RESET);
    HAL_SPI_Transmit(&hspi4, (uint8_t *)&spi_addr, 2, 100);
    value = ((uint8_t *)&ftw)[0];
    HAL_SPI_Transmit(&hspi4, ((uint8_t *)&value), 1, 100);

    spi_addr[0] = ((uint8_t*)&FTW_Addr7)[1];
    spi_addr[1] = ((uint8_t*)&FTW_Addr7)[0];
```

---

```

    HAL_SPI_Transmit(&hspi4, (uint8_t *)&spi_addr, 2, 100);
    value = ((uint8_t *)&ftw)[1];
    HAL_SPI_Transmit(&hspi4, ((uint8_t *)&value), 1, 100);

    spi_addr[0] = ((uint8_t *)&FTW_Addr8)[1];
    spi_addr[1] = ((uint8_t *)&FTW_Addr8)[0];
    HAL_SPI_Transmit(&hspi4, (uint8_t *)&spi_addr, 2, 100);
    value = ((uint8_t *)&ftw)[2];
    HAL_SPI_Transmit(&hspi4, ((uint8_t *)&value), 1, 100);

    spi_addr[0] = ((uint8_t *)&FTW_Addr9)[1];
    spi_addr[1] = ((uint8_t *)&FTW_Addr9)[0];
    HAL_SPI_Transmit(&hspi4, (uint8_t *)&spi_addr, 2, 100);
    value = ((uint8_t *)&ftw)[3];
    HAL_SPI_Transmit(&hspi4, ((uint8_t *)&value), 1, 100);

    spi_addr[0] = ((uint8_t *)&FTW_AddrA)[1];
    spi_addr[1] = ((uint8_t *)&FTW_AddrA)[0];
    HAL_SPI_Transmit(&hspi4, (uint8_t *)&spi_addr, 2, 100);
    value = ((uint8_t *)&ftw)[4];
    HAL_SPI_Transmit(&hspi4, ((uint8_t *)&value), 1, 100);

    spi_addr[0] = ((uint8_t *)&FTW_AddrB)[1];
    spi_addr[1] = ((uint8_t *)&FTW_AddrB)[0];
    HAL_SPI_Transmit(&hspi4, (uint8_t *)&spi_addr, 2, 100);
    value = ((uint8_t *)&ftw)[5];
    HAL_SPI_Transmit(&hspi4, ((uint8_t *)&value), 1, 100);
    HAL_GPIO_WritePin(CS_GPIO_Port, CS_Pin, GPIO_PIN_SET);

    // Update registers
    HAL_GPIO_WritePin(IO_UPD_GPIO_Port, IO_UPD_Pin,
    GPIO_PIN_SET);
    osDelay(1);
    HAL_GPIO_WritePin(IO_UPD_GPIO_Port, IO_UPD_Pin,
    GPIO_PIN_RESET);
}

```

The AD9912 instruction word and byte data can first be the most significant bit (MSB) or the least significant bit (LSB). The default for the AD9912 is MSB first. When the MSB first mode is active, the instruction and data bytes must be written from MSB to LSB. There are two parts to a communication cycle with the AD9912. The first writes a 16-bit instruction word into the AD9912, coincident with the first 16 SCLK rising edges. The instruction word provides the AD9912 serial control port with information regarding the data transfer, which is the second part of the communication cycle. The instruction word defines whether the upcoming data transfer is a read or a write, the number of bytes in the data transfer, and the starting register address for the first byte of the data transfer. The procedure for writing and updating value on the evaluation board is like this:

1. Reset Chip Select Bar (CSB), Pin 61,

2. Write instruction word (refer to the desired address),
3. Write the data,
4. Repeat procedures 2 and 3 until all the data is transmitted,
5. Set Chip Select Bar (CSB),
6. Update new data by toggling IO\_UPDATE, Pin 60.

The frequency address (FTW) starts from 0x01A6 (the least significant bit) for 48 bits. Each address has 16 bits, and six addresses are to be registered. Instruction word defines the type of communication (read or write), number of data bits to be transmitted each time, and address. All the instructions for the FTW are set for writing and transferring 8-bit data each time.

As the frequency is 48 bits, it needs to be registered in a variable by 64-bit type, which is uint64 here, and transmitted data is 8 bits; therefore, it is registered in 8-bit type, which is uint8 here. The communication type is MSB. Therefore, each 8-bit is transferred from the most significant bit. For example, the address (0x01A6) is 2 bytes. first we need to transfer 01 then A6, therefore ((uint8\_t\*)&FTW\_Addr6)[1] take 01 and put it in spi\_addr[0] and ((uint8\_t\*)&FTW\_Addr6)[0] take A6 and put it in spi\_addr[1]. As it is mentioned, address 0x01A6 for starting of FTW is the LSB; the least significant value of frequency, which is ((uint8\_t \*)&ftw)[0], needs to be registered in this address.

The software developed on the microcontroller is easy to use and similar to the previous one developed for the magnetic field controller. to get help or close the connection, use the commands below, write the command, and send it to the server by applying the enter key.

```
help
exit
```

For sending value, the format of the command used is:

```
< DDS:NAME > < value >
```

Where “DDS:NAME” refers to the variable name, “value” represents a preset value that can vary depending on the chosen NAME. Multiple parameters can be set using a single command by separating them with a semicolon “;” sign:

```
< DDS:NAME > < value >; < NAME > < value >; ...
```

To retrieve the value, minimum, and maximum of each name, use these commands:

```
< DDS:NAME >?
< DDS:NAME > :MIN
< DDS:NAME > :MAX
```

The most common NAMEs are presented in Table B.1.

As an example, the command to set frequency and amplitude value is:

```
DDS:FREQ 120.045; AMP 20.1
```

---

Table B.1: The most common NAMES

<b>NAME</b>	<b>Comment</b>
FREQ	Set output frequency
AMP	Set amplitude of output
REF	Set reference frequency limited by 100, 250, and 1000 MHz

---

## Appendix C

# Step-by-step instructions for auto relocking of the ECDLs by Python

Part of the JSON file is written below:

```
# language = Json
{
    "general": [
        {
            "path": "C:\\Users\\stront\\Mehrdad\\
                AutoRelocking_ECDL_Python",
            "IP": "192.168.3.212",
            "PORT": 5015,
            "WLMPrec": 4
        }
    ],
    "chName": [
        {
            "description": "[name, target frequency,
                PiezoRelockMode (0 or 1),
                CurrentRelockMode (0 or 1),
                update (0 or 1), portNamePiezo,
                portNameCurrent, portNameInput,
                cavityLock, wavemeterLock, laserDrift]"
        },
        {
            "5": [
                "5: Re-Pumper(679)", # optional name
                "441.3327",         # target frequency
                1,                  # send feedback to piezo set on 1
                0,                  # send feedback to current set on 1
                0,                  # update in each cycle set on 1
                "Dev2/ao2",         # port name for piezo
                "Dev2/ao3",         # port name for current
                "",                  # port name for input
                0,                  # for cavity lock set on 1
                1,                  # for wavemeter lock set on 1
                1                    # to apply laser drift set on 1
            ]
        }
    ]
}
```

```

    ],
    },
],
"IParam": [
    {
        "description": "[min, max, last_value ,
                        cur_drift0 , cur_drift1 , drift_no]"
    },
    {
        "5": [
            -1.0,      # minimum scan range value
            1.0,      # maximum scan range value
            0,         # don't change
            0.0,       # don't change
            1.0,       # don't change
            0.0        # don't change
        ],
    }
],
"PztParam": [
    {
        "description": "[min, max, last_value ,
                        piezo_drift0 , piezo_drift1 , t_drift0 ,
                        t_drift1 , drift_no , t1Drift , firstDrift_t]"
    },
    {
        "5": [
            -3.0,      # minimum scan range value
            3.0,      # maximum scan range value
            0,         # don't change
            0.0,       # don't change
            1.0,       # don't change
            0.0,       # don't change
            0.0,       # don't change
            0,         # don't change
            0.0,       # don't change
            60         # don't change
        ],
    }
],
"refDataInfo": [
    {
        "description": "[no peaks diff , freq_diff_thr ,
                        freq_diff_std , transmission level]"
    },
    {
        "5": [
            0,         # don't change
            5e-05,     # frequency threshold
            4e-05,     # reduce frequency threshold

```

---

```

        0          # cavity transmission level
    ],
    }
]
}

```

---

This file has five primary keys, including "general"; the operator should define the path that the main auto relocking program is inside, the IP address, and the server port on which the wavemeter program is running. Moreover, WLMPrec is dependent on the precision of the wavemeter. The one I am testing has four digits precision. The following key is "chName"; you can set all the parameters for each channel. I wrote some comments in front of each line for extra explanation. It is not included in the actual file as the JSON does not support the comment. The next one is "IPParam" which defines the parameters of current relocking. The parameters with the comment "don't change" should not be changed. The program saves these parameters, and when the program stops after a while, the operator should rerun it. The program will read these parameters for extra information and improve the relock. The following key, "PztParam" is used for piezo relocking. The last one is "refDataInfo"; here, you can define the frequency threshold of relocking and an extra parameter to reduce the frequency threshold. This is used when the program is in the relocking mode. At this time, the frequency threshold would be reduced by this parameter to let the auto relocking program set the frequency close to the target.

In this program version, a track of information and data would be saved every five minutes. The first information is the one which is commented by "don't change". The others will be saved as a CSV file in two different files in the data folder of the program's main folder. The format of the name of file for one of them is "chx\_relock\_data\_date.csv" and the other one "chx\_relock\_data\_event\_date.csv", chx is the channel number which that laser beam is connected to the switcher of the wavemeter, and date is current date therefore by starting new day two new files would be created. For example, if the laser beam is connected to channel 5 of the wavemeter, these two files look like this: "5\_relock\_data\_08\_21\_2023.csv" and "5\_relock\_data\_event\_08\_21\_2023.csv". The first file, which has the name "relock\_data", keeps track of the time, frequency, and transmission of that laser whenever the program reads this channel information from the wavemeter and signal from cavity transmission. The second file with the name "relock\_data\_event" is to track auto relocking events at what time the laser got unlocked and how long it took to relock it again.

Before running the main auto relocking program, the server should be run on the system with wavemeter software. Source code is available here [104]. A batch file named 'run\_Server.bat' is in the source code folder. By running this batch file, the server starts running, but before running it, it needs to be modified based on the computer that is going to be run. First, the path of the activate file needs to be set. To find this path, you can go to the directory in which Python is installed. Second is the path of this program. At the end, a command to run the server with defining IP address, port number, dll path of wavemeter, and version number of wavemeter. IP address must be the private IP address of the system, which is accessible by the internal network, and to find it, the operator can run 'ipconfig' in cmd. The port number can be any number the operator can leave as a default, but if any other device uses this port, the operator needs to change it to another number. The dll path of the wavemeter is usually the same, but if it is different



on the system, find that path and paste it here. The last one is the wavemeter version, which depends on the model of the wavemeter the operator is using.

After running the server, if the server starts listening, a message will be printed that the server is listening on this IP address and port number, as shown in Figure C.1. This IP address and port number should be set in the JSON file to let the auto relocking program as a client connect to the server and get information about the wavemeter. In the auto relocking source code folder, there is a batch file to run the program named 'run\_AutoRelocking.bat'. Here, similar to the server program, the operator needs to modify this batch file, but only the activated path and path of the program. After running this batch file, the auto relocking program will start working by checking all the laser frequencies, as shown in Figure C.2. As seen in this figure, to stop the program, the operator needs to write y and enter the program will stop working. Also, a status would be printed to let the operators know. For example, if one of the lasers is in the mode of relocking, a message shows that this laser is relocking; therefore, the wavemeter is locked on that channel. Alternatively, if relocking is not successful, it will written, and that laser will not be checked for relocking after that. The auto relocking program's complete documentation and open-source code are available here [96].

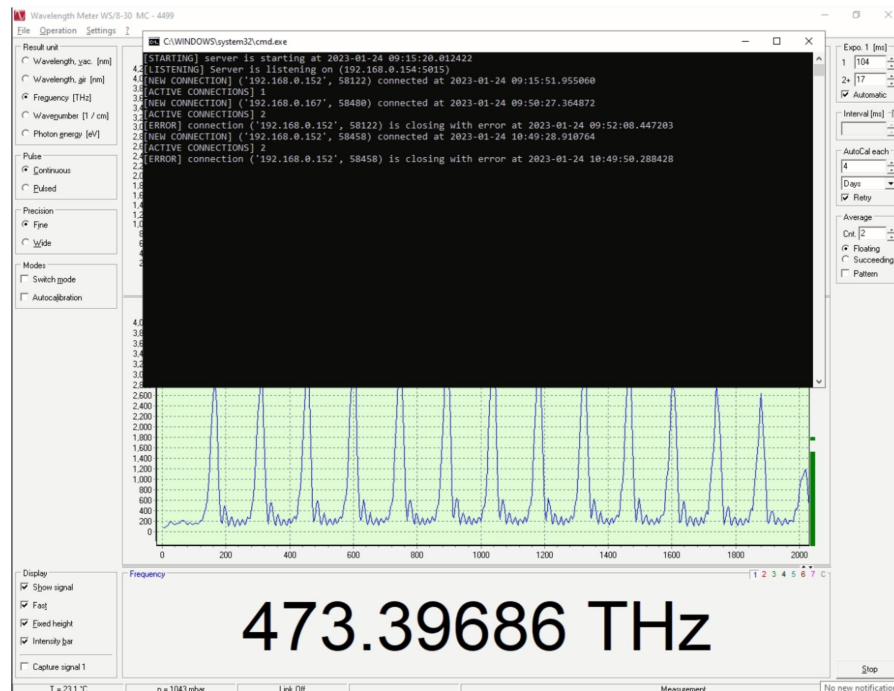


Figure C.1: Server program running on the computer, which the wavemeter is installed on.

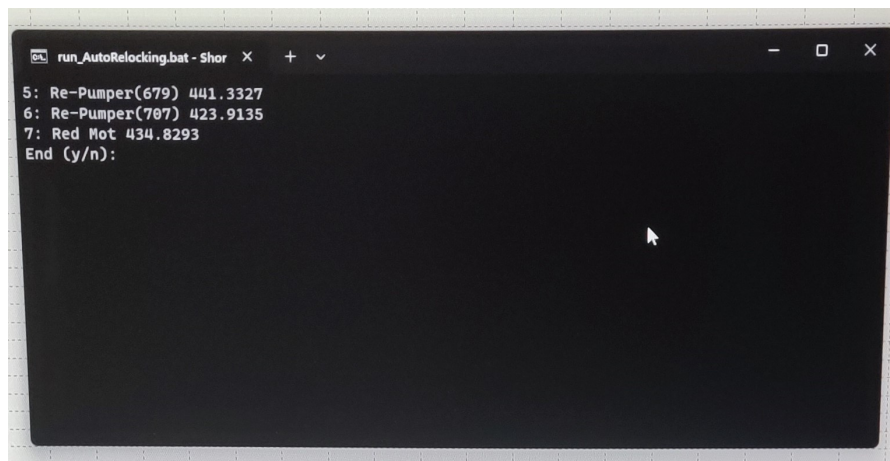


Figure C.2: Auto relocking program when it is running.

---

## Appendix D

### Auto relocking resources using Red Pitaya

The resources for this project have been made available as open source on a GitHub page. Additionally, an introductory tutorial on the web application can be found on our YouTube channel. For further details and access to the GitHub resources and YouTube video, you can scan the provided QR code.



Figure D.1: GitHub QR Code



Figure D.2: YouTube QR Code

**Date: 26, Jan, 2023**  
**Name: Mehrdad Zarei**

**Email: mehr.zarei1@gmail.com**

## **Project**

This project is for automatically relocking the External Cavity Diode Lasers (ECDLs) by wavemeter and/or cavity transmission using Redpitaya.

## **Overview**

In this project I am presenting a web application dedicated for Redpitaya board for automatically and real-time relocking the external-cavity diode lasers (ECDLs) by cavity transmission and/or wavemeter signals. Here specifically this web application is used in Strontium (Sr) Optical Tweezer Machine for quantum computing and simulation. But it can be used in different cold atom applications, such as optical atomic clocks, transportable optical clocks, future satellite missions, space missions, and wherever you want to fully control the ECDLs. First of all I will explain a little bit about this machine then will explain how this web application is used to improve this machine.

## **Introduction**

We are working on Sr Optical Tweezer Machine for quantum computing and simulation. In the Fig. 1 you see a small view of this project. The Sr atoms are cooled down to level of micro kelvin or even less than that during laser cooling and magneto optical trapping (MOT). After cooling down, Sr atoms are trapped in optical tweezers, controlled by spatial light modulator (SLM) and acousto-optic deflector (AOD) to create different patterns of Sr atoms like Fig. 2.

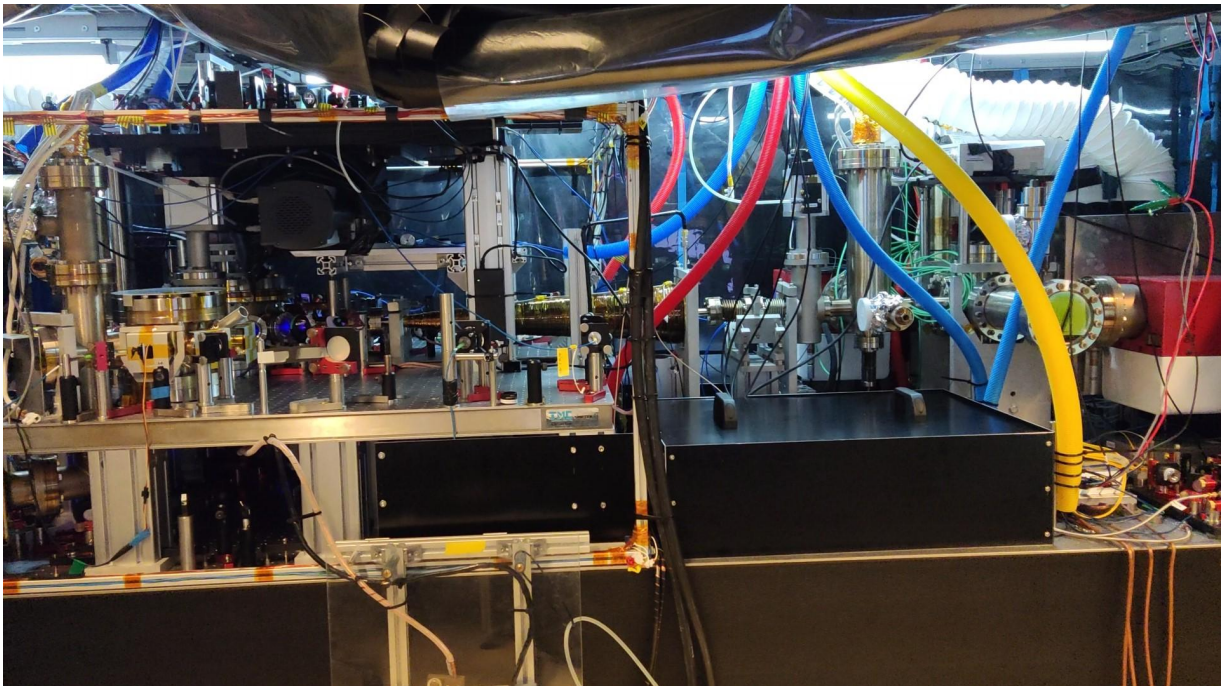


Fig. 1: A view of the Sr Optical Tweezer Machine.

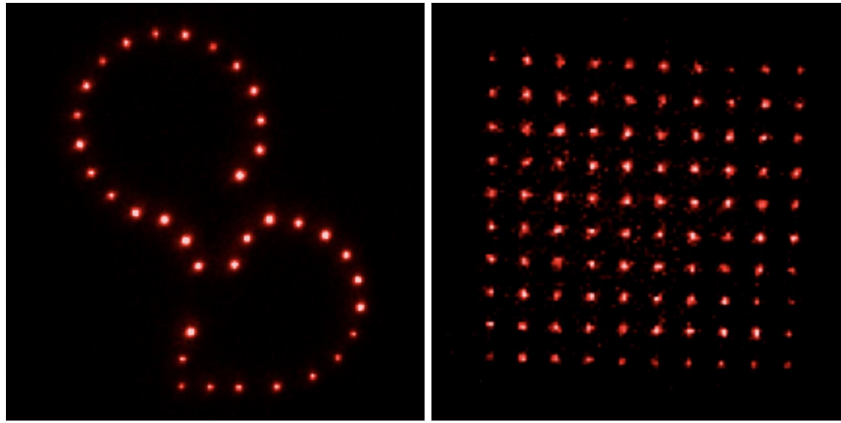


Fig. 2: Different patterns of Sr atoms, trapped in optical tweezers.

At the end after trapping Sr atoms in optical tweezers, we do the Rydberg spectroscopy by shining the Rydberg laser with 316.5 nm wavelength on the Sr atoms.

Note: For more information about this project click on [Strontium Quantum Gas Group](#).

One of the big challenges in this project is that, Rydberg laser have to be locked on an exact frequency otherwise we are not able to do spectroscopy. Rydberg laser is locked to a cavity by the Pound–Drever–Hall (PDH) technique with FALC driver from Toptica company, this cavity is also locked to another stable laser (689 nm) with DigiLock driver from Toptica company which is called transfer cavity that transfer the stability of the 689 nm to the Rydberg laser. The problem is that these kind of lock are not stable for long time and laser would be out of lock because of electronic noises, mechanical noises, temperature drift, and .... Therefore I developed a web application for Redpitaya to be able manually and automatically control the piezo and current driver of the Rydberg laser.

Schematic diagram of this project is shown in the Fig. 3. As you see we have two ECDLs (1070 nm and 1550 nm) controlled by laser driver from Toptica company for this project. Laser light from ECDLs would be amplify with fiber amplifiers to have more than of watts intensity to send them to sum frequency generation (SFG) to have red light (633 nm), and then light is going to second harmonic generation (SHG) to produce UV light (316.5 nm) for spectroscopy. Part of the red light after SFG is going to the wavemeter from HighFinnese company to measure the wavelength and to the transfer cavity to be locked by FALC driver. Transfer cavity is locked also to 689 nm laser which is very stable by DigiLock driver.

### Relocking ECDL using Redpitaya

When the 633 nm laser is locked to the cavity (we are interested only on the mode  $TEM_{00}$ ) part of light is transmitted and is detected by a photo diode (PD) and camera for monitoring. PD signal is amplified and going to the input 1 of the Redpitaya to be processed and monitored. Redpitaya get information of the wavemeter and DigiLock from the server which is running on the PC that wavemeter is installed on. After processing information on the Redpitaya, an appropriate feedback is sent to the piezo and current controller of the 1550 nm from output 1 and 2 respectively.

Note: There is a recorded video about this project with more details for running this project, on YouTube which you can watch it [here](#).

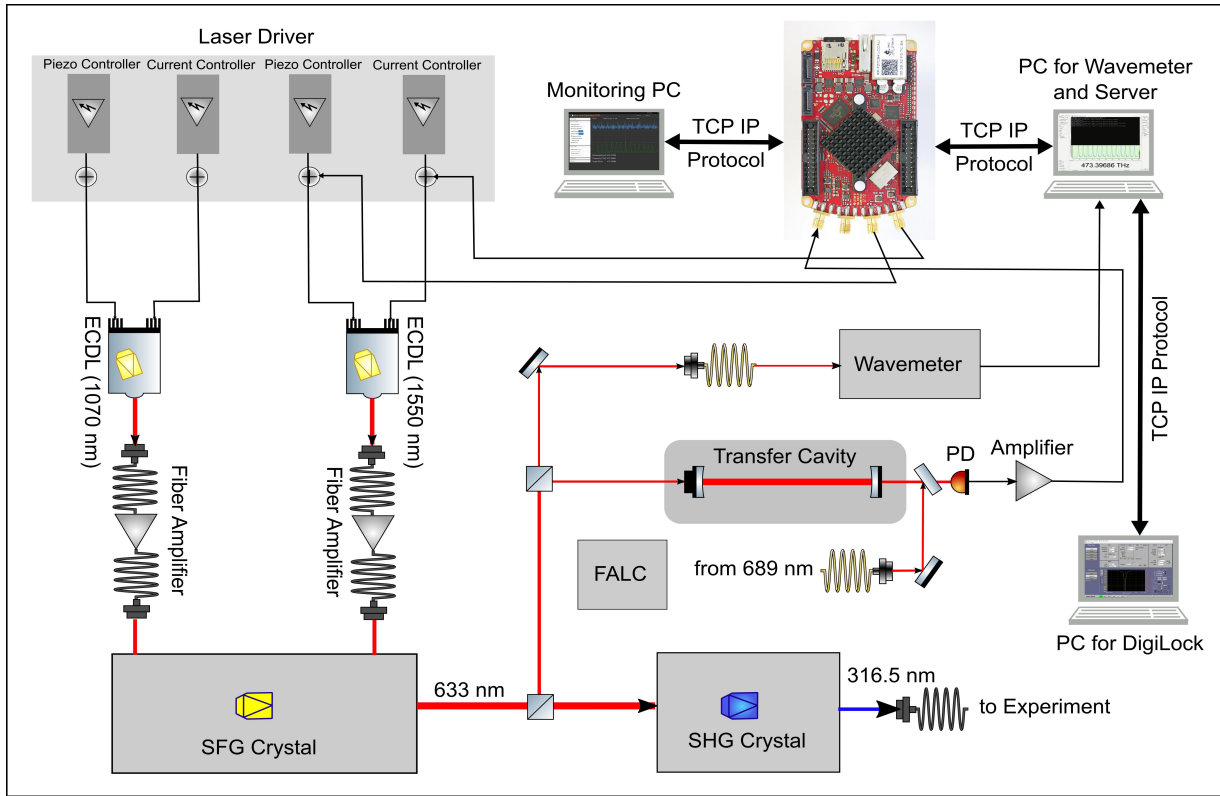


Fig. 3: Schematic diagram of the project.

## 1. Installing RedPitaya

Redpitaya installed on an amplifier board which is providing power supply also for the Redpitaya and its connections is shown in the Fig. 4, PD signal is connected to the amplifier (we are amplifying the signal 25 times) then is going to the input 1 of the redpitaya. Output 1 is dedicated to send feedback to the piezo controller and output 2 is for current controller. Input 2 is just to monitoring any other signal if you need.

Note: If you don't need to amplify the signal, directly connect it to input 1.

Warning: The signal should be in the range of Redpitaya ( $\pm 1$  V for LV and  $\pm 20$  V for HV).

Note: Output 1 and 2 for Redpitaya is limited on  $\pm 1$  V, if you need more voltage to scan longer range of frequency, use an amplifier and remember to set this range on the web application.

Warning: Before applying voltage on the laser driver, be careful about the limitation of the laser driver to avoid damaging the laser.

Laser driver is shown in the Fig. 5, as you see for applying feedback from Redpitaya to the piezo we used an analog interface, maybe in your case is different. As the feedback voltage is limited to 1 V, perhaps is not enough to scan whole range of frequency to find target frequency, therefore first find the target frequency manually by scan controller which is signed in the Fig. 5.



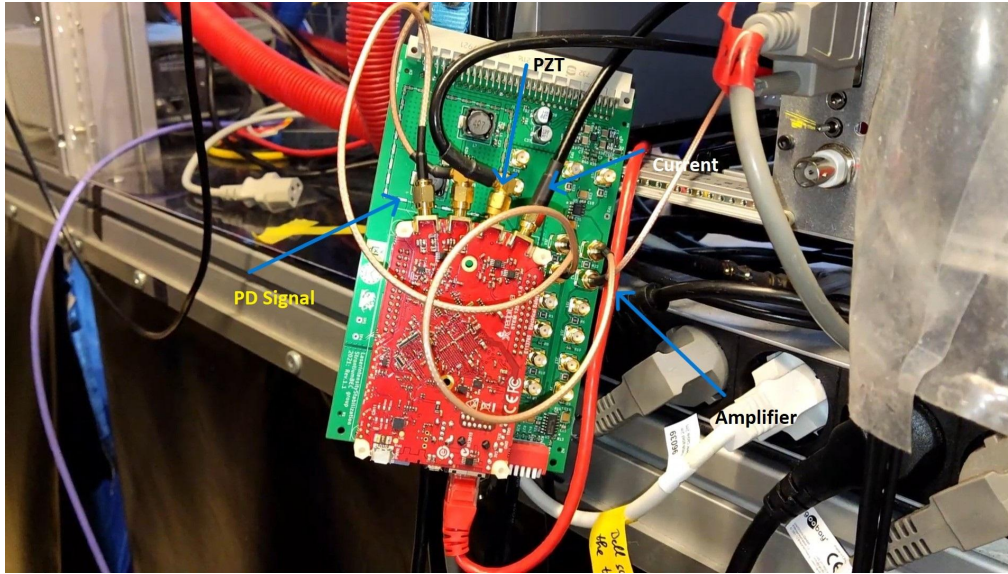


Fig. 4: Redpitaya and its connections.

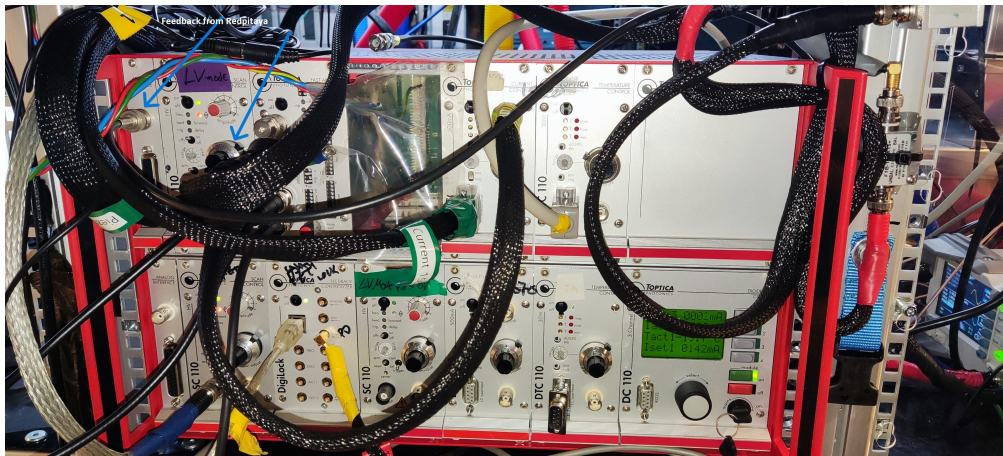


Fig. 5: Laser driver and connected feedback signal from Redpitaya.

## 2. Run the Server on the Wavemeter's PC

First of all run the server on the wavemeter's PC, after running the server a message is written that server is running on a specific IP and Port number which have to be set in the batch file which run the server file. In the Fig. 6 a running server is shown. For connecting to the server from web application you have to set these IP and Port number which the server is listening on it on the web application.

Note: If you want to use Wavemeter or DigiLock, Server have to be running on the Wavemeter's PC.

Note: For downloading the server application click on [Wavemeter API Server](#).

## 3. Run the DigiLock software

DigiLock software for locking transfer cavity to the 689 nm laser should be running. And the IP and Port number on the DigiLock software which is shown in the Fig. 7 should be set in the web application to let the Redpitaya to remotely control and lock the cavity.

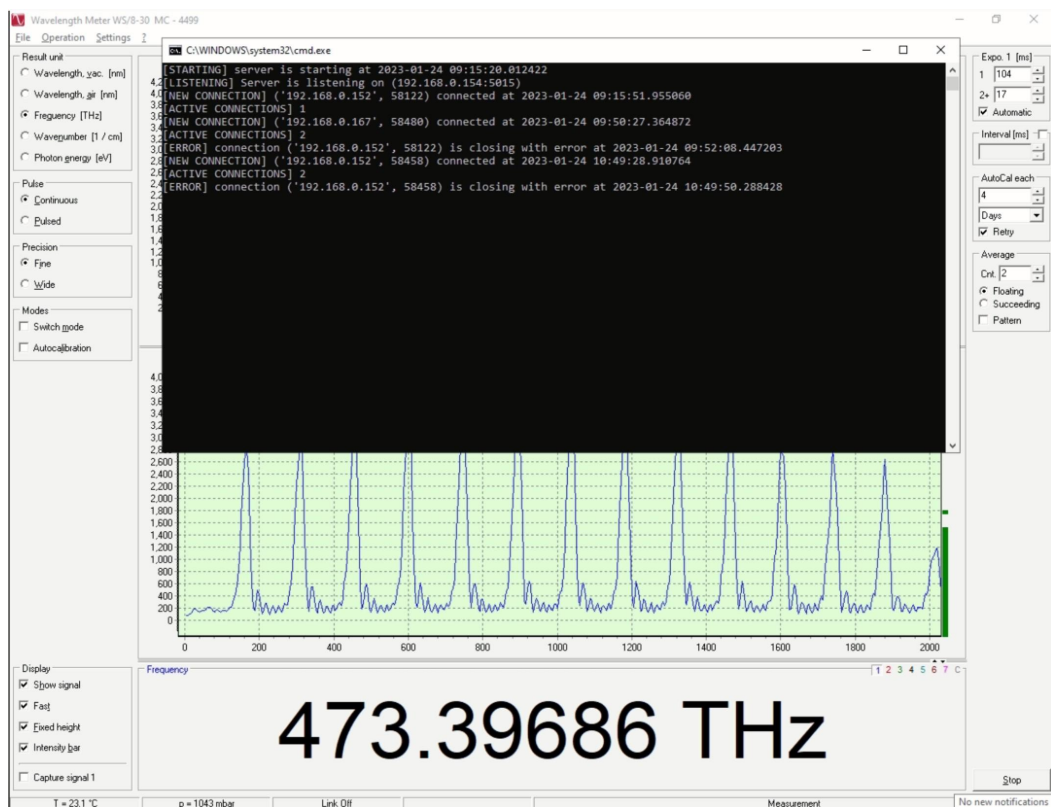


Fig. 6: Running server on the wavemeter's PC.

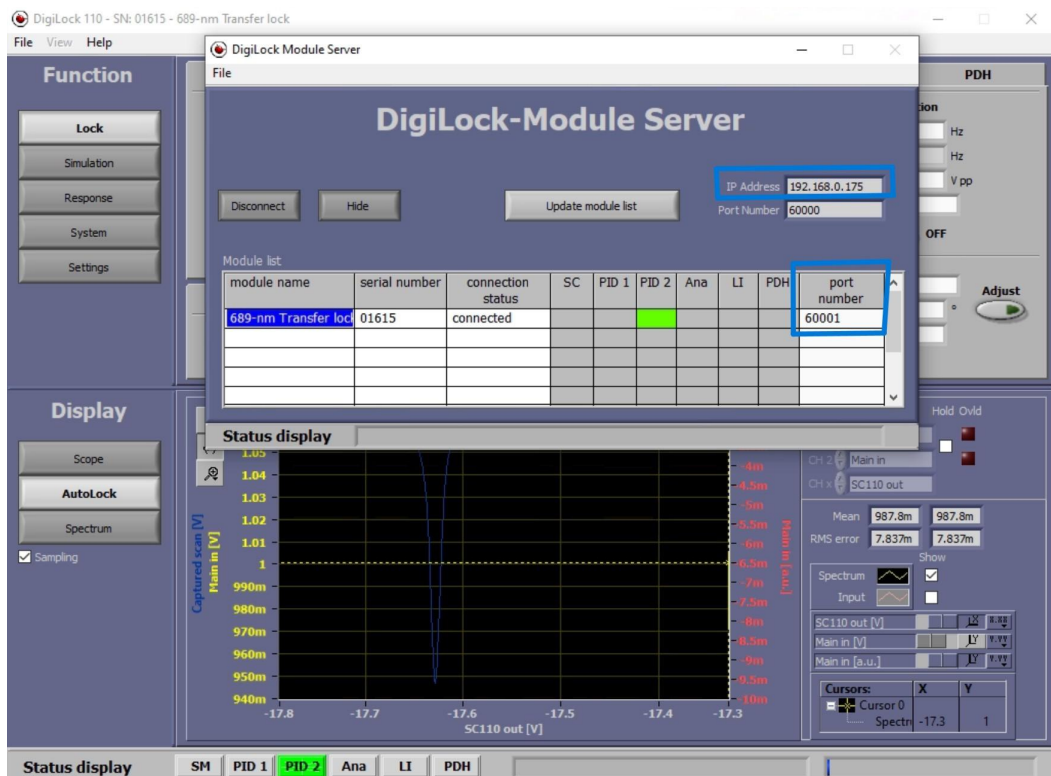


Fig. 7: DigiLock software and its IP and Port number.



#### 4. Run the program on the web application

After setting initial parameters on the web application run the program to monitor cavity transmission and wavemeter's information. The algorithm operates in two modes: Either in manual mode or in automatic mode, when the laser is kept on the lock frequency. There are two different types of input signals which are selectable: cavity transmission and/or wavemeter signal. After processing the signals by the software, appropriate feedback is sent to the piezo and/or current controller of the laser driver. The relocking algorithms verify the lock by comparing the value of the cavity transmission signal and/or by comparing the frequency difference between preset frequency and frequency measured by the wavemeter. If one of those values is below a predefined threshold, the algorithm starts scanning the piezo to find the target frequency.

Note: For setting transmission level in the situation which we want to lock the laser to the cavity, this value should be set in the level that if transmission (Mean In1 in the Fig. 8) get lower than that, the algorithm start relocking the laser. If the transmission voltage gap when laser is locked and out of lock is small, change the x range and y range which is shown in the Fig. 8 to have a stable average signal (Mean In1).

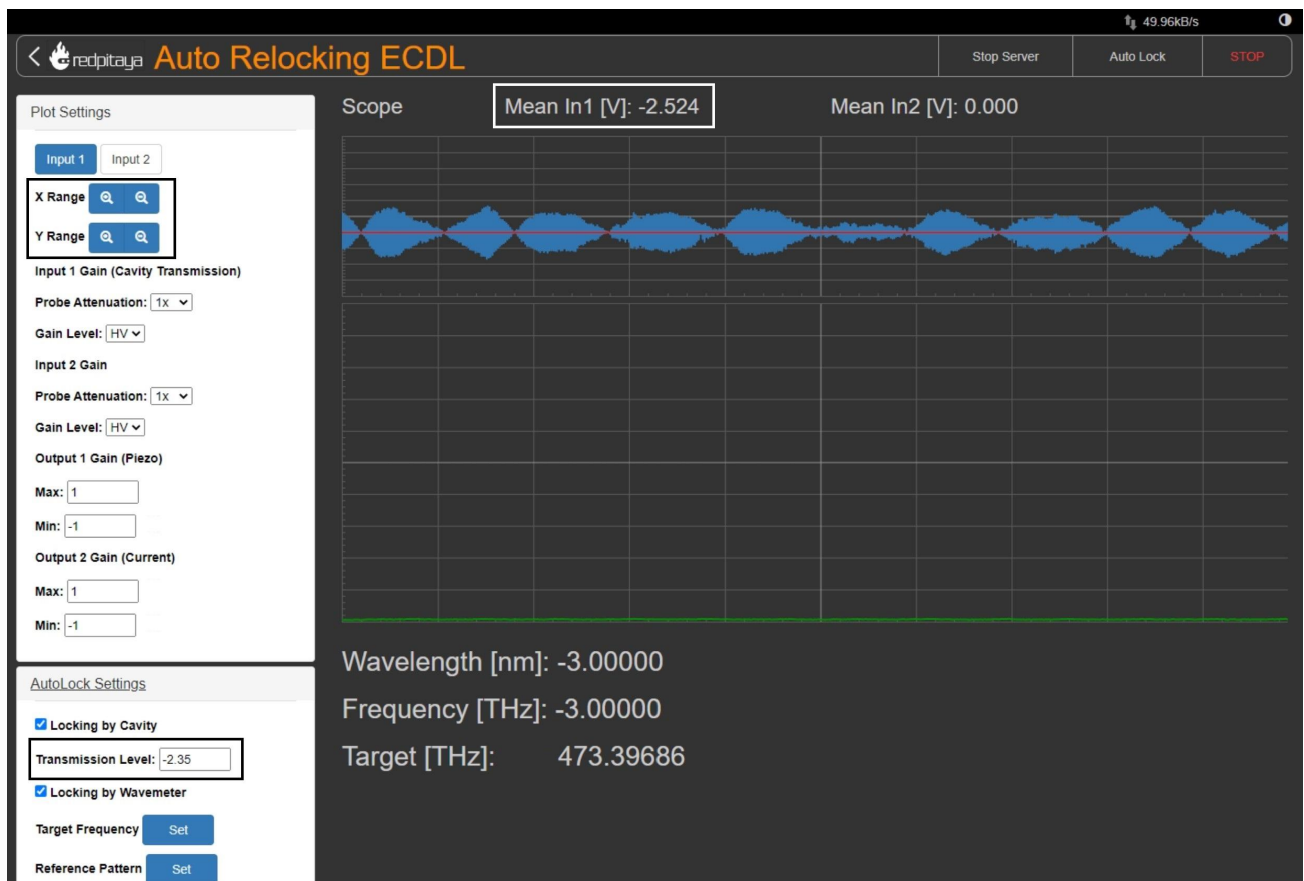


Fig. 8: Setting x and y range to stable transmission signal.

In the Fig. 9 there is a whole view of the web application developed for this project, in the Fig. 10, cavity transmission on the camera is shown and also locked cavity by DigiLock which all are automatically done by web application running on the Redpitaya.

Note: To download the source code of web application click on [Auto Relocking Web Application](#).

Note: To see a full instruction for developing this web application click on [Manual](#).

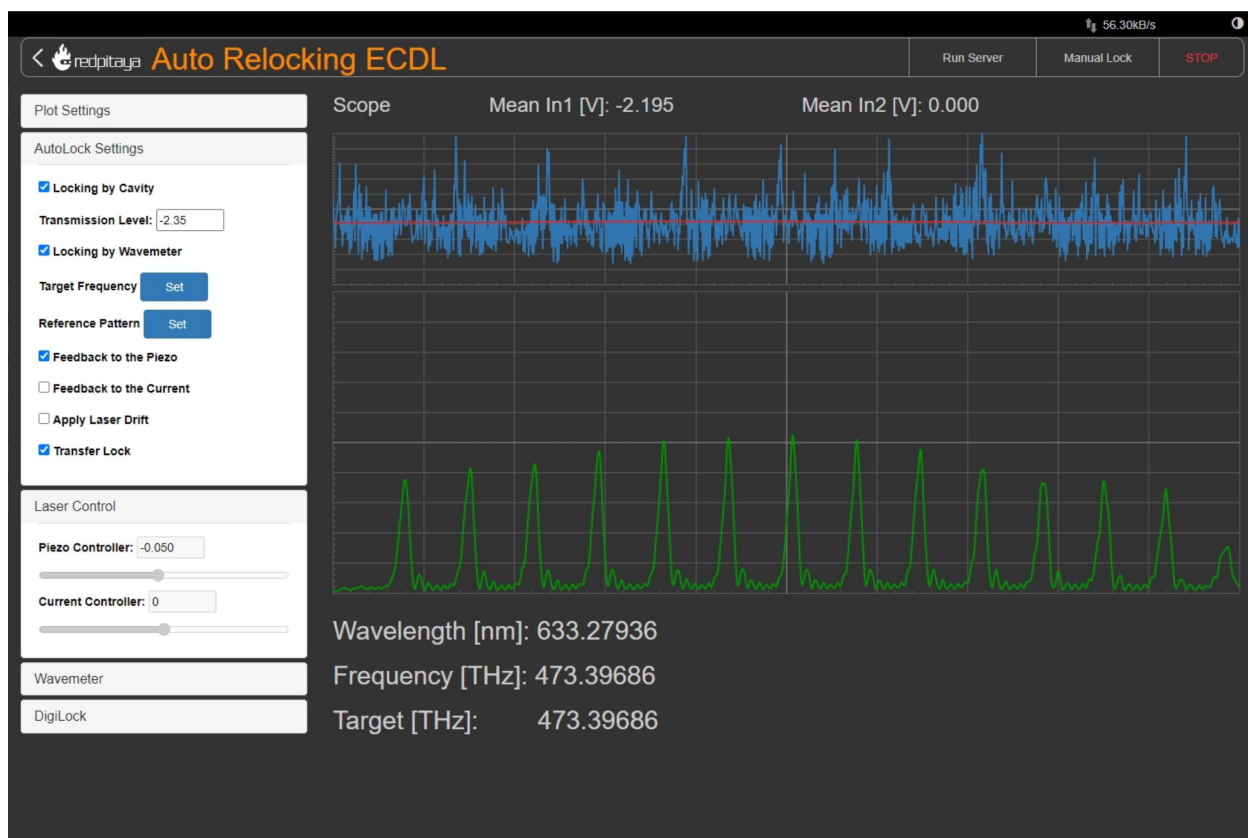


Fig. 9: Web application running on the Redpitaya.

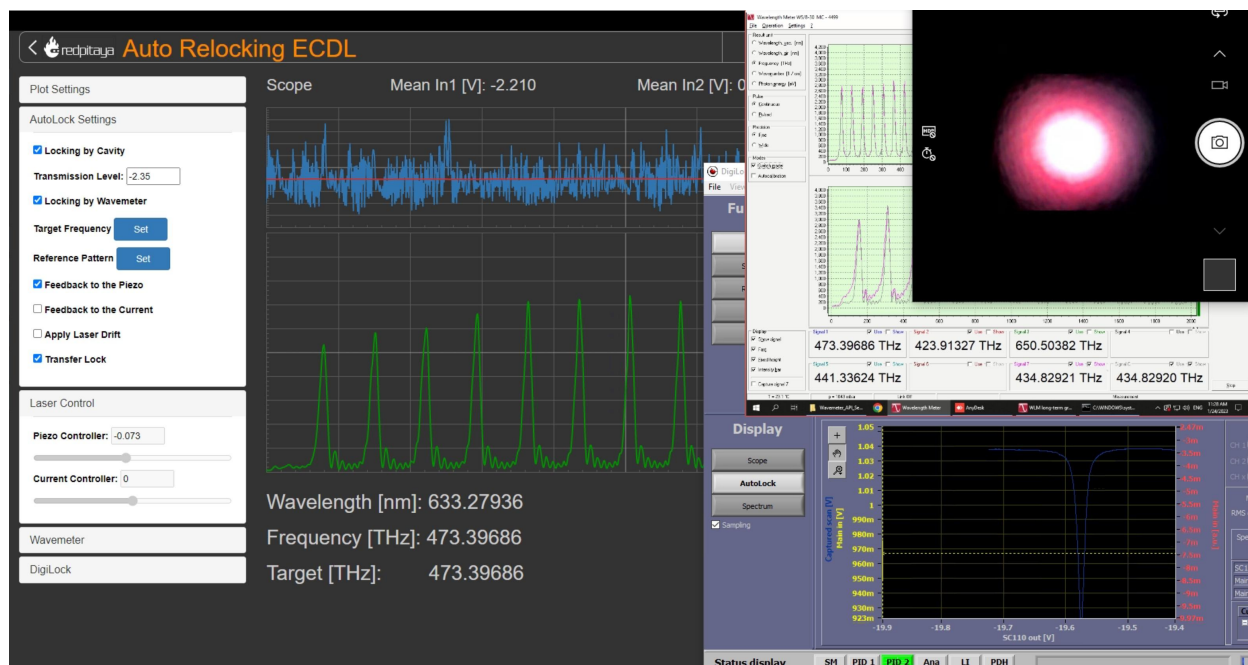


Fig. 10: Locked Rydberg laser and cavity by web application.

## Where is used this Web Application

This application is used wherever you want to fully control the ECDLs. This web application works in two mode, manual and automatic mode. In each mode it is usable for:

### 1. Manual Mode

- \* Controlling Piezo Voltage of the Laser Driver
- \* Controlling Current Voltage of the Laser Driver
- \* Monitoring Wavemeter
- \* Monitoring Cavity Transmission

### 2. Automatic Mode

- \* Relocking ECDLs only by Cavity Transmission
- \* Relocking ECDLs only by Wavemeter
- \* Relocking ECDLs by Cavity Transmission and/or Wavemeter
- \* Relocking Transfer Cavity by DigiLock
- \* Monitoring Wavemeter
- \* Monitoring Cavity Transmission

## Caution

Please before applying any voltage on your laser driver, first monitor them on the oscilloscope and limit the range based on the feature of your laser driver. The author will not take any responsibility for damaged lasers.

## Acknowledgment

This project 18SIB05 ROCIT has received funding from the EMPIR program co-financed by the Participating States and from the European Union's Horizon 2020 research and innovation program. This project has received funding from the European Union's Horizon 2020 Research and Innovation Program No 820404, (iqClock project). This project has received funding from the European Union's Horizon 2020 research and innovation program under grant agreement No 860579 (MoSaiQC project). The project is partially performed at the National Laboratory FAMO (KL FAMO) in Toruń, Poland and were supported by a subsidy from the Polish Ministry of Science and Higher Education.

I am a PhD student at the Nicolaus Copernicus University under supervision Michal Zawada, but this project has been done at the University of Amsterdam in the Strontium quantum gas group under supervision Florian Schreck during my secondment.



---

# Bibliography

1. Xinju, L. *Laser Technology* ISBN: 9781420091717. <https://books.google.nl/books?id=zQbMBQAAQBAJ> (CRC Press, 2010).
2. Jiang, Y. Y. *et al.* Making optical atomic clocks more stable with  $10^{-16}$  level laser stabilization. *Nature Photonics* **5**, 158–161. ISSN: 1749-4893. <http://dx.doi.org/10.1038/nphoton.2010.313> (Jan. 2011).
3. Young, B. C., Cruz, F. C., Itano, W. M. & Bergquist, J. C. Visible Lasers with Subhertz Linewidths. *Phys. Rev. Lett.* **82**, 3799–3802. <https://link.aps.org/doi/10.1103/PhysRevLett.82.3799> (19 May 1999).
4. Chou, C. W., Hume, D. B., Koelemeij, J. C. J., Wineland, D. J. & Rosenband, T. Frequency Comparison of Two High-Accuracy  $\text{Al}^+$  Optical Clocks. *Phys. Rev. Lett.* **104**, 070802. <https://link.aps.org/doi/10.1103/PhysRevLett.104.070802> (7 Feb. 2010).
5. Photonics, T. *Diode Laser Series DL 100 for spectroscopic applications in physics and chemistry* [https://wiki.kip.uni-heidelberg.de/KIPwiki/images/1/18/Toptica\\_DL100\\_Werbung.pdf](https://wiki.kip.uni-heidelberg.de/KIPwiki/images/1/18/Toptica_DL100_Werbung.pdf).
6. Hawthorn, C. J., Weber, K. P. & Scholten, R. E. Littrow configuration tunable external cavity diode laser with fixed direction output beam. *Review of Scientific Instruments* **72**, 4477–4479. ISSN: 0034-6748. eprint: [https://pubs.aip.org/aip/rsi/article-pdf/72/12/4477/19295455/4477\1\\\_online.pdf](https://pubs.aip.org/aip/rsi/article-pdf/72/12/4477/19295455/4477\1\_online.pdf). <https://doi.org/10.1063/1.1419217> (Dec. 2001).
7. Black, E. D. An introduction to Pound–Drever–Hall laser frequency stabilization. *American Journal of Physics* **69**, 79–87. ISSN: 0002-9505. eprint: [https://pubs.aip.org/aapt/ajp/article-pdf/69/1/79/10115998/79\1\\\_online.pdf](https://pubs.aip.org/aapt/ajp/article-pdf/69/1/79/10115998/79\1\_online.pdf). <https://doi.org/10.1119/1.1286663> (Jan. 2001).
8. Foot, C. *Atomic Physics* ISBN: 9780198506959. [https://books.google.nl/books?id=\\_CoSDAAAQBAJ](https://books.google.nl/books?id=_CoSDAAAQBAJ) (OUP Oxford, 2005).
9. Ramsey, N. F. A Molecular Beam Resonance Method with Separated Oscillating Fields. *Phys. Rev.* **78**, 695–699. <https://link.aps.org/doi/10.1103/PhysRev.78.695> (6 June 1950).
10. Michael, J. M. *Quantum Metrology and Many-Body Physics: Pushing the Frontier of the Optical Lattice Clock* Theses (University of Colorado, 2013).
11. Boyd, M. M. *High precision spectroscopy of strontium in an optical lattice: Towards a new standard for frequency and time* PhD thesis (University of Colorado, Boulder, Jan. 2007).

12. Westergaard, P. *Strontium Optical Lattice Clock: In Quest of the Ultimate Performance* Theses (Ecole nationale supérieure des telecommunications - ENST, Oct. 2010). <https://theses.hal.science/tel-00541420>.
13. Rosenband, T. *et al.* Frequency ratio of Al<sup>+</sup> and Hg<sup>+</sup> single-ion optical clocks; metrology at the 17th decimal place. *Science (New York, N.Y.)* **319**, 1808–1812. ISSN: 0036-8075. <https://zenodo.org/record/1230892/files/article.pdf> (Mar. 2008).
14. Peik, E. *et al.* Limit on the Present Temporal Variation of the Fine Structure Constant. *Phys. Rev. Lett.* **93**, 170801. <https://link.aps.org/doi/10.1103/PhysRevLett.93.170801> (17 Oct. 2004).
15. Fortier, T. M. *et al.* Precision Atomic Spectroscopy for Improved Limits on Variation of the Fine Structure Constant and Local Position Invariance. *Phys. Rev. Lett.* **98**, 070801. <https://link.aps.org/doi/10.1103/PhysRevLett.98.070801> (7 Feb. 2007).
16. Blatt, S. *et al.* New Limits on Coupling of Fundamental Constants to Gravity Using <sup>87</sup>Sr Optical Lattice Clocks. *Phys. Rev. Lett.* **100**, 140801. <https://link.aps.org/doi/10.1103/PhysRevLett.100.140801> (14 Apr. 2008).
17. Bjerhammar, A. On a relativistic geodesy. *Bulletin Geodesique* **59**, 207–220 (Sept. 1985).
18. Delva, P. & Lodewyck, J. *Atomic clocks: new prospects in metrology and geodesy* 2013. arXiv: [1308.6766](https://arxiv.org/abs/1308.6766) [physics.atom-ph].
19. Schiller, S. *et al.* Einstein Gravity Explorer-a medium-class fundamental physics mission. *Exp. Astron.* **22**, 573–610. <http://eprintpublications.npl.co.uk/5121/> (2009).
20. Chou, C. W., Hume, D. B., Rosenband, T. & Wineland, D. J. Optical Clocks and Relativity. *Science* **329**, 1630–1633 (2010).
21. Derevianko, A. & Pospelov, M. Hunting for topological dark matter with atomic clocks. *Nature Physics* **10**, 933–936. ISSN: 1745-2481. <http://dx.doi.org/10.1038/nphys3137> (Nov. 2014).
22. Itano, W. M. *et al.* Quantum projection noise: Population fluctuations in two-level systems. *Phys. Rev. A* **47**, 3554–3570. <https://link.aps.org/doi/10.1103/PhysRevA.47.3554> (5 May 1993).
23. Dick, G. Local oscillator induced instabilities in trapped ion frequency standards. *Proceedings of the 34th Annual Precise Time and Time Interval Systems and Applications Meeting (ION, 1987)*, 133–147. [https://tycho.usno.navy.mil/ptti/1987papers/Vol%2019\\_13.pdf](https://tycho.usno.navy.mil/ptti/1987papers/Vol%2019_13.pdf) (1987).
24. Allan, D. Statistics of atomic frequency standards. *Proceedings of the IEEE* **54**, 221–230 (1966).
25. Nicholson, T. *et al.* Systematic evaluation of an atomic clock at  $2 \times 10^{18}$  total uncertainty. *Nature Communications* **6**. ISSN: 2041-1723. <http://dx.doi.org/10.1038/ncomms7896> (Apr. 2015).
26. Takamoto, M., Hong, F., Higashi & et al, R. An optical lattice clock. *Nature* **435**. <https://doi.org/10.1038/nature03541> (2005).

27. Bober, M. *et al.* Strontium optical lattice clocks for practical realization of the metre and secondary representation of the second. *Measurement Science and Technology* **26**, 075201. <https://dx.doi.org/10.1088/0957-0233/26/7/075201> (June 2015).
28. Hinkley, N. *et al.* An Atomic Clock with  $10^{18}$  Instability. *Science* **341**, 1215–1218. ISSN: 1095-9203. <http://dx.doi.org/10.1126/science.1240420> (Sept. 2013).
29. Bloom, B. J. *et al.* An optical lattice clock with accuracy and stability at the  $10^{18}$  level. *Nature* **506**, 71–75. ISSN: 1476-4687. <http://dx.doi.org/10.1038/nature12941> (Jan. 2014).
30. Kohno, T. *et al.* One-Dimensional Optical Lattice Clock with a Fermionic  $^{171}\text{Yb}$  Isotope. *Applied Physics Express* **2**, 072501. <https://dx.doi.org/10.1143/APEX.2.072501> (June 2009).
31. Park, C. Y. *et al.* Absolute frequency measurement of  $1S_0(F = 1/2) - 3P_0(F = 1/2)$  transition of  $^{171}\text{Yb}$  atoms in a one-dimensional optical lattice at KRISS. *Metrologia* **50**, 119. <https://dx.doi.org/10.1088/0026-1394/50/2/119> (Feb. 2013).
32. Hachisu, H. *et al.* Trapping of Neutral Mercury Atoms and Prospects for Optical Lattice Clocks. *Phys. Rev. Lett.* **100**, 053001. <https://link.aps.org/doi/10.1103/PhysRevLett.100.053001> (5 Feb. 2008).
33. Yi, L., Mejri, S., McFerran, J. J., Le Coq, Y. & Bize, S. Optical Lattice Trapping of  $^{199}\text{Hg}$  and Determination of the Magic Wavelength for the Ultraviolet  $^1S_0 \leftrightarrow ^3P_0$  Clock Transition. *Phys. Rev. Lett.* **106**, 073005. <https://link.aps.org/doi/10.1103/PhysRevLett.106.073005> (7 Feb. 2011).
34. Bloch, I., Dalibard, J. & Nascimbène, S. Quantum simulations with ultracold quantum gases. *Nature Physics* **8**, 267–276. ISSN: 1745-2473. <http://dx.doi.org/10.1038/nphys2259> (Apr. 2012).
35. Barredo, D., de Léséleuc, S., Lienhard, V., Lahaye, T. & Browaeys, A. An atom-by-atom assembler of defect-free arbitrary two-dimensional atomic arrays. *Science* **354**, 1021–1023. eprint: <https://www.science.org/doi/pdf/10.1126/science.aah3778>. <https://www.science.org/doi/abs/10.1126/science.aah3778> (2016).
36. Urech, A. *Single strontium atoms in optical tweezers* Theses (Universiteit van Amsterdam, 2023).
37. Plassmann, T. *A strontium Rydberg laser for quantum simulation with tweezer arrays* Theses (Universiteit van Amsterdam, 2021).
38. Kovačević, D. *DEVELOPMENT OF AN OPTICAL FREQUENCY STANDARD* Theses (University of Zagreb, Nicolaus Copernicus University, 2023).
39. Bilicki, S. *Strontium optical lattice clocks: clock comparisons for timescales and fundamental physics applications* Theses (Observatoire de Paris - SYRTE, Nov. 2017). <https://theses.hal.science/tel-01711318>.
40. Madjarov, I. S. *Entangling, controlling, and detecting individual strontium atoms in optical tweezer arrays* Theses (California Institute of Technology, 2021). <https://resolver.caltech.edu/CaltechTHESIS:01292021-001639979>.



41. Haensch, T. & Schawlow, A. Hänsch, T. W. & Schawlow, A. L. Cooling of gases by laser radiation. *Opt. Commun.* **13**, 68–69. *Optics Communications* **13**, 68–69 (Jan. 1975).
42. Metcalf, H. & Van der Straten, P. *Laser Cooling and Trapping* <https://books.google.nl/books?id=i-40VaXqrj0C> (Springer, 1999).
43. Chanelière, T., Meunier, J.-L., Kaiser, R., Miniatura, C. & Wilkowski, D. Extra-heating mechanism in Doppler cooling experiments. *J. Opt. Soc. Am. B* **22**, 1819–1828. <https://opg.optica.org/josab/abstract.cfm?URI=josab-22-9-1819> (Sept. 2005).
44. Targat, R. *et al.* Experimental realization of an optical second with strontium lattice clocks. *Nature Communications* **4** (July 2013).
45. Falke, S. *et al.* A strontium lattice clock with  $3 \times 10^{-17}$  inaccuracy and its frequency. *New Journal of Physics* **16**, 073023. <https://dx.doi.org/10.1088/1367-2630/16/7/073023> (July 2014).
46. Ushijima, I., Takamoto, M., Das, M., Ohkubo, T. & Katori, H. Cryogenic optical lattice clocks. *Nature Photonics* **9** (Feb. 2015).
47. Akamatsu, D. *et al.* Spectroscopy and frequency measurement of the  $^{87}\text{Sr}$  clock transition by laser linewidth transfer using an optical frequency comb. *Applied Physics Express* **7**, 012401. <https://dx.doi.org/10.7567/APEX.7.012401> (Dec. 2013).
48. Pizzocaro, M. *et al.* Absolute frequency measurement of the  $^1\text{S}_0\text{--}^3\text{P}_0$  transition of  $^{171}\text{Yb}$ . *Metrologia* **54**, 102. <https://dx.doi.org/10.1088/1681-7575/aa4e62> (Jan. 2017).
49. Stellmer, S., Tey, M. K., Huang, B., Grimm, R. & Schreck, F. Bose-Einstein Condensation of Strontium. *Phys. Rev. Lett.* **103**, 200401. <https://link.aps.org/doi/10.1103/PhysRevLett.103.200401> (20 Nov. 2009).
50. Xu, X., Loftus, T. H., Hall, J. L., Gallagher, A. & Ye, J. Cooling and trapping of atomic strontium. *J. Opt. Soc. Am. B* **20**, 968–976. <https://opg.optica.org/josab/abstract.cfm?URI=josab-20-5-968> (May 2003).
51. He, C., Hajiyeve, E., Ren, Z., Song, B. & Jo, G.-B. Recent progresses of ultra-cold two-electron atoms. *Journal of Physics B: Atomic, Molecular and Optical Physics* **52**, 102001. <https://dx.doi.org/10.1088/1361-6455/ab153e> (Apr. 2019).
52. Grimm, R., Weidemüller, M. & Ovchinnikov, Y. B. in (eds Bederson, B. & Walther, H.) 95–170 (Academic Press, 2000). <https://www.sciencedirect.com/science/article/pii/S1049250X0860186X>.
53. Derevianko, A. & Katori, H. Colloquium: Physics of optical lattice clocks. *Rev. Mod. Phys.* **83**, 331–347. <https://link.aps.org/doi/10.1103/RevModPhys.83.331> (2 May 2011).
54. Katori, H., Takamoto, M., Pal’chikov, V. G. & Ovsiannikov, V. D. Ultrastable Optical Clock with Neutral Atoms in an Engineered Light Shift Trap. *Phys. Rev. Lett.* **91**, 173005. <https://link.aps.org/doi/10.1103/PhysRevLett.91.173005> (17 Oct. 2003).



55. Takamoto, M., Katori, H., Marmo, S. I., Ovsiannikov, V. D. & Pal'chikov, V. G. Prospects for Optical Clocks with a Blue-Detuned Lattice. *Phys. Rev. Lett.* **102**, 063002. <https://link.aps.org/doi/10.1103/PhysRevLett.102.063002> (6 Feb. 2009).
56. Witkowski, M. *et al.* Photoionization cross sections of ultracold 88Sr in 1P1 and 3S1 states at 390 nm and the resulting blue-detuned magic wavelength optical lattice clock constraints. *Optics Express* **30**, 21423. ISSN: 1094-4087. <http://dx.doi.org/10.1364/OE.460554> (May 2022).
57. Takano, T., Mizushima, R. & Katori, H. Precise determination of the isotope shift of 88Sr–87Sr optical lattice clock by sharing perturbations. *Applied Physics Express* **10**, 072801. <https://dx.doi.org/10.7567/APEX.10.072801> (June 2017).
58. Takano, T. *et al.* Geopotential measurements with synchronously linked optical lattice clocks. *Nature Photonics* **10**, 662–666 (Oct. 2016).
59. Dicke, R. H. The Effect of Collisions upon the Doppler Width of Spectral Lines. *Phys. Rev.* **89**, 472–473. <https://link.aps.org/doi/10.1103/PhysRev.89.472> (2 Jan. 1953).
60. Zettili, N. *Quantum Mechanics: Concepts and Applications* ISBN: 9780470026786. <https://books.google.nl/books?id=6jXlpJCSz98C> (Wiley, 2009).
61. Leibfried, D., Blatt, R., Monroe, C. & Wineland, D. Quantum dynamics of single trapped ions. *Rev. Mod. Phys.* **75**, 281–324. <https://link.aps.org/doi/10.1103/RevModPhys.75.281> (1 Mar. 2003).
62. Eschner, J., Morigi, G., Schmidt-Kaler, F. & Blatt, R. Laser cooling of trapped ions. *J. Opt. Soc. Am. B* **20**, 1003–1015. <https://opg.optica.org/josab/abstract.cfm?URI=josab-20-5-1003> (May 2003).
63. Wineland, D. J. & Itano, W. M. Laser cooling of atoms. *Phys. Rev. A* **20**, 1521–1540. <https://link.aps.org/doi/10.1103/PhysRevA.20.1521> (4 Oct. 1979).
64. Blatt, S. *et al.* Rabi spectroscopy and excitation inhomogeneity in a one dimensional optical lattice clock. *Phys. Rev. A* **80**, 052703. <https://link.aps.org/doi/10.1103/PhysRevA.80.052703> (5 Nov. 2009).
65. Taichenachev, A. V. *et al.* Magnetic Field-Induced Spectroscopy of Forbidden Optical Transitions with Application to Lattice-Based Optical Atomic Clocks. *Phys. Rev. Lett.* **96**, 083001. <https://link.aps.org/doi/10.1103/PhysRevLett.96.083001> (8 Mar. 2006).
66. Allen, L. & Eberly, J. H. Optical resonance and two-level atoms. <https://www.osti.gov/biblio/7365050> (Jan. 1975).
67. Riehle, F. *Frequency Standards: Basics and Applications* ISBN: 9783527605958. <https://books.google.nl/books?id=Y095NIpuyb0C> (Wiley, 2006).
68. Kash, M. M. Atom–Photon Interactions: Basic Processes and Applications, Claude Cohen-Tannoudji, Jacques Dupont-Rock, & Gilbert Grynberg. 1992; paperback edition issued in 1998. John Wiley & Sons, Inc. (New York). 656 pp. \$44.95. ISBN 0-471-29336-9. *Laser and Particle Beams* **18**, 717–718. <https://api.semanticscholar.org/CorpusID:121906655> (2000).

69. Ludlow, A. D., Boyd, M. M., Ye, J., Peik, E. & Schmidt, P. O. Optical atomic clocks. *Rev. Mod. Phys.* **87**, 637–701. <https://link.aps.org/doi/10.1103/RevModPhys.87.637> (2 June 2015).
70. Swallows, M. D. *et al.* Suppression of Collisional Shifts in a Strongly Interacting Lattice Clock. *Science* **331**, 1043–1046. eprint: <https://www.science.org/doi/pdf/10.1126/science.1196442>. <https://www.science.org/doi/abs/10.1126/science.1196442> (2011).
71. Westergaard, P. G. *et al.* Lattice-Induced Frequency Shifts in Sr Optical Lattice Clocks at the  $10^{-17}$  Level. *Phys. Rev. Lett.* **106**, 210801. <https://link.aps.org/doi/10.1103/PhysRevLett.106.210801> (21 May 2011).
72. Beloy, K. *et al.* Atomic Clock with  $1 \times 10^{-18}$  Room-Temperature Blackbody Stark Uncertainty. *Phys. Rev. Lett.* **113**, 260801. <https://link.aps.org/doi/10.1103/PhysRevLett.113.260801> (26 Dec. 2014).
73. Boyd, M. M. *et al.* Nuclear spin effects in optical lattice clocks. *Physical Review A* **76**. ISSN: 1094-1622. <http://dx.doi.org/10.1103/PhysRevA.76.022510> (July 2007).
74. Jackson, J. *Classical Electrodynamics* ISBN: 9780471309321. <https://books.google.nl/books?id=FOBBEAAAQBAJ> (Wiley, 1998).
75. Akatsuka, T., Takamoto, M. & Katori, H. Three-dimensional optical lattice clock with bosonic  $^{88}\text{Sr}$  atoms. *Phys. Rev. A* **81**, 023402. <https://link.aps.org/doi/10.1103/PhysRevA.81.023402> (2 Feb. 2010).
76. Morzyński, P. *et al.* Open-source electronics ecosystem for optical atomic clocks. *Measurement Science and Technology* **34**, 075022. <https://dx.doi.org/10.1088/1361-6501/acc5a1> (Apr. 2023).
77. Origlia, S. *et al.* Towards an optical clock for space: Compact, high-performance optical lattice clock based on bosonic atoms. *Phys. Rev. A* **98**, 053443. <https://link.aps.org/doi/10.1103/PhysRevA.98.053443> (5 Nov. 2018).
78. Liu, L. *et al.* *Tests of Cold Atom Clock in Orbit* 2017. arXiv: 1709.03256 [physics.atom-ph].
79. Heß, M. *et al.* The ACES mission: System development and test status. *Acta Astronautica* **69**, 929–938. ISSN: 0094-5765. <https://www.sciencedirect.com/science/article/pii/S0094576511001913> (2011).
80. Lévêque, T. *et al.* PHARAO laser source flight model: Design and performances. *Review of Scientific Instruments* **86**, 033104. ISSN: 0034-6748. eprint: [https://pubs.aip.org/aip/rsi/article-pdf/doi/10.1063/1.4914025/15817902/033104\\_1\\_online.pdf](https://pubs.aip.org/aip/rsi/article-pdf/doi/10.1063/1.4914025/15817902/033104_1_online.pdf). <https://doi.org/10.1063/1.4914025> (Mar. 2015).
81. Wang, W. *et al.* Compressing the fluctuation of the magnetic field by dynamic compensation. *Review of Scientific Instruments* **89**, 033110. ISSN: 0034-6748. eprint: [https://pubs.aip.org/aip/rsi/article-pdf/doi/10.1063/1.5017793/15951843/033110\\_1\\_online.pdf](https://pubs.aip.org/aip/rsi/article-pdf/doi/10.1063/1.5017793/15951843/033110_1_online.pdf). <https://doi.org/10.1063/1.5017793> (Mar. 2018).

82. Li, L. *et al.* Automatic compensation of magnetic field for a rubidium space cold atom clock\*. *Chinese Physics B* **25**, 073201. <https://dx.doi.org/10.1088/1674-1056/25/7/073201> (June 2016).
83. Ledziński, A. & Zarei, M. *Compensation coils current controller (3x03A) version V1*. RepOD <https://doi.org/10.18150/YHSPTP>. 2022. <https://doi.org/10.18150/YHSPTP>.
84. Zarei, M., Ledziński, A., Bober, M., Zawada, M. & Morzyński, P. *Automatic Real-time Control of Magnetic Field in an Optical Atomic Clock* in *2022 Joint Conference of the European Frequency and Time Forum and IEEE International Frequency Control Symposium (EFTF/IFCS)* (Apr. 2022), 1–4.
85. Ledziński, A. *DDS AD9912 single channel controller version V1*. 2022. <https://doi.org/10.18150/YCLR91>.
86. Devices, A. *AD9912 Data Sheet* 2010. <https://www.analog.com/media/en/technical-documentation/data-sheets/ad9912.pdf>.
87. Zarei, M. *DDS controller model AD9912 remotely through Ethernet connection (TCP/IP) on STM32H743ZI* Zenodo <https://doi.org/10.5281/zenodo.10253141>. July 2022. <https://github.com/mehrdadzarei/DDS-controller-AD9912-by-STM32>.
88. Takamoto, M. *et al.* Test of general relativity by a pair of transportable optical lattice clocks. *eng. Nature photonics* **14**, 411–415. ISSN: 1749-4885 (2020).
89. Gellesch, M. *et al.* Transportable optical atomic clocks for use in out-of-the-lab environments. English. *Advanced Optical Technologies* **9**, 313–325. ISSN: 2192-8576 (Oct. 2020).
90. Ritter, S. *et al.* *Opticlock: Transportable and Easy-to-Operate Optical Single-Ion Clock* in *OSA Quantum 2.0 Conference* (Optica Publishing Group, 2020), QTh5B.6. <https://opg.optica.org/abstract.cfm?URI=QUANTUM-2020-QTh5B.6>.
91. Saffman, M. Quantum computing with atomic qubits and Rydberg interactions: progress and challenges. *Journal of Physics B: Atomic, Molecular and Optical Physics* **49**, 202001. ISSN: 1361-6455. <http://dx.doi.org/10.1088/0953-4075/49/20/202001> (Oct. 2016).
92. Aguilera, D. N. *et al.* STE-QUEST—test of the universality of free fall using cold atom interferometry. *Classical and Quantum Gravity* **31**, 115010. ISSN: 1361-6382. <http://dx.doi.org/10.1088/0264-9381/31/11/115010> (May 2014).
93. Dinkelaker, A. N. *et al.* Autonomous frequency stabilization of two extended-cavity diode lasers at the potassium wavelength on a sounding rocket. *Applied Optics* **56**, 1388. ISSN: 1539-4522. <http://dx.doi.org/10.1364/AO.56.001388> (Feb. 2017).
94. Zarei, M. *et al.* *Autonomous Frequency Stabilization in Cold Atom Experiments* in *2023 Joint Conference of the European Frequency and Time Forum and IEEE International Frequency Control Symposium (EFTF/IFCS)* (2023), 1–2.

95. Zarei, M. *AutoRelocking ECDLs by PyQt5* Dec. 2023. [https://github.com/mehrdadzarei/AutoRelocking\\_ECDL\\_Laser\\_pyQt](https://github.com/mehrdadzarei/AutoRelocking_ECDL_Laser_pyQt).
96. Zarei, M. *Auto Relocking ECDLs, by Python* Dec. 2023. [https://github.com/mehrdadzarei/AutoRelocking\\_ECDL\\_Python](https://github.com/mehrdadzarei/AutoRelocking_ECDL_Python).
97. Bober, M., Zachorowski, J. & Gawlik, W. *Designing Zeeman slower for strontium atoms towards optical atomic clock* 2010. arXiv: 1006.1554 [physics.atom-ph].
98. Ebadi, S. *et al.* Quantum phases of matter on a 256-atom programmable quantum simulator. *Nature* **595**, 227–232. ISSN: 1476-4687. <http://dx.doi.org/10.1038/s41586-021-03582-4> (July 2021).
99. Schine, N., Young, A. W., Eckner, W. J., Martin, M. J. & Kaufman, A. M. Long-lived Bell states in an array of optical clock qubits. *Nature Physics* **18**, 1067–1073. ISSN: 1745-2481. <http://dx.doi.org/10.1038/s41567-022-01678-w> (July 2022).
100. Covey, J. P., Madjarov, I. S., Cooper, A. & Endres, M. 2000-Times Repeated Imaging of Strontium Atoms in Clock-Magic Tweezer Arrays. *Phys. Rev. Lett.* **122**, 173201. <https://link.aps.org/doi/10.1103/PhysRevLett.122.173201> (17 May 2019).
101. Urech, A., Knottnerus, I. H. A., Spreeuw, R. J. C. & Schreck, F. Narrow-line imaging of single strontium atoms in shallow optical tweezers. *Phys. Rev. Res.* **4**, 023245. <https://link.aps.org/doi/10.1103/PhysRevResearch.4.023245> (2 June 2022).
102. Cooper, A. *et al.* Alkaline-Earth Atoms in Optical Tweezers. *Phys. Rev. X* **8**, 041055. <https://link.aps.org/doi/10.1103/PhysRevX.8.041055> (4 Dec. 2018).
103. Zarei, M. *et al.* *Automatic Relocking ECDL in Optical Tweezer Machine for Quantum Computing and Simulation* in (Optica Publishing Group, 2023). [https://opg.optica.org/abstract.cfm?URI=EQEC-2023-ea\\_p\\_9](https://opg.optica.org/abstract.cfm?URI=EQEC-2023-ea_p_9).
104. Zarei, M. *Wavemeter API server based, by Python* Dec. 2023. [https://github.com/mehrdadzarei/Wavemeter\\_API\\_Server\\_by\\_Python](https://github.com/mehrdadzarei/Wavemeter_API_Server_by_Python).
105. Zarei, M. *Auto Relocking ECDLs, by RedPitaya* Dec. 2023. [https://github.com/mehrdadzarei/AutoRelocking\\_ECDL\\_Laser\\_by\\_Redpitaya](https://github.com/mehrdadzarei/AutoRelocking_ECDL_Laser_by_Redpitaya).

